Synthesis of graphene platelets

REBECCA SUSAN EDWARDS

Synthesis of graphene platelets

A thesis submitted for the partial fulfilment of the requirement for the

Degree of

Doctor of Philosophy

In the faculty of Science of

Durham University

By

Rebecca Susan Edwards

Durham University

Department of Chemistry

University Science Laboratories

South Road

Durham

2015

Copyright

Declaration

This work was conducted in the Department of Chemistry at Durham University between October 2010 and January 2014. The work has not been submitted for a degree in this, or any other university. It is my own work, unless otherwise indicated.

Acknowledgements

I would like to take this opportunity to thank all the people who have in any way contributed to the work in this thesis. Although all of these cannot be mentioned by name I hope that each person knows how much I appreciate the time, support, encouragement and resources expended upon me throughout my time in Durham; some of which was from people who stood nothing to gain in return. In terms of help from other PhD/postdoctoral students groups I would like to extend my particular thanks to members of the JSOE group for their assistance with XRPD, and to David Johnson from the NRC group for BET surface area measurements. In my own lab group I would like to extend my gratitude to all members past and present for interesting discussions on my work and for their companionship thorough the trials and tribulations of PhD life. The work in chapter 5 was conducted alongside Emily Sole, and the work in chapter 6 was conducted alongside Michael Tynan, so these two group members in particular (both fourth year project students at the time) should be acknowledged for their important contributions to my work. I would also like to acknowledge the valuable contributions from the departmental services team; not only the brilliant departmental analytical services (TGA, ICP) but also the mechanical and electrical workshops and the glassblowers; who play a vital role in enabling novel research to be undertaken.

Special thanks go to Leon Bowen and Budhika Mendis from the Durham University Physics Department for their training on the SEM and TEM respectively (and for the images in chapter 5). Electron microscopy has been one of true highlights of my studies, which was enhanced all the more by the excellent guidance and genuine friendliness of these tutors. Thanks are also extended to the members of the National Engineering and Physical Sciences Research Council (EPSRC) XPS Users' Service at Newcastle University (NEXUS), and the EPSRC UK National Solid-State NMR Service at Durham, who provided an excellent service and produced data that was key to the conclusions of a number of the chapters contained within this work.

I must, of course, extend thanks to the EPSRC and the Durham University Chemistry Department for my PhD funding. It has been a privilege to study in such a well-equipped and all-inclusive environment and an inspiration to be surrounded by so many prominent academics. Naturally my warmest thanks go to my supervisor,

Professor Karl Coleman, not only for his invaluable academic support and key insights into my work but also, and perhaps more so, for his good humour throughout.

Finally I must acknowledge my friends and family for all their love and support; their contribution to my success is immeasurable.

Please note that the data presented in this work are available from http://dx.doi.org/10.15128/kk91fm24c.

Dedication

I dedicate this work to Peter Coyne (1948 – 2012).

Abstract

Graphene, a single-layer of graphite, is frequently termed a ‘wonder material’ due to the wide range of extraordinary properties it possesses and the potential it has for uses in a broad variety of different applications. Key to the realisation of graphene’s use in applications is the ability to produce large scale quantities of graphene with consistent quality, which remains a challenge to the field. The aim of this thesis was to investigate the synthesis of graphene via a number of different methodologies in order to develop novel techniques that are suitable to scale and that provide graphene materials that are useful in different applications. To this aim, four studies were carried out; two involving the ‘top-down’ synthesis of graphene from graphite and two involving the ‘bottom-up’ synthesis of graphene from molecular precursors. In the first study a series of intermediate materials between graphene oxide (GO) and reduced GO (rGO) were successfully produced using a well-controlled reduction reaction, and the trend in their properties was explored, while in the second study rGO was successfully produced using a novel method that is simple, scalable and environmentally friendly. In both these studies a novel method of handling GO was used that eliminated the requirement for the final, time consuming purification step of GO synthesis. In the third study bulk graphene platelets were successfully produced using a novel chemical vapour deposition (CVD) method, and in the final study the templated growth of graphene via CVD over metal microcrystals was investigated. The work builds on some relatively new concepts for graphene synthesis; including tailoring the graphene product to the particular application and size/shape control for bulk scale graphene platelets, and also presents an interesting case study on carbon growth on copper which may provide new insights into carbon synthesis in these systems.

Table of Contents

List of abbreviations

2D	Two dimensional
3D	Three dimensional
a-C	Amorphous carbon
a-C:H	Hydrogenated amorphous carbon
BF	Bright field
CNTs	Carbon nanotubes
CVD	Chemical vapor deposition
DF	Dark field
DLC	Diamond–like carbon
DMF	Dimethylformamide
ED	Electron diffraction
EDXS	Energy-dispersive X-ray spectroscopy
EELS	Electron energy loss spectroscopy
EFTEM	Energy filtered transmission electron microscopy
FFT	Fast Fourier transform
FTIR	Fourier transform infrared
FWHM	Full width at half maximum
GIC	Graphite intercalation compound
GO	Graphene oxide
GrO	Graphite oxide
h-BN	Hexagonal boron nitride
HRTEM	High resolution transmission electron microscopy

MAS	Magic-angle spinning
NMP	N-Methylpyrrolidone
PVA	Poly(vinyl alcohol)
rGO	Reduced graphene oxide
SAED	Selected area electron diffraction
SEM	Scanning electron microscopy
SSNMR	Solid state nuclear magnetic resonance
STEM	Scanning transmission electron microscopy
ta-C	Tetrahedral amorphous carbon
TEM	Transmission electron microscopy
TGA	Thermogravimetric analysis
UV-Vis	Ultraviolet–visible
WEG	Worm-like exfoliated graphite
XPS	X-ray photoelectron microscopy

Chapter 1: Literature Review

The following chapter aims to provide a brief overview of the structure and properties of graphene along with a more detailed account of the different methods currently used for its production. The potential applications of graphene are discussed and the relationship between synthesis methods and applications is considered.

1.1 Introduction

The isolation of graphene by Geim and Novoselov in 2004 saw a new allotrope of carbon added to the list of other useful and well-studied allotropes that includes graphite, diamond, fullerenes and carbon nanotubes (CNTs).[1, 2] These crystalline forms of carbon sit alongside disordered forms of carbon such as diamond-like carbon (DLC) to make up a varied range of carbon-based materials that offer both academically interesting systems and a plethora of real world applications.[3] The number of publications relating to graphene has increased almost exponentially since its discovery,[4] whereby in 2013 the number of articles published on the subject equated to over 40 per day.[5] This intense interest is, in large part, due to the wide range of outstanding properties reported and predicted for the material, but also because graphene represents an ideal system for studying two dimensional (2D) materials in terms of fundamental physics.[6] The study of graphene and its applications spans a broad variety of academic fields and has been the catalyst for research in a number of related systems including other 2D materials like silicene and single-layer hexagonal boron nitride (h-BN),[7, 8] and graphene derivatives such as graphane and graphyne (table 1).[9, 10] Furthermore, the field of graphene itself can be subdivided to take into account the dimensions of the material; leading to distinct research areas for graphene nanoribbons,[11] graphene quantum dots,[12] and, more recently, three dimensional (3D) graphene architectures such as graphene foams.[13] The current literature review focuses on graphene platelets and films, although other geometries of graphene are also mentioned.

Table 1: A summary of several of the materials that have garnered enhanced interest due to the success of graphene research.

Material	Description	Ref
Silicene	Single-layer silicon. Predicted to have a buckled honeycomb structure with sp^3/sp^2-like hybridised Si atoms and similar electronic properties to graphene. Must be grown, as layered silicon (to exfoliate) does not exist in nature.	14
h-BN	Alternating B and N atoms in a honeycomb arrangement. Also known as "white graphene". Dielectric with a large band gap (>5 eV). Can either be grown or isolated from bulk BN.	15
Graphane	Fully saturated hydrocarbon with a formula of CH. Predicted to have a structure where sp^3 carbons form a hexagonal network and H atoms are bonded to C on both sides of the plane (alternating). Made by hydrogenation of graphene. Electrical insulator.	16
Graphyne	Layered carbon sheet containing hexagons of carbon (sp^2) connected by linear carbon chains (sp). Predicted to be a semiconductor with a moderate band gap (0.5-0.6 eV) and to have mechanical properties similar to graphite. Must be synthesised.	17

1.1.1 Structure

The term 'graphene' refers to a single layer of graphite, with sp^2 hybridised carbon atoms arranged in a hexagonal lattice and partially filled π-orbitals above and below the plane of the sheet. Seemingly contrary to this, the term 'graphene' is commonly prefixed by 'monolayer', 'bilayer' or 'few-layer'. This categorisation has been made as the electronic properties of bi and few layer graphene (where 'few' is not rigorously defined but is generally expected to be < 10 layers) are distinct from the electronic properties of graphite.[18, 19] While monolayer graphene is generally accepted to exist in a rippled form with no stacking of sheets,[20-22] few-layer graphene can have a number of stacking arrangements, including ABAB (Bernal stacking), ABCABC (rhombohedral stacking), and less commonly AAA.[23, 24] Few-layer graphene with no discernible stacking order is also common, and is termed 'turbostratic'. The interlayer spacing for turbostratic graphene (>0.342 nm) has been found to be larger than that of crystalline graphene (0.335 nm),[25] which is thought to enable rotation and translation of the graphene sheets due to the increased distance resulting in weaker inter-planar bonding.

The edges of graphene can be described as having armchair or zigzag motifs (figure 1), with the two edge types leading to different electronic and magnetic properties.[26, 27]

Generally speaking, graphene has a mixture of these two edge forms, although synthesis of graphene structures with defined edges is a growing area of research given the potential to tune the properties for specific applications.[28] In particular, graphene nanoribbons have received a great deal of attention as quantum confinement effects (due to reduced dimensions) are thought to lead to novel electronic properties including the opening up of a band gap, as reviewed in detail elsewhere.[29, 30]

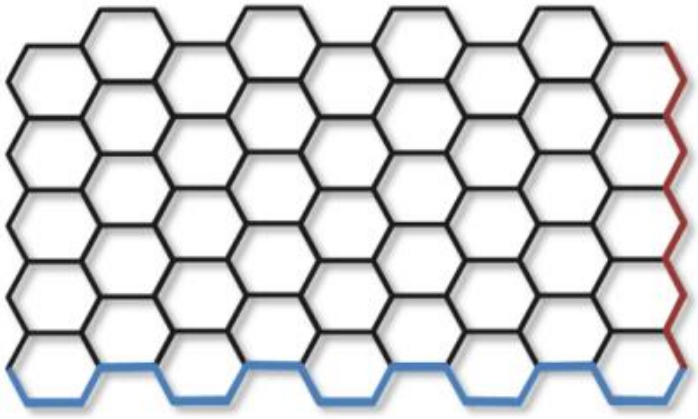

Figure 1: Graphical representation of armchair (blue) and zigzag (red) edges in monolayer graphene.

1.1.2 Properties

It is easy to see why graphene has been termed a "wonder material" when looking at the physical properties measured and predicted. As a single layer of carbon atoms, graphene is the thinnest material known yet it is impermeable to gases,[31] and it is stronger than steel (Young's modulus ~ 1TPa).[32] Furthermore graphene's room temperature thermal conductivity (up to ~5000 W/mK) rivals the values obtained for bundles of carbon nanotubes and is over double the next best thermal conductor known, diamond.[33] Being single layer, graphene also has an extremely high surface area; with a theoretical value of 2630 m^2g^{-1} and is almost transparent; absorbing only ~2.3% of white light.[34] Graphene has also shown good 'foldability', recovering its electrical properties after bending and unbending.[35] The thermal,[36] electronic,[37] and general properties of graphene have been reviewed in detail elsewhere.[38]

The electronic properties have perhaps received the most attention. Graphene has been shown to have extremely high charge carrier mobilities,[39] with values in excess of 200 000 $cm^2V^{-1}s^{-1}$ reported for freely suspended graphene,[40] making it an excellent conductor of electricity. This conductivity arises due to the unusual behaviour of the

propagating electrons in graphene, which are said to act as massless fermions, best described by a Dirac-like equation rather than the Schrödinger equation used for conventional systems.[37] As a consequence of this, electrons in graphene reportedly travel at a Fermi velocity (v_F) of ~1 x 10^6 ms^{-1}, and can travel distances in the order of micrometers without scattering; a phenomenon which is referred to as ballistic transport.[41] This behaviour, and a number of other quantum relativistic effects exhibited by graphene such as the quantum Hall effect,[42] makes graphene an interesting material to study from a fundamental physics perspective.[43] It should be noted that the electronic properties of bilayer graphene are distinct from monolayer, and hence this material is studied in its own right as a structure that has a tuneable band gap and its own interesting quantum relativistic effects; for example an integer quantum Hall effect.[44, 45]

It is worth mentioning that many of the amazing properties have been recorded on high quality, small area monolayer graphene samples, and may not be achievable for larger, bulk scale sheets. An example of this is that while ballistic transport is believed to have been observed experimentally by Miao *et al.* for short graphene strips, evidence of diffusive transport (where scattering does occur) was seen for larger samples.[46] Electron scattering of graphene is thought to be caused by impurity defects and topological lattice defects within the graphene sheet,[47-49] and to be worsened by interactions with the substrates resulting in surface stabilised ripples, interfacial phonons, surface charge traps and fabrication residues.[40] Recently the elastic stiffness and strength of CVD grown graphene has been shown to be comparable with the values for pristine graphene despite the presence of grain boundaries in the former.[50] This is a promising finding, however it is noted by the authors that this result was true for graphene etched and transferred in a specific way; and other common practices for graphene etching and removal (etching metal with $FeCl_3$ and baking off polymer support in air) severely weakened the grain boundaries.

In addition to the presence of defects affecting the properties of graphene the number of layers also has an impact. Further to the surface area and transparency of graphene decreasing going from monolayer to few-layer graphene,[51] other physical properties have been observed to change upon increasing thickness; although there has been limited work in this area. The extent to which graphene thickness impacts the properties is likely to vary depending on what's being studied, for example while a gradual change in electronic properties has been calculated for increasing numbers of

layers,[19, 52, 53] the experimentally measured thermal conductivity has been shown to be very sensitive to graphene thickness; with the value for four graphene layers being almost the same as that of bulk graphite.[54] The change in hardness and elastic modulus has also been reported for different thicknesses of graphene,[55] where a linear decrease for both properties was measured as the number of layers increased up to four.

1.2 Applications

Whilst each of graphene's properties is remarkable in its own right, it is the combination of so many outstanding properties in one material that makes graphene promising for such a broad range of applications. In particular the combination of high electrical conductivity, flexibility and transparency has inspired many of the envisaged future applications of graphene such as roll-up and wearable electronics, in addition to a plethora of other real work applications where graphene may find a use, such as energy storage materials, polymer composites, transparent electrodes, and sensors (figure 2). The applications of graphene are discussed briefly below and have been extensively reviewed elsewhere.[5, 56-59]

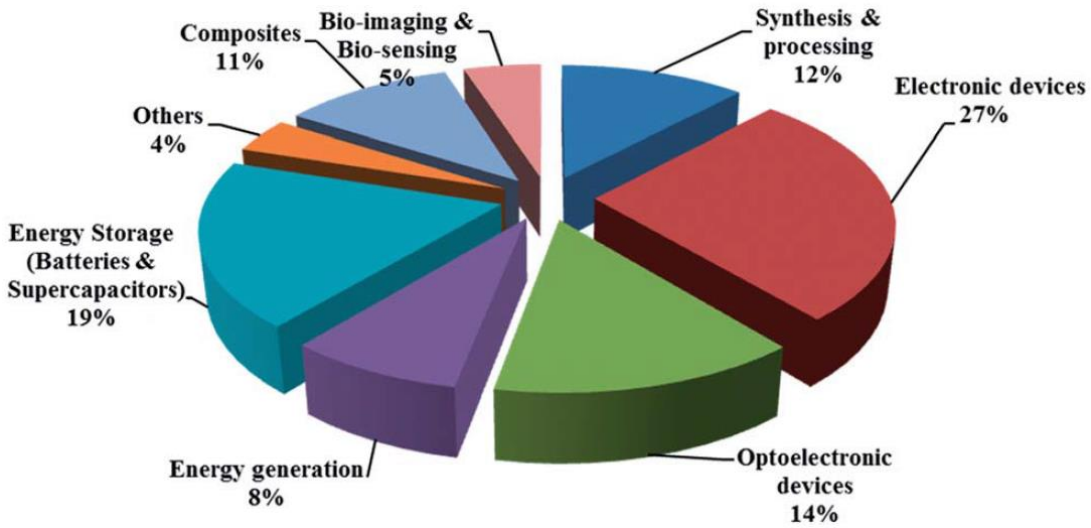

Figure 2: A chart summarising the interest in graphene for different applications.[56]

1.2.1 General applications

The properties of graphene which appear attractive will depend on the particular application, as summarised below for a number of different applications (figure 3). The progress in the use of graphene in these applications (transistors,[60] energy storage devices,[61] electrodes,[62, 63] conductive inks,[64] polymer composites[65, 66] and sensors[67, 68]) has been reviewed or discussed in detail elsewhere, along with discussions on a range of other applications such as metal-free catalysis[69] and biomedicine.[70]

	Electrical Conductivity	Strength	Elasticity	Surface Area	Transparency	Thermal Conductivity	Chemcial Inertness	Gas impermeability
Transistors	✓	×	×	×	×	×	✓	×
Energy storage devices	✓	×	×	✓	×	×	✓	×
Electrodes	✓	□	□	□	□	×	✓	×
Electrically conductive inks	✓	×	✓	×	□	×	✓	×
Polymer composites	✓	✓	✓	✓	□	✓	✓	□
Sensors	✓	×	□	×	×	×	✓	□

Figure 3: A summary of which of graphene's properties are important for the different applications; where a tick indicates importance, a cross indicates relative unimportance and a square indicates that the property is sometimes important.

In displays, graphene has considerable potential to replace indium tin oxide (ITO). Replacing ITO, used as a transparent conducting film in devices such as displays, organic light emitting diodes (OLEDs) and solar cells, is a pressing requirement as indium is a finite resource and its cost is rising due to increased use in a range of technological applications.[71] A single layer of graphene is more optically transparent than ITO (approx. 98 and 90 % respectively) but for the films measured to date it has a much higher electrical resistance (2000-5000 Ω and 50 Ω respectively). The resistance can be reduced by increasing the number of graphene layers but this is achieved at the expense of reduced transparency.[72] Alternatively doping with nitric acid has been shown to decrease the sheet resistance of graphene films,[73] with sheet resistance as

low as ~30 Ω/□ having been reported for doped sheets of 90 % transparency.[73] Graphene's real advantage over ITO is that it is flexible while ITO is brittle,[74] making the likely transition to flexible electronics easier.

In electronics, graphene has the potential to produce smaller, faster devices than silicon but it suffers from the major pitfall that a band gap needs to be engineered to achieve the "on" and "off" states required in digital electronics.[75] Graphene can be described as a 'semi-metal' or a 'zero-band-gap' semiconductor as the conductance and valence bands touch in the Brillouin zone,[76, 77] however it is possible to create a band-gap by confining the lateral dimensions of graphene (for example forming 'nanoribbons' by lithography[78] or unzipping carbon nanotubes[11]), applying strain,[79] or via electrical or chemical doping.[80-82]

The use of graphene in some applications can be an exercise in compromise. This is particularly true for graphene in polymer composites. It is thought that by dispersing graphene platelets in polymer matrices the favourable properties of graphene will be exhibited by the composites,[83] where in addition to its remarkable physical properties, graphene stands out from other fillers such as carbon nanotubes due to its large surface area; which allows high levels of contact with the polymer. In order to take advantage of this large surface area and to maximise its effectiveness as a filler, the dispersion of graphene must be good; containing reasonable quantities of unagglomerated thin sheets. The problem is that high quality, defect free graphene is not very soluble.[84] Instead the majority of graphene composites have been produced using 'graphene oxide' or 'reduced graphene oxide', as the functional groups that these materials contain allow better dispersions and, in some case, better interactions with the polymer matrix.[85] The downside is that functionalisation disrupts the sp^2 hybridisation of the graphene sheets and subsequently degrades their physical properties.[86] Good dispersions are also required for conductive inks to prevent the agglomeration of graphene nanosheets during deposition and drying, so similar considerations need to be taken into account for the use of graphene in these applications. It is worth emphasising that real-life composite applications will require large volumes of filler material and that synthesis methods to produce graphene should take this into consideration and should be amenable to scale. This will also be true if graphene platelets are to be used for energy storage materials such as supercapacitors,[87, 88] where recently graphene based supercapacitors have been shown to store almost as much specific energy as nickel hydride batteries.[88]

1.2.2 The relationship between synthesis and applications

It is important to note that the quantity and form of graphene required depends on the particular application; while some applications such as transparent electrodes and sensors require thin films of graphene, other applications such as energy storage devices (e.g. batteries and supercapacitors) and polymer composites require relatively large quantities of graphene nanosheets or platelets (figure 4). Furthermore the importance of using high quality, monolayer graphene will vary with application type, for example no noticeable improvement in electrochemical activity has been observed going from few-layer to monolayer graphene,[89] and defects in the material are thought to enhance both the electrochemical[90] and hydrogen storage[91] ability of graphene sheets.

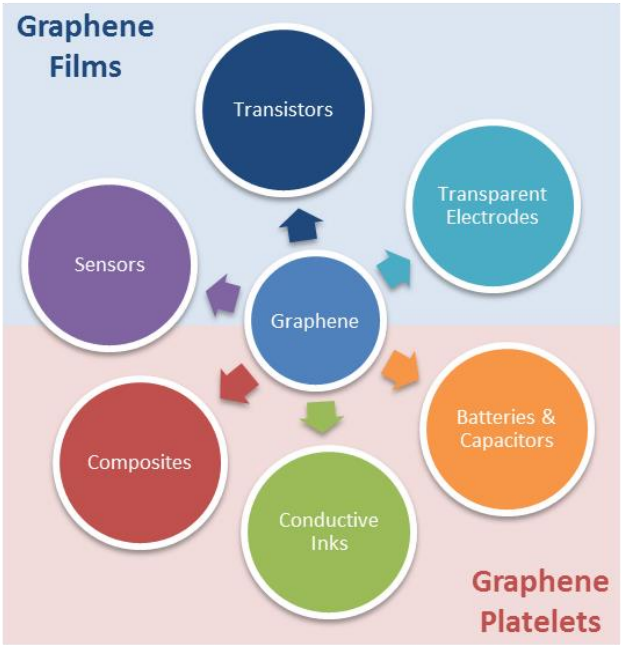

Figure 4: A summary of the form (films/platelets) of graphene required for different applications.

In order for graphene's potential to be fully realised, methods for its synthesis need to be developed that can produce good quality material reproducibly. Although this still remains a significant challenge, a number of different routes to synthesise graphene have been demonstrated over recent years, as discussed in section 1.3. Some of the methods, by their very nature, lend themselves better to certain applications than others. An example of this is that growth on SiC results in graphene on a wide-band gap semiconductor, which is appropriate for the fabrication of graphene devices operable at room temperature without the need for film transfer,[92-94] whereas graphene grown on metals requires transferring to insulating substrates for these applications. In

contrast, material used for field emission applications needs good ohmic contact so graphene grown on metals is a more obvious choice.[58] Similarly graphene films can be formed from individual graphene nanosheets by processes such as spin coating,[95] drop casting,[96] spraying,[97] electrophoretic deposition[98] and Langmuir-Blodgett methodologies,[99] but these films are less conducting due to both poor contact between the sheets and defects at the sheet edges, and hence are less suitable for applications that require high electrical conductivity.[100]

1.3 Synthesis

Graphene synthesis can be split into two different types of approach; 'top-down' and 'bottom-up'. 'Top-down' approaches involve breaking apart the stacked layers of graphite to yield single graphene sheets, whereas 'bottom-up' methods involve synthesising graphene from alternative carbon containing sources (figure 5). For 'top-down' methods separating the stacked sheets means that the van der Waals forces that hold the layers together must be overcome, which is not a trivial task despite the relatively low interlayer bonding energy.[101] Key challenges in this area include effectively separating the layers without damaging the sheets and preventing re-agglomeration of the sheets once the layers have been exfoliated. 'Top-down' approaches (figure 6) generally suffer from low yields, require numerous steps, and have the common disadvantage that natural graphite is a finite resource that is on the European list of scarce materials,[102] and requires mining and processing prior to use. Graphite can be produced synthetically under high temperature conditions,[103] but it is not really suitable for graphene production due to poor levels of graphitisation and irregular morphologies. For 'bottom-up' methods (figure 7) high levels of graphitisation must be promoted to produce good quality material, so these methods generally require high temperatures. The processes involved are usually simple, although the material produced can contain higher levels of defects than observed for 'top-down' methods. In addition to forming graphene nanosheets, 'bottom-up' methods can also be used to form large area graphene films via growth on certain substrates.

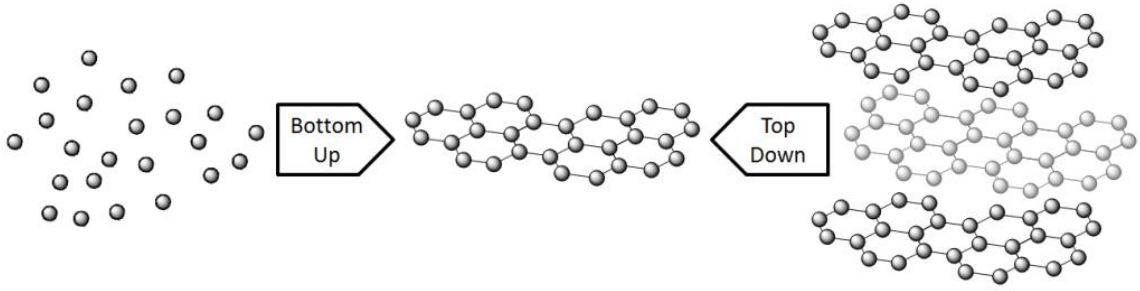

Figure 5: A schematic of 'bottom-up' and 'top-down' graphene synthesis

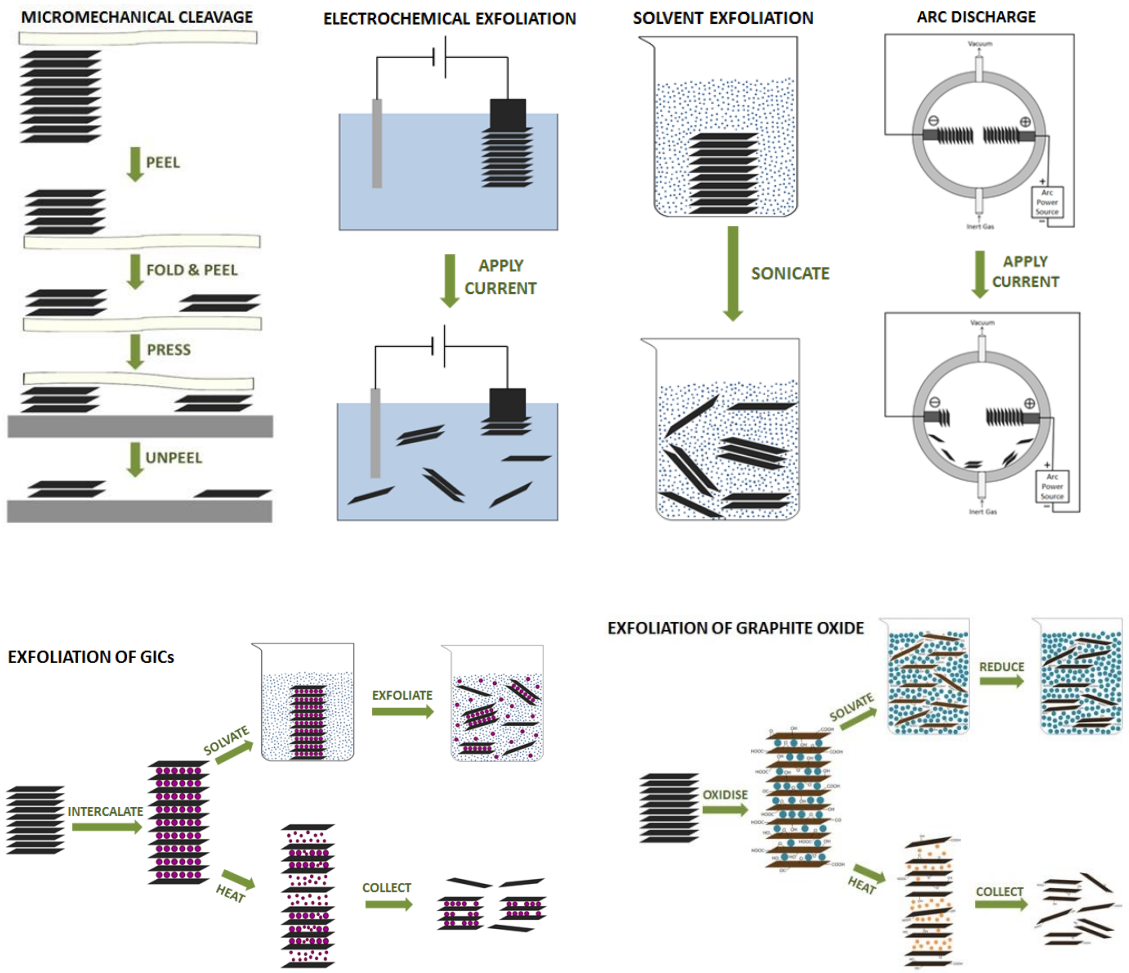

Figure 6: 'Top-down' approaches for synthesising graphene directly from graphite.

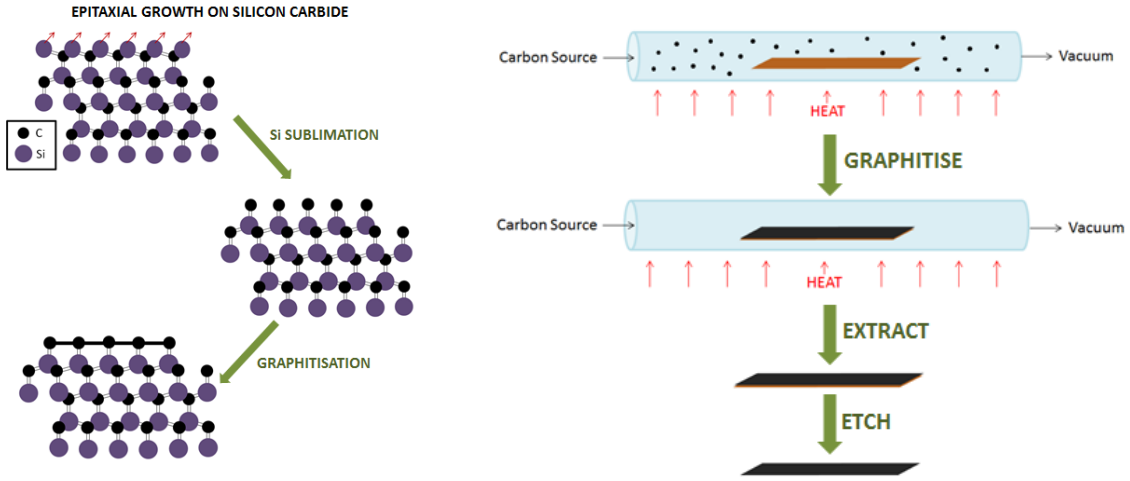

Figure 7: 'Bottom-up' approaches for growing graphene films from alternative carbon sources.

1.3.1 'Top-down' Methods

1.3.1.1 Micromechanical cleavage

The 'scotch tape' or 'peel-off' method involves the exfoliation of graphite using adhesive tape to cleave the layers apart, and was the first method used to experimentally isolate graphene.[1] Repeated cleavage yields mono-, bi- and few-layer graphene which are identified by optical microscopy over specially prepared SiO_2(300 nm)/Si substrates, taking advantage of the change in refractive index between graphene and 300 nm thick silicon dioxide. The sheets are of high quality as a result of the limited graphite processing required, but the method is slow and labour intensive so the material produced is often reserved for study of the fundamental properties of graphene rather than use in commercial applications.

1.3.1.2 Electrochemical exfoliation

Electrochemical exfoliation of graphite generally involves using graphite as a sacrificial electrode and collecting the exfoliated material from the electrolyte solution. The exfoliation process can result in oxidised or non-oxidised graphene depending on which electrode the graphene is produced from (the anode or cathode respectively), where both suffer from the same lack of selectivity in terms of controlling the sheet thickness and the same issues regarding agglomeration of the exfoliated material in solution. An early example of electrochemical exfoliation described the use of surfactants to prevent aggregation,[104] however these surfactant molecules were difficult to remove and surfactants have been shown elsewhere to be detrimental to the electrical and electrochemical properties of graphene,[105] and hence this is not a widely adopted technique. In 2011, sulfuric acid was shown to be an effective electrolyte for graphite exfoliation; which was attributed to intercalation of $[SO_4]^{2-}$ ions.[106] Since then the production of >80% 1-3 layer graphene flakes has been reported for the exfoliation of graphite in 0.1 M H_2SO_4,[107] and the production of >85% 1-3 layer graphene flakes has been reported for the exfoliation of graphite in 0.1 M $(NH_4)_2SO_4$.[108] In this latter study a yield of ~16.3 g was reported for 30 minutes reaction time, which acts as evidence that electrochemical exfoliation is a scalable technique.

Other strategies for electrochemical exfoliation include combining electrochemical intercalation with solvent based exfoliation,[109, 110] and, more recently, using plasma-assisted exfoliation.[111] In the former, high yields of few-layer graphene (>70% and ~80%) were reported for exfoliating lithium intercalated graphite electrodes in either a

mixed solvent of dimethylformamide (DMF) and propylene carbonate,[109] or pure water (figure 8).[110] Exfoliation in water was thought to be assisted by the formation of hydrogen gas between the graphitic layers due to the reaction between lithium and water. For plasma-assisted exfoliation hydrogen was also thought to play a part; by promoting expansion and subsequent exfoliation of the surface layer of the graphite electrode.[111] The material produced by plasma-assisted exfoliation was relatively thick (~10-30 nm thick), but produced a rate that is quoted as six times faster than conventional methods. The electrochemical exfoliation of graphite has been comprehensively reviewed elsewhere.[112]

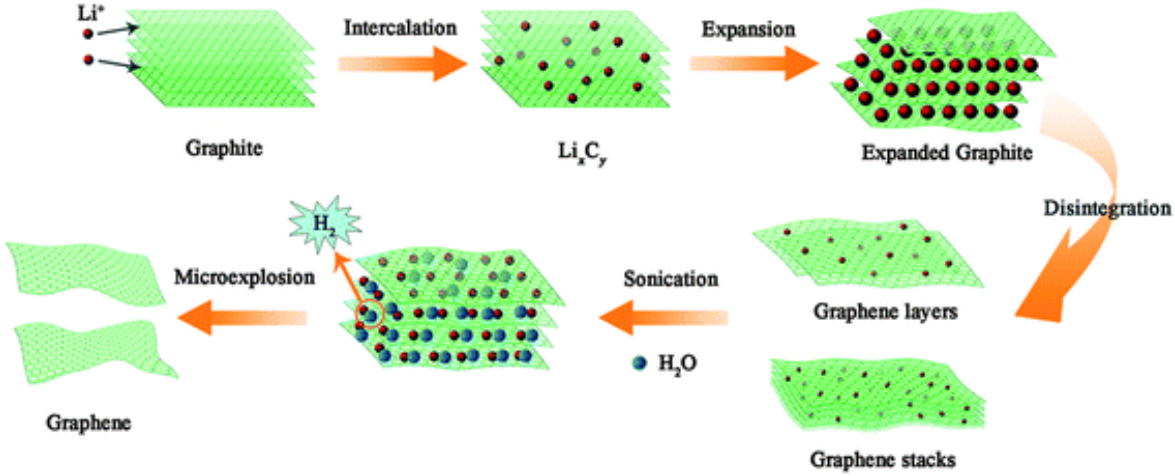

Figure 8: A sketch showing the formation steps of graphene sheets through Li intercalation-expansion-microexplosion processes.[110]

1.3.1.3 Exfoliation of graphite intercalation compounds

Numerous strategies have been utilised for the production of graphene from graphite intercalation compounds (GICs), including solvent-assisted and thermal exfoliation. For solvent-assisted exfoliation, GICs are generally sonicated in solution to aid exfoliation, although spontaneous exfoliation of alkali metal GICs in N-methylpyrrolidone (NMP) has been reported.[113] In addition to the intercalation of solvent molecules expanding the layers,[114] interaction with the solvent may cause gas to be expelled. This aids exfoliation, as seen for the sonication of lithium GICs in water discussed above, and for sonication of alkali metal GICs in ethanol; where alkali metal ethoxide and hydrogen gas were formed.[115]

The effect of thermal expansion of GICs was reported as early as 1916 for heating graphite-bromine intercalation compounds,[116] but marked interest in the field did not

begin until the late 1960s, when foils of exfoliated graphite were designed as gasket and sealant materials.[117] Heating of GICs generally causes thermal decomposition of the intercalates into gaseous species that push the layers apart. 'Expanded graphite', also known as 'exfoliated graphite', has many industrial applications such as thermal insulators and composite filler materials,[117] and more recently has been considered as a precursor for graphene.[117] The most common method for expanded graphite formation is via the exposure of graphite to strong acids to yield a GIC (often graphite bisulfate) which is then exfoliated by rapid thermal heating or, more recently, by microwave radiation.[118] Single to few-layer graphene has been reported for expanded graphite ground in ethanol,[119] or sonicated in NMP (figure 9),[120] and repeated cycles of intercalation-exfoliation followed by sonication in DMF has been shown to yield over 50% single and bi-layer graphene.[121] Other examples of GICs designed for thermal exfoliation include graphite co-intercalated with iron chloride ($FeCl_3$) and nitromethane (CH_3NO_2),[122] and graphite intercalated with ionic liquid crystals (ILC).[123] In the former iron chloride is used to promote the intercalation of nitromethane, which decomposes at relatively low temperatures (~100 °C) under microwave radiation, while in the latter mild heating is used to promote ILC intercalation due to their reduced viscosity at higher temperatures, and stronger heating (to 700 °C) is used to induce thermal decomposition. Using a similar principle supercritical carbon dioxide has been utilised to exfoliate graphite, based on intercalation of the CO_2 in the supercritical phase followed by rapid expansion upon depressurisation to form gaseous CO_2, which forces the graphitic layers apart.[124]

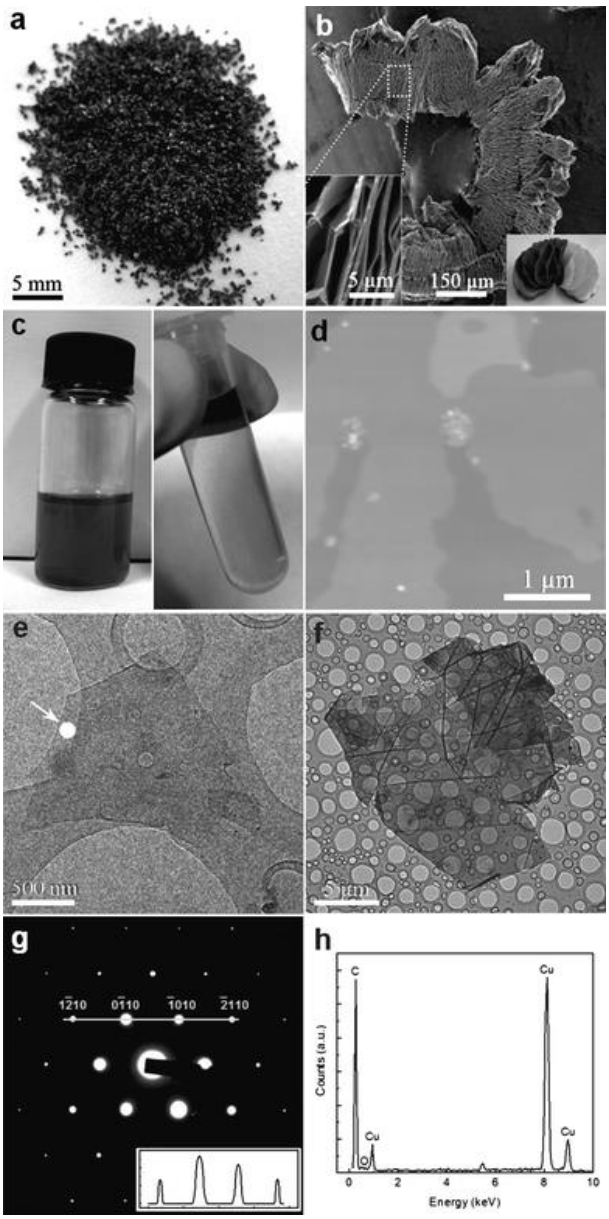

Figure 9: Graphene from liquid phase exfoliation of worm-like exfoliated graphite (WEG). Photograph of WEG (a), SEM image of WEG (b), uniform dispersions upon sonication (c, left) and centrifugation (c, right), AFM image (d) and TEM image (e) of the monolayer graphene sheets, TEM image of the monolayer graphene sheets (f), electron diffraction from the white spot marked in e (g), EDXS spectrum of the graphene sheet in f (h).[120]

1.3.1.4 Solvent-based exfoliation

For solvent-based exfoliation, dispersions of graphite are exposed to either bath or probe sonication, which acts to separate the layers via the injection of thermal shock into the material through acoustic cavitation (the formation, growth and collapse of bubbles).[125] The exfoliation of unmodified, natural flake graphite via sonication in solvents was reported in 2008 by two separate groups,[126, 127] and since then there have been numerous reports of exfoliation in a range of different media; with the aim of

producing stable, highly concentrated dispersions of monolayer graphene. In an early study of graphene dispersibility in 40 different solvents it was concluded that the best solvents for creating concentrated dispersions have a Hildebrand solubility parameter of δ_T ~ 23 $MPa^{1/2}$, Hansen solubility parameters of δ_D ~ 18 $MPa^{1/2}$, δ_P ~ 9.3 $MPa^{1/2}$ and δ_H ~ 23 $MPa^{1/2}$, and surface tension close to 40 mJ/m^2.[84] The solvent that gave the highest absolute concentration was found to be cyclopentanone (~0.0085 mg/mL), while the solvent which contained the highest proportion of monolayer graphene was NMP.

Highly concentrated dispersions of graphene are desirable as they require smaller volumes of potentially expensive and hazardous solvents. Several strategies for achieving high graphene concentrations have been reported including simply increasing sonication time or sonicating with a sonic probe rather than a sonic bath.[128, 129] A further strategy involves the pre-sonication of graphene in different solvents then isolation via filtration and redispersion in the desired media.[129, 130] This method has been used to create graphene dispersions with concentrations of up to 63 mg/mL graphene in NMP.[129] The strategy of pre-sonication has also been used to produce more concentrated dispersions of graphene in ethanol, through a multi-step solvent exchange process.[131] The dispersion of graphene in low boiling point solvents is an important challenge as many of the best solvents for graphene have high boiling points (for example NMP has a boiling point >200 °C) which makes their removal difficult when forming films or coatings from solution. Extended sonication (48 hours) of graphite in 'poor' but low boiling point solvents has been shown to yield graphene concentrations approximately half the value reported for NMP after 460 hours of sonication,[132] however it should be noted that while prolonged sonication time improves the dispersibility of graphene it also decreases the average flake size and increases the defect concentration.[128]

Another strategy for exfoliation of unmodified graphite flakes involves sonication in aqueous surfactant solutions,[133, 134] which has the advantage of avoiding expensive and often harmful solvents. In addition, surfactants can prevent re-aggregation of the graphene due to the repulsive potential barrier between surfactant-coated sheets; the importance of which has been studied with regard to graphene dispersion for both ionic and non-ionic surfactants.[135] Polymers have also been shown to be effective additives to aid the exfoliation and dispersion of graphite in different solvents,[136] and are thought to act through steric stabilisation rather than electrostatic stabilisation (as is the case

with surfactants.) A range of other exfoliation/dispersion agents for graphite have been reported and are reviewed in detail elsewhere.[137] Other, general reviews of solvent-based exfoliation also exist.[138, 139]

It should be noted that recently solvent-based exfoliation of graphite has been demonstrated using shear mixing rather than sonication.[140, 141] In these cases exfoliation was observed when the local shear rate exceeded a critical value (~10^4 s^{-1}.) Exfoliation has been reported for both shear mixing in NMP,[140] and in an aqueous surfactant solution,[141] where the latter was performed in a commercial kitchen blender. These methods produced graphene with higher concentrations than reported for graphite exfoliation via sonication and are suitable to scale but suffer the same pitfalls in terms of using expensive solvents, the difficulties of removing surfactants, and the reduction of the sheet size during processing.

1.3.1.5 Exfoliation of graphite oxide

The synthesis of graphene via the exfoliation of graphite oxide (GrO) can be described as a multi-step reaction where graphite is oxidised to GrO, GrO is exfoliated to graphene oxide (GO), and GO is reduced to graphene (figure 10). The material produced via this method is generally termed 'reduced graphene oxide' (rGO) or 'functionalised graphene', as the structure is distinct from graphene due to the presence of residual oxygen functionalities and other defects that form during the oxidation process.[142, 143] Despite the fact that rGO is not a precise analogue of graphene, this method is generally regarded as one of the most promising routes to bulk scale production of graphene platelets, and as such it is the topic of a large number of reviews.[144-148]

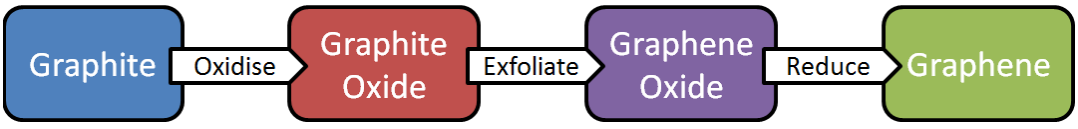

Figure 10: A flow diagram to illustrate the various stages involved in the production of graphene via GrO.

The oxidation of graphite using concentrated acid and strong oxidants has been known since 1840,[149] but the process experienced renewed interest in 2006 after the

discovery that GrO could be readily exfoliated to GO; the oxidised analogue of graphene.[150] Initially much of this interest focussed around the reduction of GO (which is necessary for the restoration of the electrical properties), but more recently GO is being considered for different applications as a material in its own right.[151, 152] The structure of GrO is not clearly defined and can be described by a number of different models, as discussed elsewhere.[147, 152] One widely accepted model is the Left-Klinowski model (figure 11),[153, 154] which describes GrO as having a layered structure with hydroxyl and epoxy groups on the basal planes and carboxylic and carbonyl groups at the sheet edges. These oxygen containing groups make GrO hydrophilic, and the presence of functional groups between layers results in graphite oxide having a larger interlayer spacing (6 – 12 Å depending on the amount of intercalated water) than graphite (3.4 Å).[155] The most prevalent method for GrO synthesis is the Hummers and Offeman method first proposed in 1958,[156] and although a number of adaptations to the methodology have been proposed since,[157-160] the original method is still widely used.

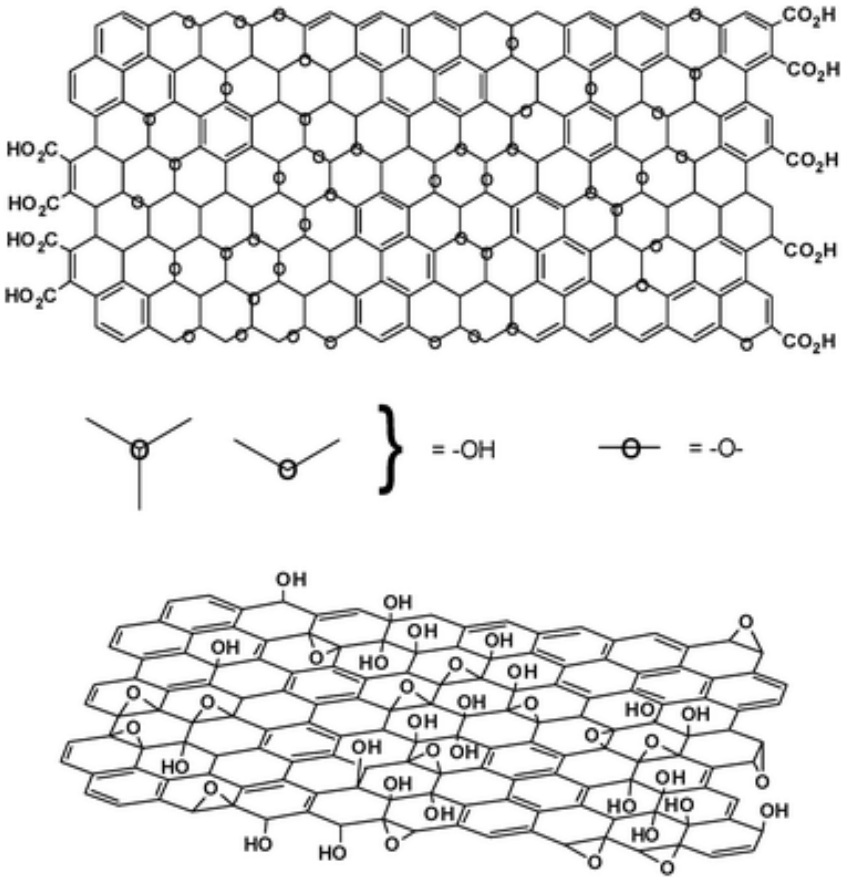

Figure 11: Variations in the Lerf-Klinowski model indicating ambiguity regarding the presence (top) or absence (bottom) of carboxylic acids on the periphery of the basal plane of the graphitic platelets of GrO.[147]

The key advantage of GrO over graphite is that it can be more readily exfoliated, using similar methods as the exfoliation of other GICs; solvent-based and thermal exfoliation.[161] High temperature thermal treatments (>1000 °C) have been shown to both exfoliate and reduce GrO, where deoxygenation is thought to occur via thermally induced bond cleavage of the C-O bonds,[162, 163] while for solvent-based exfoliation the reduction is carried out as a separate step. The reduction of GO in solution has been demonstrated for a number of different techniques and is the focus of many of the aforementioned reviews. The chemical reduction of GO is widely studied, with special focus on the development of methodologies that use "green" reducing agents.[164] Other methods of GO reduction include electrochemical reduction,[165] and the exposure of solutions of GO to different energy sources such as microwaves,[166] lasers,[167] infrared,[168] and solar radiation.[169] One of the key issues surrounding solution based reduction is that GO sheets become less hydrophilic upon reduction and tend to aggregate and precipitate, making complete reduction difficult.[170] The addition of stabilisers, for example surfactants can help in this regard,[171] but must be removed afterwards to fully restore electrical conductivity.[105]

It should be noted that the oxygen functionalities on GO make it an effective starting material for producing functionalised graphene, which can be useful to aid dispersion of the material (or its reduced analogue) in different solvents and enhance its interaction with different media. The functionalisation of GO has been reviewed in detail elsewhere.[149, 172]

1.3.1.6 Arc discharge

Arc discharge, where a direct current is passed between high purity graphite electrodes, has been widely used in the synthesis of carbon nanomaterials including fullerenes and carbon nanotubes (CNTs).[173] More recently arc discharge has been used to synthesise few-layer graphene in a number of different buffer gases.[174-176] The presence of hydrogen gas in the buffer is thought to be important to terminate dangling carbon bonds and hence inhibit the rolling-up and closing of graphitic sheets,[174, 175] and a mixture of helium and hydrogen gas was found to produce the highest crystallinity material from a number of different buffer gases studied.[176] Arc discharge has also been used to synthesise nitrogen and boron doped graphene sheets.[177, 178]

1.3.1.7 Unzipping carbon nanotubes

Graphene or few-layer graphene can be synthesised by unzipping single or multi-walled CNTs respectively using wet chemistry methods such as strong oxidising agents,[179] or by physical methods such as laser irradiation[180] and plasma etching.[181, 182] This unzipping results in graphene nanoribbons, with ribbon widths dictated by the diameter of the tubes. Graphene nanoribbons are considered as quasi one dimensional materials, and have different properties depending on their width and edge type (armchair/zigzag), as discussed elsewhere.[183, 184] CNT unzipping occurs via C-C bond fission which is often initiated at defect sites, leading to irregular cutting.[185] Recently the synthesis of well-regulated nanoribbons has been demonstrated via unzipping of flattened CNTs, where attack occurs preferentially along the bent edges (figure 12).[186] Producing graphene from carbon nanotubes is set to raise interesting questions as graphene is often seen as a replacement or alternative to CNTs.

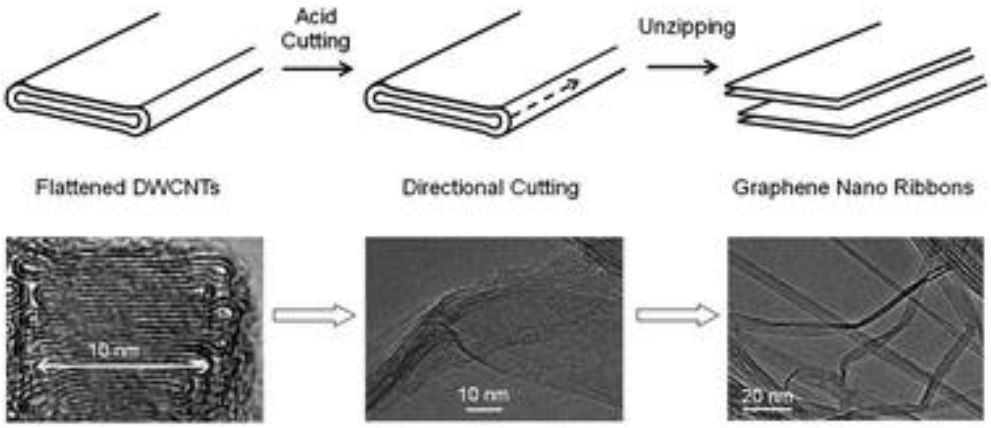

Figure 12: A schematic of directional unzipping of flattened carbon nanotubes (top) and corresponding TEM images (bottom).[186]

1.3.2 'Bottom-up' Methods

1.3.2.1 Epitaxial growth on silicon carbide

The formation of graphene on silicon carbide (SiC) proceeds via the preferential sublimation of silicon from the SiC surface and subsequent graphitisation of the excess carbon atoms left behind.[187] This process occurs at high temperatures (> 1000 °C) and is generally performed in ultra-high vacuum (UHV) conditions, although growth in argon atmospheres[188-190] or in the presence of small quantities of disilane[191] has been shown to reduce the rate of silicon sublimation relative to UHV conditions, allowing higher temperatures to be used and hence resulting in higher quality graphene. Preferential Si

sublimation can also be induced by pulsed electron irradiation, which has been used to produce high quality, millimetre-scale graphene with 1 – 3 layers (figure 13).[192]

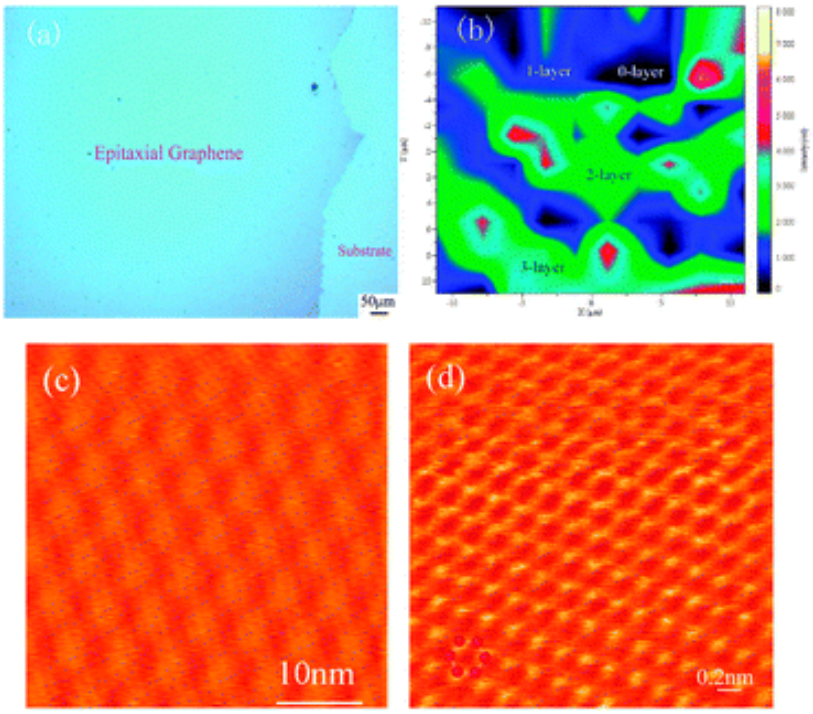

Figure 13: Large scale graphene films grown on 4H-SiC. Optical microscope image of a millimeter-sized carbon film (a), Raman mapping of the intensity of G peaks; the image scale is 20 μm^2 (b), STM image showing the irradiated area is covered by atomic flat graphene flakes (c), atomic resolution image for the well organised graphene (d).[192]

Hexagonal phase silicon carbide (4H-SiC or 6H-SiC) has been widely used for graphene synthesis although more recently growth over cubic phase SiC has also been demonstrated.[193-195] Graphene forms nearly commensurate structures with both the silicon-rich SiC(0001) and carbon rich SiC($000\bar{1}$) faces of hexagonal SiC, and has been grown on both.[196] While in both cases there is an interface layer between the graphene and 'bulk' SiC, a marked difference has been observed between the structures of graphene grown on the different faces; where graphene formation on the Si-rich face is the most studied, and hence well understood, of the two.[197] For the Si-rich face graphene grows in a single orientation (rotated 30° with respect to SiC) and exhibits regular Bernal stacking.[198] The graphene produced is relatively high quality, although the uniformity of graphene with ≤2 layers is rather poor due to surface pits that form as a result of steps in the SiC surface.[199] In contrast, graphene formed on the C-rich face exhibits rotational stacking; where each of the rotations forms a commensurate structure with either SiC or the underlying graphene layer.[196, 200] This rotational misalignment is thought to be the origin of the higher electrical conductivity

measured for graphene on the C-rich face compared with the Si-face, due to the rotation causing electronic decoupling of the layers, resulting in monolayer-like properties for the stacked multilayer.[201] Growth on the C-rich face occurs at lower temperatures than for the Si-rich face and the rate of growth decreases to a lesser extent with graphene thickness, meaning graphene with >10 layers is common for C-face SiC.[197] Like the Si-rich face, the C-rich face is sensitive to the SiC surface, and the presence of unintentional oxide (Si_2O_3) has been shown to affect graphene uniformity.[202] In addition, restricted graphene grain sizes have been observed for material grown on the C-rich face; attributed to the lower growth temperatures used.[197]

The demanding growth conditions are one of the key disadvantages of growing graphene on SiC. One solution that allows lower temperature conditions (700-800 °C) is nickel catalysed growth, where a thin layer of nickel is deposited on the surface of the SiC prior to annealing, and graphene forms on the upper nickel surface.[203-206] While this method uses lower temperatures, it has the additional cost of using a transition metal and necessitates the transfer of graphene to insulating substrates for use in electronic applications. Graphene growth directly on SiC is generally for wafer-based applications, such as electronic devices or components, and as such it is not normally necessary to remove the graphene from the underlying substrate. The transfer of graphene directly from SiC has been demonstrated,[207, 208] although is hindered by the strong interactions between the two materials.[209] SiC is commercially available but expensive (particularly for large area films) so a hurdle for its use in commercial applications will be reducing this cost. Cubic SiC is cheaper to produce,[193] so may pose a solution, but graphene growth on this phase is still in its infancy. The epitaxial growth of graphene on SiC has been reviewed recently.[210]

1.3.2.2 Chemical vapour deposition

1.3.2.2.1 Growth of graphene films on metal substrates

Chemical vapour deposition (CVD), where graphene is formed by the high temperature pyrolysis of carbon containing gases, has been widely used to grow graphene films on transition metal substrates and represents a very active area of graphene research. CVD graphene growth can be categorised as proceeding through either surface-catalysed or segregation methods depending on the metal (figure 14).[211, 212] For surface catalysed reactions the decomposition of the carbon containing species and graphene formation occur at the metal surface, and growth can be described as “self-limiting” to monolayer graphene as the surface is pacified once covered. For

segregation, graphene forms via the diffusion of carbon dissolved in the bulk metal to the metal surface, which generally occurs upon cooling due to the reduced solubility of carbon in metals at lower temperatures. The number of graphene layers produced by segregation depends on various factors including the amount of carbon dissolved and the rate of cooling.[213, 214]

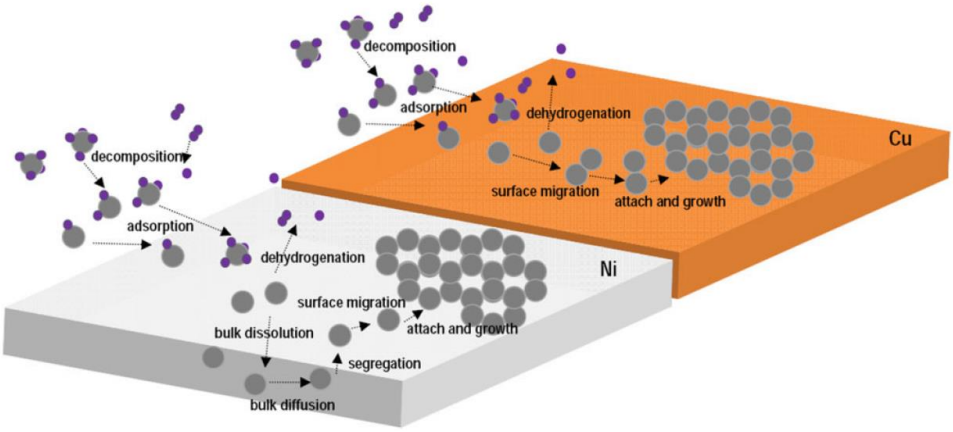

Figure 14: Growth kinetics in CVD-produced graphene on various catalysts: the case of CH_4 on Ni and Cu (segregation and surface catalysed methods respectively).[215]

Graphene growth has been demonstrated on a wide range of metals, including group 8 – 10 transition metals (Fe,[216, 217] Ru,[218-220] Co,[221-224] Rh,[225, 226] Ir,[227, 228] Ni,[35, 229-234] Pd,[235, 236] Pt,[237, 238] Cu,[239-245] Au[246]) and a number of alloys (Co-Ni,[247-250] Au-Ni,[251] Ni-Mo,[252] stainless steel[253, 254]). The optimum conditions for CVD growth vary depending on the metal, with different factors (pressure, temperature, carbon exposure) impacting graphene quality and thickness to different extents depending on the system. In addition, the strength of graphene-metal interaction differs, which can impact the degree of graphene rippling, the sensitivity of graphene to defects in the metal surface, and the ease of graphene transfer to arbitrary substrates. While there are a number of fundamental properties that affect the potential of a metal for use in large-scale CVD growth, ultimately cost and availability are likely to be two of the most important factors, particularly as the metal is generally etched during graphene transfer (figure 15). To date copper and nickel have received the most attention, with graphene films of diagonal lengths up to 30 ” having been grown and transferred from polycrystalline copper foils.[255] Graphene growth on copper is thought to proceed via the surface catalysed mechanism,[239] resulting in monolayer graphene growth for a range of reaction conditions, whereas growth on nickel proceeds via segregation and is more difficult to control,[213] although it has the advantage of not requiring UHV conditions, as used in the majority of syntheses of graphene on copper.

Figure 15: A schematic of graphene growth and removal from metal surfaces.

Continuous graphene growth has been observed over the metal grain boundaries of polycrystalline films of both copper[256] and nickel.[231] This is important as although studying growth over single crystal metals can provide valuable mechanistic information, the difficulty in growing large-area single crystal metals prohibits their use in the production of large-scale graphene films. Instead polycrystalline metal films, in the form of polycrystalline foils or thin films deposited by sputter coating or electron beam evaporation, are likely to be the future for large area CVD grown graphene films.[257] One of the key challenges for growth over polycrystalline films is the behaviour of graphene at the grain boundaries, where even if growth over grain boundaries is continuous, the sites have been shown to lead to defects such as nucleation of multi-layer graphene, which degrade the properties of the graphene films.[230] Work is underway to engineer high quality polycrystalline films by careful control of the metal deposition and annealing conditions.[258]

CVD growth over metals has the disadvantage that harsh growth conditions are required, especially for the metals that utilise UHV conditions. Improving these conditions can be complicated, for example while growth over copper has been demonstrated under atmospheric pressure conditions, patches of multi-layer graphene were observed on the surface; suggesting that unlike in UHV conditions, the growth is not self-limiting to monolayer graphene.[259] Attempts have also been made to reduce the temperatures required for growth, for example using carbon sources with lower decompositions temperatures.[260, 261] Another strategy for reducing growth temperatures is the use of plasma-enhanced CVD; where graphene growth has been reported for substrate temperatures of 500 °C or less,[262-264] as discussed elsewhere.[215, 265]

Metal films are electrically conducting so to enable the use of CVD grown graphene films in a number of electronic applications, transfer of graphene films onto insulating substrates is required. The transfer of graphene from different metals has been demonstrated using a variety of chemical etchants to release the graphene from the metal.[257] This process can be damaging to the films, so often a polymer support is used

to prevent the films from cracking.[266, 267] The general method for this is to spin coat the polymer onto the graphene surface, etch the underlying metal, place the graphene on the new substrate, and dissolve the polymer to yield naked graphene. Furthermore graphene transfer onto flexible substrates has been demonstrated using industrially compatible techniques such as hot press lamination[268] and roll-to-roll transfer;[269] allowing the transfer of large area films. As for transfer using a polymer stamp these processes also require etching of the metal, which is both costly and wasteful. Recently transfer via electrochemical delamination has been posed where only a small amount of the metal is etched, allowing the copper substrate to be reused in subsequent growth reactions.[270]

It should be noted that in addition to CVD growth via vapours introduced into the furnace during the reaction, graphene has been grown from solid carbon sources positioned on top of the substrate, for example the transition metal mediated graphitisation of films of amorphous carbon,[271, 272] nanodiamond,[273] polymers,[274, 275] and self-assembled monolayers (SAMs).[276] The growth of monolayer graphene on copper has even been achieved by thermally decomposing cookies, chocolate, grass, and cockroach legs (figure 16).[277]

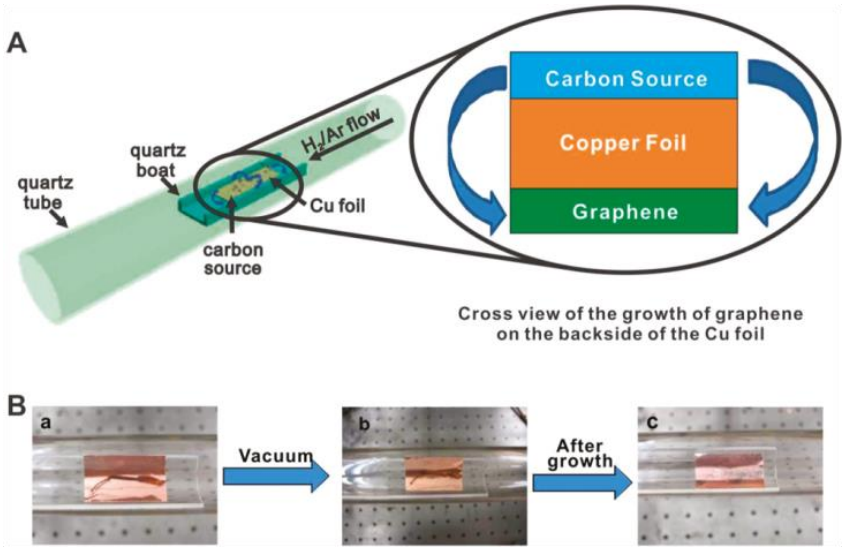

Figure 16: Diagram of the experimental apparatus for the growth of graphene from food, insects, or waste in a tube furnace (A), and growth of graphene from a cockroach leg (B) showing one roach leg on top of the Cu foil (a), the roach leg under vacuum (b) and the residual roach leg after annealing at 1050 °C for 15 min (c). The pristine graphene grew on the bottom side of the Cu film (not shown).[277]

1.3.2.2.2 Substrate-free

Further to growing graphene films, CVD has been also used to synthesise graphene platelets. Substrate-free synthesis has the advantage that specific substrates do not need to be purchased or prepared and that the removal of graphene from the substrate is not required. Additionally, as the material is collected outside the furnace, graphene can be produced via continuous rather than batch processing. An early example of substrate-free growth is the work by Dato *et al.*,[278, 279] where the growth of single and bilayer graphene was reported via atmospheric pressure, microwave enhanced CVD of ethanol. More recently a route to produce few-layer graphene via substrate-free CVD has been demonstrated using thermal decomposition of sodium ethoxide in ethanol.[280] Both methods yield large quantities of graphene.

1.3.2.3 Miscellaneous methods

Graphene nanosheets have been synthesised by a number of other 'bottom-up' methods, resulting in material with different thicknesses and morphologies. One of the best known of these is graphene synthesis via the flash pyrolysis of the solvothermal product of sodium and ethanol.[281] The synthesised graphene product is reported as having a 'foam like structure' consisting of individual graphene sheets that are held together into a porous structure (figure 17), but which can be separated into individual sheets by several minutes' sonication in ethanol. The yield for this reaction is reported as 0.5 g of graphene per solvothermal reaction (0.1 g of graphene per 1 mL ethanol) which is relatively high, however the material produced is more defective than graphene platelets from 'top-down' approaches based on the appearance of the Raman spectrum (figure 17), the C/O ratio (~6.4) and the electrical conductivity, which was ca. 5 orders of magnitude lower than graphite. This illustrates one of the main challenges for 'bottom-up' growth of platelets: catalysing the formation of a well-graphitised product. A number of routes to produce few-layer graphene via the reduction of carbon containing species have also been demonstrated, using methods such as igniting magnesium in dry ice (figure 18),[282] and calcining calcium carbonate with magnesium powder.[283] These methods highlight a further challenge for 'bottom-up' growth of graphene platelets: control of the carbon morphology to form flat sheets.

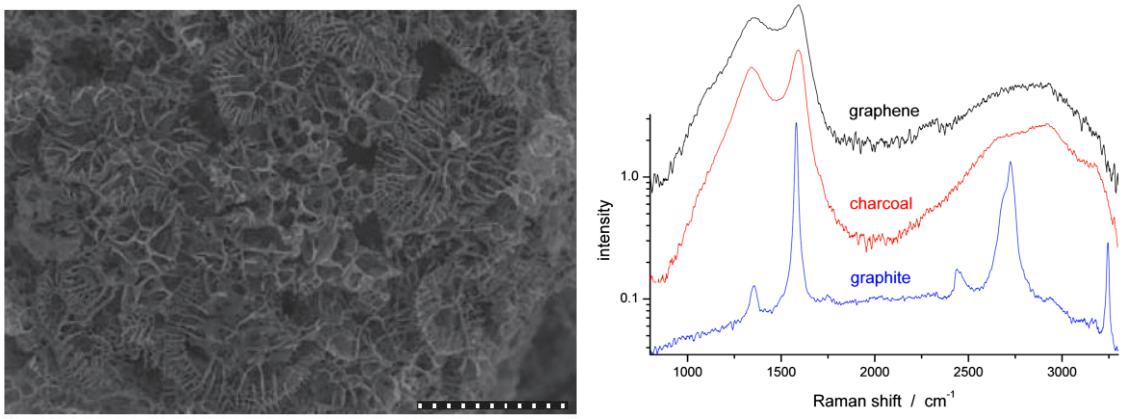

Figure 17: SEM image of the as-synthesised graphene structures; scale bar 15 μm (left) and Raman spectra of the as-synthesised graphene with graphite and charcoal as comparisons (right). Adapted from reference 281.

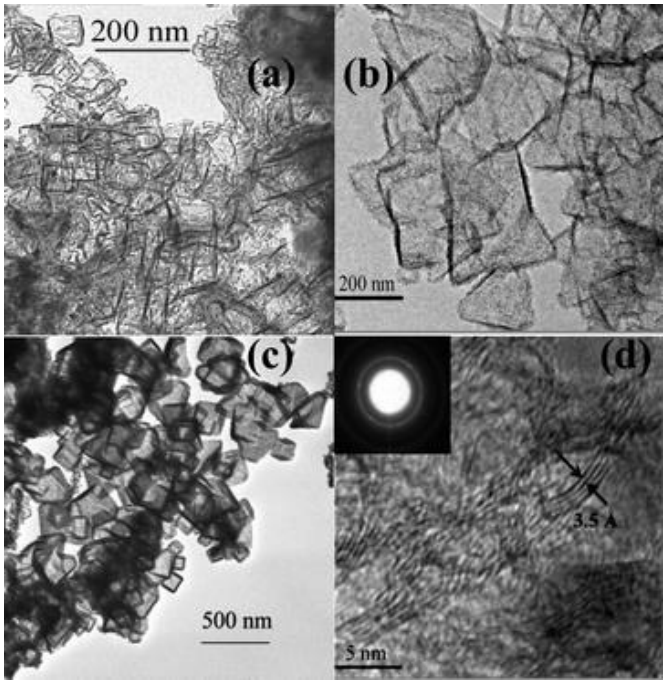

Figure 18: TEM images of few layer graphene produced by burning magnesium metal in dry ice. Graphenes with an average length of 50-100 nm (a) larger size graphene sheets with an average length of 300 nm (b) crystalline graphenes with an average length of 200 nm (c) high-resolution TEM image of few-layer graphenes, with the number of layers ranging from 3-7 (d) and electron diffraction pattern of graphenes (inset).[282]

Recently Xu et. al have presented an approach to graphene nanosheet synthesis that involves both 'bottom-up' and 'top-down' approaches.[284] In this work graphite is produced via high temperature synthesis and carbonisation of metal phthalocyanine in

a microwave-heater at 450 °C and then exfoliated to graphene by rapid cooling. The final product was few-layer graphene with a crumpled sheet morphology (figure 19).

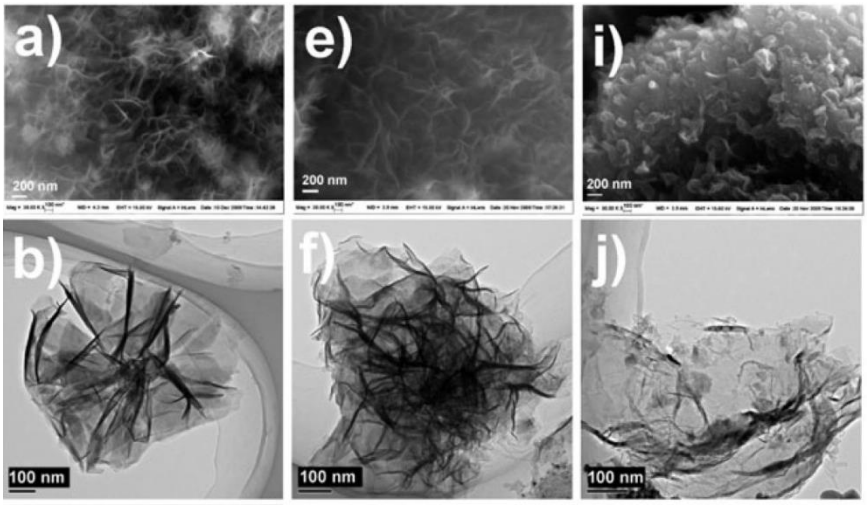

Figure 19: SEM (top) and TEM (bottom) images of graphene produced from metal phthalocyanine using different cooling methods; water (a,b), water and ice (e,f), and liquid nitrogen (i,j). Adapted from reference 284.

The 'bottom-up' synthesis of transparent graphene films has been demonstrated by heating electrically insulating substrates (quartz, SiO_2/Si) spin coated with solutions of polyaromatic hydrocarbons (PAHs) in chloroform to 1100 °C to cause fusion of the molecules and result in graphene films of varying thickness depending on the concentration of PAH solution.[285] PAH chemistry has also been utilised to synthesise structures containing as many as 222 carbon units (37 benzene units) with disk diameters of 3.2 nm,[286] termed 'nanographene', in addition to the formation of graphene nanoribbons using similar methodologies.[287, 288]

1.4 Conclusion

Graphene is an exciting material that continues to attract a large amount of academic interest and financial support over ten years after its initial isolation.[289] The controlled, large scale synthesis of high quality graphene still remains a challenge, although understanding of the processing techniques required to achieve this goal is growing as the body of graphene-based research is expanding rapidly. The methods currently used for graphene synthesis all have their advantages and disadvantages, and which process is used should be guided by the end-application of the material. With so many varied applications is it likely that multiple methods will be need to be mastered to

realise the full potential of graphene. While single layer graphene platelets have been produced using methods amenable to scale, the major products of most large-scale methods are few-layer graphene or thin graphite platelets. Still, many of these materials have shown promise in applications and fill an unoccupied niche, which will help to drive further research in the area.[290] The future of graphene and some of the graphene-like materials produced in the pursuit of graphene is difficult to predict, but it's likely that they are going to play a very important part in many applications.

Chapter 2: Characterisation of carbon nanomaterials

The following chapter is designed to introduce the key characterisation techniques which can be used to gain insight into carbon nanomaterials. As each technique has its own limitations and ambiguities, it is necessary to combine results from a series of different analyses to build an understanding of the materials. In-depth discussion of the theory and background of the characterisation techniques is outside the scope of this work; instead this chapter will focus on the use of these techniques to characterise carbon nanomaterials, and, if possible, to distinguish between them. Where different methods of analysis can be used for a given characterisation technique, the method of analysis used in the current work is highlighted and the reason behind the choice is given.

2.1 Transmission electron microscopy

Transmission electron microscopy (TEM) is a powerful technique for the analysis of carbon nanomaterials due to its high spatial resolution. In this method a thin sample is exposed to a beam of electrons typically created using either LaB_6 filaments or field emission guns (FEGs). In conventional TEMs the electron beam is almost parallel, whereas for scanning TEMs (STEMs) the electron beam is focussed onto a point in the sample plane and scanned across the area of interest.[291] The electron beam energy should be selected such that a large number of electrons can penetrate the sample without causing sample damage. Generally beam acceleration voltages of 80 to 300 keV are used, although for carbon systems beam damage has been demonstrated at energies as low as 100 keV.[292] The information that can be obtained from the TEM depends on the detectors available within the microscope set-up, and will be discussed in detail below.

Transmission electron microscopes may be fitted with X-ray detectors to allow elemental analysis of the sample to be collected via energy-dispersive X-ray spectroscopy (EDXS). EDXS is discussed in the scanning electron microscopy section.

2.1.1 Imaging

Bright-field (BF) images are obtained from electrons that have undergone no, or only small-angle, scattering events while passing through the sample. Carbon allotropes with different morphologies such as sheets and tubes can be easily discerned via BF imaging (figure 20), providing a rapid means of identification. Lateral size distribution within a sample can also be readily obtained by comparing BF images of multiple regions of the TEM grid. Furthermore an idea of thickness distribution can be gained from the relative contrast of different specimen areas, but can be analysed more accurately using other techniques discussed below.

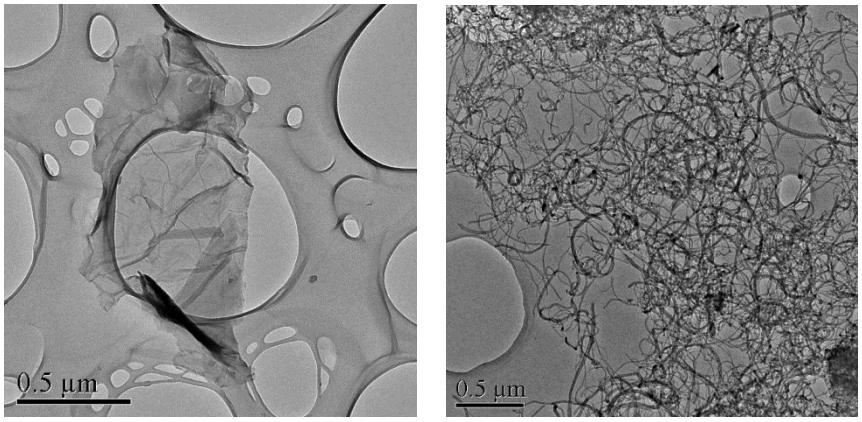

Figure 20: BF TEM images of a graphitic sheet (left), CNTs (right).

Dark-field (DF) images; obtained from electrons which have undergone large-angle scattering events, are less common than BF images but can provide valuable insight into the crystalline structure of materials. This has been shown to be beneficial when analysing graphene; where the BF images of graphene sheets had no discernible features but the DF image showed a number of crystalline grains (figure 21).[293] These grains correspond to the selected in-plane lattice orientations, and a series of images with different aperture filters is required to get a complete map of the grain structure. In addition to analysing in-plane crystallinity, DF imaging has also been utilised to study stacking faults in bilayer graphene.[294]

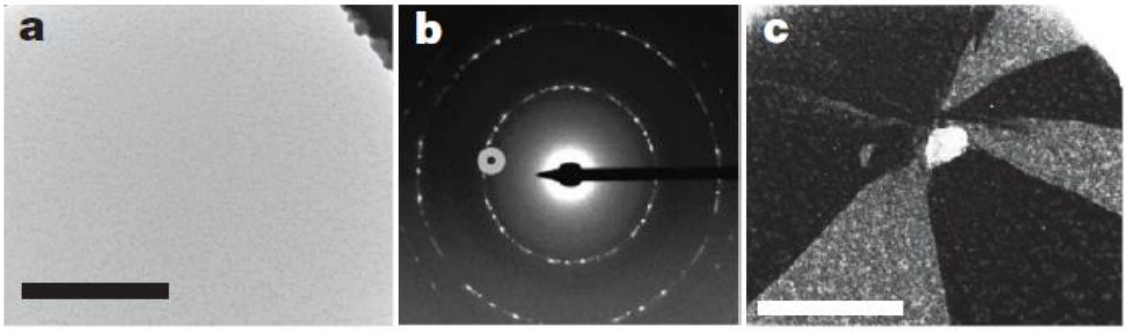

*Figure 21: Large-scale grain imaging in single-layer graphene using TEM, showing the BF image (a), diffraction pattern from the region shown in **a** (b) and DF image of the region shown in **a**, using an aperture to select electrons diffracted through a small range of angle (shown by the circle in **b**) (c). Scale bars = 500 nm. Adapted from reference 293.*

At high magnifications, high resolution TEM (HRTEM) images provide detailed information on the structure of materials. As the electrons penetrate the sample, the internal structure of materials can be probed, which is useful in the case of multi-walled carbon nanotubes; where the number and quality of the graphitic walls can be analysed, and the type of tube (straight-walled or cup-stacked) can be discerned. If the edge of a graphitic sheet is curled up the number of graphitic layers in the sheet can be counted to give an accurate thickness measure of the sheet.[21] It should be noted that a number of studies caution using this method, as a single 'lattice fringe' or 'edge line' can, in certain cases, represent single or bilayer graphene.[295, 296]

The observation of Moiré fringes (or patterns) in HRTEM images of folded single-layer graphene or few-layer graphene indicates that the overlapping sheets have different orientations. The fast Fourier transform (FFT) of the HRTEM image can be used to find the rotation of the sheets by measuring the angle between the sets of spots with 6-fold rotational symmetry, as per electron diffraction (see section 2.1.2). If a mask is placed over these spots, the inverse of the FFT yields a reconstruction of the graphene sheet from which the spots arose (figure 22).[297] Atomic scale HRTEM has be used to observe defects in graphene and single walled nanotubes,[298, 299] and the edge type (arm-chair or zig-zag) of few-layer graphene sheets.[300]

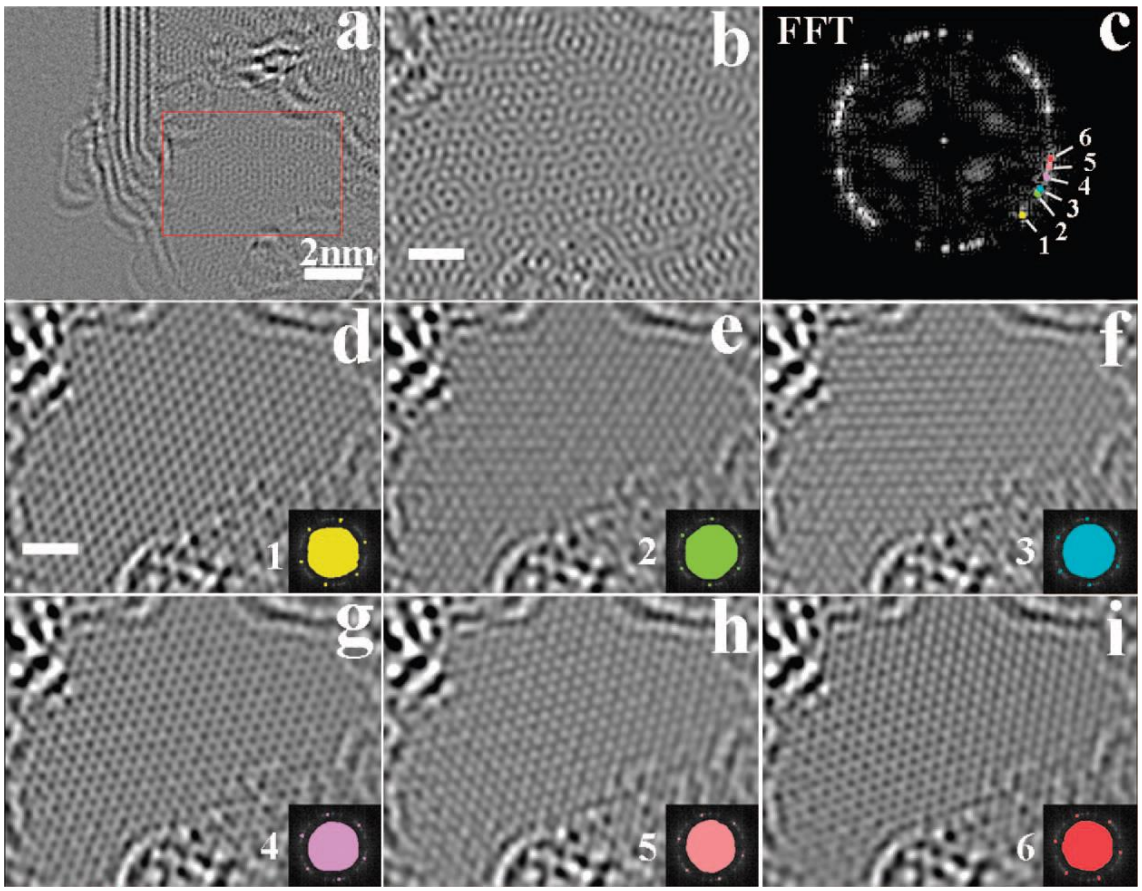

Figure 22: HRTEM image of the edge of a few-layer graphene nanosheet with at least six layers (a), HRTEM image of the region indicated in ***a****, showing a complex Moiré pattern due to the relative rotations of the six layers (b), FFT of* ***b*** *showing six sets of hexagonal spots corresponding to six different graphene layer orientations (c), and reconstructed images showing the graphene layer associated with the relative set of spots indicated in* ***c*** *(d – i). Inserts show the FFT masks used.*[297]

2.1.2 Electron diffraction

In addition to passing through thin samples to allow imaging, electrons can be elastically scattered by the crystal lattices of a solid, akin to light being scattered by a diffraction grating. Diffraction maxima occur when Bragg's condition is satisfied, i.e. when waves interfere constructively. The crystal must be orientated correctly in order to see a particular reflection from a crystal plane, and as such samples are often tilted within the electron microscope to gain more information on their structure. Electron diffraction (ED) patterns from specific regions of a sample can be obtained by inserting a select area aperture into the TEM column, in a process termed 'select area electron diffraction' (SAED).

The lattice parameters of the solid can be extracted from the distances between diffraction spots, allowing chemical identification of the species. In addition, the appearance of the diffraction pattern provides information on the crystallinity of the sample, where a single array of diffraction spots indicates that the material is single crystalline over the length scale measured, and multiple arrays of diffraction spots can be caused by overlapping crystals that have different orientations relative to one another. For graphene and graphene oxide a single array consists of two sets of spots with six-fold rotational symmetry, and rings of spots could be indicative of a series of overlapping sheets misaligned with one another, or could be a sign that the material is polycrystalline; with a large number of small single crystallites arranged irregularly in space making up some (or all) of the individual graphitic layers (figure 23).

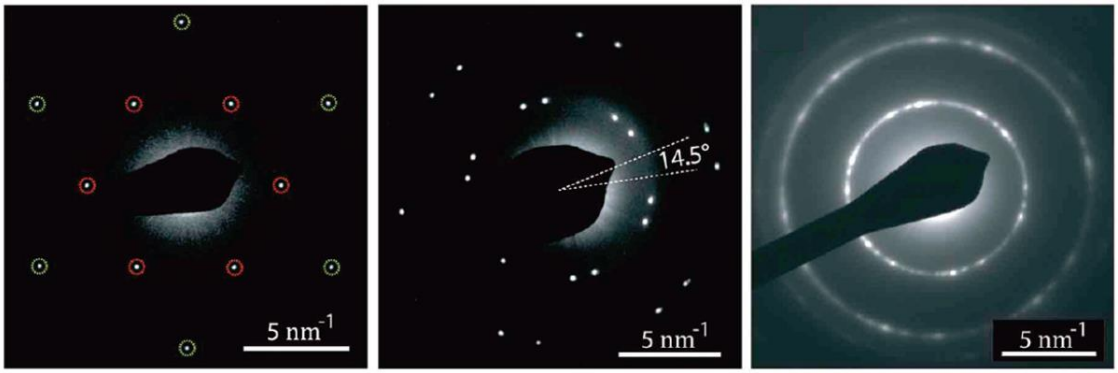

Figure 23: SAED pattern for a graphene oxide sheet, highlighting the two different sets of diffraction spots (left), SAED for two overlapping graphene oxide sheets that are offset by 14.5 ° (centre) and ED pattern from a film of graphite oxide about 15-20 layers thick which illustrates rings of spots (right). Adapted from reference 301.

As graphite and diamond have different crystallographic structures, the two can be readily distinguished via ED. In addition, graphene can be distinguished from graphite by the absence or presence respectively of the peak corresponding to the interlayer spacing (~3.4 Å).[302] Graphene, graphite and diamond all have peaks ca. 2 Å and 1.2 Å, so it is the additional features that provide distinction (figure 24). Peaks around 2 Å and 1.2 Å are typically observed for all amorphous carbon materials in the form of diffuse rings with no discernible spots.

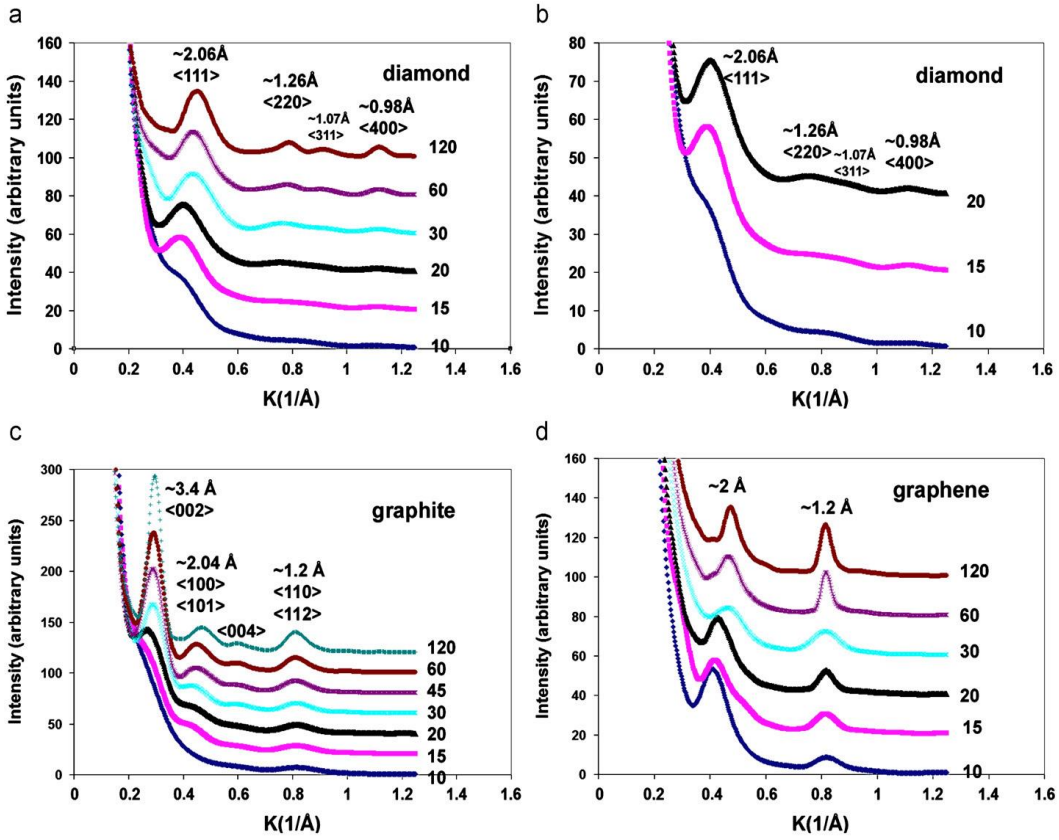

Figure 24: Calculated electron scattering intensities for nanocrystalline diamond (a, b), graphite (c) and graphene (d). The parameter of the curves is the average grain (cluster) size of the solid expressed in average number of atoms. Amorphous materials are interpreted as nanocrystals of grain size in the order of 10 – 30 atoms.[302]

The relative intensity of the diffraction spots has been used to distinguish between single and multi-layer graphene,[303] and to discern the stacking sequence of thin graphitic films.[24] The dependency of the intensity ratio between $\{11\bar{2}\,0\}$ and $\{1\bar{1}\,00\}$ spots on graphene structure has been demonstrated using simulated diffraction patterns (figure 25);[300] where for monolayer graphene the spots in the inner set are more intense than those in the outer set, whereas the opposite is true for graphene sheets with >1 layer.

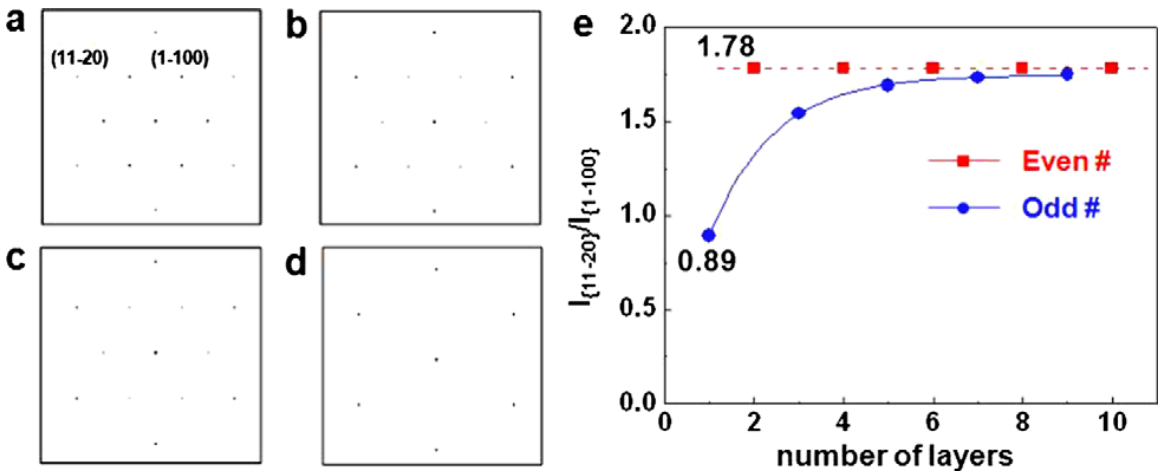

Figure 25: Simulated diffraction patterns for monolayer graphene (a), bi-layer graphene with AB stacking (b), bi-layer graphene with AA stacking (c), and three-layer graphene with ABC stacking (d), and a plot showing the intensity ratio variation of the diffraction spots marked in a) with the number of AB stacked graphene layers.[300]

ED of scrolled edges of graphene sheets has been shown to be similar to that of CNTs (figure 26);[303] with outward stretching of the hk.0 spots. This outward stretching occurs due to the apparent decrease in the interplanar spacings of kh.0 planes for the inclined walls of CNTs.[304] Careful analysis of electron diffraction patterns can be performed to determine the chiral indices of carbon nanotubes, although this requires high quality data on straight regions of isolated tubes.[305] The approaches used to analyse diffraction patterns of CNTs have been reviewed elsewhere.[306]

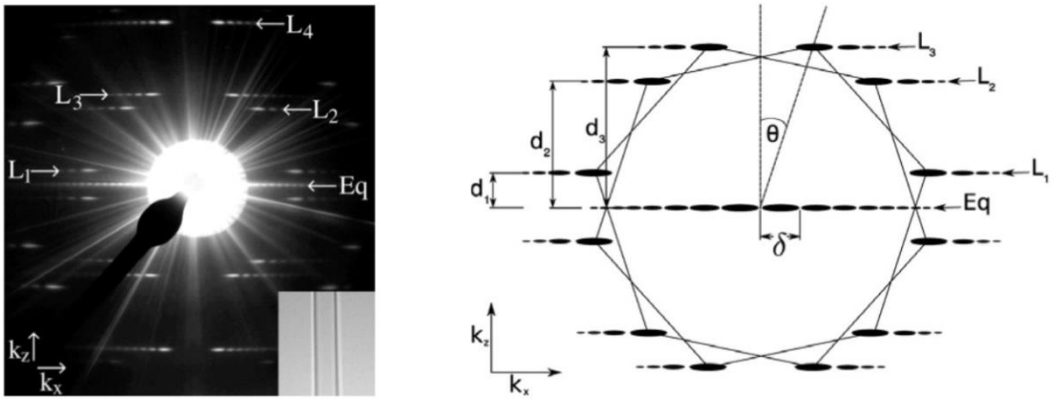

Figure 26: SAED of an individual SWCNT with its real space image inset (left), and a schematic depiction of the diffraction pattern obtained from a SWCNT (right), where hexagons mark the first order reflections from the graphite lattice, L_1-L_3 indicate the first three layer lines, d_1-d_3 indicate the axial distances of the layer lines, 'Eq' marks the equatorial oscillation (with oscillatory period, δ) and θ represents the chiral angle. Adapted from reference 306.

2.1.3 Electron energy loss spectroscopy

Electron energy loss spectroscopy (EELS) utilises inelastically scattered electrons to gain chemical information on the sample. As the electron beam passes through the sample, electronic transitions in its atoms can be promoted, leading to beam electrons with energy losses characteristic of the atoms in the sample. Spectra are generally presented as a plot of the electron intensity against energy loss. The low-loss spectrum (0-100 eV) provides information on the valence structure of the materials, while at higher energies the core levels of the atoms are probed. The amount of each atom can be quantified by comparing the relative intensities of the core level edges, yielding information on the elemental composition of the sample, as described elsewhere.[307]

The low-loss spectra of graphite and diamond have different characteristic features (figure 27).[308] Graphite has two clear bands, at ~7 and ~27 eV, which correspond to the π-plasmon and the (σ + π) 'bulk' plasmon peaks respectively; and diamond has a broad peak that can be split into two components; at 24 and 33 eV, for the surface and bulk σ-plasmons. The spectrum of amorphous carbon is similar to that of graphite, but with a less pronounced π-plasmon and the (σ + π)-plasmon peak shifted to lower energy.

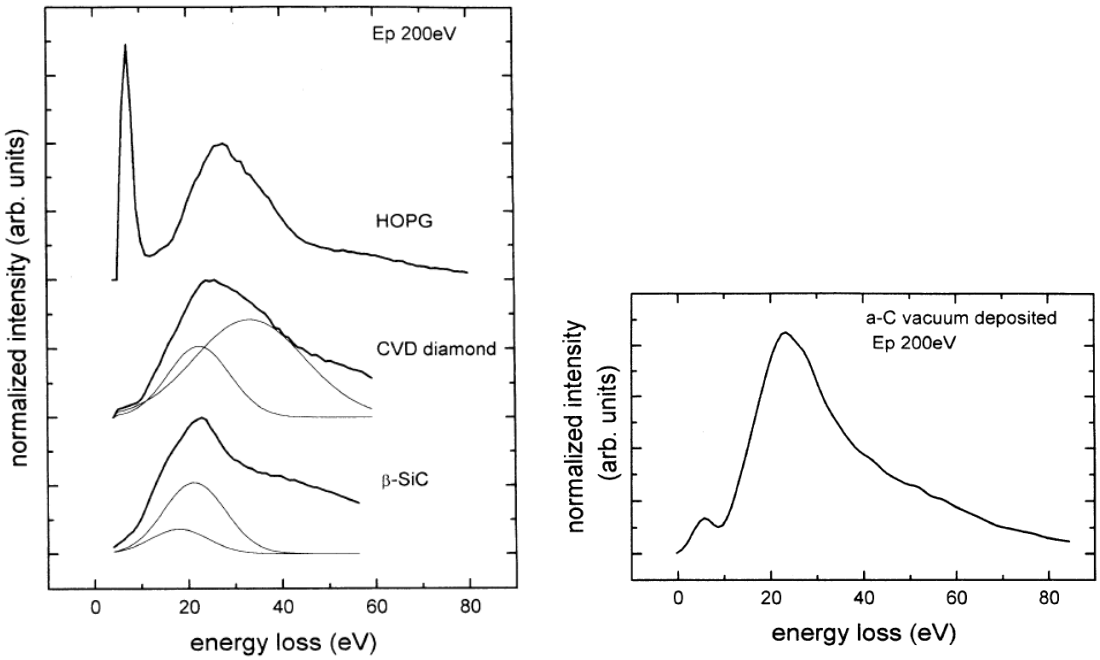

Figure 27: Low-loss EELS spectra of HOPG, diamond and β-SiC (left) and amorphous carbon (right).[309]

The carbon core loss region, termed the 'K-edge' corresponds to the promotion of electrons from the 1s (K) orbital to the unoccupied, anti-bonding 2p orbitals. For graphitic materials the electrons in the 1s orbital can be promoted to either the π* or σ* orbitals (energies ~285 eV and ~291 eV respectively),[310] whereas for diamond only the latter transition can occur (figure 28). EELS in often used in the analysis of amorphous carbon films as the ratio of sp^2:sp^3 carbon can be obtained by integration of appropriate regions of the carbon K-edge.[308, 311] Methods to perform this quantification have been compared elsewhere.[312]

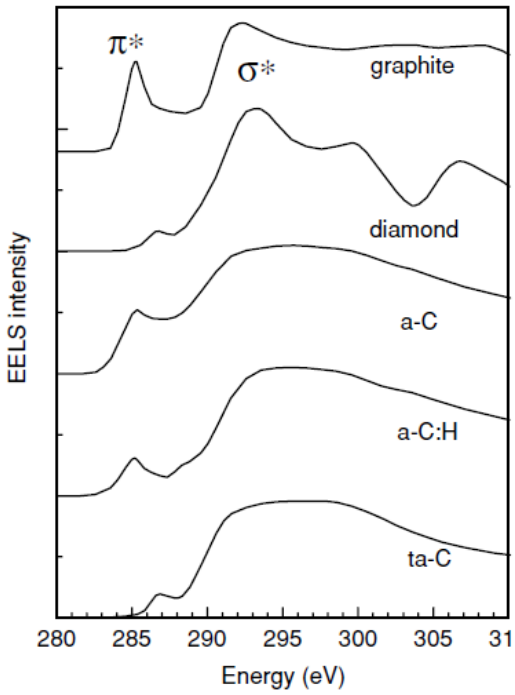

Figure 28: C K-edge EELS spectra for graphite, diamond, amorphous carbon (a-C), hydrogenated amorphous carbon (a-C:H), and tetrahedral amorphous carbon (ta-C).[311]

2.1.4. Energy filtered transmission electron microscopy

Energy filtered TEM (EFTEM) maps are obtained by analysis of inelastically scattered electrons. As for EELS, the electrons have characteristic energy losses related to absorption of energy by the atoms in the sample. Elemental maps can be obtained by detecting only the specific energy ranges corresponding to a type of atom. For the analysis of carbon nanomaterials, EFTEM mapping can provide information on the presence and distribution of heteroatom functionalities and impurities (figure 29).

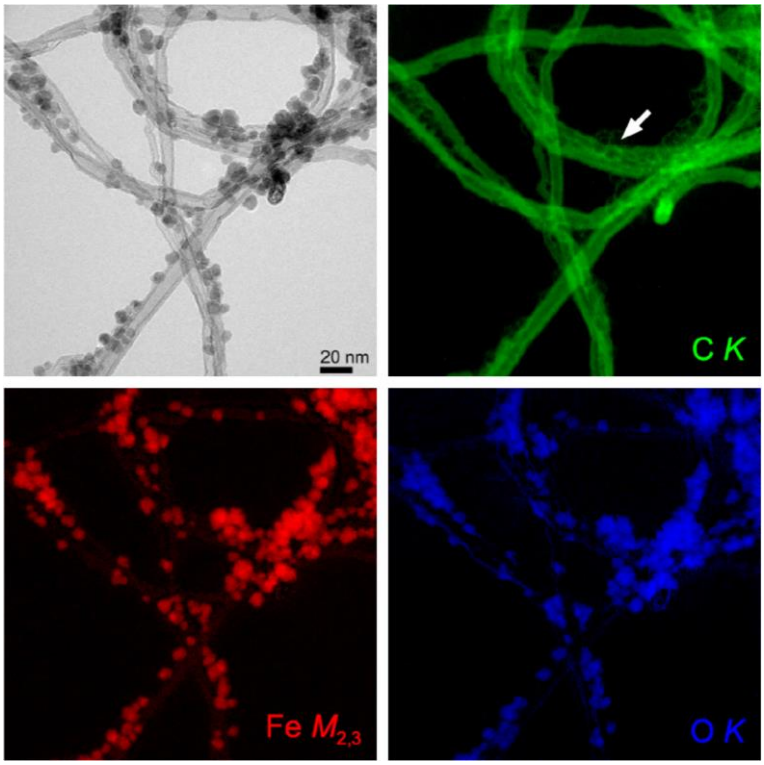

Figure 29: Zero-loss filtered TEM image of MWCNTs decorated with Fe_3O_4 nanoparticles, and corresponding EFTEM elemental maps of carbon (green), iron (red) and oxygen (blue) obtained from the C-K, Fe-$M_{2,3}$ and O-K edges. The white arrow indicates the presence of grooves on the MWNT.[313]

EFTEM can also be used to acquire thickness maps of thin regions of a sample, based on the inelastic mean free path for electron scattering (λ).[314] Generally these maps are obtained by comparing the total unfiltered image intensity with the zero-loss intensity, using the 'log-ratio' technique.[315] The thickness of the sample (t) at any particular point can be obtained from the intensity of the t/λ map, provided that λ is accurately known. The mean free path for inelastic scattering depends on a number of factors such as the density of the sample material, the energy of the incident electrons and the collection semi-angle, so more accurate results are obtained if λ is calibrated for the particular system using a region of known thickness.[316] Whilst this technique could potentially be used to determine the thickness and hence number of graphitic layers in few-layer graphene, examples of this procedure in the literature are difficult to find. This is likely to be as a result of the fact that the number of graphite layers can be easily discerned from HTREM images (assuming the entire edge has folded up).

In the present study EFTEM thickness mapping was used as a guide to inform the approximate thickness of area of sheets which did not contain up-turned edges. In order to achieve this, the following procedure was carried out:

1. t/λ statistics were collected for a number of different thin platelets of pure graphite (< 20 graphene layers) using EFTEM thickness mapping
2. The number of graphene layers constituting a thin platelet was ascertained from an HTREM image, assuming that each edge line represented a single graphitic layer
3. The t/λ value that corresponded to one graphene layer was calculated by dividing the mean t/λ value over a given area of the platelet and the number of layers in the platelet (as counted by HTREM.)
4. The error associated with the t/λ value was found by repeating steps 2 and 3 of this procedure for 8 different graphite platelets

To find the approximate thickness of an unknown sample, the average t/λ value for an area of the unknown sample was divided by the t/λ value for one graphene layer that had been calculated via the above analysis of graphite ($t/\lambda = 0.010 \pm 0.001$). This afforded an approximate thickness for the unknown sample in terms of the number of graphitic layers.

2.2 Scanning electron microscopy

2.2.1 Imaging

In scanning electron microscopy (SEM) a focussed electron beam with energy typically between 0.5 and 50 keV is scanned across a sample within a vacuum chamber. An image of the surface is constructed from backscattered and/or secondary electrons; the latter of which are produced as a result of ionisation events within the sample. Unlike TEM, SEM cannot probe the internal structure of samples, and has lower resolution, but has the advantage that large samples (in the order of centimetres) can be analysed with good depth of field. This is useful for characterising the overall morphology of carbon materials such as expandable graphite (figure 30), and for imaging 3D nanomaterial arrays such as graphene foams or CNT forests.[317-320]

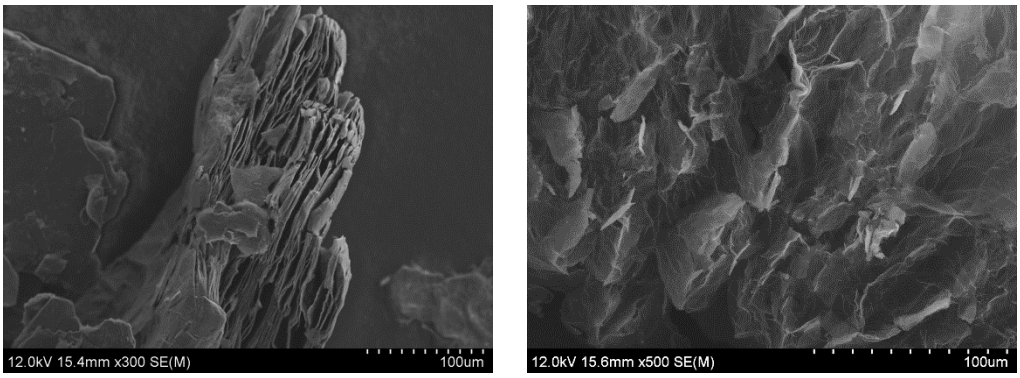

Figure 30: SEM images of expandable graphite before (left) and after (right) exfoliation.

2.2.2 Energy Dispersive X-ray Spectroscopy

The interaction of electrons from an electron beam with atoms in a solid can lead to the ejection of core level electrons, and subsequently to X-ray fluorescence; when an electron from an outer shell moves to replace the ejected core electron. The X-rays released in this process are characteristic of the atoms in the sample, and can be used for elemental analysis. EDXS results can be presented as a plot of energy against counts as a simple display of the elements present. The intensities of the peaks can give quantitative information on the elemental composition of the sample if the machine has been calibrated using suitable standards. EDXS results can also be presented as maps, showing the distribution of a particular element across a sample. EDXS is useful for the analysis of impurities in carbon samples, such as residual catalyst, or for analysing materials functionalised with heteroatoms (figure 31). It should be noted that elements can only be detected if the energy of the electron beam is sufficient to eject core electrons.

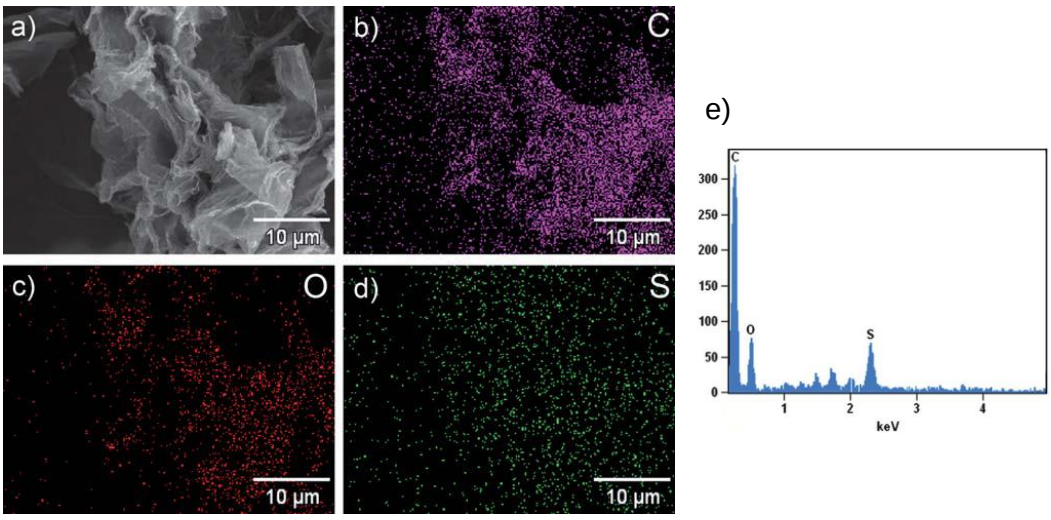

Figure 31: SEM image of the sulfonated graphene (a), corresponding quantitative EDXS elemental mapping of C (b), O (c) and S (d) and the overall EDXS spectrum (e). Adapted from reference 321.

2.3 X-ray photoelectron spectroscopy

X-ray photoelectron spectroscopy (XPS) is a surface-sensitive analytical technique which provides quantitative information on the chemical composition of samples. Data is collected by bombarding a sample held within a vacuum chamber with X-rays, and measuring the number and energy of the electrons that are emitted. Typically soft X-rays are used (commonly Mg Kα or Al Kα), which can penetrate microns into the bulk of the sample.[322] Adsorption of X-rays by atoms in the solid causes the ejection of electrons from either core or valence levels of the atoms, a fraction of which escape into the vacuum system to be detected. This process is known as 'photoemission'. In the simplest case the electrons are ejected with energy equal to the X-ray energy minus the binding energy of electron, although in some cases the emitted electron loses energy by promoting a valence electron to a higher unfilled level, leaving the atom in an electronically excited state. This process is called "shake-up", and can be identified by the presence of 'satellites' at the low kinetic energy side the core-level peak.

X-ray excited Auger electron spectroscopy (XAES) is a technique that accompanies XPS. Auger emission is a three electron process which occurs when a core-level electron hole is filled with an electron from a higher band, and energy released during the process causes the ejection of another electron from a higher level band (figure 32). It should be noted that while XPS is considered a "non-destructive" technique, for certain materials, such as graphite oxide, there is evidence that the sample changes upon prolonged exposure to the X-rays.[323]

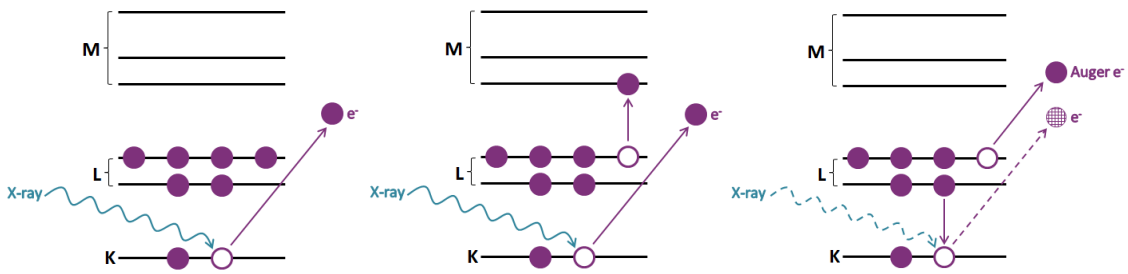

Figure 32: A schematic representation of the processes that lead to the core-level photoemission peak (left), the "shake-up" satellite (centre), and the Auger line (right) in XPS spectra.

A range of information can be sought from XPS spectra of carbon nanomaterials, depending on the elements visible in the survey scan, the shape and position of the C 1s core-level band, the width of the differentiated Auger line, and the valence band features. These features are discussed in detail below.

2.3.1 Survey Scan

The survey scan is a plot of electron intensity against energy. While the energy measured is the kinetic energy of the emitted electron, it is usual to display the survey scan in terms of electron binding energy, since this is the parameter of interest.[322] The electron binding energy is characteristic of the element so can be used for element identification, and the intensity of a peak is proportional to the density of the atom from which the electrons are emitted, so can be used to find the relative proportion of each element in a sample. This process, termed 'electron spectroscopy for elemental analysis', is useful in the case of functionalised carbon nanomaterials, as the proportion of heteroatoms gives a measure of the level of functionalisation; for example the level of oxidation for graphite oxide can be expressed in terms of the carbon:oxygen ratio (figure 33).[324]

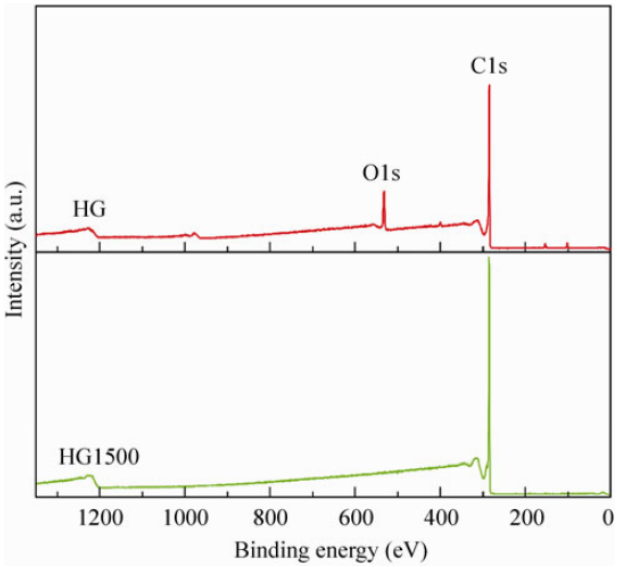

Figure 33: Survey X-ray photoelectron spectra for chemically reduced graphite oxide before (top) and after (bottom) thermal annealing at 1500 °C.[324]

The accuracy of this quantification relies on the sole source of the heteroatom being the functional group; rather than sample impurities or the underlying substrate, and upon the distribution of the functional groups on the surface being representative of the bulk sample. It is not possible to distinguish between atoms or molecules which are covalently attached to the carbon nanomaterial and those which are absorbed on the surface via the survey scan, and so caution should be taken when quantifying levels of covalent functionalisation. In this case a closer inspection of the core-level peaks of carbon and the heteroatoms is required to gain additional information on the level of functionalisation. The survey scan, assuming clean instrumentation and a well-defined underlying substrate, can act as a useful tool for analysing sample impurities, as detection limits are typically around 0.1 atomic percent.[322]

2.3.2 Core-level peaks

Core-level peaks with reasonable signal to noise can be obtained by performing high resolution scans over relatively narrow, systematically selected, binding energy ranges. The binding energy of core-level electrons is sensitive to the chemical environment of the atom, such that the peak for a particular element can be split into discrete chemical components (with varying binding energies) if its atoms are in different environments. The electron intensity is independent of the chemical state of the atoms, so the area underneath the peak for each component is proportional to the number of atoms in the particular chemical environment. The range in binding energies, also known as

"chemical shift", for the different components of an element is relatively small (typically less than 10 eV), with peak widths ~ 1 eV.[322] As a consequence the peaks for the various components often overlap, making their contribution to the overall peak shape (and hence relative proportion of the atomic environment) difficult to determine.

The area of the component parts can be obtained by 'peak fitting' or 'peak modelling'. This is a mathematical process in which peaks with user defined lineshapes are combined to create a synthetic envelope with an overall lineshape similar in appearance to the experimentally obtained photoelectron peak. The peak fitting process can be subjective, since the number of component peaks and choice of peak positions, lineshape and background have a marked effect on the overall outcome of the analysis.[325, 326]

Peak fitting is frequently used in the analysis of oxidised carbon materials. In these studies the carbon 1s peak is generally split into a number of different carbon-oxygen bonded components, depending on results from other characterisation techniques or according to similar experiments in the literature. A list of chemical shifts quoted in the literature and the carbon-oxygen components assigned to these binding energies is detailed below (table 2). Note that in some cases the assignments do not agree, and that exact binding energies reported in the literature often vary slightly from those given in the table.

Table 2. C 1s binding energies for various carbon-carbon and carbon-oxygen functionalities.[324]

Binding energy (eV)	Assignment
284.6	Graphitic C=C (sp^2 carbon)
285.3	Defective graphite structure *OR* Hydroxyl C-OH groups
286.3	Epoxy/ether C-O groups *OR* sp^3 carbon (free radical, C-O or C-N)
287.7	Carbonyl C=O groups
289.0	Carboxylate COOH groups
290.8	$\pi \rightarrow \pi^*$ shake-up satellite of C=C

Fitting a large number of components increases the potential for errors so frequently only a subset of the peaks given above is used in fitting. Carbon-oxygen peaks are shifted toward high binding energies relative to the graphitic peak as oxygen is more electronegative than carbon. For graphitic materials with relatively low levels of oxygenation, the C 1s peak generally appears as an asymmetric peak with a relatively featureless broad tail at high binding energies, which contains the carbon-oxygen components (figure 34). The peak fitting of such materials is complicated by the inherent asymmetry of the graphitic peak (at 284.6 eV), which has a broad tail on the high energy side that merges with the carbon-oxygen components. The asymmetry of the graphitic peak is well documented in the literature and can be fitted using a Doniach-Sunjic lineshape.[327] The physical origin of this asymmetry is discussed elsewhere.[328, 329]

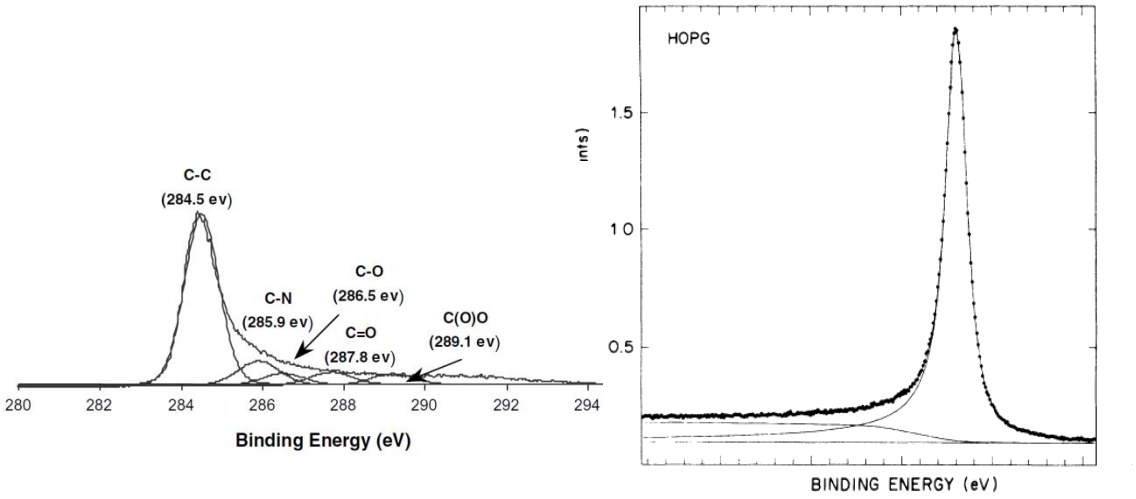

Figure 34: The C 1s XPS spectra of reduced graphite oxide, showing low levels of oxygen functionalities (left) and asymmetric graphite peak (right). Adapted from references 170 and 328.

It follows that direct oxidation of graphite materials is accompanied by a destruction of crystalline order; i.e. disruption to the sp^2 bonded network by formation of sp^3 hybridised carbon. It has been proposed that this disruption should be compensated for by the addition of a relatively broad symmetrical peak (> 1.5 eV FWHM compared with < 1 eV for the sp^2 peak), shifted by ≤ 1 eV to higher binding energy than the graphitic sp^2 peak.[330] While this smaller peak is often combined into the asymmetry of the sp^2 peak in primarily graphitic materials,[331] fitting the C 1s peak into sp^2 and sp^3 component peaks is frequently used to estimate the sp^2/sp^3 ratio of amorphous carbon films.[332-334]

Typical XPS spectra for graphite, diamond and other carbonaceous materials show that the positions of the peaks are shifted, with the graphite C 1s at 284.5 eV, the (a-C:H) C 1s at 284.5 – 286.4 eV, and the diamond C 1s at 291.4 eV (figure 35).[333] The shifts for the latter two are attributed partially to chemical 'charging': the build-up of electrons on the surface of non-conducting samples leading to changes in the apparent binding energy, and partially due to the change in environment of the carbon atoms. It is common for the C 1s binding energy of functionalised graphitic materials which are prone to charging, such as oxidised CNTs and graphite oxide, to be energy calibrated to the sp^2 carbon peak; generally set to a value in the range of 284.3 -284.7 eV.

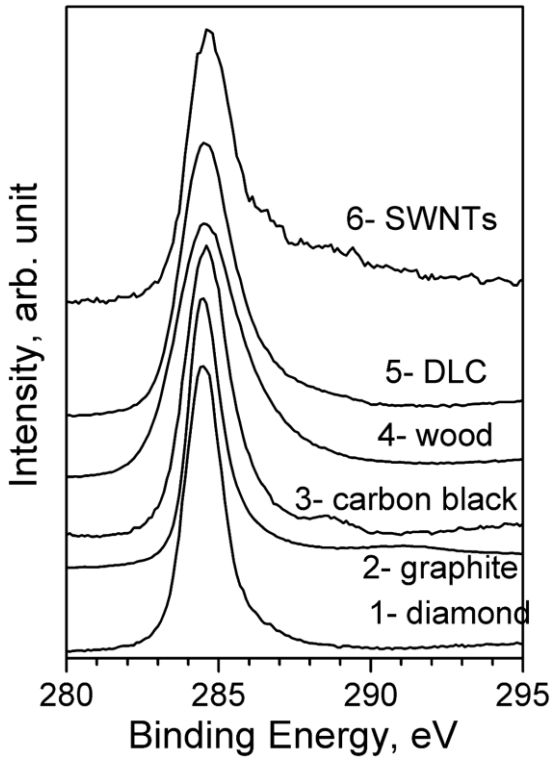

Figure 35: XPS C 1s spectra for different carbon samples.[335]

In the current study peak fitting of the C 1s was performed to help quantify trends in the XPS spectra of graphene, GO, and any intermediates between the two. Whilst it is acknowledged that peak fitting may not afford experimentally accurate results, it does provide a means of quantifying trends within a data set, particularly if the fitting parameters are suitably constrained. A Tougaard background was chosen as this has been previously shown to result in higher levels of agreement with theoretical data than linear or Shirley backgrounds,[336, 337] and has been previously used for the analysis of carbonaceous materials with different levels of graphitisation.[338] The majority of the peaks were fitted with a Voigt-type function (a convolution of Gaussian and Lorentzian lineshapes) to take into account the Lorentzian nature of the individual vibrational

bands and the Gaussian line broadening due to instrument effects,[325] and to be consistent with many other literature examples of peak fitting GO.[163, 324, 339] The exception to this was the C=C peak, which is known to be asymmetric in graphite and hence likely to contain some asymmetry in the case of GO. Rather than using the Doniach-Sunjic lineshape to fit the C=C peak (as this shape may not be valid given the large chemical differences between graphite and GO), an alternative asymmetric lineshape was utilised. This lineshape chosen was the experimental lineshape for rGO reduced using hydrazine hydrate,[170] the spectrum for which was measured on the same spectrometer. While this approach is likely to introduce some inaccuracy due to residual functional groups, it was hoped that by anchoring the fit to an experimental lineshape, a more reliable fit would be obtained. This strategy, although not widely used, has been reported elsewhere for XPS fitting of GO.[340] The relative proportions of different carbon-carbon and carbon-oxygen containing groups reported in the proceeding chapters are the results of least-square criterion for the 'best fit' of the C 1s spectral lineshape for peaks with constrained positioned and FWHMs. The reported C/O ratios have been calculated from the relative areas of the different peaks and the relative proportion of atoms in the different functional groups (e.g. for C=O the C/O ratio is 1, for COOH the C/O ratio is 0.5). An example fit is provided in figure 36 and more details of the fitting parameters are provided in section 7.1.1.

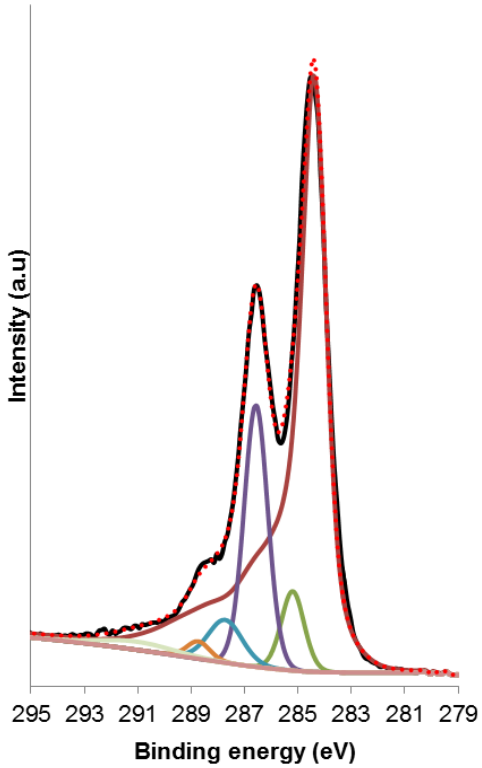

Figure 36: C 1s experimental lineshape (black) fit into C=C (maroon), C-C (green), C-O (purple), C=O (blue), COOH (orange) and Pi-Pi (light green) components with a Tougard background (pink), using a measured rGO lineshape to fit the C=C. The dashed red line shows the sum of the fit components as an indication of the quality of the fit.

2.3.3 Auger line

The core-valence-valence (CVV) Auger line is observable in XPS spectra of carbon materials due to XAES processes. In the case of carbon, the core electron is ejected from the K level (1s shell), leading to the annotation of carbon KVV. The shape of this line varies depending on the hybridisation of the carbon atoms as a result of the difference in the valence band density of states for different carbon environments (figure 37). Details on the electronic origin of the various features of these lineshapes can be found elsewhere.[341, 342]

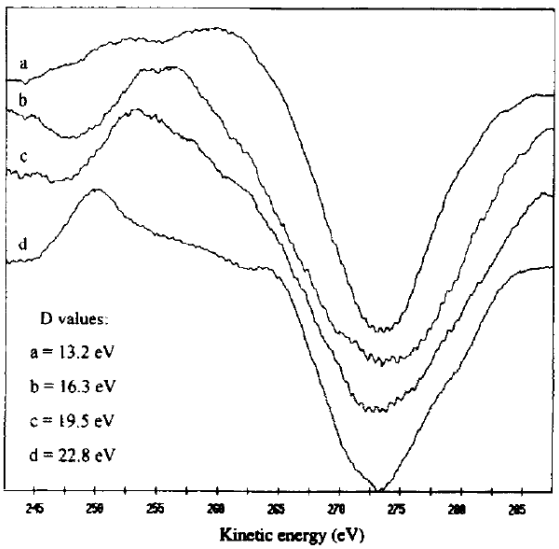

Figure 37: Auger C KLL spectra for natural diamond (a), cathodic arc-deposited amorphous carbon (b), magnetron sputtered amorphous carbon (c) and HOPG (d).[334]

It has been suggested that the sp^2/sp^3 ratio of mixed valency carbonaceous systems can obtained by peak fitting the C KVV lineshape,[343] however it is more common to extract this information from the first derivative of the lineshape. In the latter case, the distance between the main positive and main negative peaks of the differentiated line is measured to yield the 'D parameter' of the material.[344] This parameter is typically used to find the sp^2:sp^3 ratios of amorphous carbon films, yielding results within 1-2% of sp^2:sp^3 ratios found by curve fitting the C 1s core-level peak.[333, 334] For these calculations diamond is considered to be 100% sp^3, graphite is considered to be 100% sp^2, and the D parameter is assumed to vary linearly between the two values. Reported D parameters vary slightly but are in the order of 14 eV for diamond and 22 eV for HOPG.[345] As the presence of oxygen has been found to affect the Auger lineshape, quantification of sp^2/sp^3 bonding for oxidised systems, such as graphite oxide, may not be valid.[343]

2.4 Raman spectroscopy

Confocal Raman spectroscopy involves focusing monochromated light on a sample and measuring the light that has been inelastically scattered, to gain information on the vibrational states of the molecules. The vibrations, characteristic of particular bonds, can act as a fingerprint to identify the sample based on databases of spectra for different chemical species, and can be predicted based on group theory. While spectra for different types of sp^2 hybridised carbon share a number of key features (figure 38),

analysis of the position, intensity and line-shape of these features can provide detailed information on the materials. The use of Raman spectroscopy to determine the chiral indices of SWNTs,[346, 347] the size of fullerenes,[348] and quality of diamond and amorphous-carbon films has been reviewed in detail elsewhere.[349, 350]

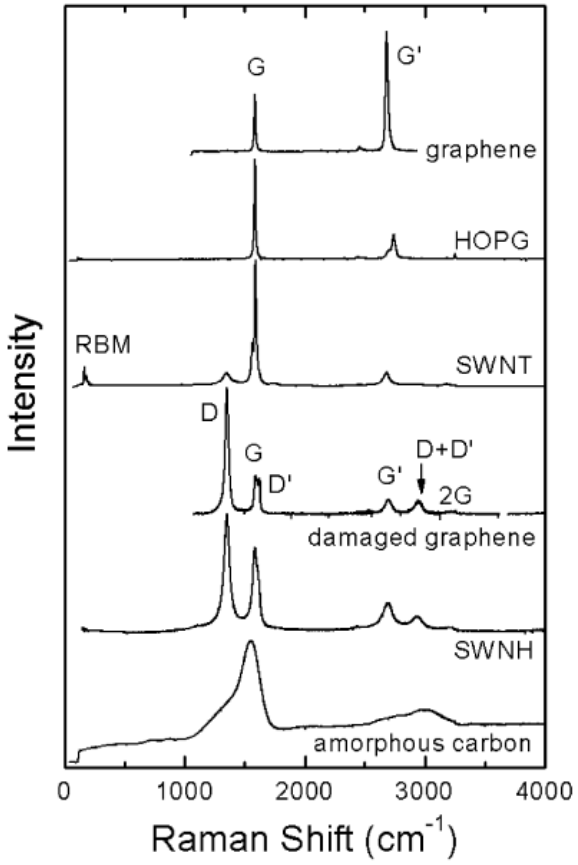

Figure 38: Raman spectra for different types of sp^2 nanocarbons. The graphene-related structures are labelled next to their respective spectra. The main features (RBM and disorder induced D, D' and D + D' bands; first-order Raman-allowed G band; and second-order Raman overtones G' and 2G) are labelled in some spectra but the assignment applies to all.[351]

The features of importance for analysing graphene are the G peak at ~1575 cm^{-1} caused by in-plane bond stretching of sp^2 carbons,[352] the 2D (or G') band at ~2500 to 2800 cm^{-1} caused by second order two-phonon processes,[25] and the D band at ~1355 cm^{-1} caused by a second order process involving a phonon and a defect in the graphitic structure.[353] As the D band is only present for samples with defects, the ratio of D to G bands can be used to provide detail on the crystallinity of graphite (figure 39). There is some debate as to whether the intensity ratio (I_D/I_G) or area ratio (A_D/A_G) should be considered, centred around the effect of the full width at half maximum (FWHM) on the area of the peak.[354, 355] The D band has been found to be sensitive to

the edge type (zigzag or armchair) and rotational stacking,[356, 357] and the G band has been found to be sensitive to the number of layers of graphene, the substrate, and the amount of doping,[355, 358] so the validity of gaining information about the crystallinity of graphene via the D/G ratio in non-ideal systems is uncertain.

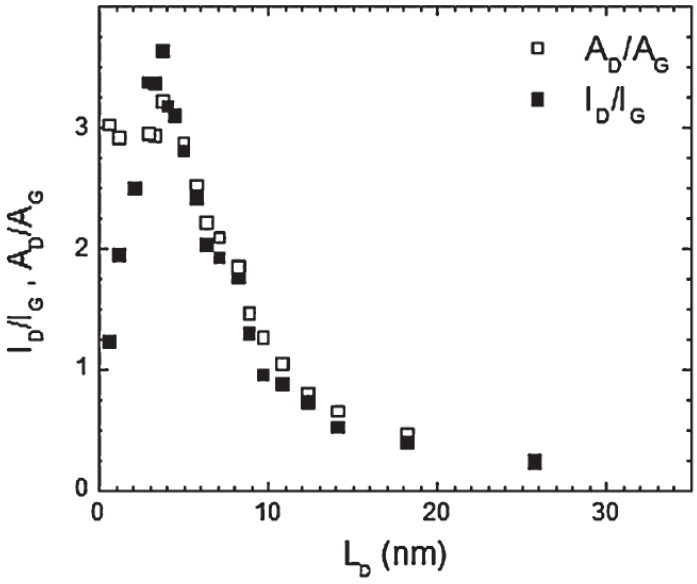

Figure 39: Evolution of the intensity ratio (filled squares) and area ratio (unfilled squares) of the D and G Raman peaks of graphene as a function of the average distance between defects (L_D). Adapted from reference 354.

The 2D band has been observed to have a distinct shape for monolayer graphene and up to 5 layer few-layer graphene, beyond which the shape becomes practically indistinguishable from that of bulk graphite (figure 40).[359] Unlike graphene with more than one layer, the 2D band of monolayer graphene appears as a single peak, which could be used as a simple identification tool for monolayer material. It is noted that while turbostratic graphite is also observed to produce a single component 2D band, the band has a FWHM over double that of monolayer graphene and is up-shifted from the monolayer peak by ~20 cm^{-1}.[359] Analysing the shape of the 2D band has also been used to measure the degree of stacking order in graphite, as an alternative to using XRD.[360]

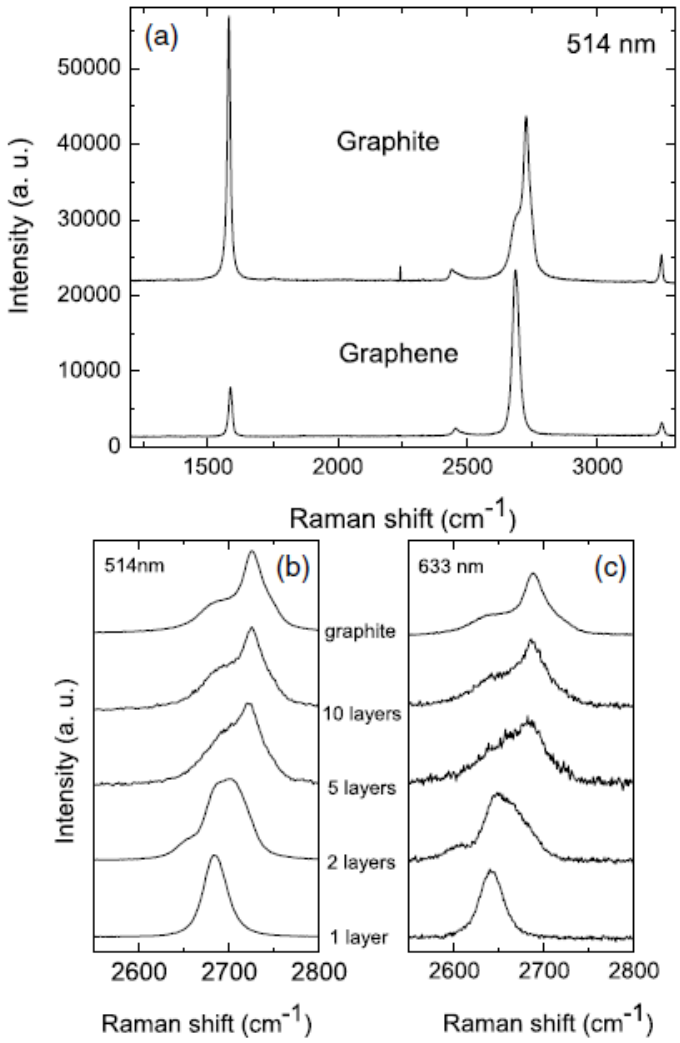

Figure 40: Comparison of Raman spectra at 514 nm for bulk graphite and graphene, scaled to have similar height of the 2D peak at ~2700 cm^{-1} (a), and evolution of the Raman spectra with the number of graphene layers using 514 nm (b) and 633 nm (c) excitations.[359]

Although Raman is an important tool for characterising carbonaceous materials, there have been relatively few Raman-based studies focusing on GO, rGO and the transition between the two. The Raman spectrum for GO is similar to that of nanocrystalline graphite; with broad D and G bands and numerous defect-induced second order bands,[361] and it has been proposed that the Raman signal from GO only originates from graphene-like clusters rather than the oxygen-rich areas of the material.[362] The breadth of the G band has been attributed, in part, to the inclusion of the defect activated D' band, which can be seen as a shoulder to the G peak in damaged graphene (see figure 38).[361, 363] The position of the G band has been reported to shift to a higher frequency upon oxidation of graphite to GO,[364] and shift to a lower frequency

upon reduction of GO to rGO,[365, 366] which has been related to differing arrangements of the sp^2 carbons in the different system. As the D band is associated with defects it could be expected that the D band would decrease upon reduction of GO due to the restoration of sp^2 carbons; however there have been numerous reports of an increasing I_D/I_G with reduction for both chemically and thermally reduced GO.[170, 362, 366] While the I_D/I_G has been shown to increase upon reduction, the FWHM of the D band has been observed to decrease.[362, 366, 367] A linear relationship between the FWHM of the D band and the relative proportion of the sp^2 carbon has been found based on comparisons between XPS and Raman results, whereby the peak width of the D band decreases as the relative proportion of sp^2 carbon increases.[362] The combination of an increasing I_D/I_G and a decreasing D band FWHM is thought to represent the formation of numerous clusters of sp^2 carbon which are smaller than the pre-existing clusters; such that the relative proportion of sp^2 carbon increases but the average size of the sp^2 clusters decreases.[366, 367]

For the majority of samples in this thesis the D and G bands are broad and overlapping, making analysis of their areas more complicated; since peak fitting is required. In order to ascertain whether the area ratios (A_D/A_G) or intensity ratios (I_D/I_G) would be most informative, the values obtained for four different analysis points of the same sample of GO were studied. These values were compared against the values obtained for 20 different samples of GO-based materials that had undergone different processing regimes. The average A_D/A_G for the four repeat points was 1.7 with a range of 0.3 (18%), while the range in A_D/A_G between the 20 different samples was 0.4. The large range within a sample relative to the range seen between different samples illustrated that it was not possible to use the area ratio to observe trends in the data. Conversely, the average I_D/I_G for GO across the different analysis points was 0.91 with a range of 0.03 (3%), while the range in I_D/I_G between 20 different GO-based samples was 0.2. This order of magnitude difference between the “within sample” and “between sample” variation makes I_D/I_G a more suitable measurement for monitoring changes in the material upon processing. In order to accurately monitor any changes in peak position, the spectrometer was calibrated to the A_{1g} Raman active mode of silicon (at 520 cm^{-1}) prior to use.

2.5 UV-Vis spectroscopy

Ultraviolet-visible spectroscopy (UV-vis spectroscopy) is commonly used to obtain chemical information about organic molecules as photons from the UV and visible range of the electromagnetic spectrum have sufficient energy to promote electronic transitions within molecules (which are characteristic of different orbital transitions). For solid materials the light that passes through the sample into the detector is equal to the incident light minus light that is scattered, reflected or absorbed, where UV-vis spectra are generally collected for dilute samples, such that reflected and scattered light is minimised. The concentration of a species in dilute solution can be found from the Beer-Lambert Law; $A = \varepsilon\ c\ l$, where A is absorbance, ε is the molar extinction coefficient of the material, c is the concentration of the material and l is the path length. This law has been used to analyse the effectiveness of a wide range of solvents for creating high concentration, stable dispersions of carbon nanomaterials,[84, 368] although it has been noted that these measurements are likely to be affected by scattering events.[369]

UV-vis is frequently used to measure the degree of reduction for rGO. In this case, the position of the absorption peaks corresponding to the $\pi \rightarrow \pi^*$ transition in the aromatic backbone is used as a measure; as the peak at ~233 nm for GO red shifts to ~270 nm upon reduction (figure 41). This shift, and the accompanying increase in the absorption for wavelengths greater than the peak, is taken to indicate restored electrical conjugation upon reduction.[370, 371] The shoulder at ~300 nm associated with the $n \rightarrow \pi^*$ transition of carbonyl groups on graphite oxide has also been shown to disappear upon reduction.[372]

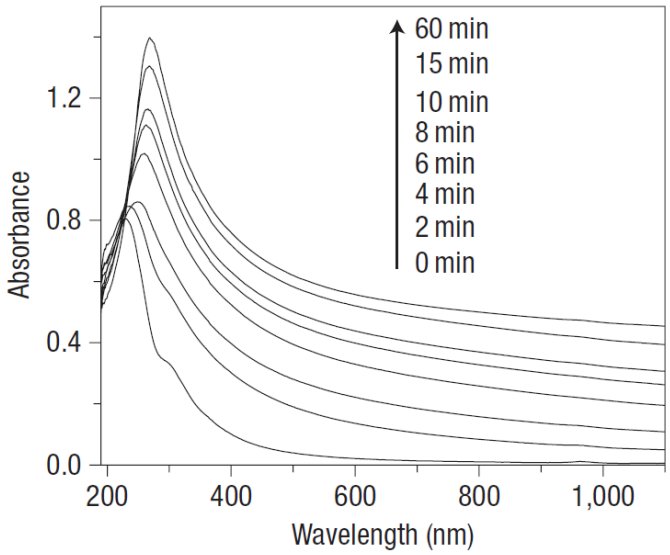

Figure 41: UV-vis absorbance spectra showing the change of GO dispersions as a function of reaction time for GO reduction using hydrazine.[370]

2.6 Solid-state nuclear magnetic resonance spectroscopy

^{13}C Solid-state nuclear magnetic resonance (SSNMR) can be used to probe the local environment of carbon atoms, where each peak represents carbon in a different bonding environment. There have been a number of high resolution ^{13}C NMR studies of carbon nanotubes, demonstrating that the line width and/or position can be used to gain information on the CNT diameter, number of walls, and electronic properties (metallic Vs semiconducting),[373-375] however in terms of carbon nanomaterials, SSNMR has been used most widely for the analysis of graphite oxide.[153, 376-378] Here a variety of different NMR techniques have been used to infer the nature of the oxygen functionalities and water binding in GO, including ^{1}H-^{13}C cross-polarisation (CP), short-contact-time CP, dipolar-dephased CP and ^{13}C single pulse magic angle spinning (MAS) NMR.[376, 378] More recently 2D $^{13}C/^{13}C$ chemical shift correlation SSNMR has been performed on ^{13}C-labelled GO in order to gain additional information about the spatial separation of the different functional groups.[379, 380] Despite the improved signal/noise for ^{13}C-labelled GO, a number of the smaller signals (101, 169, 193 ppm) were not assigned in these works; with the main findings centring around the assignment of the epoxide, hydroxyl and sp^2 carbons at chemicals shifts of ~60, 70 and 130 ppm respectively. In other reports, the peak at 101 ppm has been assigned to lactols,[377] or epoxy pairs,[381] while the peak at ~169 has been assigned to ester carbonyls or carboxylate groups, and the peak at 193 ppm has been assigned to

ketones (figure 42).[377, 382, 383] In addition to this, peaks in the regions of 110-120 ppm and 160 ppm have been assigned to phenolic groups forming during the reduction of GO to rGO.[153]

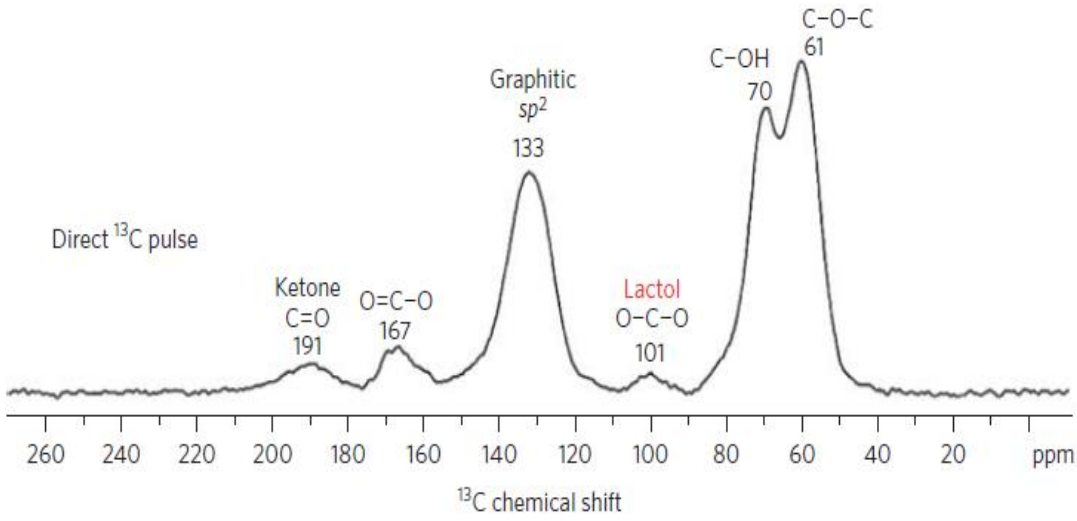

Figure 42: Solid state ^{13}C magic-angle spinning (MAS) NMR spectrum of graphite oxide. Direct ^{13}C pulse spectrum obtained with 12 kHz MAS and a 90 ^{o} ^{13}C pulse (10,000 scans). The peak highlighted in red (~101 ppm) is assigned to carbons of five- and six-membered-ring lactols. Adapted from reference 377.

SSNMR has been identified as a useful tool to monitor the reduction of GO, particularly due to the simplicity of comparing the relative ratios of the different functionalities in the ^{13}C MAS single pulse spectra; which provides a semi-quantitative survey of all the carbon species.[157, 382] Despite this there do not appear to be any literature examples of peak fitting of these spectra, akin to the fitting of the C1s XPS spectra, and instead the analysis is purely qualitative. In this thesis the ^{13}C MAS direct excitation SSNMR spectra have been peak fit into different carbon environments to afford a simple, semi-quantitative means of comparing the relative proportions of carbon functionalities for different samples within a set. To minimise the dependency on accurate fitting (due to the compilations of coalescing peaks), the spectra were fit into 'regions' which denote similar functionalities (table 3). The area of the peaks in the given region were summed to give total contributions from the different carbon environments; broadly categorised as carbons with single bonds to oxygen, aromatic carbons, and carbons with multiple bonds to oxygen. Values obtained from the fitting allow an approximate percentage change in the sample to be ascertained and enable simple graphs to be plotted to illustrate the changes upon processing (figure 43), as an alternative to using stack plots of SSNMR spectra.

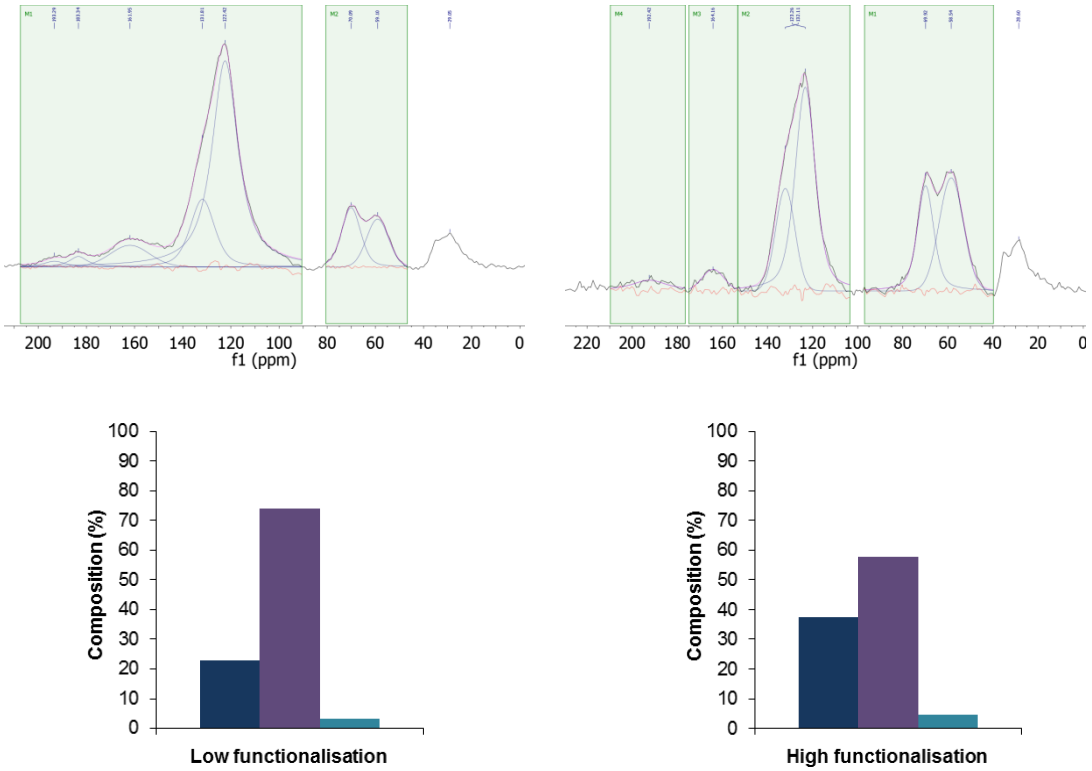

Figure 43: ^{13}C direct excitation MAS SSNMR spectra of GO with a low (left) and high (right) level of functionalisation (top) with associated plots of region 1 (dark blue), region 2 (purple) and region 3 (light blue) functional groups based on the peak fittings (bottom) in the contributions described in table 3. Full scale peak fits for each graph can be found in appendix A.

Table 3: Summary of fitting regions for ^{13}C MAS direct excitation SSNMR spectra

Region	Chemical shift range (ppm)	Functionalities
1	55 – 115	Epoxide, hydroxyl, lactol
2	115 – 165	Graphitic sp^2, phenol
3	165 – 195	Ester carbonyl, carboxylate, ketone

2.7 Thermogravimetric Analysis

Thermogravimetric analysis (TGA) involves monitoring the mass of a substance as it is heated in a controlled environment. Mass plots are generally given as a function of temperature or time, and yield information on the thermal stability of the material being analysed. In some cases the TGA gas flow is outputted through a mass spectrometer or Fourier transform infrared (FTIR) spectrometer to gain information on the species

that are released upon heating. For the analysis of carbon nanomaterials, the onset of thermal decomposition can be used as a measure of the overall crystallinity of the sample, since defect sites are more prone to thermal oxidation.[384, 385] The onset of thermal decomposition has also been shown to decrease upon exfoliation of graphite; which has been attributed to reduced interlayer interactions between the exfoliated sheets compared with graphite with well-ordered stacking.[115, 386] For this reason the lower thermal stability of graphene compared with graphite is not necessarily taken as an indication of reduced crystallinity in the latter.

Different carbon allotropes have different typical thermal decomposition temperatures (table 4), which can be used to measure carbon impurities such as amorphous carbon in graphitic samples.[387, 388] The onset of burn of the carbon backbone can also be used as a means to measure the reduction of GO, as the onset shifts to higher temperatures upon reduction to reflect the change in the relative proportion of sp^3 and sp^2 carbons.[389, 390] In addition to the onset of burn for the carbon backbone at temperatures over 500 °C, GO also exhibits a low temperature weight loss around 200 - 230 ºC that has been assigned to the loss of oxygen functionalities of GO, in agreement with XRD and FTIR data.[389, 391, 392] A decrease in the percentage mass loss in this region indicates a lower proportion of oxygen functionalities, and hence is evidence of reduction of the GO structure.[167, 393, 394] The general principle of low temperature weight losses corresponding to the removal of functional groups is often used as a means to quantify the functionalisation of carbon materials in general.[395] It should be noted that TGA is also useful as a tool to measure impurities, for example residual metal catalyst, which can be quantified from the residual after complete burning of the organic matter.

Table 4: Typical thermal decomposition onsets for different carbon allotropes in air.[396, 397]

Carbon allotrope	Thermal decomposition onset (°C)
C_{60}	420
Amorphous carbon	585
Diamond	630
Graphite	645
Nanotubes/nanoparticles	695

Chapter 3: Synthesis and properties of partially reduced graphene oxide produced via graphite oxide

3.1 Introduction

The reduction GO, as discussed in the introduction, is generally considered the most promising route to bulk scale 'graphene'. It should be remembered that the defects formed during the oxidation of graphite ultimately limit the properties of rGO, so for certain applications, such as those which require high electrical conductivity, rGO does not represent a suitable substitute for pristine graphene. For other applications, however, rGO does appear to represent a suitable bulk scale alternative to graphene, and in some cases the processing-induced defects have actually been found to be beneficial.[90, 91] While the thought processes behind converting graphite to graphene via oxidation, exfoliation, and reduction are easy to follow, the practicalities of the methodology are complex, as variation is introduced in every step of the reaction. First, the size and crystallinity of the starting graphite has been found to influence the speed of reaction,[392] the resulting sheet size,[398] and relative proportion of the different oxygen functionalities of GrO formed.[399] Second, the oxidation conditions have been found to influence the size and level of functionality of GrO; leading to many adaptations to the original Hummer's method such as changing the relative proportions of reactants,[157, 400-402] changing the reaction temperature,[159, 403, 404] or performing successive oxidation steps.[405] Third, the exfoliation step has been found to be influenced by the level of GrO oxidation,[401, 402] the amount of mechanical force exerted during liquid-phase exfoliation,[406] and the temperature used for thermal exfoliation.[407] Finally, the method of reduction has been shown to result in rGO with widely differing C/O ratios and varying properties (such as electrical conductivities), and as such this latter step is the focus of numerous reviews.[144-146, 148]

Much of the work in this field has been dedicated to achieving complete reduction of graphene oxide, to achieve a material that most resembles pristine graphene. As an aside from this, researchers are also revisiting the properties of GO as a material in its own right. Unlike graphene, GO is fluorescent over a broad range of wavelengths;[408] which could be useful for biological applications such as drug delivery and live cell imaging.[409] It has also shown promise in water purification systems,[410] and in certain polymer composites, where GO has been found to improve mechanical properties of polyimide nanocomposites to a greater extent than rGO.[411] Furthermore, in stark contrast to graphene, GO has excellent dispersibility in aqueous systems, and its range

of oxygen functionalities provide a means of functionalising GO to make it dispersible in organic solvents.[412-415]

The perfect material for applications such as conductive inks would combine the best properties of graphene and GO, and be both highly conductive and highly dispersible. These two properties, however, seem mutually exclusive for graphitic materials, since functionalisation to improve dispersibility has a negative impact on electrical conductivity due to disruption of the sp^2 network. On this basis, it is clear that a compromise has to be made, and that the material used for a particular application should be chosen based on the relative importance of these two factors. With this in mind, the following chapter focusses on the properties of a series of intermediate materials between GO and rGO. In addition a novel method of handling GO is introduced to attempt to overcome one of the key problems associated with bulk scale production of GrO, gelling of the partially purified product to afford a solid which is difficult to handle and to purify further.[416]

3.2 Processing and handling of graphene oxide

In order to obtain a series of intermediate materials between GO and rGO, a reduction technique with a relatively long reaction time was chosen, such that materials from different points in the reaction could be easily separated. The chosen method involved refluxing GO in water for various lengths of time. Heating GO in water at 95 °C has previously been shown to increase the C:O ratio; where partially reduced GO was collected after over 70 h of heating.[417] During this heating process the degree of solid settling from the reaction solution increased with time, indicating continued reduction of GO up to ~50 h, after which time the reaction rate appeared to plateaux. For the current study, GO made via the Hummers' method was refluxed in water for 4, 8, 12, 24 or 120 h.

The Hummers' method of producing GO proceeds via a number of steps (figure 44).[156] In the final step of this reaction, as the washings approach pH neutral, the material undergoes a colour change from yellow to dark brown, accompanied by a swelling of the material to form a gel-like solid. Once the gel-like solid has formed, further rinsing to remove excess salts and acids becomes difficult, so in many cases the GO is further

purified by successive mixing with water and separation via centrifugation, which still represents a time-consuming process.

The purified GO collected contains a large amount of water, which makes storage and accurate weighing of the material more difficult than handling dry material, and prevents the full characterisation of the product, particularly in terms of the stoichiometry. Removal of the water to yield either a dark brown, hard, film-like solid or light brown foam-like solid can be achieved by heating GO in a vacuum oven or by freeze-drying respectively. Reduction of GO is accompanied by a change in colour from brown to black, and forms a black solid which can be easily collected by filtration and dries to form a powder-like material, rather than a hard, film-like solid. This means that rGO is easier to handle and store than its GO counterpart.

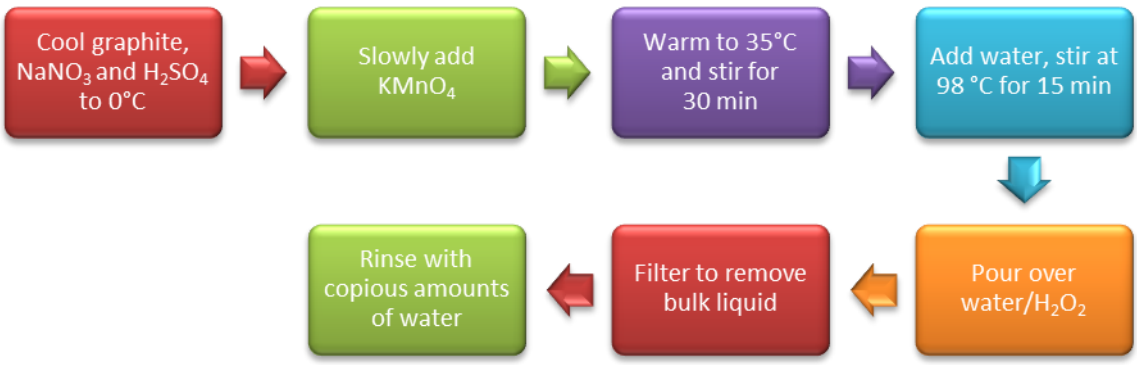

Figure 44: A schematic of the Hummers' reaction split into a number of different steps.

As the final step of the Hummers' reaction is so time consuming, reduction of the unpurified material collected before this step was trialled (figure 45). In this approach the residual salts and acids were removed from the reduced rather than the oxidised material, as the former can be rinsed quickly via filtration. To our knowledge this is the first example of producing rGO directly from unpurified GO. In order to test the impact of omitting the final step, the materials produced after refluxing either 'pre-wash' or 'post-wash' GO in water for 24 h were compared. For many of the characterisation techniques, analysis was repeated for multiple batches of 'post-wash' and 'pre-wash' GO, to compare the variation between the different processing methods with the variation between different batches.

Figure 45: A schematic of the Hummers' reaction split into a number of different steps, illustrating the points from which 'pre-wash' and 'post-wash' GO are obtained.

Before refluxing in water, 'post-wash' GO was a dark brown, gel-like solid, while 'pre-wash' GO was a yellow-brown, wet, clumpy solid. After refluxing both reaction mixtures filtered easily to yield damp, black solids that dried to free-flowing powders. TEM of the materials produced from both 'post-wash' and 'pre-wash' GO revealed crumpled, sheet-like materials (figure 46, top). The sheets were confirmed to be both carbonaceous and graphitic using EFTEM mapping and EELS (see appendix A). The ED patterns of these sheets showed two strong set of spots, indexed to the graphite (100) and (110) planes for the inner and outer sets respectively, and a third, weak set of spots close to the (110) set, indexed to the graphite (200) planes.[302, 418] The presence of spots signified crystalline order, although the breadth of the spots suggested a partially disordered system. Calculations from thickness mapping of these sheets (figure 46, bottom), using the method described in section 2.1.4, suggested their thinnest regions were approximately 25 ± 9 and 20 ± 10 layers for refluxed 'post-wash' and 'pre-wash' GO respectively. The TEM samples were prepared from the dried materials using a minimal amount of sonication (< 5 minutes), and thinner sheets would be expected if the TEM dispersion was prepared using more mechanical energy.

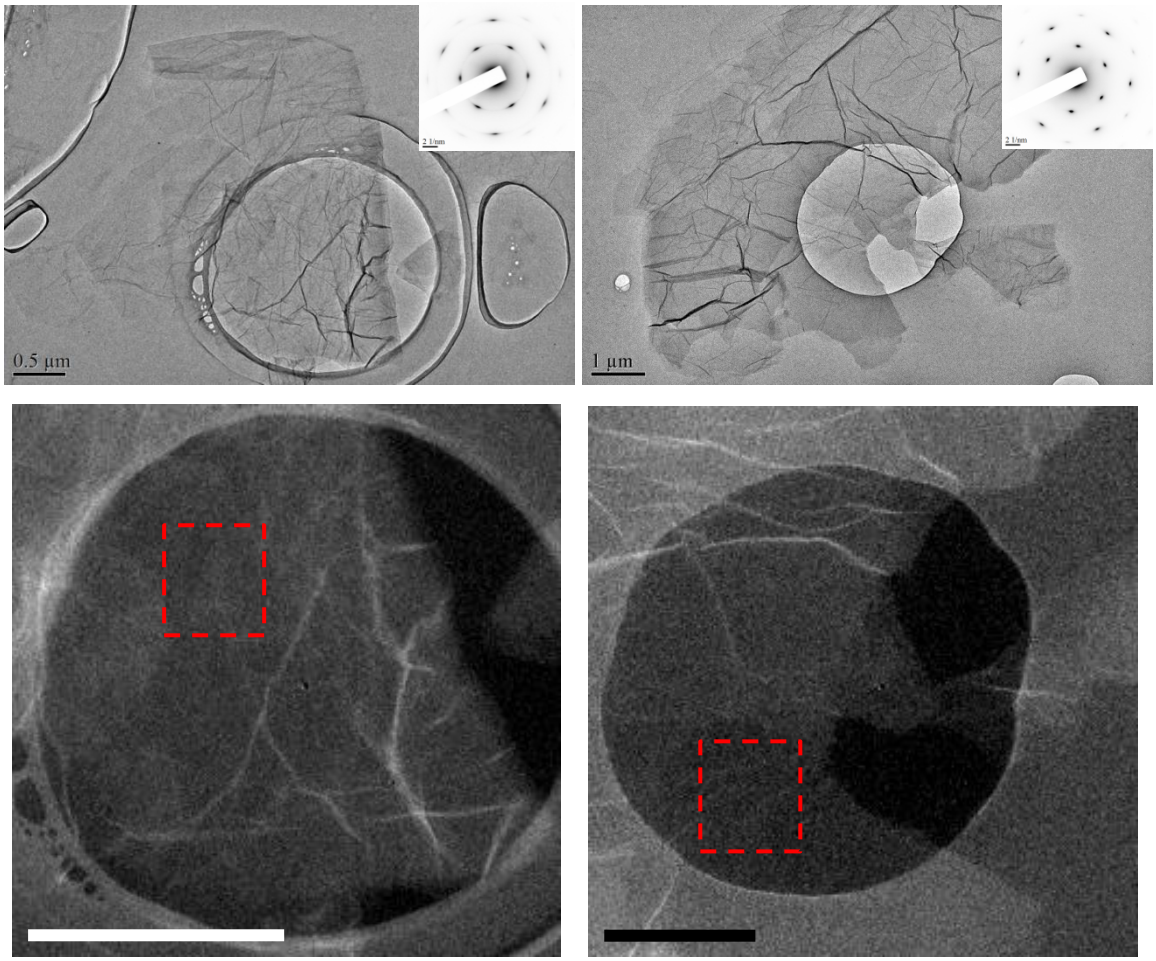

Figure 46: TEM images with inverted ED patterns inset (top) and EFTEM thickness maps (bottom) of the materials produced by refluxing 'post-wash' (left) and 'pre-wash' (right) GO in water for 24 h. The scale bars for thickness maps represent 1 µm, and the red boxes indicate the regions from which the thickness calculations were performed. The inner and outer rings in the SAED pattern are indexed to the (100) and (110) graphitic planes respectively.

Raman spectra of water-refluxed, 'pre-wash' and 'post-wash' GO were almost identical and showed the typical large, broad D band and broad G peak of GO,[364] along with the disorder induced and second order bands consistent with functionalised graphitic materials (figure 47).[419] The I_D/I_G ratios were the same within errors for the two materials; with values of 0.95 ± 0.02 and 0.93 ± 0.02 for 'pre-wash' and 'post-wash' GO respectively, and the FWHM of the D bands were also the same within error for the two; with values of 165 ± 3 and 164 ± 2 cm^{-1} respectively. These results indicated that the defect levels and crystallinity of the materials produced by refluxing 'post-wash' or 'pre-wash' GO were the same.

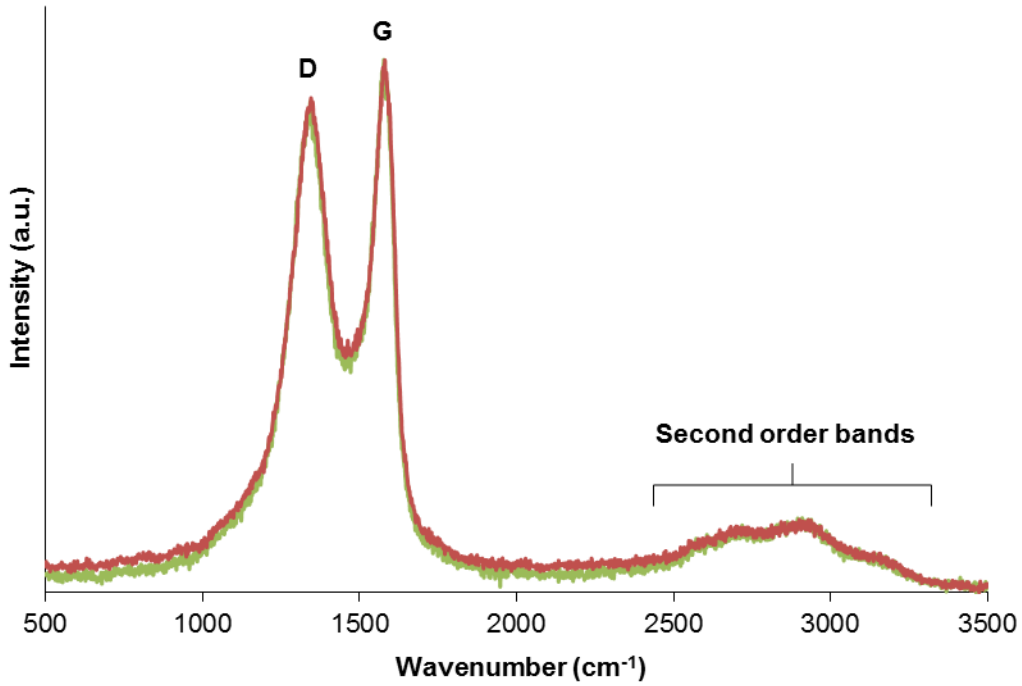

Figure 47: Raman spectra of the materials produced by refluxing 'post-wash' (green) and 'pre-wash' (red) GO in water for 24 h, normalised to the height of the G peak. Spectra were recorded using 532 nm laser excitation.

The burn profiles of the materials in air suggested that the materials had similar defect levels as the high temperature thermal stability of the materials was the same (figure 48). The mass loss at ca. 200 °C, attributed to the loss of labile oxygen-containing groups,[391] was also similar for both materials; with values of 25 and 23 wt.% for 'pre-wash' and 'post-wash' GO respectively; suggesting that the degree of functionalisation was not affected by omitting the final GO purification step. The residual after complete burn was 1 wt.% for both 'post-wash' and 'pre-wash' GO, which indicated low levels of inorganic impurities from the Hummer's reaction for both processing methods.

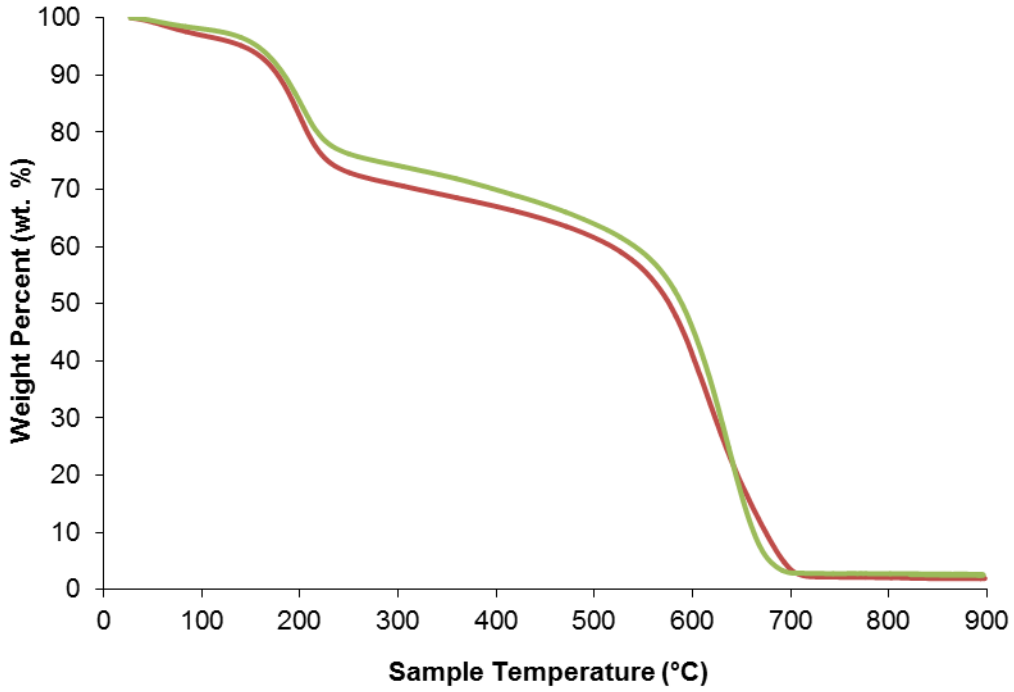

Figure 48: TGA spectra of the materials produced by refluxing 'post-wash' (green) and 'pre-wash' (red) GO in water for 24 h, corrected to 100 % mass at the end of the dwell at 30 °C (30 min), before the ramp from 30 – 900 °C at 10 °C/min in air.

To ascertain whether starting from 'pre-wash' rather than 'post-wash' GO affected the type or proportion of oxygen functionalities in the graphitic system, XPS and SSNMR were performed on the different materials. The XPS survey scans revealed the clear presence of carbon, oxygen and silicon, the latter of which is likely to have originated from the underlying silicon substrate (figure 49). In addition, boron and phosphorus were detected, which were both contaminants (table 5). The presence of different amounts of these contaminants and potentially different contributions from SiO_2 means the C/O ratio calculated from the survey scan is not a reliable measure of the material. The absence of additional peaks for the material produced from 'pre-wash' GO compared with the 'post-wash' GO (e.g. Mn or K) confirmed the TGA-based finding that omitting the initial rinsing step did not result in high levels of impurities in the system.

Table 5: The atomic concentrations for the materials produced by refluxing 'post-wash' and 'pre-wash' GO in water for 24 h, calculated from the XPS survey scans. The errors are reported as 95 % confidence intervals based on three repeats.

	Atomic concentration (%)					
Sample	**O 1s**	**C 1s**	**P 2p**	**B 1s**	**Si 2p**	**C/O**
Post-wash	26.2 ± 0.1	27 ± 4	6.1 ± 0.3	11 ± 1	34 ± 3	1.1 ± 0.2
Pre-wash	24.9 ± 0.3	47 ± 5	2.2 ± 0.4	7 ± 1	19 ± 3	1.9 ± 0.2

The C 1s XPS lineshape was very similar for the materials produced via refluxing 'post-wash' and 'pre-wash' GO in water for 24 h (figure 50). The fitting of the C 1s peak into various carbon-oxygen components showed that both materials contained large amounts of C-O functionalities, with an overall calculated C:O ratio of ~3.0 for both the materials based on the C 1s fit. The presence of C-O functionalities was also supported by SSNMR (figure 51), by the occurrence of large peaks at ~60 and ~70 ppm, associated with epoxide and hydroxide groups respectively.[379]

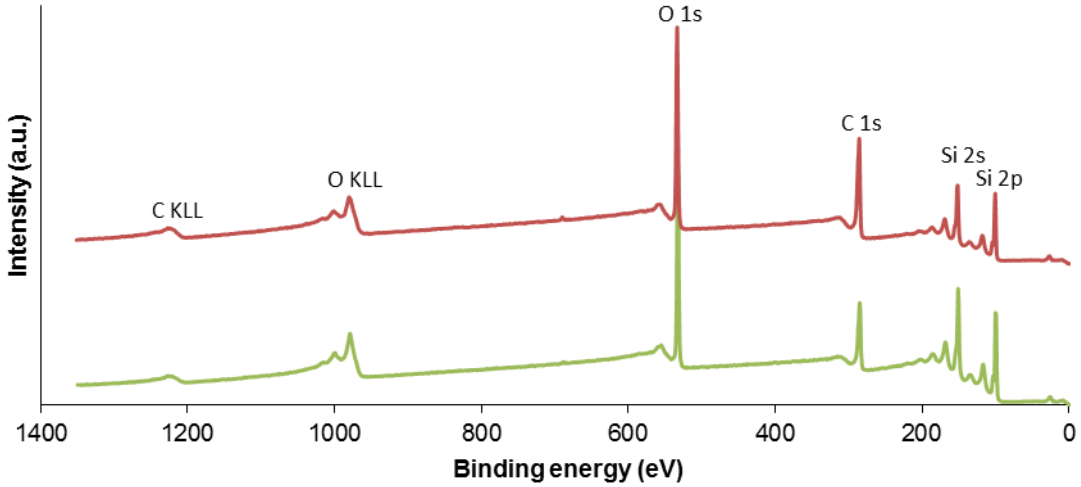

Figure 51: A stack plot of XPS survey scans of the materials produced by refluxing 'post-wash' (green) and 'pre-wash' (red) GO in water for 24 h.

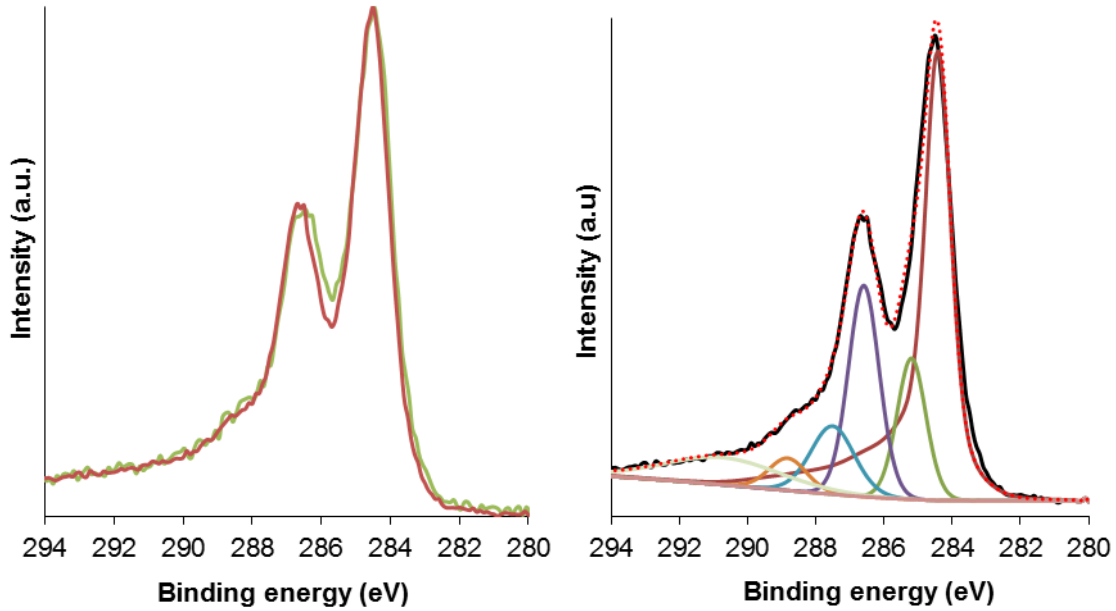

Figure 50: C 1s XPS spectra of the materials produced by refluxing 'post-wash' (green) and 'pre-wash' (red) GO in water for 24 h normalised to the C=C peak (left), and the peak fit for the 'pre-wash' sample (right), showing the peaks assinged to C=C (maroon), C-C (green), C-O (purple), C=O (blue), COOH (orange) and π-π (light green) and the Tougaard background (pink), where the C=C was fit using a measured rGO lineshape. The dashed red line shows the sum of the fit components and is an indication of the quality of the fit. Fits for both materials are provided in appendix A.

Table 6: Results of peak fitting the C 1s lineshape of the refluxed samples into different carbon-oxygen components. The errors are reported as 95 % confidence intervals based on three repeats.

	Percentage composition of C 1s (%)					
Sample	**C=C & C-C**	**C-O**	**C=O**	**COOH**	**π-π**	**C/O**
Post-wash	63 ± 1	19 ± 2	7.1 ± 0.5	3.4 ± 0.5	7.4 ± 0.8	3.0 ± 0.2
Pre-wash	61.5 ± 0.5	18.1 ± 0.4	8.1 ± 0.2	3.6 ± 0.2	8.7 ± 0.3	2.99 ± 0.02

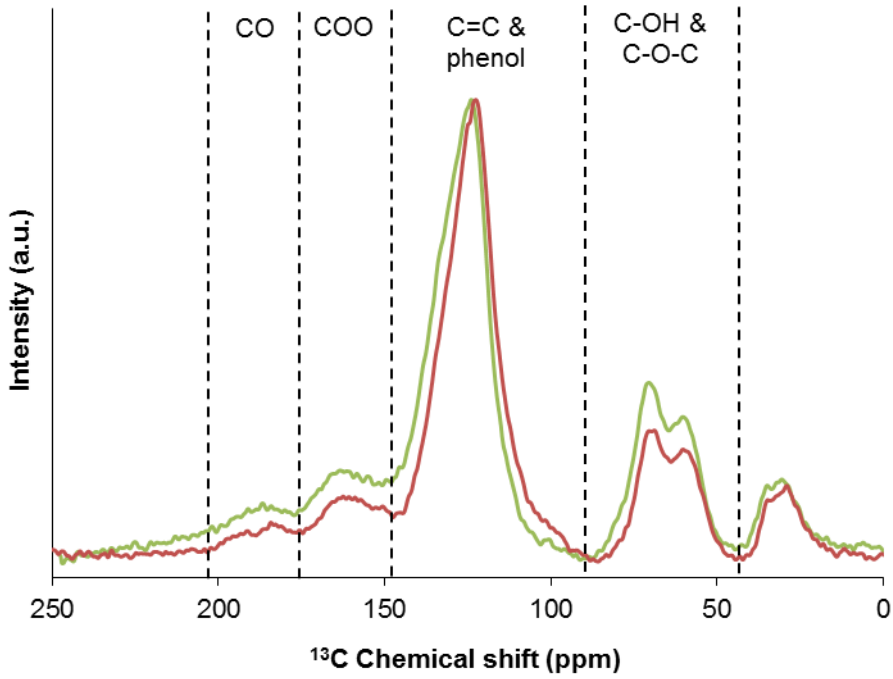

Figure 51: ^{13}C direct excitation MAS SSNMR spectra for batch one (left) and batch two (right) materials produced by refluxing 'post-wash' (green) and 'pre-wash' (red) GO in water for 24 h. The spectra were normalised to the C=C and phenol peak. Fits for both materials are provided in appendix A.

UV-vis was obtained for the materials sonicated in water, as described in section 7.1.13. The peak maxima for the 'pre-wash' and 'post-wash' material were the same within experimental error (254 nm), indicating a similar degree of reduction for the materials (figure 52).[371] The appearance of the solutions and absorbance at 660 nm were also similar, suggesting that omitting the initial rinsing step did not negatively impact the dispersibility of the materials. Some variation in the dispersibility of the materials is expected as the aggregation upon drying is likely to vary across different materials, which will impact the degree of exfoliation upon sonication, and hence the exact concentration of material dispersed.

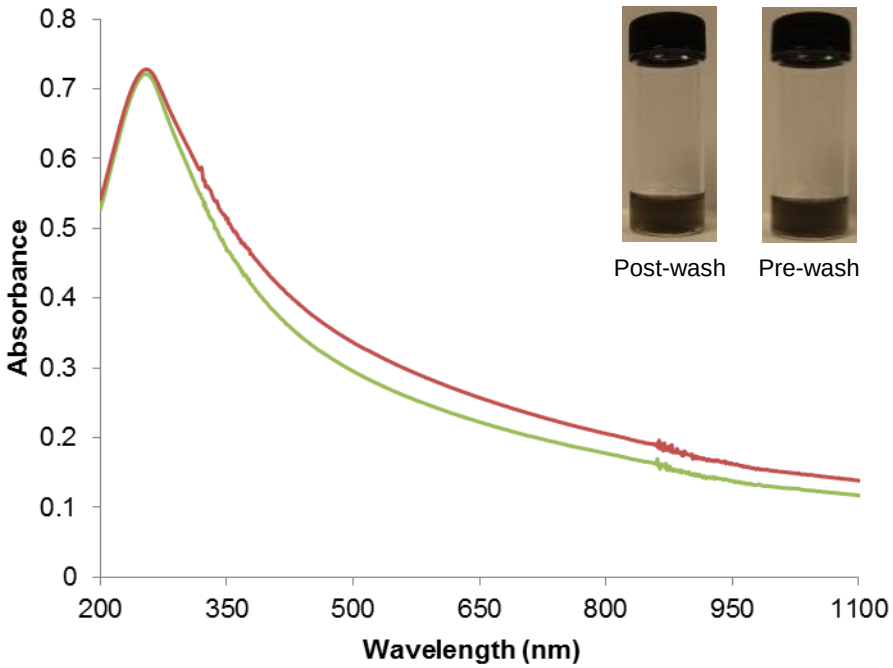

Figure 52: UV-vis spectra of aqueous dispersions of the materials produced by refluxing 'post-wash' (green) and 'pre-wash' (red) GO in water for 24 h, collected on dispersions formed by sonicating 10 mg of solid in 10 ml of water for 15 min. Photographs of the dispersions are inset.

Finally, to test the impact of omitting the initial rinsing step on the electrical conductivity, four-point probe measurements were taken on air-dried, thin films of the material formed by filtration of aqueous solutions of the material (table 7). Bulk electrical measurements were also carried out on thin pellets of the material using a bespoke pellet press (see section 7.1.15). The values obtained were similar across the different materials, with slightly lower resistances measured for the 'pre-wash' sample than for the 'post-wash' samples.

While the products of refluxing 'post-wash' or 'pre-wash' GO may have been expected to be different due to the presence of residual salts and acids for the 'pre-wash' material, the data presented above suggests that the presence of impurities during the reflux reaction did not affect the carbon product obtained. The analysis was completed for multiple batches of material which demonstrated that the small amounts of variation seen between the 'post-wash' and 'pre-wash' was of the same order as the variation between different batches of starting material; supporting the conclusion that omitting the final step of the Hummers' reaction had no impact on the obtained product. With

this in mind, the partially reduced intermediates between GO and rGO described in the following sections were prepared by refluxing 'pre-wash' GrO.

Table 7: Electrical measurements of thin films and pellets of the materials produced by refluxing 'post-wash' and 'pre-wash' GO in water for 24 h. The errors are reported as 95 % confidence intervals based on three repeats.

	Pellet		Film
Starting GrO	**Resistance (Ω)**	**Resistivity (Ω m)**	**Sheet Resistance (Ω/□)**
'Post-wash'	3.3×10^4	250	$(1.2 \pm 0.3) \times 10^7$
'Pre-wash'	1.2×10^4	90	$(6.6 \pm 0.3) \times 10^6$

3.3 Characterisation of intermediates between GO and rGO

The materials produced after 4, 8, 12, 24 and 120 h of refluxing 'pre-wash' GO in water were visibly different from one another. After 4 h of refluxing the material appeared similar to 'post-wash' GrO; a brown gel-like solid which was difficult to filter and required centrifugation to aid purification. After 8 and 12 h of refluxing the material was visibly darker but still relatively slow to filter compared with the material produced via refluxing for 24 h; which appeared completely black and filtered readily. After 120 h of refluxing the material appeared black-grey, similar to the starting graphite, and filtered with ease. TEM performed on samples in the set confirmed that the material remained sheet-like in nature after reflux (see appendix A).

3.3.1 Chemical changes during processing

XRD spectra of the refluxed materials (figure 53) showed that as the reflux time increased, the peak at $2\theta \approx 12°$, corresponding to the GO (001) plane,[167, 392] became broader and less intense; suggesting a decrease in the out-of-plane crystalline ordering of the materials. This has been observed elsewhere during the reduction of GO to rGO, and is thought to be caused by the removal of oxygen-containing groups from between the graphitic layers.[393, 420] The peak at $2\theta \approx 43°$; corresponding to the graphitic (100) plane,[418] was more pronounced for GO refluxed for 12 h or more, which may indicate

an increase in the in-plane crystalline ordering of these materials compared with materials refluxed for shorter periods. The peaks marked by asterisks, at 2θ ≈ 21.6° and 24°, were present in the blank run of petroleum jelly on the glass slide and not inherent to the carbon-based products.

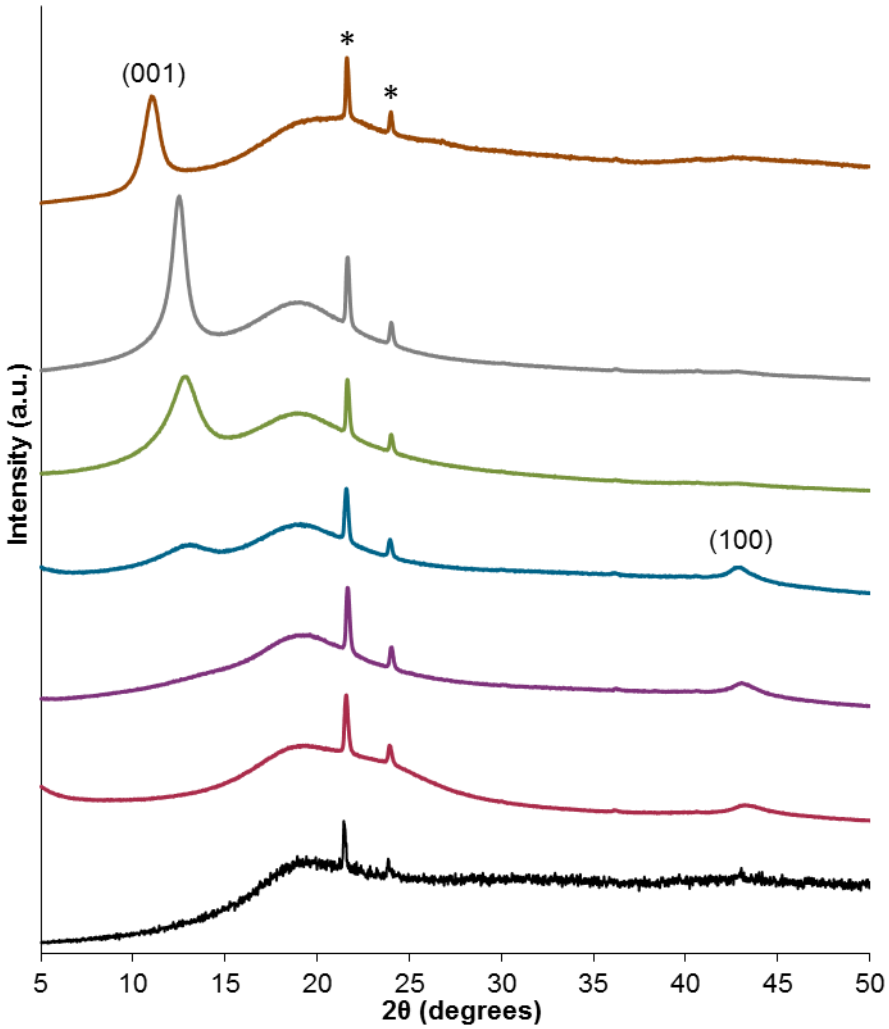

Figure 53: XRD patterns stack plot of the materials produced by refluxing GO in water for 4 h (grey), 8 h (green), 12 h (blue), 24 h (purple) and 120 h (red) with the sample blank shown (black) and 'post-wash' GO as a reference (brown). The peaks marked by asterisks are evident in the sample blank and hence are not inherent to the carbon product. Patterns were recorded using Cu $K\alpha_{1,2}$ radiation (λ = 1.54 Å) and normalised to the peak at $2\theta \approx 19°$.

Raman spectra of the materials refluxed for different lengths of time showed the same general features consistent with GO and rGO (figure 54). A slight increase in the I_D/I_G ratio, along with a decrease in the FWHM of the D band was observed with increasing reflux time, particularly for the samples refluxed for 24 and 120 h. As discussed in section 2.4, these combined observations suggest the formation of small sp^2 domains

upon refluxing, which is consistent with reduction of the material. An increase in I_D/I_G ratio upon reduction has been observed elsewhere for alternative water-based methods.[167, 171, 393] While the G band has been reported to shift upon reduction previously,[365, 366] there is no trend in the position of the G band in the current study, with the average values for each sample falling within the range of 1590 ± 3 cm^{-1}. Note that the signals were too weak to collect reliable FTIR spectra for all samples using the ATR configuration.

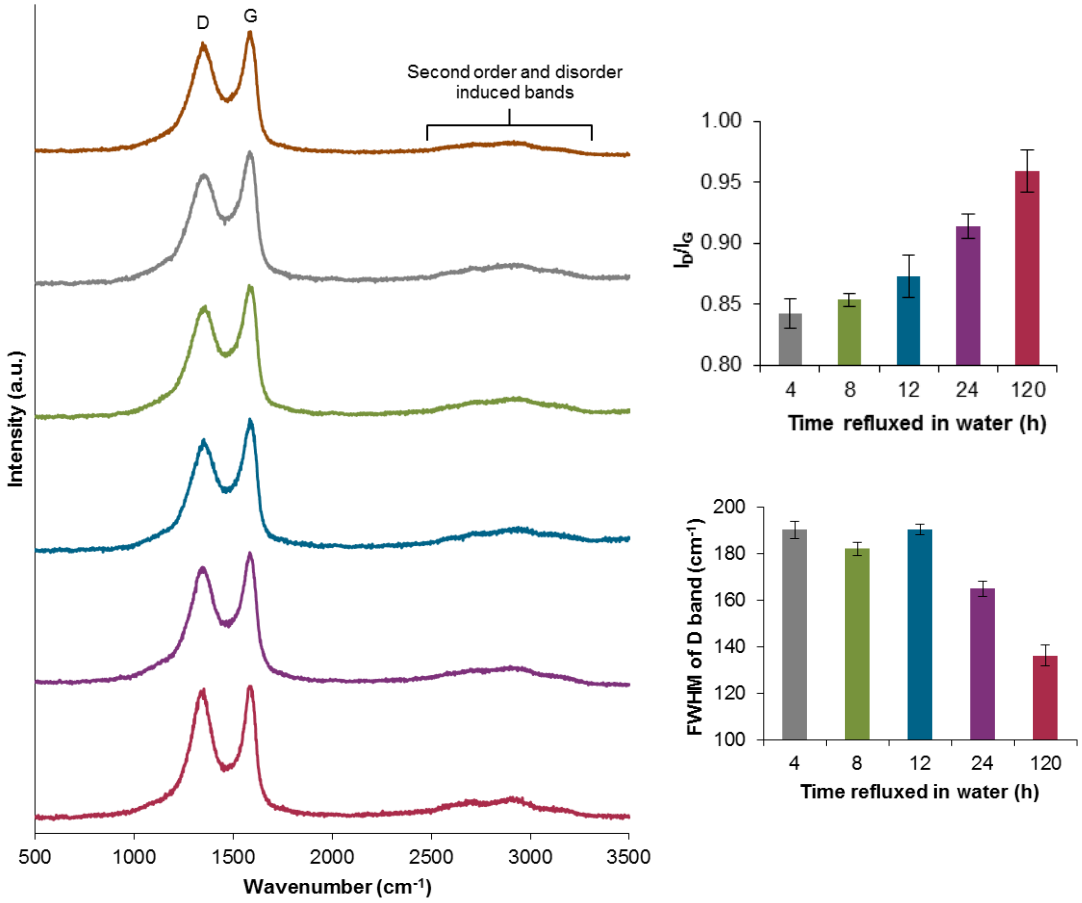

Figure 54: Raman spectra stack plot (left), and graphs of the relative I_D/I_G ratios (top right) and D band FWHM (bottom right) for the materials produced by refluxing GO in water for 4 h (grey), 8 h (green), 12 h (blue), 24 h (purple) and 120 h (red) and 'post-wash' GO as a reference (brown). Raman spectra were recorded using 532 nm laser excitation and normalised to the height of the G peak.

The TGA profiles of the different materials showed that the mass loss ca. 200 °C was approximately the same for materials refluxed in water for 4 – 12 h, lower for the sample refluxed for 24 h, and significantly lower for the sample refluxed for 120 h (figure 55). As the mass loss at this temperature is associated with the loss of labile oxygen functionalities,[391] the general trend of decreasing mass loss with increasing reflux time supports the conclusion that the GO material was progressively reduced. Further to this there was a general trend of increasing temperature of onset of burn with increasing reflux time (table 8). This onset is often attributed to the burning of the carbon backbone and a shift to higher temperature can be ascribed to an increase in the relative proportion of sp^2 compared with sp^3 carbon,[389] hence the observed shift agreed with the findings from the Raman spectroscopy; that sp^2 carbon was created upon refluxing. The residuals at 900 °C for the refluxed samples were relatively low in all cases (<3 wt. %), suggesting that the material was relatively pure.

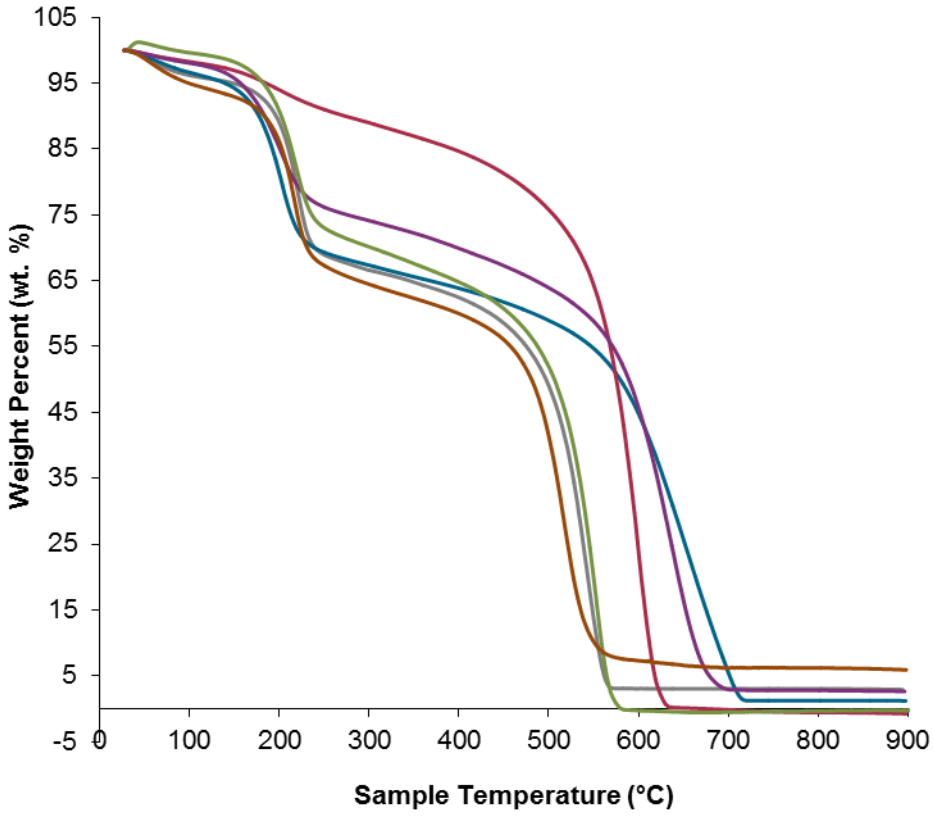

Figure 55: Overlaid TGA profiles of the materials produced by refluxing GO in water for 4 h (grey), 8 h (green), 12 h (blue), 24 h (purple) and 120 h (red) and 'post-wash' GO as a

reference (brown), corrected to 100 % mass at the end of the dwell at 30 °C (30 min), before the ramp from 30 – 900 °C at 10 °C/min (in air).

Table 8: Numerical data extracted from TGA profiles of the materials produced by refluxing GO in water for various amounts of time. The error reported in the residual at 900 °C is the 95 % confidence level based on two repeats of the 4 h refluxed sample.

Time refluxed in water (h)	Mass loss for 150-250 °C (wt. %)	Onset of burn (°C)	Residual at 900 °C (wt. %)
4	26	510	2.9 ± 0.8
8	25	510	0.3 ± 0.8
12	25	580	1.2 ± 0.8
24	20	610	2.6 ± 0.8
120	6	550	-0.8 ± 0.8

SSNMR spectra displayed the expected trend of decreasing oxygen functionalities (epoxy and hydroxyl groups) with increasing reflux time (figure 56). Fitting of the SSNMR lineshape into different regions allowed a semi-quantitative analysis of this trend, where the ratio of aromatic carbon to C-O-x was found to vary between ~50:50 for the material refluxed for 4 h to ~100:0 for material refluxed for 120 h (figure 37). This finding was consistent with the TGA results and with other reports of chemical reduction of GO studied via SSNMR.[377, 421] The proportion of carboxyl and carbonyl groups was low and remained relatively consistent across all samples.

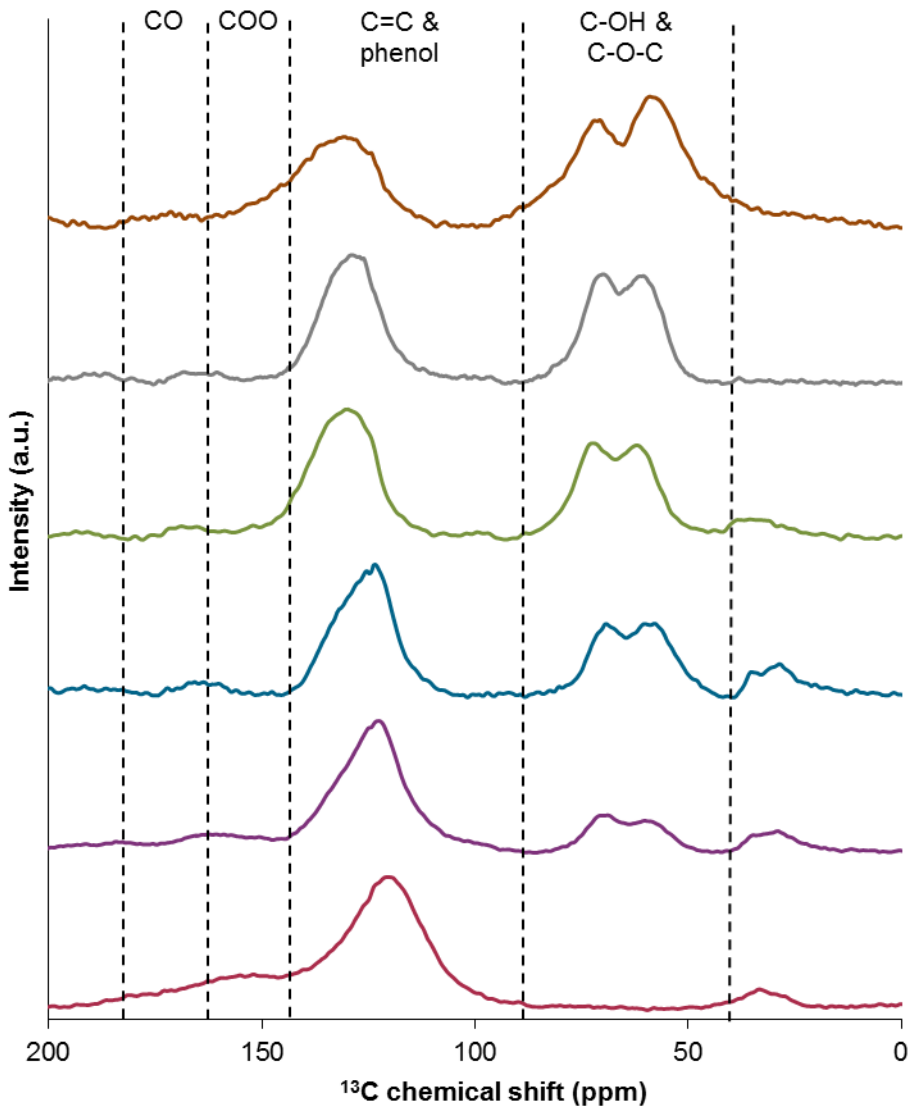

Figure 56: ^{13}C direct excitation MAS SSNMR spectra stack plot of the materials produced by refluxing GO in water for 4 h (grey), 8 h (green), 12 h (blue), 24 h (purple) and 120 h (red), and 'post-wash' GO as a reference (brown). The spectra were normalised to the C=C and phenol peak. Fits for all materials are provided in appendix A.

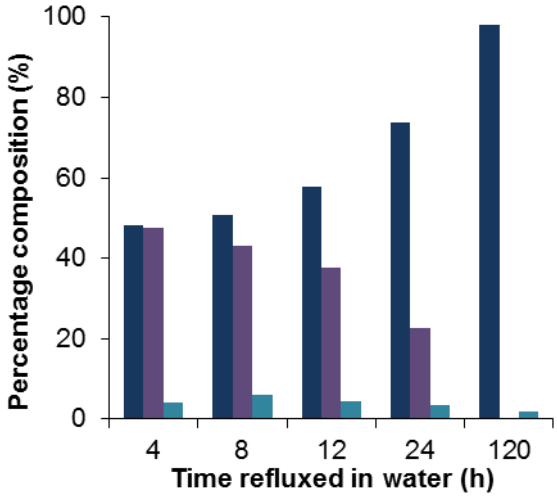

Region 1	Region 2	Region 3
C=C	C-O-C	O=C-O
Phenol	C-OH	C=O

Figure 57: A graph to show the relative area contributions of different regions of the SSNMR spectra to the total carbon environment (left) and a table detailing the different regions (right).

In agreement with SSNMR, the C 1s XPS lineshapes exhibited a decrease in the peak corresponding to C-O with increasing reflux time (figure 58). The results of fitting the XPS lineshapes into different bonding components supported the SSNMR based conclusion that low levels of carboxyl and carbonyl groups were present and relatively consistent across all samples (table 9). Peak fitting also revealed that the relative proportion of the C=C and π-π components increased with increasing reflux time, suggesting that aromaticity was increased during the reflux process. The C/O ratio calculated from the peak fitting confirmed the observable trend of increasing C/O with increasing reflux time, although the absolute values obtained should be treated with caution as they are dependent on the fitting parameters used. The plot of the relative contributions of the different bonding components to the carbon environment, grouped to reflect the regions in the SSNMR spectra, showed the same trend as the SSNMR data; with the aromatic carbon to C-O-x ratio increasing with increased reflux time (figure 59). While the SSNMR showed a decrease of the aromatic carbon to C-O-x ratio from ~50:50 to ~100:0, XPS showed a decrease from ~75:25 to ~95:5. This difference may be due to incomplete relaxation of the aromatic carbon during SSNMR measurements, leading to an overestimation of the relative proportion of C-O-x groups or as a result of the XPS fitting process underestimating the C-O-x contribution due to residual C-O-x groups in the r-GO lineshape used to fit the C=C component. The finding that the relative proportion of C-O-x functionalities and the overall C/O ratios decreased upon refluxing GO in water is consistent with previously reported water-mediated reduction of GO.[417, 421]

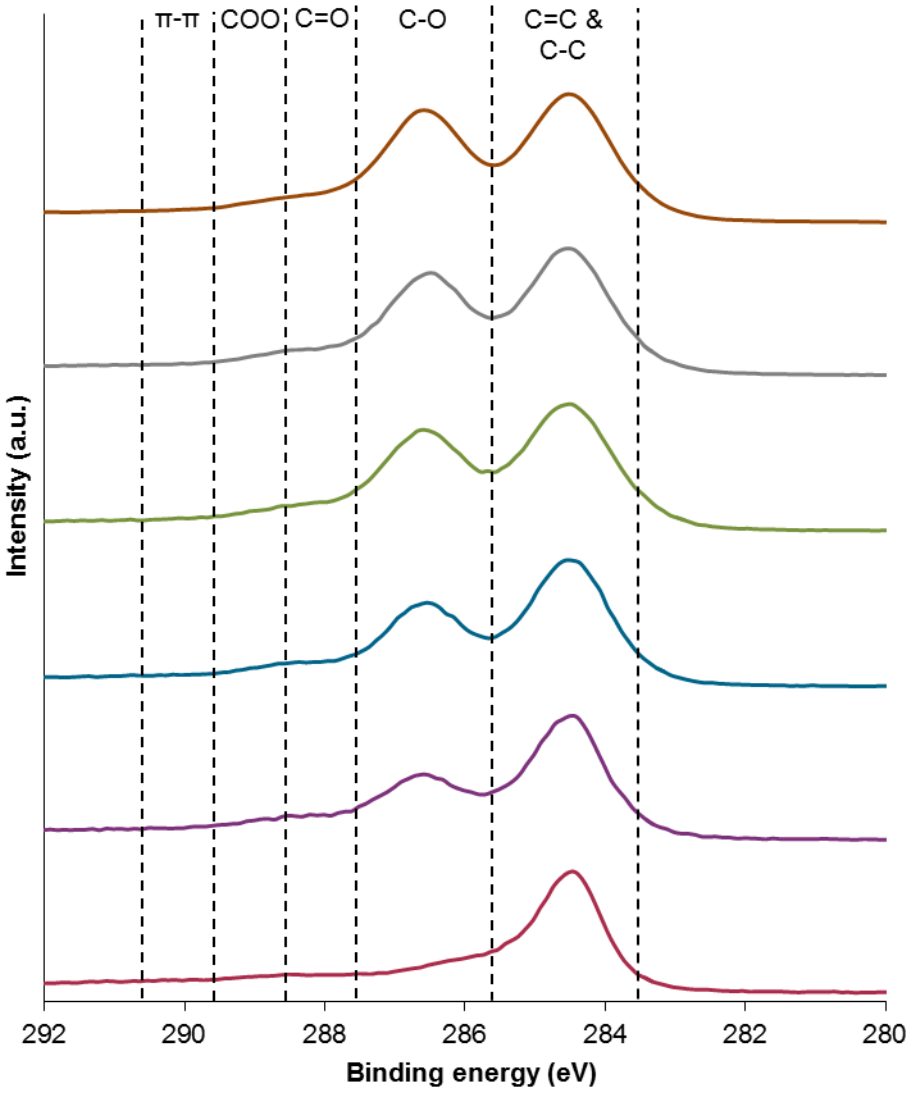

Figure 58: C 1s XPS spectra stack plot of the materials produced by refluxing GO in water for 4 h (grey), 8 h (green), 12 h (blue), 24 h (purple) and 120 h (red), and 'post-wash' GO as a reference (brown). The spectra were normalised to the C=C peak. Fits for all materials are provided in appendix A.

Table 9: Results of peak fitting the C 1s lineshapes for the refluxed materials into different carbon-oxygen components. The errors are reported as 95 % confidence intervals based on three repeats.

	Percentage composition of C 1s (%)					
Reflux Time	**C=C and C-C**	**C-O**	**C=O**	**COOH**	**Pi-Pi**	**C/O**
4	68 ± 3	23 ± 3	6.1 ± 0.2	1.7 ± 0.1	1.0 ± 0.3	3.1 ± 0.3
8	72 ± 1	20 ± 1	5 ± 1	1.9 ± 0.1	1.2 ± 0.2	3.5 ± 0.2
12	75.8 ± 0.2	16.9 ± 0.5	4.1 ± 0.1	1.4 ± 0.6	1.7 ± 0.1	4.2 ± 0.1
24	78 ± 2	11.9 ± 0.9	5 ± 1	1.9 ± 0.3	3.4 ± 0.4	4.9 ± 0.4
120	87 ± 1	2.5 ± 0.5	1.4 ± 0.7	1.4 ± 0.1	8.0 ± 0.5	15 ± 2

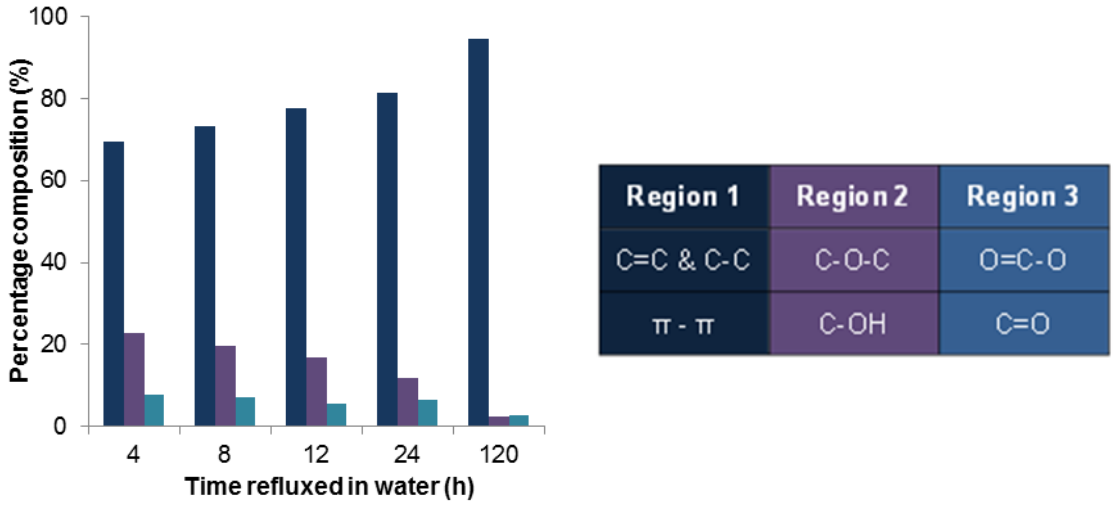

Figure 59: A graph to show the relative area contributions of different regions of the XPS spectra to the total carbon environment (left) and a table detailing the different regions (right).

3.3.2. Properties of partially reduced graphene

In order to evaluate the dispersibility of the GO at various stages of reduction, the refluxed material was sonicated in water to form dispersions. These dispersions, prepared by the method described in section 7.1.13, were markedly different from one another in appearance; where increased reflux time led to visibly less dispersible material. This trend can be observed for the solutions diluted 5-fold in high purity water (figure 60). The dispersibility of GO refluxed in water for 24 h was slightly higher, but

approximately equivalent to that of GO reduced chemically using hydrazine hydrate (rGO), using the method described by Park *et al*.[394] The dispersibility of GO refluxed in water for 120 h was considerably less than that refluxed for 24 h, but still greater than bulk graphite. Note that internal rGO and graphite samples have been used for dispersibility comparisons rather than comparing with the literature due to the difficulties of exactly replicating the dispersion conditions used elsewhere.

Figure 60: Photos of the dispersions created by sonicating 10 mg of solid material produced by refluxing GO in water for 4, 8, 12, 24 and 120 h (left to right) in 10 ml of water, taken 24 h after sonication and diluted 5-fold with addition water, and photos of equivalent dispersions of GO reduced using hydrazine (blue outline) and 'pre-wash', 325 mesh graphite (green outline).

UV-vis was performed on diluted dispersions (5-fold dilution for material refluxed for 24 or 120 h, 50-fold dilution for material refluxed for 4, 8 or 12 h) to quantify the difference in dispersibility between the materials (figure 61). The dispersions were analysed 24 h after initial sonication to allow material that was poorly suspended to settle out, and diluted to suit the detection limits on the spectrometer. It should be noted that as partially reduced GO formed suspensions rather than solutions, the 'absorbance' measured is likely to contain contributions from light scattering, which itself is affected by particle size. The UV-vis data supported the observable trend of decreasing material dispersibility with increasing reduction time, and assuming the same molar extinction coefficient at 660 nm for the different graphitic materials, GO refluxed for 8, 12, 24 and 120 h was 30, 55, 75 and 90 % less dispersible respectively than GO refluxed for 4 h. If the 4 h refluxed sample is taken to be fully dispersed, this relates to a change in concentration of solid in solution from 1 mg/ml to 0.1 mg/ml. The assumption that the molar extinction coefficient is the same across the different samples may be an oversimplification; as partially reduced GO has been shown to absorb more strongly across the visible spectrum than GO.[421] This has been attributed to the restoration of aromatic rings in the graphitic back-bone upon reduction (see section 2.5). As the trend of increased absorbance upon reduction opposes the trend seen in this data, the

overall trend of decreasing dispersibility with increasing reduction level remains valid regardless of the potential differences in molar extinction coefficients.

The dispersions analysed 8 days after sonication (one week after initial analysis) displayed the same trend in concentration as seen after 24 h; with more reduced materials resulting in less concentrated solutions (figure 62, left). There was no obvious trend in the stability of the solutions with time, although the solution containing the most reduced material was shown to be the least stable; reducing in concentration by ~50% despite having the lowest concentration initially. As previously discussed, the shift in the peak ca. 230 nm for GO, ascribed to the restoration of electrical conjugation upon reduction, can be used as a measure of reduction. In the current work the peak maxima of the refluxed materials showed an upward trend between 234 nm for the material refluxed for 4 h and 266 nm for the material refluxed for 120 h; acting as further confirmation that materials with varying reduction levels were successfully produced. Plotting the position of the UV-vis peak maximum versus the absorbance at 660 nm demonstrated the anticipated trend of decreasing dispersibility with increasing reduction level (figure 62, right).

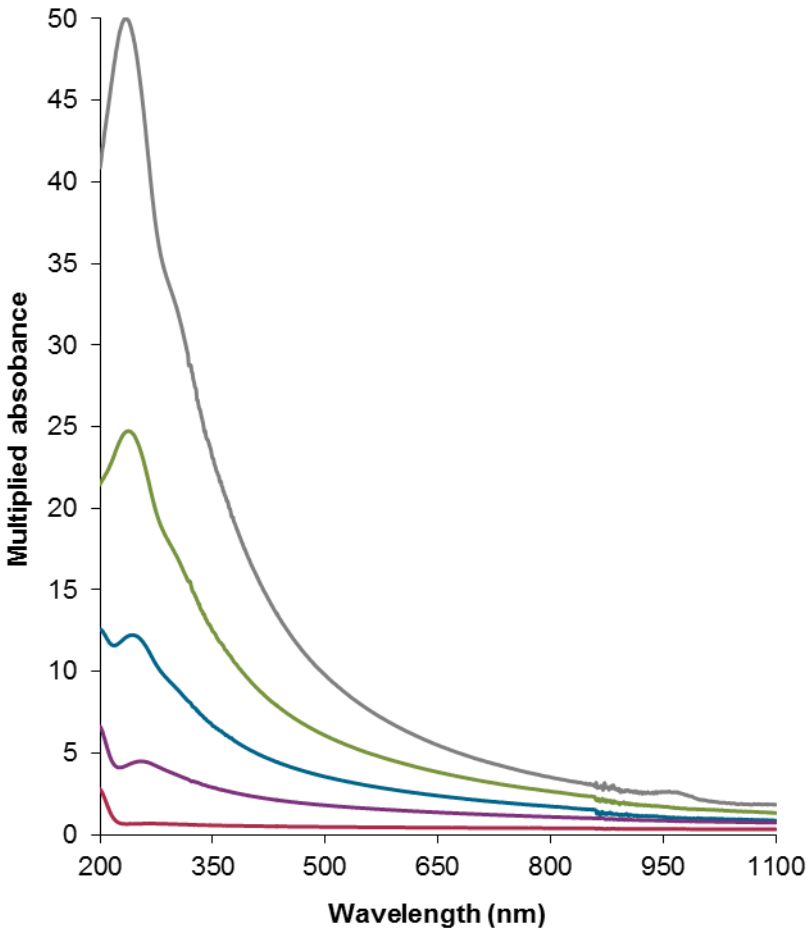

Figure 61: UV-vis spectra of aqueous dispersions of the materials produced by refluxing GO in water for 4 h (grey), 8 h (green), 12 h (blue), 24 h (purple) and 120 h (red) multiplied to account for dilution factors.

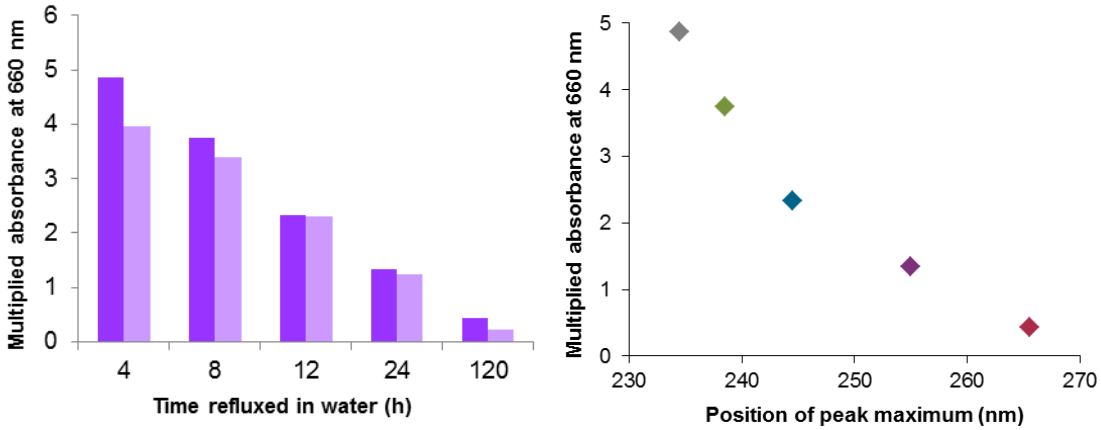

Figure 62: A plot of the absorbance at 660 nm for each material 24 h (dark purple) and 8 days (light purple) after sonication (left), and a chart to show the correlation between peak height and absorbance at 660 nm (right).

Electrical measurements were made on both thin films of the refluxed GO materials created by vacuum filtration and on solid pellets (table 10). The resistance of the film of GO refluxed for 8 h was too high to measure using a 4-point probe assembly and the resistance of the GO refluxed for 4 h was too high to measure using either technique. The results from the pellets showed an overall trend of decreasing resistivity with increasing reflux time, with a 7 orders of magnitude reduction in the resistivity of the material between the samples refluxed in water for 8 and 120 h. The results from the thin films confirmed the trend, with a 4 orders of magnitude decrease in sheet resistance between the samples refluxed in water for 12 and 120 h. These results are in agreement with previously reported measurements of thin films of processed GO materials,[417] where a 5 orders of magnitude decrease in resistance was reported after heating in water at 95 °C for over 70 h. The electrical conductivity of the GO refluxed in water for 120 h was lower than that of graphite or rGO produced via reduction of GO using hydrazine hydrate (table 11), suggesting that the material produced via refluxing in 120 h was still an intermediate material between GO and rGO rather than being fully reduced.

Table 10: Electrical measurements of thin films and pellets of the materials produced by refluxing GO in water for various lengths of time.

	Pellet		Film
Time refluxed in water (h)	**Resistance (Ω)**	**Resistivity (Ω m)**	**Sheet Resistance (Ω/□)**
4	-	-	-
8	2.9×10^{7}	2.2×10^{5}	-
12	3.5×10^{6}	2.8×10^{4}	$(2.2 \pm 0.1) \times 10^{8}$
24	1.2×10^{4}	9.2×10^{1}	$(6.6 \pm 0.3) \times 10^{6}$
120	4.4×10^{1}	3.4×10^{-1}	$(3.0 \pm 0.1) \times 10^{4}$

Table 11: Electrical measurements of thin films and pellets of 325 mesh graphite and rGO produced via the hydrazine hydrate-mediated reduction of GO.

	Pellet		Film
Sample	**Resistance (Ω)**	**Resistivity (Ω m)**	**Sheet Resistance (Ω/□)**
rGO	-	-	$(1.5 \pm 0.2) \times 10^{2}$
Graphite	5.8×10^{-1}	7.5×10^{-3}	$(5.7 \pm 0.8) \times 10^{2}$

Comparison of the relative dispersibilities and electrical conductivities of the partially reduced GO materials showed that there was a clear correlation between the two (figure 62). In agreement with the original hypothesis, the material that had the greatest aqueous dispersibility (indicated by the UV-vis absorbance at 660 nm) had the lowest electrical conductivity (indicated by resistance). This result highlights the important trade-off between these two properties upon reduction of GO, and hence the advantages of being able to tailor the level of reduction to a particular application. Other properties than have been shown to vary controllably with GO oxidation/reduction level in the literature are the electrochemical properties,[401] the band gap,[422] and the dispersibility of the material in a polymer matrix.[423]

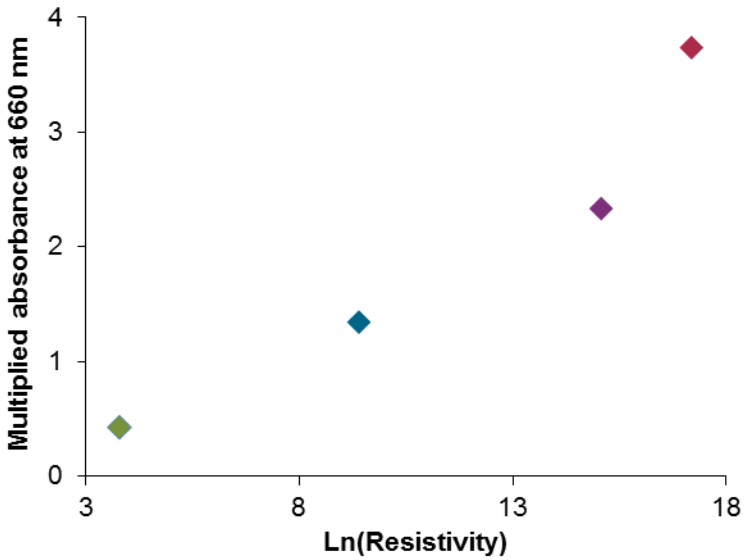

Figure 63: Plot of absorbance at 660 nm against the natural logarithm of the resistance for GO refluxed in water for 8 h (green), 12 h (blue), 24 h (purple) and 120 h (red).

3.3.3 Mechanism of reduction

The reduction of GO at relatively low temperatures and in the absence of chemical reducing agents has been reported in the literature for both solvent[423-425] and solvent-free systems.[426-429] In order to try to decouple the effects of solvent and temperature in the current study, the results of refluxing GO in water were compared with the results of heating freeze-dried GO foams in a tube furnace at 100 °C. GO foams formed by freeze-drying a solution of purified GO in water were used rather than GO film dried down from wet GO as the former was believed to be a more suitable analogue of a GO solution (based on the higher amounts of exposed surface area for the freeze-dried material). Akin to the colour changes observed when refluxing GO in water, colour changes from brown to brown/black and black were seen upon heating the GO foams for 24 h and 120 h respectively (figure 64).

The shift in the UV-vis λ_{max} and the decrease in electrical resistance (table 12) supported the observation that GO foams can be partially reduced by heating to 100 °C. This is a lower temperature than used elsewhere for solvent-free GO reduction, but thermal decomposition as low as 70 °C has been previously noted in the literature,[430] so partial reduction is not unexpected. The UV-vis and electrical conductivity results showed that for the same reaction times GO refluxed in an aqueous system was reduced more than GO heated in air, and that roughly the same

level of reduction was induced upon heating in air for 120 h as was achieved by heating in water for 24 h. It should be noted that a portion of GO foam was also heated to 150 °C in air for 24 h, resulting in a materials that had the same UV-vis λ_{max} as GO refluxed in water for 120 h and an order of magnitude lower electrical resistance (see appendix A). This suggests that low temperature heating of GO foams may merit further investigation as a potential means of obtaining rGO.

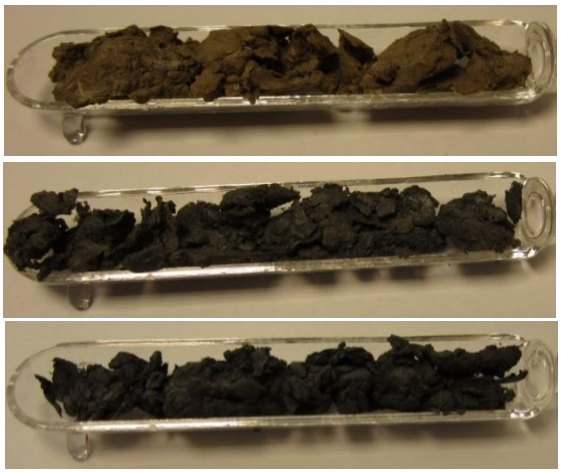

Figure 64: Freeze dried GO foam before heating (top) and after heating to 100 °C in a tube furnace for 24 h (middle) or 5 days (bottom).

Table 12: UV-vis λ_{max} for GO reduced by refluxing in water and by heating at 100 °C in a tube furnace.

	UV-vis peak maximum (nm)		**Sheet Resistance (Ω/□)**	
Time heated at 100 °C (h)	**Refluxed in water**	**Heated in furnace**	**Refluxed in water**	**Heated in furnace**
0	235	236	-	-
24	255	238	$(6.6 \pm 0.3) \times 10^6$	$(4 \pm 3) \times 10^8$
120	266	254	$(3.0 \pm 0.1) \times 10^4$	$(1.58 \pm 0.03) \times 10^6$

Interestingly, during the write-up of this work a paper was published in which the effects of heating aqueous GO solutions and freeze-dried GO foams at temperatures of either 50 °C or 80 °C for up to 9 days were investigated.[431] The study concluded that the electrical conductivity of GO could be enhanced without any associated GO reduction.

This process was suggested to occur through 'phase transformation' of the material; where functional groups on the GO surface separated into oxidised and graphitic regions via temperature driven oxygen diffusion, forming new conduction paths in the material without affecting the C/O ratio. It should be noted that while the authors claim that no reduction occurred, the appearance of the C 1s XPS spectra suggests otherwise (figure 65). This study highlights the dangers of not confining peak widths when fitting spectra, as the same C/O ratios were calculated for all three spectra despite the visible differences. In the current study a wide range of analytical tools were utilised to confirm the genuine reduction of GO upon treatment in water, and hence a different mechanism than 'phase transformation' is required to explain the measured increase in electrical conductivity.

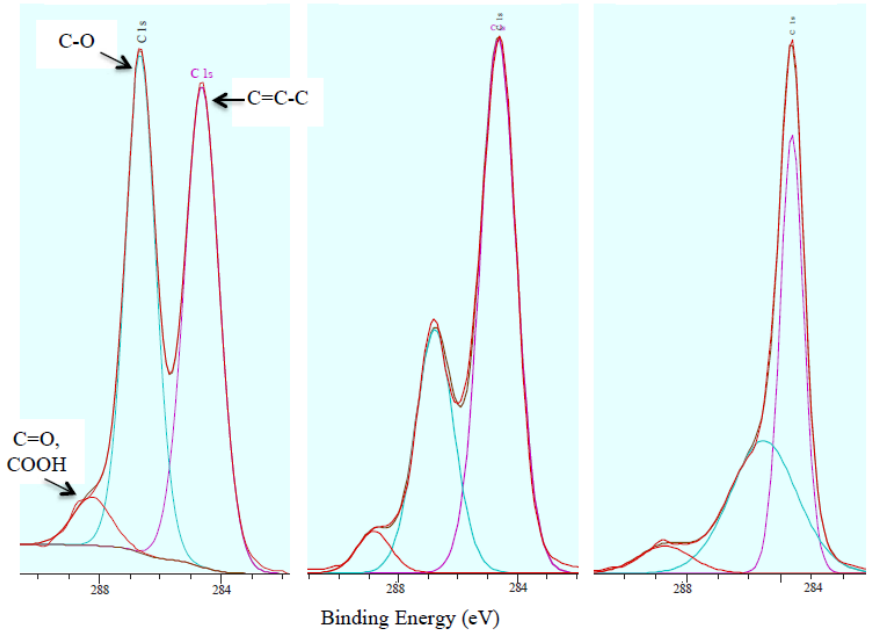

Figure 65: C1s XPS spectra of freeze-dried GO foams before heating (left) and after heating to 50 °C (middle) and 80 °C (right) showing overall line shape and fitting into different carbon bonding components, taken from the supporting information of the article of reference 431.

A number of studies on aqueous-based reduction of GO in the presence of acid can be found in the literature.[417, 421, 432] In an early study, Zhou *et al.* showed that exfoliated graphite oxide could be reduced via a hydrothermal method by heating a solution of GO in water to 120 °C for 6 h.[421] The authors suggest that this reaction occurs via acid catalysed dehydration of GO; where the acid catalysed reaction is enhanced by the higher concentration of protons in supercritical water than in normal, liquid phase

water. Later Liao *et al.* also speculated in their report of aqueous reduction of GO at 95 °C (pH ~3) that the main mechanism for oxygen reduction and conversion of sp^3 to sp^2 carbon was dehydration (figure 66).[417] The authors assert that the presence of H^+ is essential to catalysing this reaction; which they state is the key difference between oxygen removal in water and in air. This would agree with the current findings of GO experiencing further reduction upon refluxing in solution than GO foams heated in air.

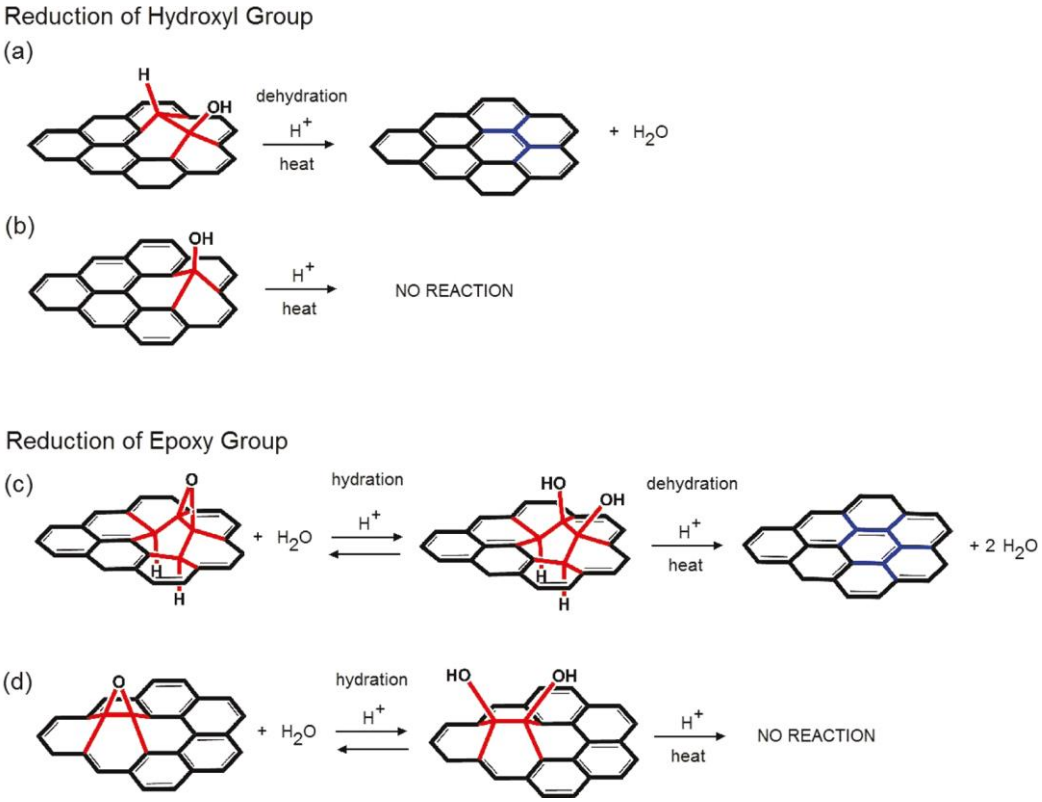

Figure 66: Schematic diagrams for the proposed reduction of hydroxyl (a and b) and epoxy (c and d) groups on GO via dehydration reactions.[417]

A further possibility is that the increased reduction in aqueous conditions compared with heating in air could potentially have been due to the removal of 'oxidative debris' from the surface of GO during refluxing and rinsing of the material. In 2011 the presence of 'oxidative debris' on the surface of graphene oxide was reported,[433] which was found to be akin to the 'oxidation debris' or 'carboxylated carbon' observed on the surface of carbon nanotubes after treatment in strong acids.[434, 435] 'Oxidative debris' is described as small, highly oxidised carbonaceous fragments adhered to the graphitic sheets by a combination of π-π stacking and hydrogen bonding, which could be removed by treatment with base (0.01 – 1 M NaOH). In this study oxidative debris was shown to account for about a third of the mass of "as produced" graphene oxide and to

be responsible for the mass loss at 200 °C seen upon burning GO in air, previously assigned to labile oxygen functionalities directly attached to the GO surface. In addition, the high water solubility of GO was attributed to oxidative debris acting as a surfactant to stabilise the graphitic sheets; as the material after base washing was insoluble in water. The 'base-wash' procedure yielded a product which was similar to reduced GO in that the material had undergone a colour change from brown to black, had a higher carbon to oxygen ratio (~4:1 as opposed to ~2:1 for GO), and was 5 orders of magnitude more electrically conducting than GO. In later work oxidative debris was shown to form regardless of the graphite oxidation method used, and to be removed by treatment with a range of bases including ammonia.[382] The authors highlighted the difference between 'reduction' and 'cleaning' of GO, i.e. whether the treatment is genuinely reducing the underlying graphitic surface or merely deoxygenating the system by removing the oxidative debris.

To test whether refluxing GO in water removed oxidative debris two comparative studies were performed. For the first of these studies GO that had been refluxed in water for 24 h was compared with GO that had been refluxed in water for 24 h then refluxed in 0.1 M potassium hydroxide for 4 h. As predicted, and in agreement with previous findings,[433] the material that had undergone the additional reflux in base had fewer epoxy and hydroxyl groups according to the XPS and SSNMR data (figure 67), and was less dispersible and more electrically conducting than the material that had only undergone 24 h refluxing in water (table 13). These findings, combined with the observation that refluxing in water yielded a colourless filtrate whilst refluxing in 0.1 M KOH yielded an orange/yellow filtrate, suggest that oxidative debris is not removed during the water reflux step, and that instead refluxing in water causes genuine reduction of the GO material.

Table 13: UV-vis λ_{max} and electrical resistance for GO processed using different methods.

GO processing method	UV-vis peak maximum (nm)	UV-vis absorbance at 660 nm	Sheet resistance of film (Ω/□)
Reflux in water for 24 h	255	1.35	$(1.2 \pm 0.3) \times 10^7$
Reflux in water for 24 h then 0.1M KOH for 4 h	262	0.30	$(1.2 \pm 0.8) \times 10^5$

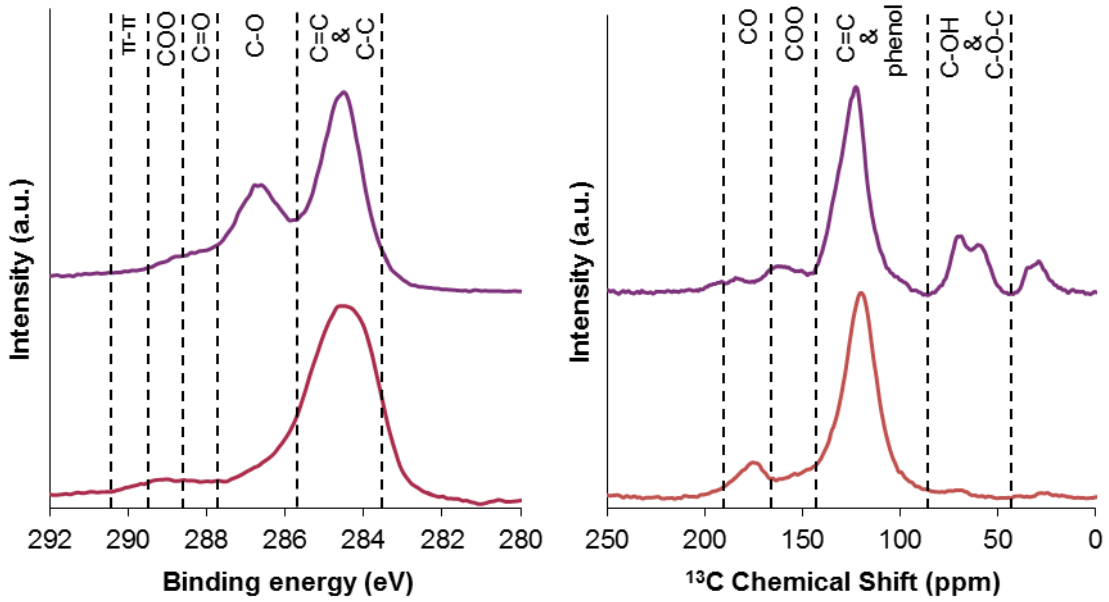

Figure 67: XPS spectra (left) and ^{13}C direct excitation MAS SSNMR spectra (right) of material formed by refluxing GO in water for 24 h (purple) and refluxing GO in water for 24 h then refluxing it in 0.1 M KOH for 4 h (red).

The second comparative study investigated the properties of GO that had been 'base-washed' and GO that had been 'base-washed' then refluxed in water for 5 days. XPS and SSNMR results showed that the low-levels of epoxy and hydroxyl groups that were present in the 'base-washed' GO were removed by the subsequent refluxing of this material in water for 5 days (figure 68). The finding of further reduction in the 'base-washed' material induced by the refluxing step was also supported by the relative λ_{max} values for the two materials, and by the two orders of magnitude lower electrical resistance for the sample after refluxing compared with the material that had only been 'base-washed' (table 14). In agreement with the first comparative study, the filtrate from the base washing method was found to be yellow; suggesting the base-promoted removal of oxidative debris; whereas the filtrate after the water reflux was colourless, suggesting that this step truly reduces the material, rather than removing oxidative debris.

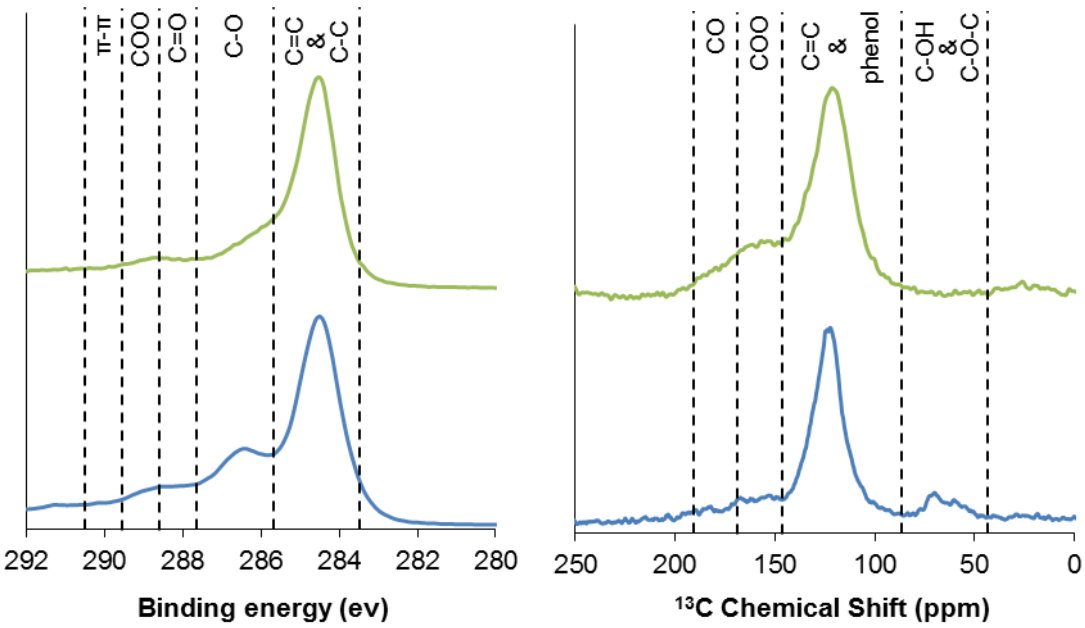

Figure 68: XPS spectra (left) and ^{13}C direct excitation MAS SSNMR (right) spectra of material formed by 'base-washing' GO (blue), and 'base washing' GO then refluxing it in water for 5 days (green).

Table 14: UV-vis λ_{max} and absorbance at 660 nm (multiplied from diluted solution), and electrical resistance measurements for thin films of GO processed using different methods.

GO processing method	UV-vis peak maximum (nm)	UV-vis absorbance at 660 nm	Sheet resistance of film (Ω/□)
'Base-wash' (Rourke method)	261	0.40	$(1.2 \pm 0.3) \times 10^6$
'Base-wash' then reflux in water for 5 days	266	1.16	$(1.2 \pm 0.4) \times 10^4$

Interestingly, the water refluxed, 'base-washed' material was significantly more dispersible than 'base-washed' material alone despite having a lower electrical resistance. The improved dispersibility of the refluxed compared with the non-refluxed 'base-washed' material could be attributed to the fact that the material became de-agglomerated upon refluxing for a prolonged period due to the energy inputted to heat and stir the solution.

3.4 Conclusions and further work

A new method for obtaining rGO from GO was trialled that omitted the final, time consuming purification step of the Hummer's reaction. Results from a range of different analysis tools suggested that omitting this step did not affect the crystallinity or purity of material obtained by subsequent reduction of this 'pre-wash' GO; which yielded the same product as equivalent processing of the 'post-wash' material. While the presence of acid is likely to restrict the reduction technique used, the results of this work are highly promising and show that there is much potential merit in further investigations into obtaining rGO directly from 'pre-wash' GO.

Refluxing GO in water for various lengths of time has been shown to be a simple and effective way of obtaining material with different degrees of oxidation, using a controlled and scalable reaction that does not require any chemical reagents and which is compatible with the production of rGO directly from 'pre-wash' GO. As per many of the mild reduction methods, the mechanism for aqueous based reduction of GO is not fully understood,[145] although an acid catalysed dehydration mechanism has been proposed to explain the removal of epoxy and hydroxyl groups from the GO surface.[417] The work in the current study supports the assertion that refluxing GO causes genuine reduction of the material rather than just removal of 'oxidative debris' from the surface. Importantly, the analysis of a range of partially reduced GO samples showed a direct relationship between the dispersibility and electrical conductivity of the materials, where one property degrades as the other improves. It is important to remember this compromise when selecting a material for a particular application, and it is clear that ascertaining the relative importance of the two factors is a key step in selecting the most appropriate material for a given system.

The next step for this work is to confirm that having a range of different partially reduced GO materials is important for optimising the enhancement brought about in different systems by adding these materials. A series of applications where electrical conductivity, dispersibility and the level of heteroatoms are likely to be key factors should be identified, and a range of materials with different C/O ratios should be tested in these systems. A recent example of such considerations being taken into account is the work by Shao *et al.*,[436] where the mechanical reinforcement of poly(vinyl alcohol) (PVA) composites was found to be highest for GO with a C/O ratio of ~4 rather than either more or less oxidised material, due to the balance of the inherent strength of the sheets and the level of oxygen functionalities that can interact with the PVA. It is likely

that other positive results that may have been missed if only GO or rGO were tested could be found in the future by trialling materials with different reduction levels in a given system.

Chapter 4: Use of arginine to aid the 'top-down' synthesis of graphene

4.1 Introduction

There is an ever-growing body of work dedicated to the 'green' reduction of GO. Many of these methods involve solution phase processing of GO using naturally occurring reducing agents such as starch or reducing sugars,[437, 438] green tea or ginseng,[439, 440] and tripeptides or amino acids.[393, 441-444] The reduction of GO in these systems is poorly understood, and the mechanisms by which reduction occurs have not been clearly defined.[145] In recent years the question of whether reduction in certain media, specifically in the presence of base, is removal of oxygen containing functional groups directly bonded to the graphitic surface or removal of 'oxidative debris' bound to the surface has been posed.[382, 408, 433] Upon inspection, ammonia is used to change the pH in a number of the aqueous based 'green' reduction methods mentioned above, meaning that it could have been the base rather than the other additives which was playing a key role in the removal of oxygen functionalities in these systems.[437, 438, 440, 442]

The pH of the solution has been shown to affect the colliodal stability of aqueous GO and rGO dispersions. Early measurements revealed stable GO dispersions in the pH range ~ 3.5 – 11.5 and stable rGO dispersions in the pH range ~6.1 – 11.5.[370] These ranges are similar to those found in more recent work, which utilised a range of different techniques to investigate the dispersibility of GO and rGO at different pHs.[445] The greater stability of these materials in basic solutions has been attributed to the fact that at basic pH the carboxylic acid groups present on GO (and to a lesser extent rGO) are negatively charged, and so repel one another via electrostatic interactions,[446] leading to stable dispersions up to the point when the increase in ionic concentration of the solution causes destabilisation.[370] The 'salting out' of GO from aqueous solutions containing neutral, acidic and basic salts has been demonstrated elsewhere in the literature,[447] highlighting the importance of electrostatics in the stabilisation of GO solutions and the balance of factors that must be taken into consideration when designing stable dispersions.

As base plays an important role in the interaction of GO with aqueous systems, this chapter investigates the use of aqueous solutions of the basic amino acid, L-arginine,

on the stabilisation and reduction of GO and rGO based materials. L-arginine is a naturally occurring α-amino acid that contains a guanidine group with a pKa of 12.48 which abstracts a proton from water when arginine is dissolved, resulting in a positively charged guanidinium group and a basic solution (figure 69).[448] L-arginine has previously been shown to suppress aggregation in systems such as proteins, peptides and fatty acids.[449] The mechanism of aggregation suppression by arginine is not clearly understood, and there are a number of factors that are thought to explain the observations, including the effects of arginine on the surface tension of water and the interaction between the aggregating species.[450, 451] In terms of interacting with different species, the combination of the different functional groups, in particular the guanidinium group, provides arginine with a lot of flexibility based on its ability to hydrogen bond with negatively and positively charged species and to form cation-π interactions with aromatic residues.[452] Importantly arginine has been shown to exhibit a hydrotropic effect, i.e. the ability to stabilise hydrophobic compounds in aqueous solutions,[449] and as such it presents a promising potential candidate for dispersion (as well as reduction) of graphene-based materials.

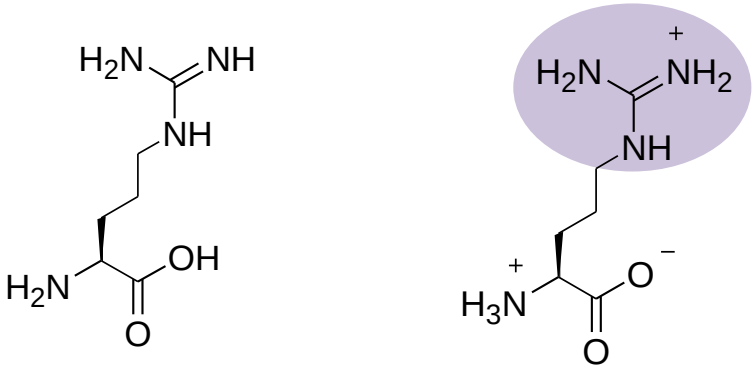

Figure 69: Molecular structure of L-arginine (left) and charged structure of arginine molecule in aqueous solution (right), showing the guanidinium group (purple).

4.2 Chemical reduction of graphene oxide in arginine

As shown in chapter 3, GO can be reduced to varying extents by refluxing it in water for different lengths of time. This reduction occurs via the removal of hydroxyl and epoxy groups from the GO surface, resulting in materials with better electrical conductivity but poorer aqueous dispersibility than GO. It was also shown, based on the characterisation techniques available, that the time consuming final rinse step of the Hummer's method for preparation of GO could be omitted without negatively impacting the final products, which may represent an important break-through for industrial-scale production of rGO. In this section the effect of adding arginine to the water prior to

refluxing was investigated. It was anticipated that refluxing in a basic solution of arginine in water could enhance this process in three possible ways:

1. The ‘oxidative debris’ that remained on the surface during the water reflux could be removed by the basic arginine solution; resulting in a more electrically conducting product
2. The addition of arginine could aid dispersion of the GO starting material due to the ionisation of carboxylate groups in basic conditions, leaving a large surface area of the material available for reduction and hence resulting in a more deoxygenated product
3. Arginine may act as an aggregation suppressor in a similar manner as seen for proteins; potentially supressing aggregation during reduction and resulting in a more dispersible product

4.2.1 Chemical changes during processing

Refluxing ‘pre-wash’ GO in arginine led to the expected colour change of the material from yellow/brown to black. This colour change occurred over a much shorter timescale than observed when refluxing in water, suggesting that the reaction is sped up by the addition of arginine. To investigate the effect of reaction time on the level of reduction and the physical characteristics of the resulting materials, ‘pre-wash’ GO was refluxed in solutions of 0.5 M arginine in water for various lengths of time, and the resulting solids were compared with other materials reduced via “green” reduction methods and samples refluxed in water only.

Processed materials were obtained by refluxing the ‘pre-wash’ solid in arginine solution for 1, 4, 8 or 24 h. With the exception of the sample refluxed for 1 h, the samples all filtered readily to afford damp solids that dried to free flowing powders. The sample refluxed for 1 h was difficult to filter and hence was purified by repeated centrifugation and decantation cycles. Whilst the solution of arginine in water was colourless before refluxing, the solution was yellow/orange after refluxing, suggesting that ‘oxidative debris’ was removed. TEM analysis confirmed that the materials retained their sheet like morphology over the time scale investigated, as expected given the reaction conditions (figure 70 and appendix B). Inspection of the TEM results for the sample refluxed in arginine for 24 h showed that thin, crumpled sheets were present, which had evidence of disrupted graphitic stacking based on the HRTEM image. The electron diffraction pattern showed two rings of spots indexed to the graphite (100) and (110)

planes for the inner and outer rings respectively, confirming the presence of in-plane crystalline ordering.[302]

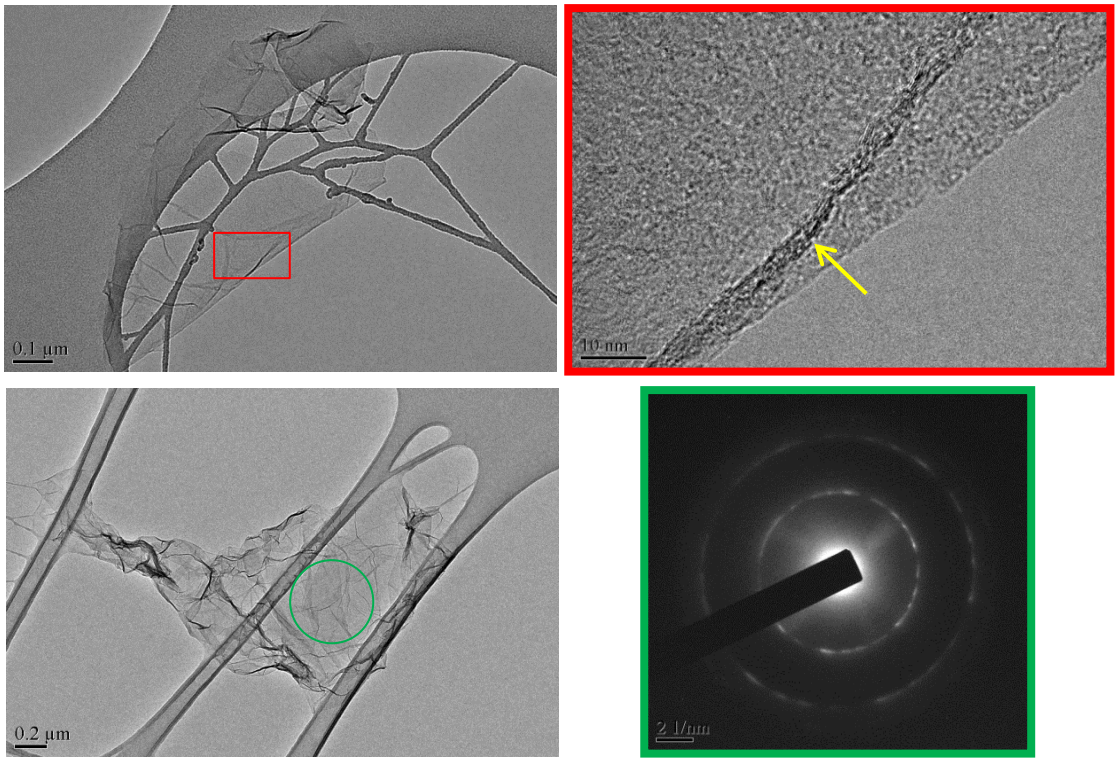

Figure 70: BF TEM images of graphitic sheets produced by refluxing 'pre-wash' GO in 0.5 M arginine in water for 24 h (left) with associated HRTEM image (top right) and SAED pattern (bottom right) taken from the areas marked in red and green respectively. The yellow arrow points to evidence of disrupted graphitic stacking, and the inner and out rings in the SAED pattern are indexed to the (100) and (110) graphitic planes respectively.

SSNMR (figure 71) and XPS (figure 72) results showed that refluxing 'pre-wash' GO in arginine for 1 h was sufficient to remove hydroxide and epoxide functionalities. It is likely that some of this reduction can be attributed to the loss of oxidative debris, the presence of which has been previously shown to contribute highly to the proportion of C-O functionalities on GO.[433] Only a minimal difference between the materials obtained after 4, 8, and 24 h reflux times can be discerned from the data, but the material produced via refluxing in 0.5 M arginine for 1 h appeared to contain a slightly higher proportion of oxygen functionalities than the materials refluxed for longer periods. This can be seen via an increased proportion of carboxylic acid and phenol functionalities based on SSNMR, and a higher proportion of carbonyl (287.8 eV) and carboxylate functionalities (289.0 eV) based on XPS. The data from the XPS survey scan suggested that the amount of residual arginine decreased with increasing reflux time (table 15), where the C/N ratio varied from 4 ± 1 to 16 ± 7 for reflux times of 1 h and

24 h respectively. As the C/N ratio is particularly high for the rGO produced via 1 h of refluxing in 0.5 M arginine, the higher intensity in the regions associated with carbonyl and carboxylate functionalities could be, in part, attributed to contributions to the signal from the residual amino acid; since arginine has been shown to have a series of XPS peaks in the range of ~286 – 289 eV.[381, 453]

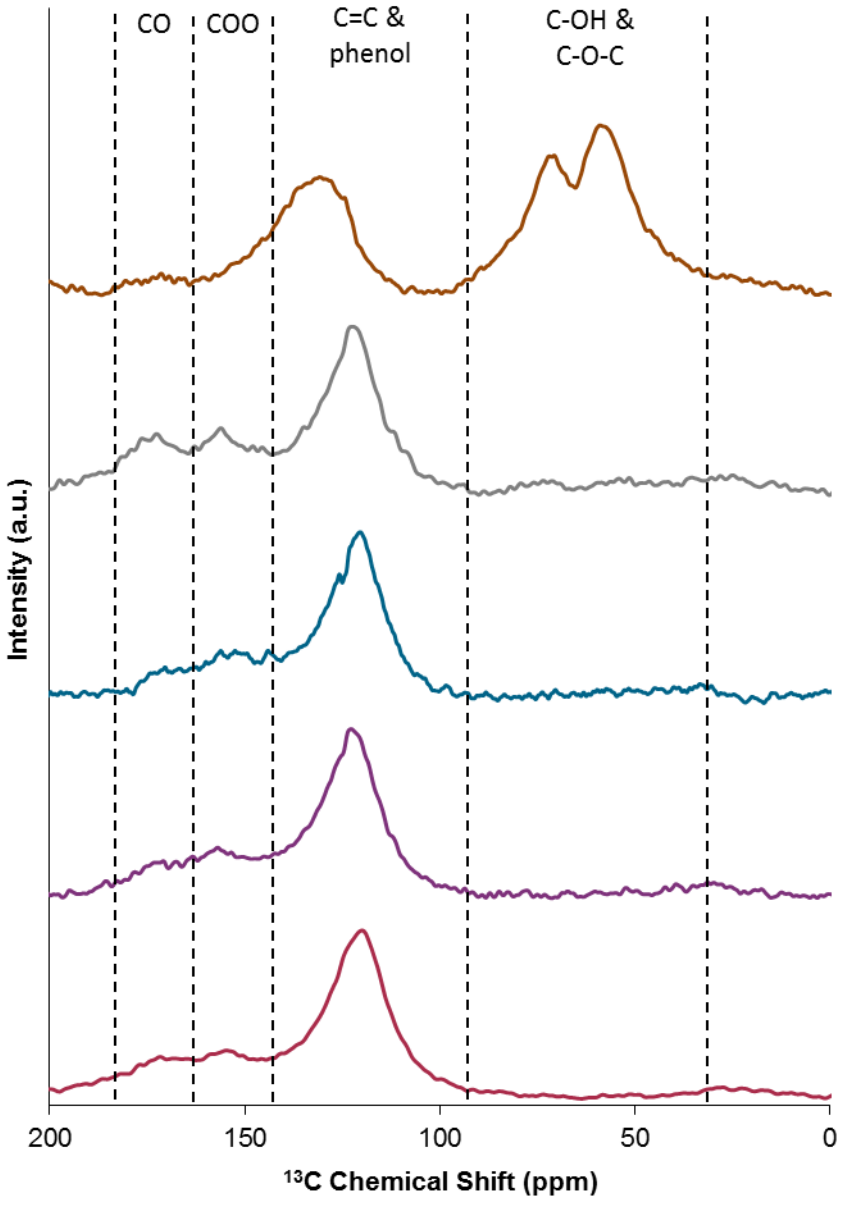

Figure 71: Stack plot of ^{13}C direct excitation MAS SSNMR spectra of 'pre-wash' GO refluxed in arginine for 24 h (red), 8 h (purple), 4 h (blue) and 1 h (grey) and 'post-wash' GO as a reference (brown). The spectra were normalised to the C=C and phenol peak. Fits for all materials are provided in appendix B.

The origin of the trend of increasing C/N ratio with increasing reflux time could be the difference in the physical behaviour of the materials after refluxing; as samples that had been refluxed for 4 h or more filtered and rinsed more easily, but is also likely to be affected by the impact of continued heating on the interactions between arginine and the graphitic surface. Arginine has previously been shown to interact strongly with GO due to hydrogen bonding and electrostatic interactions between the functional groups of the two species.[454-456] As GO is reduced the number of oxygen functionalities decreases, and hence the interactions with arginine diminish. The reduced interactions between arginine and rGO compared with the arginine and GO suggest that arginine would be more easily removed from the former, which is consistent with the trend in the current data set. It should be noted that arginine residues have been shown to strongly interact with non-functionalised graphitic surfaces (see section 4.3), so the presence of residual amino acid in the rGO sample produced by 24 h refluxing is not unexpected. The method for arginine removal has not been optimised and it is likely that the C/N ratio could have been increased by utilising different processing methods.

Table 15: C/N ratios of rGO produced by refluxing 'pre-wash' GO in 0.5 M arginine for different lengths of time. The errors are reported as 95 % confidence intervals based on three repeats.

Reflux time (h)	Average C/N Ratio
0	100 ± 20
1	4 ± 1
4	12 ± 1
24	16 ± 7

The presence of residual arginine complicated the fitting of the SSNMR and XPS spectra due to the contributions to the lineshapes from the different carbon environments in the amino acid. Indeed, a poor fit was achieved for the XPS C 1s lineshape of the 1 h refluxed sample (see appendix B), which highlighted that this approach is not valid unless the contributions from the arginine can be corrected for. Although the C1s spectra have not been fit into different bonding components, it is still possible to compare this work with other systems via a qualitative examination of the C 1s lineshape. The reduction of GO via heating it to 95 °C for 1 h in an aqueous solution of glucose/ammonia is a particularly relevant study as it involves the use of a naturally occurring species in a basic media.[438] Inspection of the C 1s lineshape after reflux in glucose/ammonia (figure 73) revealed that there is a defined peak relating to

C-O functionalities (at binding energy ~286-287 eV), which is not present in the lineshape for the material obtained by refluxing 'pre-wash' GO in arginine for 1 h. This suggests that arginine is a more effective additive than glucose/ammonia to induce the reduction of GO in an aqueous-based system.

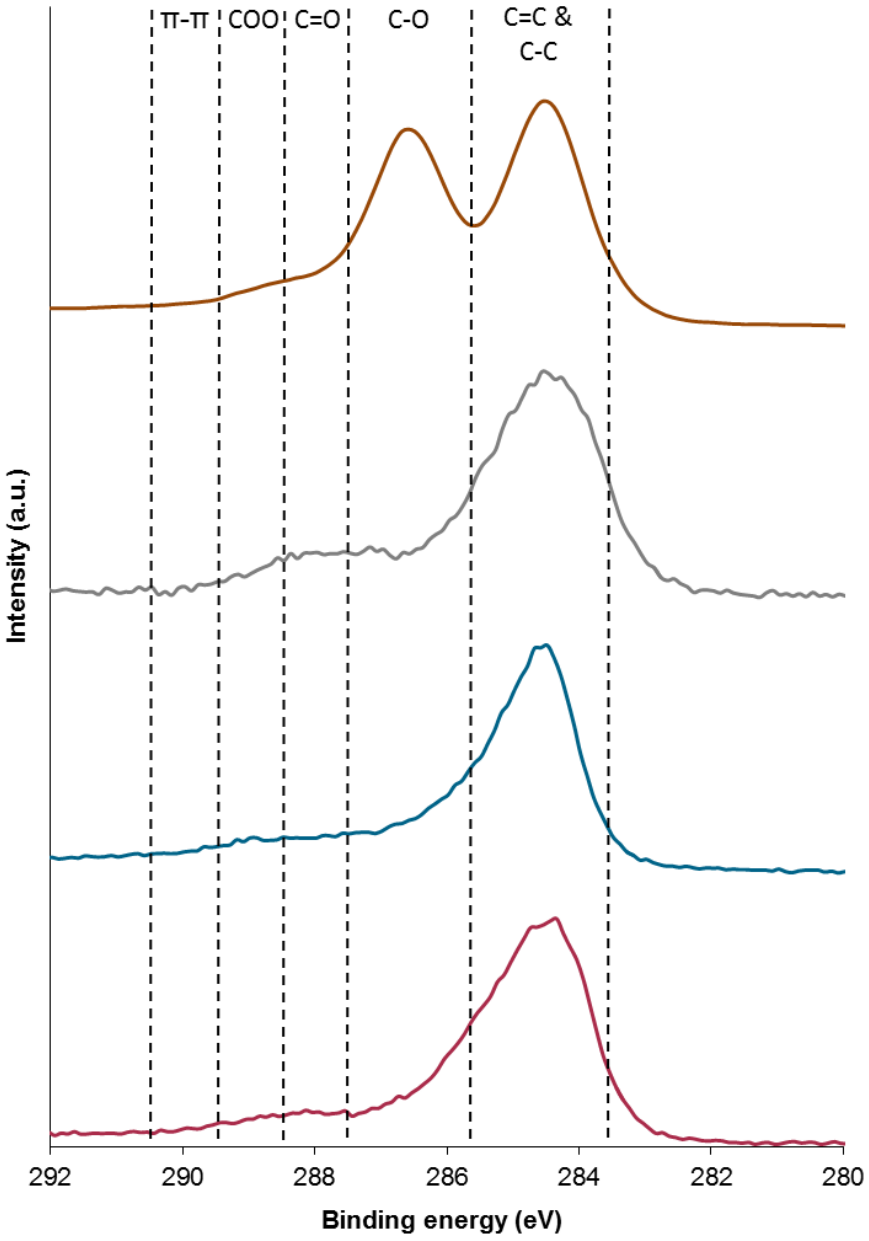

Figure 72: Stack plot of the C1s XPS spectra of 'pre-wash' GO refluxed in arginine for 24 h (red), 4 h (blue) and 1 h (grey) and 'post-wash' GO as a reference (brown). The spectra were normalised to the C=C peak. Fits for all materials are provided in appendix B.

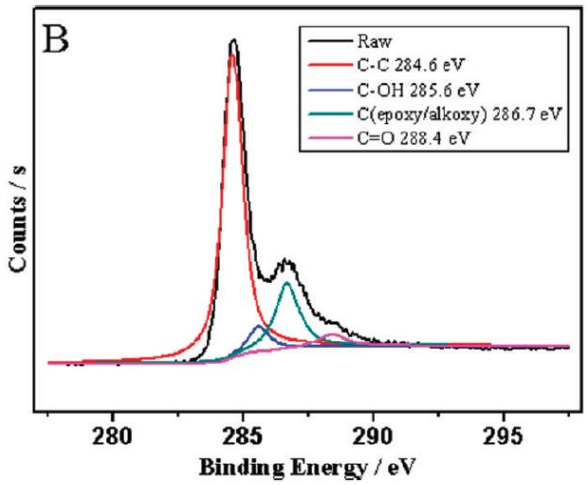

Figure 73: C1s XPS spectra of material produced via stirring an aqueous solution of GO with glucose and ammonia at 95 °C for 60 minutes. Adapted from reference 438.

UV-vis of aqueous dispersions of the refluxed samples confirmed that the chemical reduction of the starting material had been achieved, based on the shift of the λ_{max} and the disappearance of the peak shoulder at ~300 nm (figure 74).[370] The peak maxima were the same within error (266 - 267 nm) for all reflux times, and were equal to the peak maximum for refluxing 'pre-wash' GO in water for 120 h. This suggests that, within the sensitivity of the technique, the same level of reduction can be achieved by refluxing 'pre-wash' GO in an aqueous solution of arginine for 1 h as achieved by refluxing it in water alone for 120 h. The peak shift upon reduction was similar to the shifts reported in the majority of other 'green' reductions of GO (table 16), where the differences between the reported peak maxima are relatively small compared with the overall shift of the GO peak (~ 30 nm). The peak maximum reported in the current study is greater than for the material produced via heating GO in glucose/ammonia which suggests, in agreement with the XPS data, that arginine induces a higher degree of reduction than glucose/ammonia.

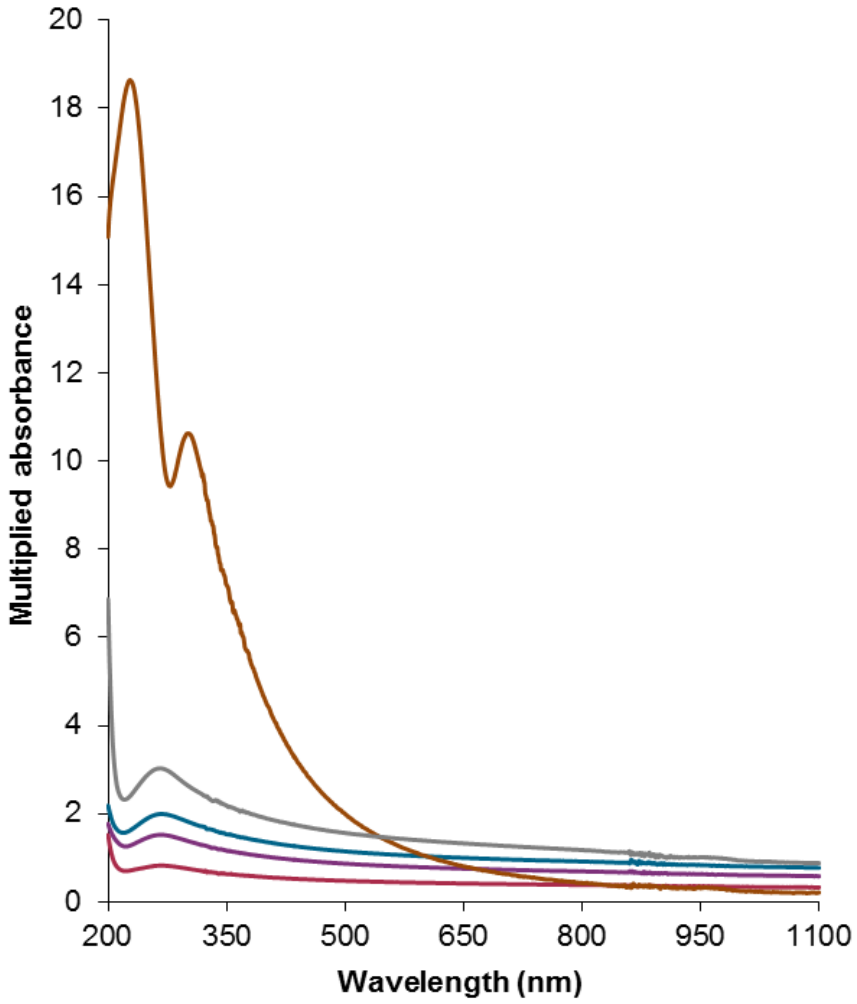

Figure 74: UV-vis spectra of aqueous dispersions of the materials produced by refluxing 'pre-wash' GO in arginine for 24 h (red), 8 h (purple), 4 h (blue) and 1 h (grey) and 'post-wash' GO for reference, multiplied to account for dilution factor.

One study of particular interest is the reduction of GO in an aqueous solution of L-ascorbic acid, NaOH and L-arginine.[455] In this work, published during the course of the current study, L-ascorbic acid was reported as the active reducing agent and L-arginine was reported as a stabiliser. The shift in the UV-vis λ_{max} reported for L-ascorbic acid mediated reduction of GO over a 12 h timescale was the same as that achieved in 1 h in the current study; where the current reduction reaction was also performed on 'pre-wash' rather the 'post-wash' GO, meaning the total time of the current study was significantly shorter than the former reaction. Interestingly the arginine-functionalised rGO that was formed from the L-ascorbic acid mediated reduction of GO was reported to be a promising material for modified glassy carbon electrodes.[455]

Table 16: UV-vis shifts reported in the literature for a number of different aqueous based 'green' reductions of GO, arranged in ascending order of the λ_{max} reported for the rGO.

		UV-vis peak maximum (nm)		
Method of reduction	**Reaction time (h)**	**GO**	**Reduced GO**	**Ref**
Stirred in water and glucose at RT, ammonia added, then refluxed	1.5	230	261	438
Heated in water, L-ascorbic acid, NaOH and L-arginine	12	231	266	455
Current study	1 - 24	232	266 - 267	-
Stirred in water and glycine at RT then refluxed	36	230	267	444
Refluxed in starch and ammonia	3	227	269	437
Refluxed in water, L-lysine, sodium cholate and ammonia	48	230	269	442
Stirred in water and L-cysteine at RT	72	230	270	393
Refluxed in green tea	6	228	271	439
Refluxed in water, L-lysine, carboxylmethyl starch and NaOH	9	231	274	443

XRPD spectra of the refluxed materials (figure 75) showed that the peak at $2\theta \approx 12°$ corresponding to the GO (001) plane was absent for all chemically reduced materials, which suggests that the out-of-plane ordering has been disrupted during the reduction reaction. This has been reported elsewhere for reduction of GO and has been attributed to the removal of oxygen containing groups and intercalated water from between the graphitic layers.[420] This change occurred more rapidly than when 'pre-wash' GO was refluxed in water, where broad peak at $2\theta \approx 12°$ was still visible after 12 h of reflux (see section 3.3). The peak corresponding to the graphitic (100) plane, at $2\theta \approx 43°$, is discernible for all XRD spectra of the reduced material, indicating that a certain degree of in-plane crystallinity is present in these samples. The peaks marked by asterisks, at $2\theta \approx 21.6°$ and 24°, are present in the blank run of petroleum jelly on the glass slide and not inherent to the carbon-based products.

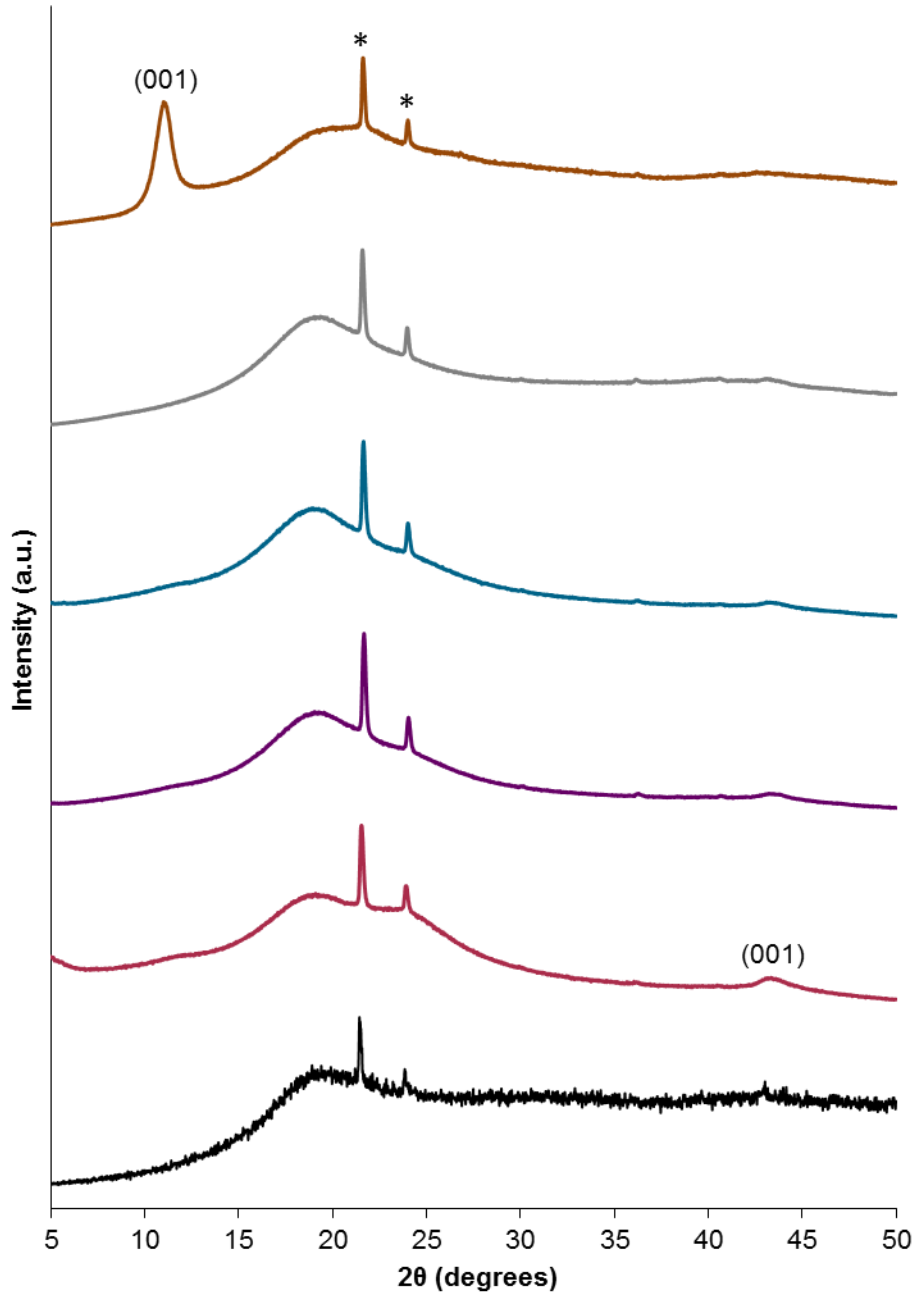

Figure 75: Stack plot of XRD spectra of 'pre-wash' GO refluxed in arginine for 24 h (red), 8 h (purple), 4 h (blue), 2 h (green) and 1 h (grey) and 'post-wash' GO as a reference, with the sample blank shown (black). The peaks marked by asterisks are evident in the sample blank and hence are not inherent to the carbon product. Spectra were recorded using Cu $K\alpha_{1,2}$ radiation (λ = 1.54 Å).

The Raman spectra of 'pre-wash' GO refluxed in arginine for various times were very similar across all materials and showed the typical large, broad D band and broad G peak of GO or rGO,[364] and disorder induced second order bands consistent with functionalised graphitic materials (figure 76).[419] The I_D/I_G ratios were the same within

errors across all materials, indicating a consistent level of defects and crystalline order. The FWHM were the same within errors for the materials refluxed for 4, 8 or 24 h but the material refluxed in water for 1 h had a broader FWHM than the other three, indicating that this material has the lowest relative proportion of sp^2 carbons. The FWHM for all samples was narrower than for material refluxed in water for 24 h (165 cm^{-1}), and the FWHM of samples refluxed for ≥4 h was around the same as the sample refluxed in water for 120 h (136 cm^{-1}), suggesting that refluxing in the presence of arginine speeds up the restoration of sp^2 carbon compared with refluxing in water alone.

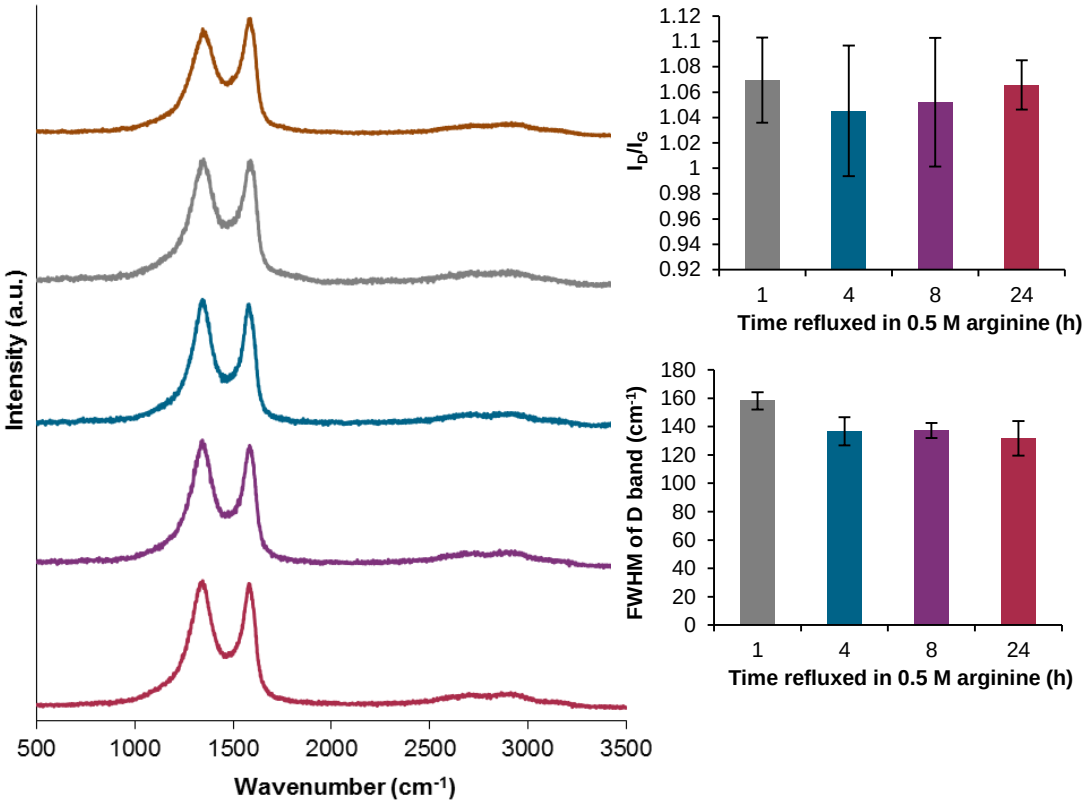

Figure 76: Stack plot of Raman spectra of materials produced via refluxing 'pre-wash' GO in arginine for 24 h (red), 8 h (purple), 4 h (blue) and 1 h (grey) and 'post-wash' GO as a reference (left), and graphs of I_D/I_G ratios and the D band FWHM for the samples refluxed for different lengths of time (right).

In agreement with the Raman data, the similarity of the burn profiles of the materials in air suggested that the rGO produced via 4, 8 and 24 h reflux time had similar defect levels (figure 77). The material refluxed for 1 h had a burn profile which was intermediate between 'post-wash' GO and the materials that had been refluxed for longer lengths of time (based on the mass loss at ~250 °C and the onset of burn),

suggesting that this sample was only partially reduced. The residuals at 900 °C for the samples refluxed for 4, 8 and 24 h were less than 1 wt. %, indicating effective removal of the inorganic contaminants during the reaction. The residual at 900 °C was higher for the sample reduced for 1 h (1.8 wt. %) which is likely to be a consequence of the more difficult purification of this sample compared with the others.

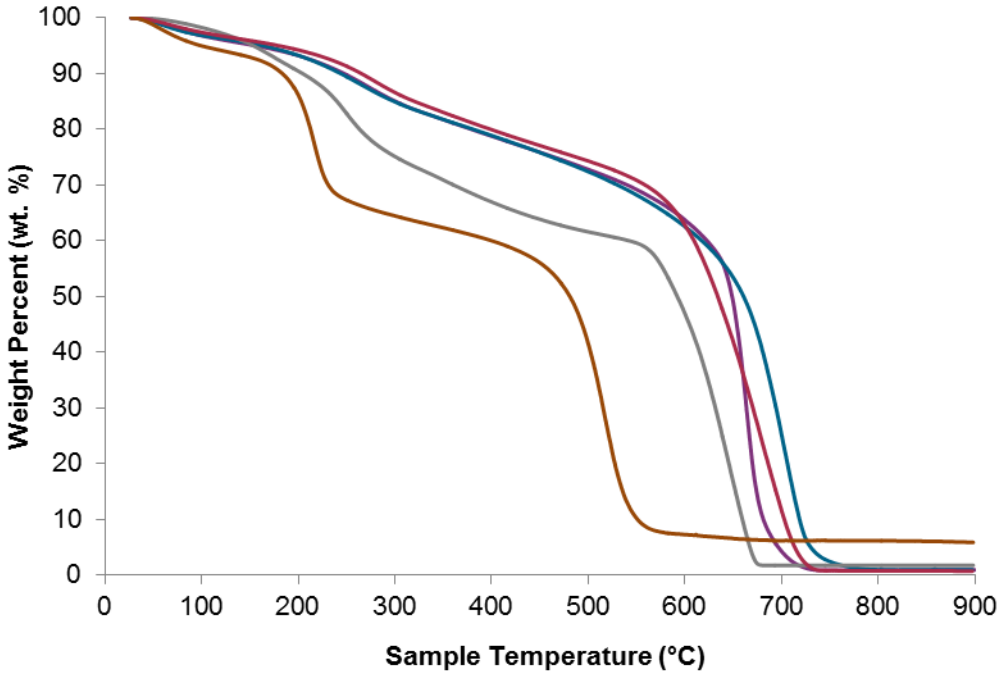

Figure 77: TGA profile of materials produced via refluxing 'pre-wash' GO in arginine for 24 h (red), 8 h (purple), 4 h (blue) and 1 h (grey) and 'post-wash' GO as a reference (brown), corrected to 100 % mass at the end of the dwell at 30 °C (30 min), before the ramp from 30 – 900 °C at 10 °C/min (in air).

4.2.2 Properties after processing

In order to evaluate the aqueous dispersibility of the as-synthesised rGO, the refluxed material was probe-sonicated in water to form dispersions of known concentration (1 mg/mL). The dispersions were noticeably different in appearance; with increased reflux times leading to visibly less dispersible materials. This trend can be observed for the solutions diluted 5-fold in pure water (figure 78). The range in dispersibility observed for the arginine refluxed samples over the timescale of 1 to 24 h was approximately the same as the range in dispersibility observed for GO refluxed in water for 24 to 120 h in the previous chapter, which supports the conclusion that the addition of arginine to the reflux solution sped up the reduction reaction.

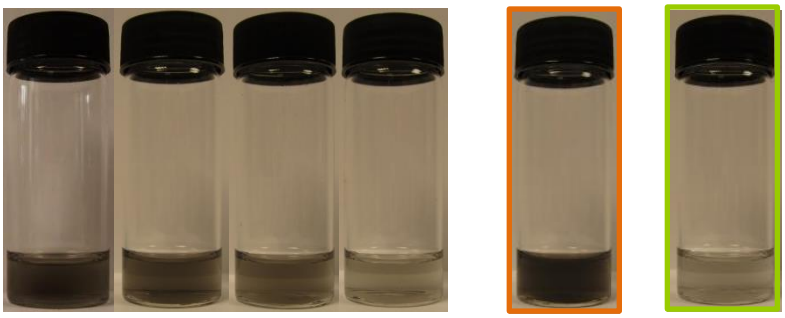

Figure 78: Photos of the dispersions created by sonicating 10 mg of solid material produced by refluxing GO in 0.5 M arginine in water for 1, 4, 8, and 24 h (left to right) in 10 ml of water, taken 24 h after sonication and diluted 5-fold with additional water, and photos of equivalent dispersions of GO refluxed in water for 24 h (orange outline) and 120 h (green outline).

The UV-vis data confirmed the trend that the dispersibility of the materials decreased with increasing reflux time. Assuming the same molar extinction coefficient at 660 nm for the different graphitic materials, 'pre-wash' GO refluxed in the presence of arginine for 4, 8, and 24 h were approximately 25, 45 and 70 % less dispersible respectively than the material refluxed for 1 h. The dispersions analysed 8 days after sonication (1 week after initial analysis) showed the same trend in concentration as seen after 24 h; where materials that had been refluxed for longer time periods resulted in less concentrated solutions (figure 79). The dispersions of materials created via refluxing for 1, 4 and 8 h experienced a ~26 % drop in absorbance after 1 week, whereas the sample that had been refluxed for 24 h experienced a ~33 % drop; suggesting that the latter is the least stable solution. This result is easily explained if the sample refluxed in arginine for 24 h is assumed to have a higher reduction level than the other samples. A higher reduction level, and hence few oxygen functionalities, would result in the 24 h refluxed sample being more hydrophobic that the other samples, which would explain the observed trend is aqueous stability. The decrease in oxygen functionalities would also cause weaker interactions with residual arginine, and hence a lesser stabilising effect for this additive. It should also be noted that the amount of residual arginine was lowest for the sample refluxed for 24 h based on the XPS results, so any positive effect of arginine's presence was expected to be less for this sample. The stability of the dispersion of material refluxed in arginine for 24 h is greater than the stability of the dispersion of material refluxed in water for 120 h; which experienced a 50 % drop in absorbance after one week (see section 3.3.2).

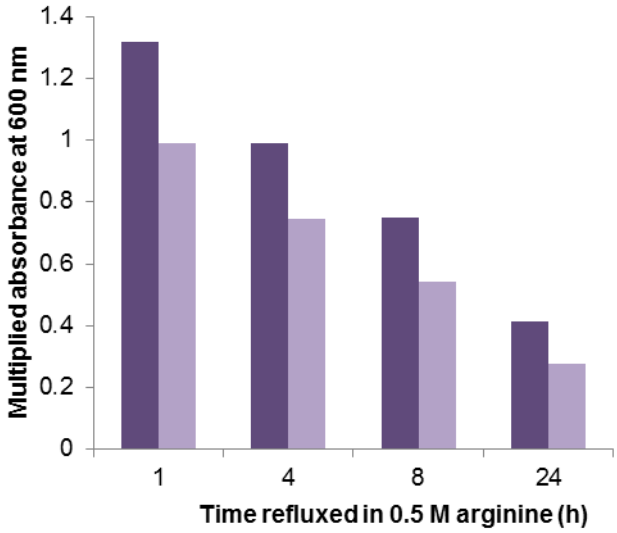

Figure 79: A plot of absorbance at 660 nm for aqueous dispersions of materials refluxed in arginine for various lengths of time 24 h (dark purple) and 8 days (light purple) after sonication and multiplied to take into account the dilution factor.

The electrical conductivity measurements showed that there was two orders of magnitude difference in resistance between the materials produced by refluxing 'pre-wash' GO in arginine for 1 h and for 24 h, and a general trend of decreasing resistance with increasing reduction time (table 17). This trend may have been an indication that reflux time changed the level of reduction; in agreement with the lower proportion of sp^2 carbon for the 1 h refluxed sample based on Raman and the decreased aqueous stability of the 24 h refluxed sample, but also was likely to be affected by the residual arginine. The trend in electrical conductivity followed the trend in the amount of residual arginine based on the XPS results, so to test the effect of residual amino acids on the electrical conductivity, thin films of rGO were formed by filtering dispersions of the rGO in water and in 0.5 M arginine, and the results of the two films were compared. The film filtered from the arginine solution had a two orders of magnitude higher electrical resistance than the film filtered from water (values of $(2 \pm 1) \times 10^6$ and $(3 \pm 1) \times 10^4$ Ω/□ respectively), demonstrating that residual arginine can have a dramatic effect on the electrical conductivity of the solid, and hence that the residual amino acid could have been masking trends in the electrical conductivity with reflux time. Despite the presence of residual arginine, the material refluxed in arginine for 24 h had a two orders of magnitude lower sheet resistance than the material refluxed in water for 24 h. The sheet resistance for the sample refluxed in arginine for 24 h was of the same order of magnitude as the sample refluxed in water for 120 h, suggesting that the addition of arginine to the reflux solution was beneficial in both speeding up the rate of reaction and in achieving high reduction levels.

Table 17: Electrical conductivity measurements for thin films and solids pellets of materials produced after refluxing of 'pre-wash' GO in water) or 0.5 M arginine in water for various lengths of time.

		Pellet		Film
Time refluxed (h)	**Reflux Media**	**Resistance (Ω)**	**Resistivity (Ω m)**	**Sheet Resistance (Ω/□)**
120	Water	4.4×10^{1}	3.4×10^{-1}	$(3 \pm 1) \times 10^{4}$
24	Water	1.2×10^{4}	9.2×10^{1}	$(6.6 \pm 0.3) \times 10^{6}$
24	0.5 M Arginine	1.6×10^{2}	1.6×10^{0}	$(8 \pm 1) \times 10^{4}$
8	0.5 M Arginine	3.3×10^{2}	2.1×10^{0}	$(1.5 \pm 0.4) \times 10^{5}$
4	0.5 M Arginine	4.1×10^{2}	2.1×10^{0}	$(1.05 \pm 0.08) \times 10^{5}$
1	0.5 M Arginine	5.9×10^{4}	4.8×10^{2}	$(6.9 \pm 0.3) \times 10^{6}$

4.2.3 Role of arginine in reflux reaction

Due to the importance of pH in the aqueous interactions of GO and rGO it could be conceived that the enhancements seen upon adding arginine to the reflux mixture were purely a pH effect. To test whether or not this was the case, 'pre-wash' GO was refluxed in 0.1 M KOH (pH 13) for 4 h and compared with the results of refluxing for 4 h in an aqueous solution of arginine (pH 12.3). In addition, refluxing in a less concentrated solution of arginine in water was investigated (0.1 M compared to 0.5 M used previously) to determine if the concentration of arginine was an important factor in the reduction, and to test if the same outcome could be achieved with less arginine.

The SSNMR and XPS spectra (figure 80) showed the clear absence of C-O and C-OH functionalities for the materials produced via refluxing 'pre-wash' GO in 0.1 M KOH, 0.1 M arginine and 0.5 M arginine. The C/N ratios for the materials produced by refluxing in 0.1 M arginine and 0.5 M arginine were calculated as 8.5 ± 0.3 and 12 ± 2 respectively based on the XPS survey scan, indicating the incomplete removal of arginine. The higher amount of residual arginine from the solution with the lower arginine concentration could be explained by less efficient reduction at lower arginine

concentrations (and hence more oxygen functionalities to react with arginine) but could also be explained by the physical behaviour of the two materials, as the sample refluxed in 0.1 M arginine was more difficult to filter and wash than the sample refluxed in 0.5 M arginine, and required purification via repeated centrifugation and decantation steps. This represents a significant disadvantage for the material refluxed in 0.1 M arginine as it necessitated a more time and energy consuming purification process than for when 0.5 M arginine was used.

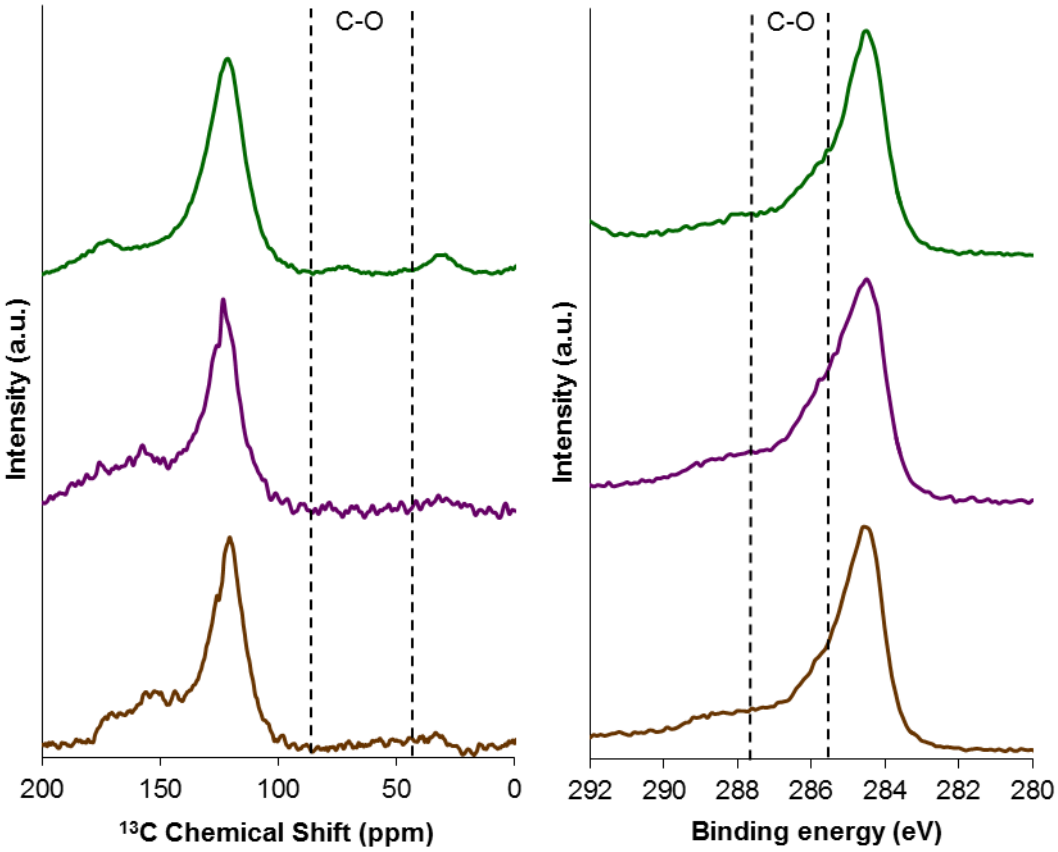

Figure 80: Direct excitation ^{13}C MAS SSNMR spectra (left) and XPS spectra (right) of 'pre-wash' GO refluxed in 0.1 M KOH (green), 0.1 M arginine in water (purple) and 0.5 M arginine in water (brown) for 4 h (left).

The Raman spectra for the 4 h refluxed materials were similar and displayed the expected broad and coalescing D, G and second order bands expected for GO based systems (figure 81). The I_D/I_G ratios and FWHMs of the D bands were the same within error for the material refluxed in either 0.1 or 0.5 M arginine, suggesting that the level of defects and crystallinity were the same in both samples. The material refluxed in 0.1 M KOH had a lower I_D/I_G ratio and a broader D band than for the arginine refluxed

samples, suggesting that this sample had the lowest proportion of sp^2 carbon of the three, and hence that arginine was a better additive than KOH for achieving reduction of 'pre-wash' GO.

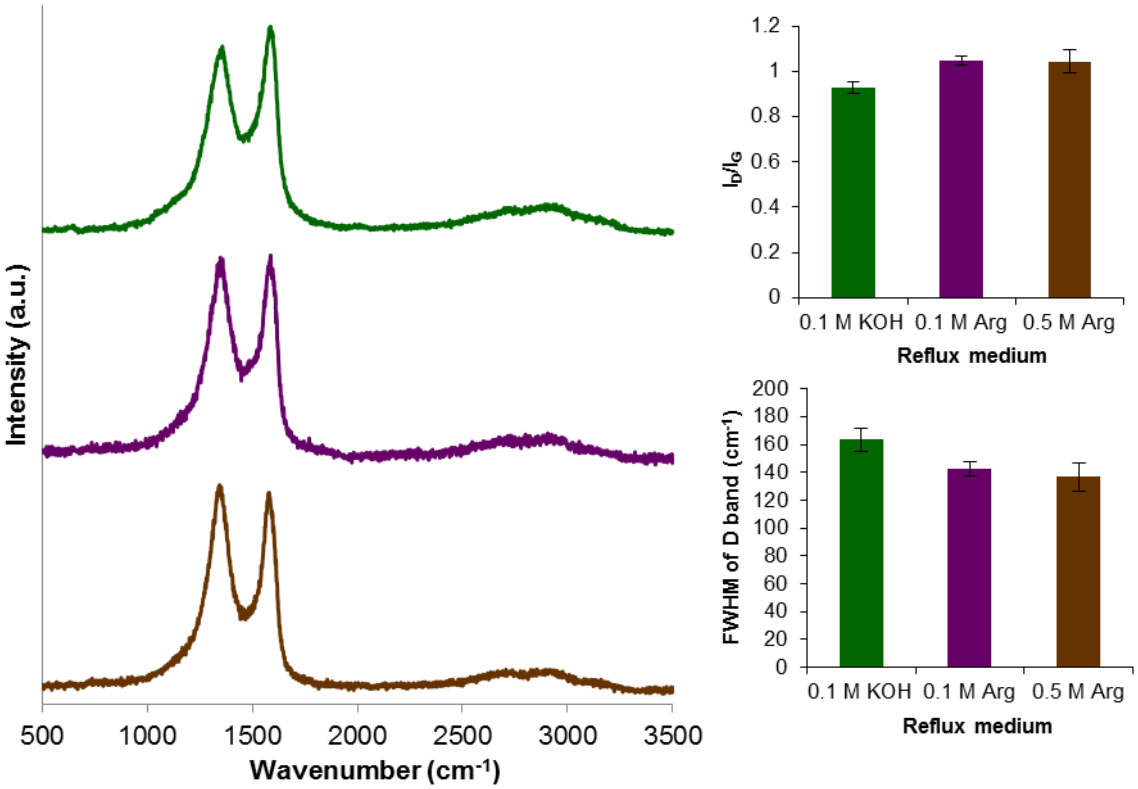

Figure 81: Stack plot of Raman spectra of 'pre-wash' GO refluxed in 0.1 M KOH (green), 0.1 M arginine in water (purple) and 0.5 M arginine in water (brown) for 4 h (left) and graphs of I_D/I_G ratios and D band FWHM for the various spectra (right).

The assertion that arginine was more effective at inducing reduction than KOH was also supported by the relative magnitude of the peak shift measured by UV-vis. The λ_{max} for material refluxed in 0.1 M KOH was 259 nm, while the value for material refluxed in 0.1 or 0.5 M arginine was 268 ± 1 nm. The peak maxima were the same within error for the two arginine samples, suggesting that the arginine concentration did not impact the level of reduction significantly over the 4 h timescale.

Electrical conductivity data measured on filtered films of the materials (table 18) showed that the material produced by refluxing in 0.1 M KOH had a higher electrical resistance than the material produced by refluxing in the presence of arginine. This result was consistent with the frequency shifts of the λ_{max} in the UV-vis spectra and acted as further evidence that the presence of arginine in the reflux media induced

reduction to a greater extent than KOH. The measured resistances illustrated that there was minimal difference between the conductivity of the materials produced by refluxing 'pre-wash' GO in 0.1 M arginine and 0.5 M arginine, although the electrical conductivity of the material refluxed in 0.5 M arginine was slightly higher. This may have been due to the higher amount of residual amino acid present for the former, based on the XPS data and given the previous observations of residual arginine increasing the sheet resistance.

Table 18: Electrical conductivity measurements for thin films of materials produced after 4 h refluxing of 'pre-wash' GO in basic media.

Reflux solution	Sheet Resistance (Ω/□)
0.1 M KOH	$(1.5 \pm 0.2) \times 10^6$
0.1 M arginine	$(1.75 \pm 0.08) \times 10^5$
0.5 M arginine	$(1.05 \pm 0.08) \times 10^5$

While the mechanism for reduction via arginine is not understood the data suggests that the perceived reduction is not purely a pH effect, since KOH of a similar pH reduced the material to a lesser extent. One possible explanation for the greater degree of reduction seen in the presence of arginine is that arginine stabilised the graphitic sheets during reduction to a greater extent that KOH did, and hence allowed a greater degree of reduction and/or removal of oxidative debris

4.3 Dispersion of graphitic materials in arginine solutions

It was anticipated that arginine should have potential as a dispersing agent for graphitic material given its ability to stabilise other hydrophobic species in solution.[449] In the case of GO, arginine's potential arises not only due to the interactions between arginine and the surface but also due to the fact that arginine is a basic amino acid, and GO has been shown to be more stable in basic conditions.[370, 445] There are a number of theoretical articles investigating the interaction of peptides with graphitic surface which report strong interactions between arginine and graphitic carbon. In a study investigating the conformational changes of an alpha helical peptide at graphene surfaces, peptide unfolding due to strong interactions between graphene and the Arg-Ile-Lys portion of the peptide was reported.[457] The strong interaction between arginine and graphene was attributed to the alkylene chain segments of the arginine side group

(-$(CH_2)_n$-), which were thought to adsorb onto the graphitic surface due to Van der Waals and hydrophobic interactions. The interactions of the side chains were also postulated to be important when dispersing SWNTs using poly-L-arginine, although in this case the interactions of the guanidinium group at the end of the chain with the surface were also stated to be important, as this group is thought to be able to interact with CNTs via hydrophobic, van der Waals and π-π interactions.[458]

In an investigation into the interactions of GXG tripetides with graphene in an aqueous environment (where G = glycine and X = a different amino acid), arginine, glutamine and asparagine were found to exhibit the strongest interactions with graphene of the 20 amino acids tested, where arginine had the most negative binding energy of the three.[459] In this study solvation effects were reported to be key to the interactions between the peptide and the graphene surface, as water was found to have a layered structure near the graphitic surface. The findings demonstrated that the first solvation shell tended to contain the peptide backbone and side groups of the central residue, and suggested that arginine had strong binding interactions due to favourable interactions between the negatively charged oxygen atoms in water molecules in the first solvation shell and the positively charged guanidinium groups of arginine molecules. In a different study, investigating the interaction of an Arg-Gly-Asp tripeptide with graphene, defective graphene and GO, the graphitic surface was found to interact with the NH_3^+, COO^-, and guanidine functional groups through weak non-covalent bonds to the π delocalised network.[454] In addition to these interactions, when oxygen functionalities were present on the graphitic surface (as is the case for GO), hydrogen bonds were calculated to exist between hydroxide groups on the surface and carboxylate and guanidine groups on the peptide, and between epoxy groups on the surface and NH_3 groups on the peptide. Strong interactions between arginine and GO have also been observed experimentally, and attributed to electrostatic interactions between charged groups on the two species.[455, 456]

To test whether the aqueous dispersion of graphene and GO improved with the addition of arginine, graphite and GO were bath and probe sonicated in water and 0.5 M arginine and the results compared. Visual inspection of the solutions (figure 82) revealed that in all cases the concentration of graphitic material was higher when arginine was present, which was confirmed by the relative absorbances of the samples recorded on the UV-vis (table 19). The data confirmed the expected trends that 1) the solutions of GO were more concentrated than the solutions of graphene and 2) the

probe sonicated solutions were more concentrated than the bath sonicated solutions. This was due to the oxygen functionalities of GO interacting favourably with the water and the increased sonic energy exerted on the sample respectively. The data also showed that the concentration of GO was improved more by the addition of arginine than the concentration of graphite, which could be expected based on the additional bonds arginine can form with GO.

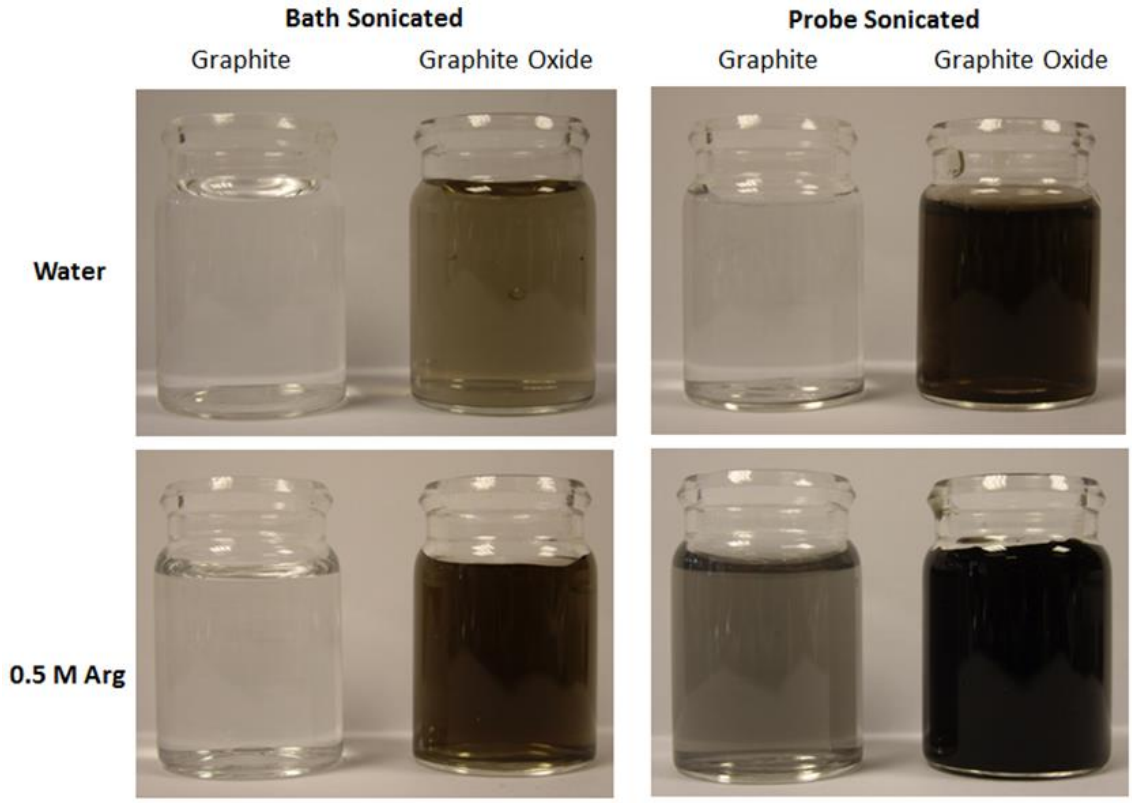

Figure 82: Photographs of solutions of graphite and graphite oxide that have undergone bath (left) or probe (right) sonication in either water (top) or 0.5 M arginine in water (bottom), taken 24 h after sonication.

Table 19: UV-vis absorbance values at 660 nm for the bath and probe sonicated solutions of graphene and GO in water and 0.5 M arginine.

	Bath Sonicated		**Probe Sonicated**	
	Graphite	**Graphite Oxide**	**Graphite**	**Graphite Oxide**
Water	0.02	0.26	0.27	0.76
0.5 M Arg	0.14	0.56	0.46	5.69
Difference	0.12	0.30	0.19	4.94

Further to increasing the total amount of material dispersed, adding arginine to the water also improved the stability of the dispersions with time. This was evident from the percentage decrease in absorbance after 1 week for the different solutions (figure 83), which in each case was less for 0.5 M arginine than for water. Further to increasing the concentration in solution it may be that arginine aided the physical exfoliation process, resulting in a higher percentage of thin sheets than achieved in water alone. Determining whether this was the case or not presents an interesting area of potential future work, as arginine could represent a 'green' way to obtain graphene directly from exfoliation of graphite.

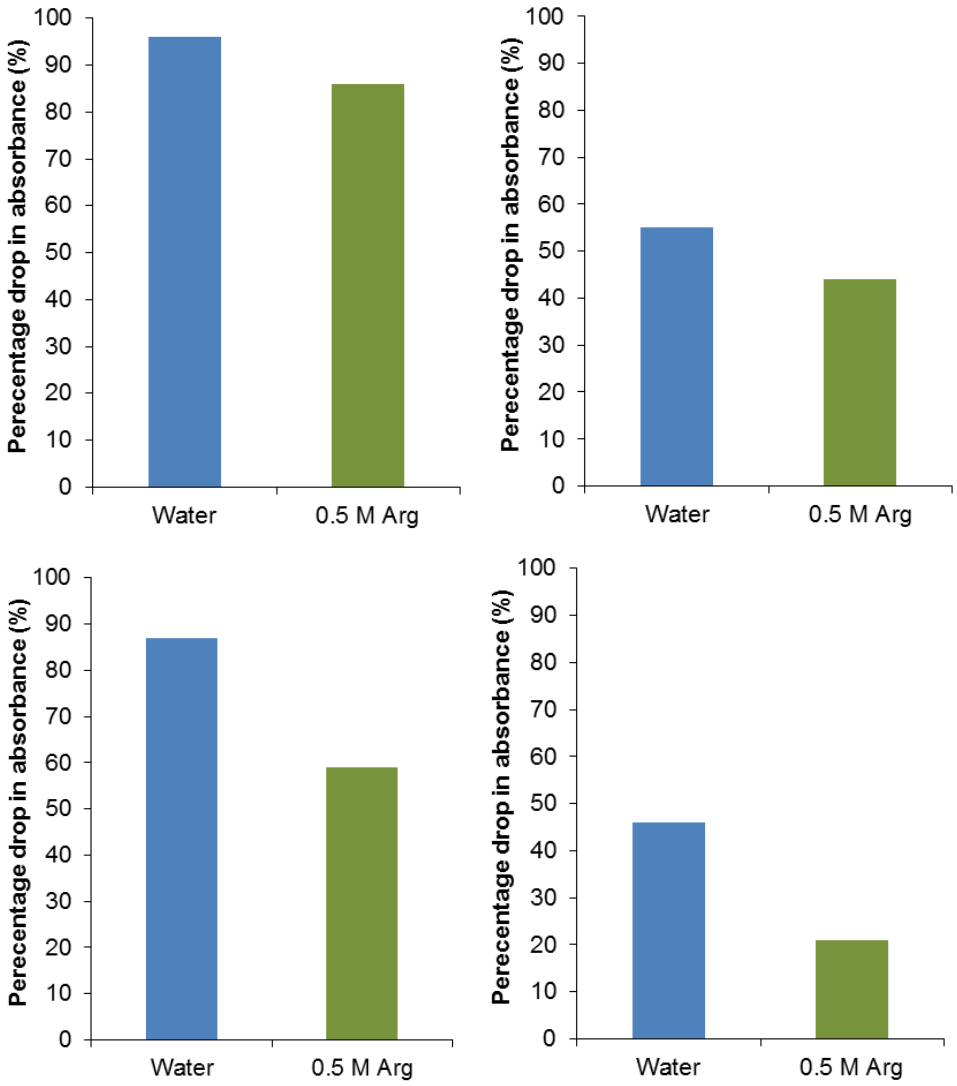

Figure 83: Graphs to show the percentage drop in UV-vis absorbance at 660 nm of aqueous dispersions graphite (left) and graphite oxide (right) over a 1 week timescale for bath (top) and probe (bottom) sonicated samples.

4.4 Hydrazine reduction in the presence of arginine

One of the key challenges for the chemical reduction of GO is preventing the aggregation and precipitation of the sheets during reduction, as this can limit the extent of overall reduction that can be achieved.[170] A potential way to combat this issue is to add a stabiliser to the reaction mixture to minimise the aggregation. This tactic has been previously reported for reduction of GO via UV irradiation in the presence of polyvinyl pyrrolidone,[171] and also for other aqueous based reductions using different molecular species as dispersants, such as sodium cholate,[442] polysaccharide,[443] and a number of different amino acids; including glycine,[444] tryptophan,[460, 461] and arginine.[455] The reduction of GO with hydrazine hydrate is a widely used technique to achieve highly reduced material.[170, 371, 394, 462] When tryptophan was used as a stabiliser in the hydrazine hydrate-mediated reduction of GO a shift from 228 to 271 nm was reported,[461] and the reaction afforded functionalised rGO with good aqueous stability, which was then used to successfully reinforce a polymer nanocomposite. Given the success of this work, and the ongoing requirement for well-dispersed graphene, a similar method was investigated in the current work but for the hydrazine hydrate-mediated reduction of GO in the presence of arginine.

The following section describes the use of arginine in the hydrazine hydrate-mediated reduction of three different graphitic materials; standard GO, 'base-washed' GO and 'water-refluxed' GO, and draws a comparison with the same reduction method in the absence of arginine. The aim of this work was to investigate whether arginine could enhance the reduction level in these systems (by preventing aggregation of material during the reaction) and to investigate if the addition of arginine led to a more dispersible final product. The three systems have different levels of deoxygenation originally; where standard GO had the highest relative proportion of oxygen and 'base-washed' GO had the lowest. The 'water-refluxed' GO material chosen for this study had been refluxed for 24 h, as this provided a sample with an intermediate level of oxygen.

While the standard GO was readily soluble in water, and hence formed a brown solution with no sediment when sonicated in either water or 0.5 M arginine prior to the reduction reaction, 'water-refluxed' GO (which is not as hydrophilic) did not fully disperse in water, and sediment was visible at the bottom of the vessel after sonication (figure 84). This sediment was not visible when 0.5 M arginine was used as the

dispersion media, demonstrating that the use of arginine can be beneficial to creating a good dispersion prior to reaction when trying to further reduce partially reduced GO. Images of the solutions after the reduction reaction demonstrated that for both extremes of initial oxidation level (GO and base-washed GO), the material reduced in water settled out of solution, while the material reduced in the presence of arginine remained dispersed (figure 85).

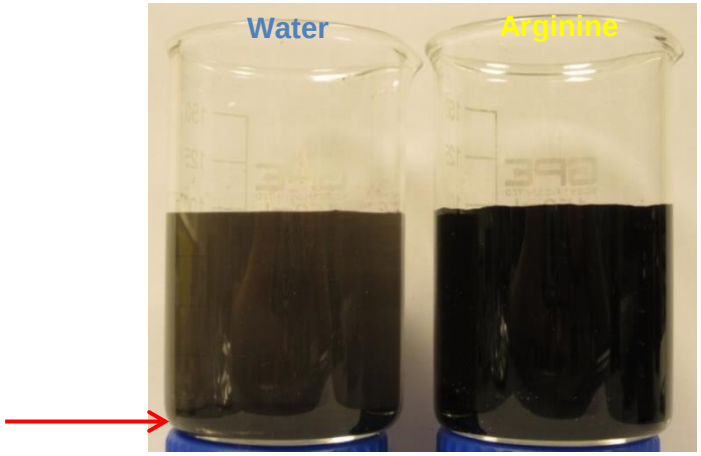

Figure 84: A photograph of dispersions of water-refluxed graphite oxide probe-sonicated in pure water or 0.5 M arginine before the hydrazine hydrate-mediated reduction, where the red arrow points to non-dispersed solid.

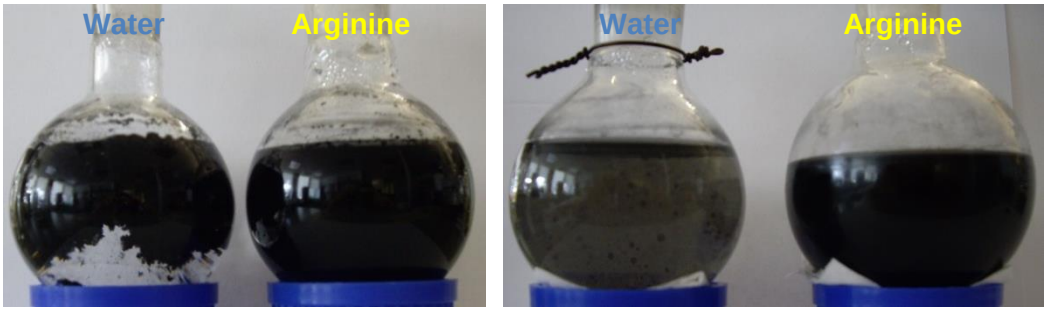

Figure 85: Photographs of *solutions after the hydrazine-induced chemical reduction of standard GO (left) and base-washed GO (right) in the presence of pure water and 0.5 M arginine.*

Interestingly, despite the appearance of the solutions after the reduction reaction, re-dispersion of the filtered, rinsed and dried material into water revealed that GO reduced in water was more dispersible than GO reduced in 0.5 M arginine (figure 86). For 'base-washed' and 'water-refluxed' GO, the material reduced in the presence of arginine was more dispersible than the material reduced in water alone, although the

difference between the two results was relatively small. The dispersions in this data set highlight some of the difficulties in handling GO-based materials. The key difficulty is that in order to achieve a dispersion of known concentration the material must be dried to obtain an accurate weight of solid; however the drying process can have an irreversibly damaging effect on the dispersibility of the material. This is particularly evident for the dispersion of standard GO before reduction, which should have been the darkest solution given the high aqueous dispersibility of GO, but actually appeared less concentrated than solution of reduced GO (figure 86, left). This is because the GO dried down to a hard film that floated on the surface of the liquid during sonication rather than breaking apart and dispersing. The discrepancy from the expected result for GO reduced in water and arginine could be due to the effect of residual arginine on the vacuum drying of the solid, because as the sample dried the relative concentration of the arginine (and thus the relative ionic concentration) would have increased, which may have caused more severe agglomeration of the material akin to the effect of "salting out" a solid, making the subsequent material more difficult to disperse. The presence of residual hydrazine hydrate and arginine can be seen from the C/N ratios calculated from the XPS survey spectra (table 20).

Table 20: C/N ratios calculated from the XPS survey spectra for different GO-based samples before and after hydrazine hydrate mediated reduction in the absecene and presence of arginine.

	C/N Ratio		
Sample	**GO**	**Water refluxed GO**	**Base-washed GO**
After reduction in 0.5 M arg	12 ± 1	21 ± 5	7 ± 1
After reduction in water	67 ± 7	120 ± 80	39 ± 6
Before reduction	100 ± 20	190 ± 70	150 ± 20

.

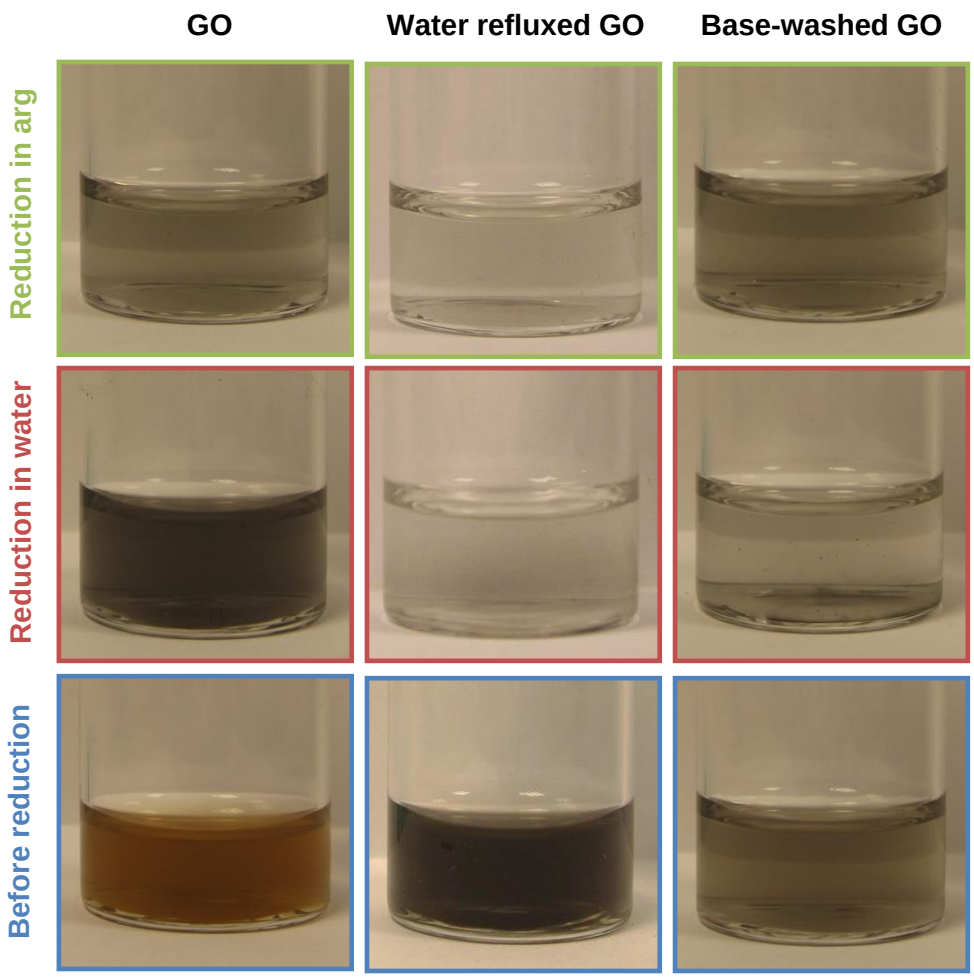

Figure 86: Photos of the dispersions of standard (left), 24 h 'water-refluxed' (middle) and 'base-washed' (right) materials before reduction (bottom) and after hydrazine hydrate-mediated reduction in water (middle) and 0.5 M arginine in water (top).

The relative absorbances of the different materials measured in the UV-vis supported the trends from the visual inspection of the dispersions (figure 87). The 'water-refluxed' and 'base-washed materials' were confirmed to be most dispersible before reduction, where the 'water-refluxed' GO was the most dispersible of the two. This was the expected outcome based on the relative proportion of oxygen containing groups for the two samples. The presence of arginine during the reduction reaction had the greatest benefit for the base-washed material, which had the lowest proportion of oxygen groups initially. The same trend in dispersibility was observed 24 h and 8 days after initial sonication.

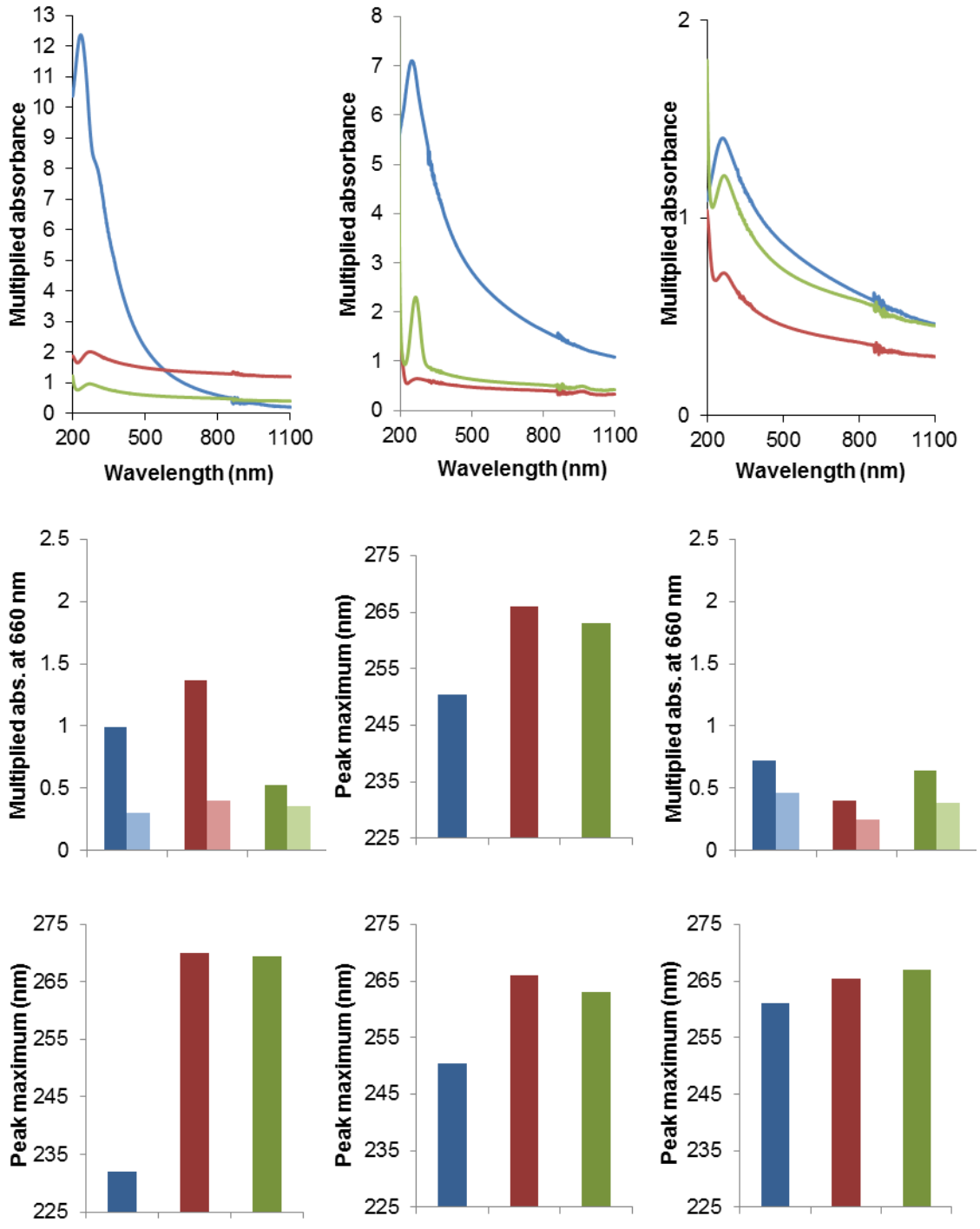

Figure 87: UV-vis spectra of the dispersions created by sonicating 10 mg of standard (left), 24 h 'water-refluxed' (middle) and 'base-washed' (right) GO before reduction (blue), after hydrazine hydrate-mediated reduction in water (red) and after hydrazine hydrate-mediated reduction in 0.5 M arginine (green) (top), and charts of the multiplied absorbances of the various solutions 24 h after sonication (dark colours) and 8 days after sonication (light colours) (middle), and peak maxima (λ_{max}) for the various solutions (bottom).

The UV-vis spectra showed that the differences in the shift of the λ_{max} upon reduction were different for the three solids. For standard GO and 'base-washed' GO the difference between the materials reduced in water and arginine is within error given the breadth of the peak (270 nm and 267 nm respectively), whereas for the 'water-refluxed' material the difference was slightly higher (266 and 263 nm respectively); where the material reduced in the presence of arginine exhibited the smallest shift. Based on these results, the presence of arginine did not impact the level of reduction achieved.

The assertion that the presence of arginine had minimal effect of the hydrazine hydrate-mediated reduction reaction was supported by the SSNMR and XPS results (figures 88 and 89), which have similar lineshapes for the material reduced in the different media, particularly with regard to the removal of the hydroxyl and epoxy groups. There was some additional intensity in the higher energy regions of the SSNMR and XPS spectra for the material refluxed in the presence of arginine, which could indicate less effective reduction, but given the results of the UV-vis λ_{max} values and the C/N ratios calculated from the XPS survey scans is probably more correctly attributed to bonding contributions from the residual amino acids, as discussed earlier in the chapter. The C/N ratio is an indication of the residual arginine, although since hydrazine also contains nitrogen atoms the ratio of graphitic carbon to amino acid carbons cannot be accurately determined. Small amounts of nitrogen can be seen in the starting materials, which is likely to be due to small amounts of residual nitrates from the Hummer's reaction. The trend in the C/N ratios in terms of the highest proportion of residual arginine (base-washed GO>GO>water refluxed GO) appears to follow the trend in intensity in the 140-180 ppm region of the SSNMR spectra and 287-290 eV region of the XPS spectra, supporting the claim that this intensity can be attributed to residual arginine.

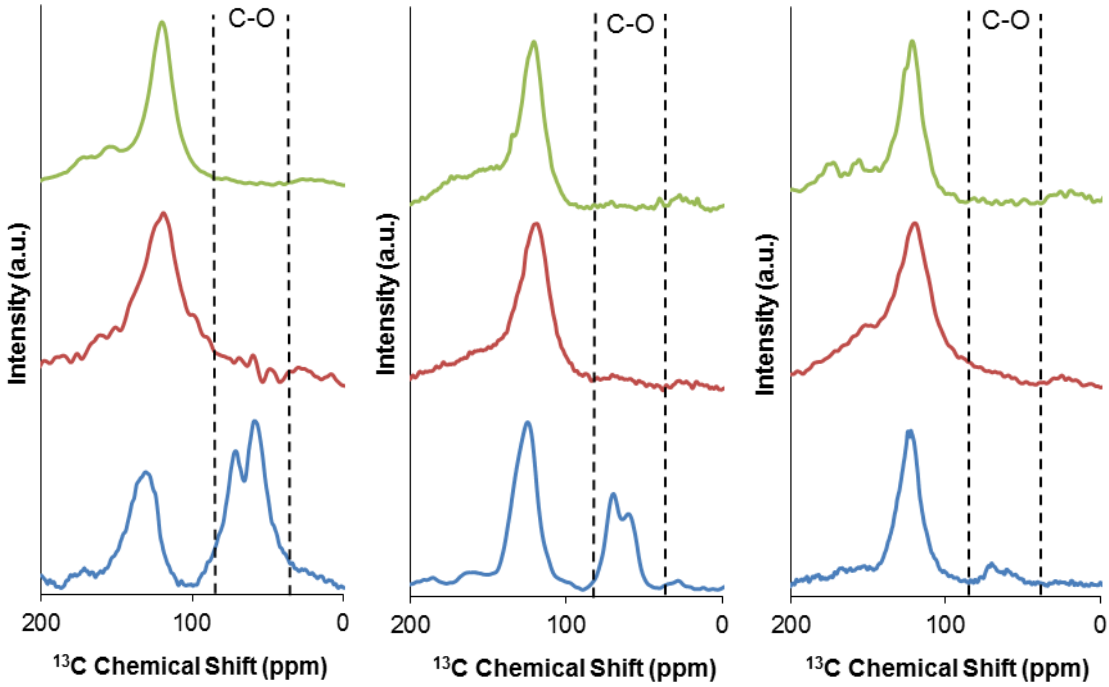

Figure 88: SSNMR spectra of standard (left), 24 h 'water-refluxed' (middle) and 'base-washed' (right) materials before reduction (blue), after hydrazine hydrate-mediated reduction in water (red), and after hydrazine hydrate-mediated reduction in 0.5 M arginine (green).

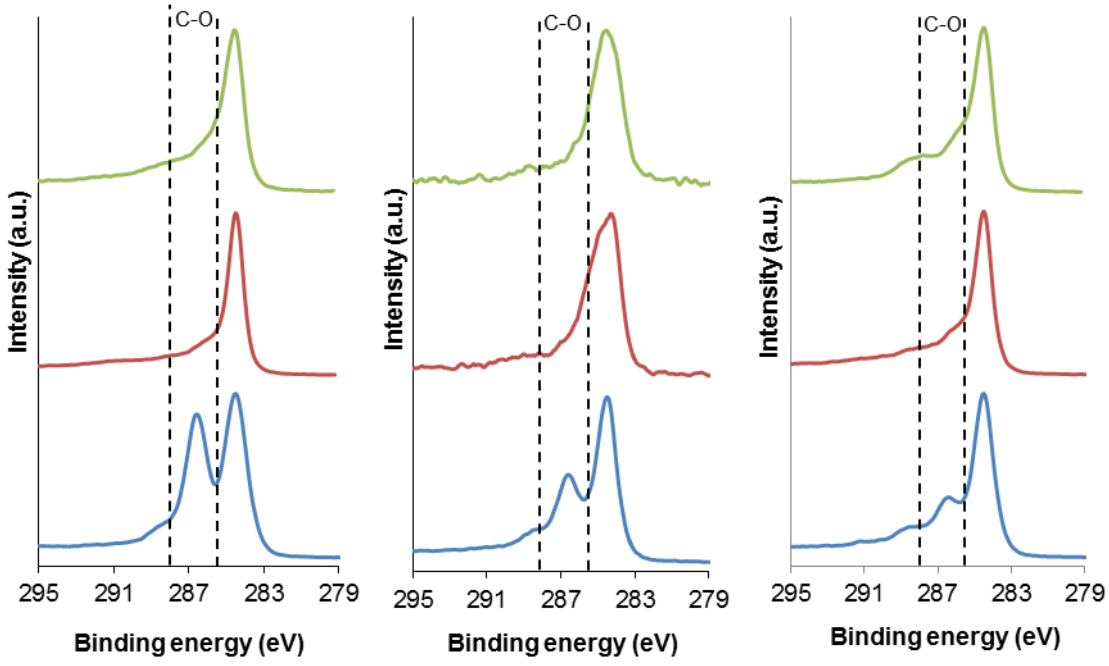

Figure 89: C 1s XPS spectra of standard (left), 24 h 'water-refluxed' (middle) and 'base-washed' (right) materials before reduction (blue), after hydrazine hydrate-mediated reduction in water (red), and after hydrazine hydrate-mediated reduction in 0.5 M arginine (green).

The electrical conductivities of the materials after reduction were higher than before reduction in all cases, as expected (table 21). For GO, the resistance of the film was too high to measure. The electrical conductivity results after reduction showed the materials reduced in water had 1 or 2 orders of magnitude lower resistance than the materials reduced in arginine. Again this was likely to be, at least in part, due to the presence of residual amino acid for the samples refluxed in the presence of arginine, so any trends relating to the inherent reduction level of the materials may have been masked. Interestingly, the lowest sheet resistance for materials reduced with hydrazine hydrate in the presence of arginine was only one order of magnitude more conducting that the material produced by refluxing 'pre-wash' GO in arginine for 4 h ($(1.3 \pm 0.2) \times 10^4$ Ω/□ and $(1.05 \pm 0.08) \times 10^5$ Ω/□ respectively). Since the former reaction must proceed via 'post-wash' GO (due to the interaction of hydrazine with acid) and requires a 12 h reflux step, the latter reaction may present the most attractive alternative for obtaining rGO functionalised with arginine.

Table 21: Electrical conductivity measurements for thin films of materials before and after reduction in the presence and absence of arginine.

	Sheet Resistance (Ω/□)		
Sample	**GO**	**Water refluxed GO**	**Base-washed GO**
After reduction in 0.5 M arg	$(1.3 \pm 0.2) \times 10^4$	$(7 \pm 1) \times 10^5$	$(1.5 \pm 0.4) \times 10^5$
After reduction in water	$(1.5 \pm 0.2) \times 10^2$	$(2.4 \pm 0.4) \times 10^4$	$(3 \pm 1) \times 10^4$
Before reduction	-	$(6.6 \pm 0.3) \times 10^6$	$(5.69 \pm 0.08) \times 10^6$

4.5 Conclusions and future work

Refluxing 'pre-wash' GO in aqueous solutions of arginine was found to be a relatively quick and effective way to produce chemically reduced GO. The reduction level of the material was found to be of same order as GO reduced using other reduction methods that utilise natural products, but crucially in the current study the reduction was performed on GO before washing which meant that the total time between graphite and rGO was significantly lower that for the other reduction techniques. The resulting material contained some residual arginine, but the rinsing process was not optimised, and more effective rinsing is likely to be possible using alternative purification techniques such as dialysis, soxhlet extraction or cross-flow filtration. The mechanism for arginine mediated reduction is not clear, although it seems that some of the

perceived reduction can be attributed to the removal of highly oxidised debris from the graphitic surface. To separate out the pH and other reducing effects the reduction of 'pre-wash' GO could be trialled in arginine solutions of different pHs; and this represents an interesting area of future work. The effect of reflux time and arginine concentration on the reduction level and physical behaviour of the material is not completely understood, but progress has been made in terms of optimising these conditions; where short reflux times (<1 h) and low arginine concentrations (0.1 M) were found to result in less well reduced products that were difficult to handle. Results from the initial trials were positive and suggest that further work into optimising this system is of merit.

Arginine was shown to improve the aqueous dispersibility of both GO and graphite, and although the addition of arginine as a dispersant in the hydrazine hydrate-mediated reduction of GO did not yield any notable improvements to the original method, there were some improvements in the dispersibility of 'water-refluxed' and 'base-washed' material that had been further reduced. The electrical conductivities of all samples appeared to be negatively affected by the presence of residual arginine, which did not readily rinse off with cold water. For systems where dispersibility is more important than electrical conductivity, and where interaction with a matrix are important, the residual arginine could be of benefit; so even if the arginine cannot be removed the use of arginine as an additive to the two different reduction methods investigated still shows promise, as these reaction could be considered as one-pot reduction and functionalisation reactions (as is the case for some of the other reduction methods).[415, 438, 444, 461]

Chapter 5: Graphene synthesis via chemical vapour deposition over cobalt catalysts

5.1 Introduction

CVD has been used extensively as a means to produce large area graphene films, where high quality films up to 30" in size have been successfully produced.[255] These films are usually grown for electronic applications, which require the high levels of electrical conductivity afforded by producing graphene at high temperatures using metal catalysts. Despite the use of CVD to produce both high quality graphene films and bulk scale carbon nanotubes, there have been limited investigations into using CVD to produce bulk scale graphene platelets, for applications such as composite materials. In fact there have been very few attempts at producing bulk scale graphene materials from 'bottom-up' processes as a whole (see section 1.3.2.3), with focus instead falling on 'top-down' synthesis methods such as solvent exfoliation of graphite or chemically or thermally reduced graphene oxide.[83] As many of the previously reported methods of producing 'bottom-up' graphene platelets afford materials that contain large amounts of defects with limited control over the carbon morphology,[281-283] there is much scope for improvement in this area of graphene synthesis.

'Top-down' methods suffer from a number of intrinsic limitations which do not apply to 'bottom-up' methods, chiefly related to their reliance on the starting material. First, graphite is a finite resource[102] which can vary heavily based on its geographical location, making producing consistent material challenging and potentially expensive in the future. Secondly, the structure of natural graphite contains defects which act as weak spots during processing, limiting the potential size of the sheets obtainable and resulting in large size distributions in the as-produced material. The size of graphene sheets has been found to significantly impact the ability of graphene to act as a filler to improve the mechanical properties of composites.[463] Here graphene sheets with 5 μm lateral dimensions were found to act as 'short fillers'; where the edge effects of the filler dominated and there was limited property enhancement, while graphene sheets with lateral dimensions of 20 μm were found to increase the strength of the composites linearly up to a 20 % graphene loading. Having larger sheets is also favourable for applications involving electrical and thermal conductivity as large sheets have fewer sheet-to-sheet junctions than smaller sheets, improving the transport of electrons or phonons through the material. For these reasons conquering 'bottom-up' growth of bulk

scale graphene may represent a necessary step in the long-term commercialisation of graphene technologies.

Cobalt is a metal which has been fairly widely studied in the CVD synthesis of graphene films, although less so than nickel and copper.[215, 257] Graphene is thought to form on cobalt substrates through an absorption-segregation mechanism (as described in section 1.3.2.2) meaning that cobalt has the potential to catalyse the growth of graphene sheets with different number of layers depending on the growth conditions. In addition to studies of graphene growth on cobalt sheets there are also a small number of articles detailing the growth of graphene on cobalt-based catalysts such as Co_3O_4 and CoO, utilising either methane or solid carbon sources.[464-466] In the following chapter the use of cobalt carbonate to produce graphene sheets from ethanol feedstock was investigated. Furthermore, inspired by the work of Forrest and Alexander which showed that sodium doping inhibited the growth of carbon nanotubes,[467] the effect of sodium doping on the yield and quality of graphene produced using cobalt carbonate based catalysts was also studied.

5.2 Synthesis and characterisation of cobalt carbonate based catalyst

Cobalt(II) carbonate was synthesised using a simple precipitation method where warm, aqueous solutions of cobalt nitrate (0.5 M) and sodium carbonate (0.65 M) were combined and heated.[468] A purple precipitate was formed which was rinsed in the centrifuge, filtered, and allowed to dry overnight. Earlier experiments revealed that cobalt carbonate oxidised with prolonged exposure to air, so after cooling, the solid was stored in a glove box in a nitrogen atmosphere until use. Cobalt carbonate made in this way served as the starting material for the sodium doped cobalt catalysts, although itself contained a small residue of sodium (0.12 wt. %) due to the synthesis method.

Sodium doped cobalt catalysts were prepared by grinding varying amounts of the as-synthesised cobalt carbonate with sodium fluoride. Sodium fluoride was chosen as the source of sodium due to its high thermal stability (T_m = 996 °C), which is beneficial as it permits high CVD growth temperatures. Elemental analysis of the products revealed sodium contents of 1.11, 2.02, 3.00, 4.59 and 8.69 weight percent, which were compared with the 0.12 weight percent starting material, a sample of which was ground

for 15 minutes for consistency. The Brunauer, Emmett, Teller (BET) surface area of the catalysts (figure 90) showed variation in surface area for the catalysts with different sodium dopings, which is likely to be due to inconsistencies in the grinding process.

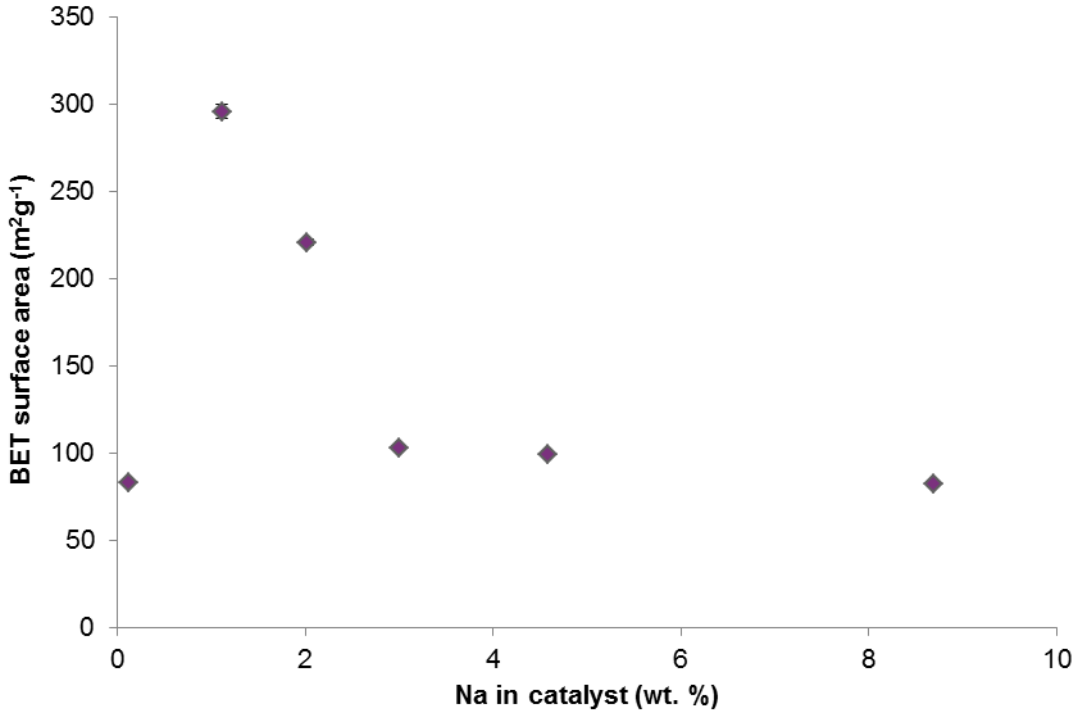

Figure 90: Plot of BET surface area of the sodium doped cobalt carbonate catalysts against percentage sodium. The greatest error in measurement was for the sample with ~1 wt % sodium (±4 m^2g^{-1}), but as this value was low in comparison with the surface area, the error bars are barely visible on the graph.

Air sensitive XRPD of the products revealed a mixture of cobalt carbonate-containing species (figure 91). No peaks were observed for the standard 2 hour scanning period, and even after 6 hours the peaks were of low intensity, indicating poor crystallinity of the synthesised cobalt carbonate. This is to be expected given that it was formed by a precipitation method and underwent no thermal annealing or aging to promote crystallisation. Peaks at 2θ = 26.4°, 39.4°, 47.0° and 53.5° corresponding to the (012), (110), (202) and (116) lattice spacings of $CoCO_3$ (JCPDS card no. 01-073-5916) were observed, alongside peaks associated with CoO (JCPDA card no. 00-009-0402) and Co_3O_4 (JCPDA card no. 00-009-0418). Peaks corresponding to NaF were not discernible in the ~2 wt.% catalyst.

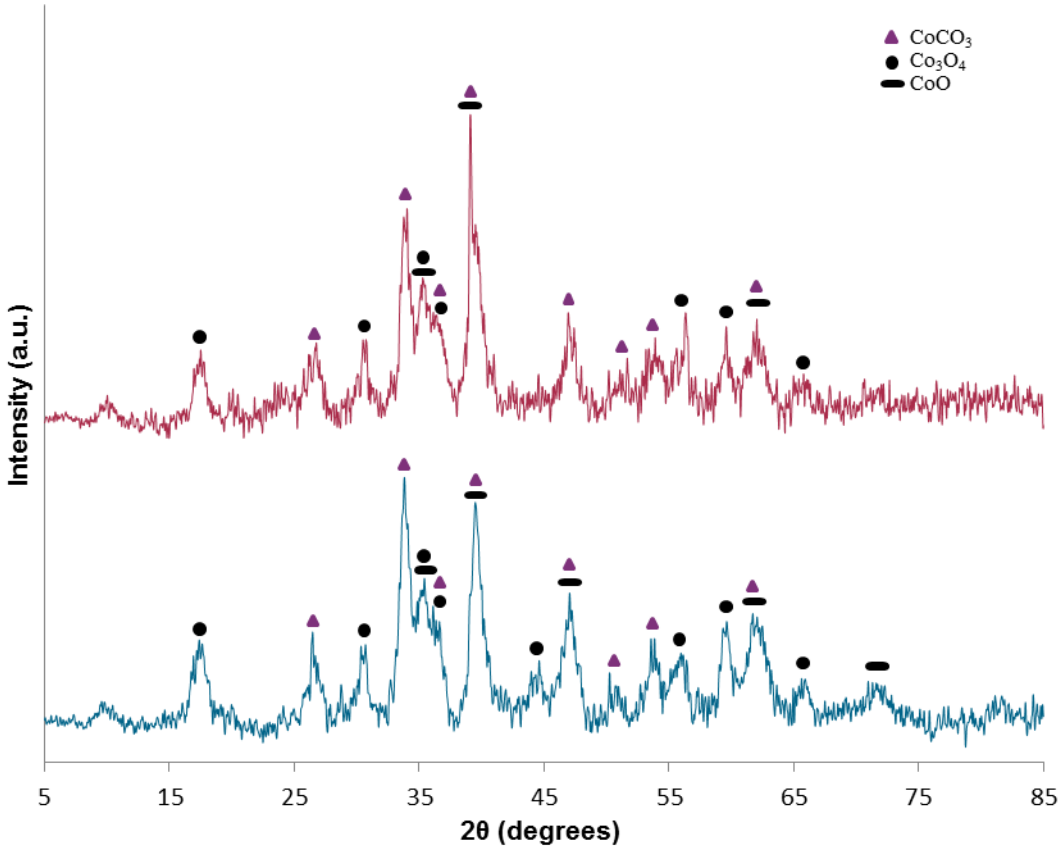

Figure 91: XRPD patterns of the undoped (blue) and doped (red) cobalt carbonate. The doped catalyst used contained 2.02 wt. % sodium. Radiation source: Cu $K_{\alpha 1,2}$ = 1.54 Å.

As the catalysts were heated to 800 °C during the CVD experiments, a variable temperature XRPD study was performed to investigate the behavior of the catalyst during heating and to probe the identity of the catalysts at the point of exposure to the bulk carbon source (figure 92). This study was performed under a flow of argon to reflect the conditions in the CVD set-up, and showed the presence of crystalline cobalt carbonate at temperatures up to 640 °C, the presence of face centered cubic (fcc) cobalt metal at temperatures of 560 °C and above, and the presence of crystalline Co_3O_4 at temperatures of 720 °C and above. These results showed that at the point of exposure of the carbon source, the catalyst contains crystalline cobalt metal and Co_3O_4.

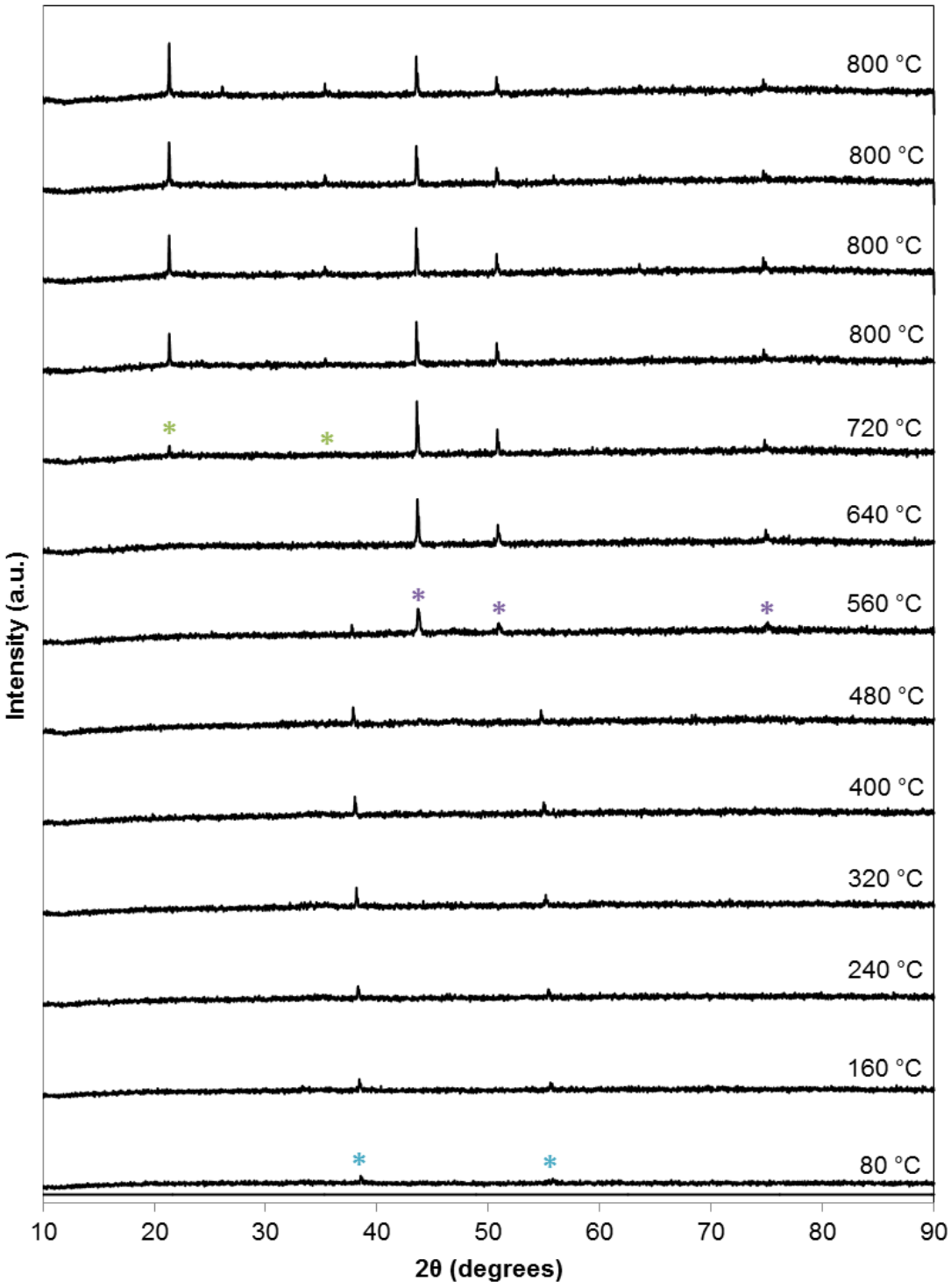

Figure 92: Variable temperature XRPD of 2.02 wt % sodium doped cobalt carbonate performed in an Ar atmosphere with the appearance of $CoCO_3$ (blue), Co (purple) and Co_3O_4 (green) peaks highlighted. Radiation source: Cu $K_{\alpha 1,2}$ = 1.54 Å. 40 minutes scans were collected at temperature intervals of 80 °C up to 800 °C at which temperature the furnace was held and multiple scans were collected.

XRPD spectra of the undoped and ~9 wt.% Na doped catalysts after the CVD reaction showed that the only crystalline cobalt-based species present in the unpurified carbon product was fcc cobalt metal (figure 93), suggesting that $Co^{(0)}$ was the high temperature catalytic species. For the doped catalyst, peaks corresponding to crystalline NaF (JCPDS card no. 36-1455) were seen alongside the Co (111), (200) and (220) peaks at 44.3°, 51.6° and 75.9° respectively (JCPDS card no. 75-1621).

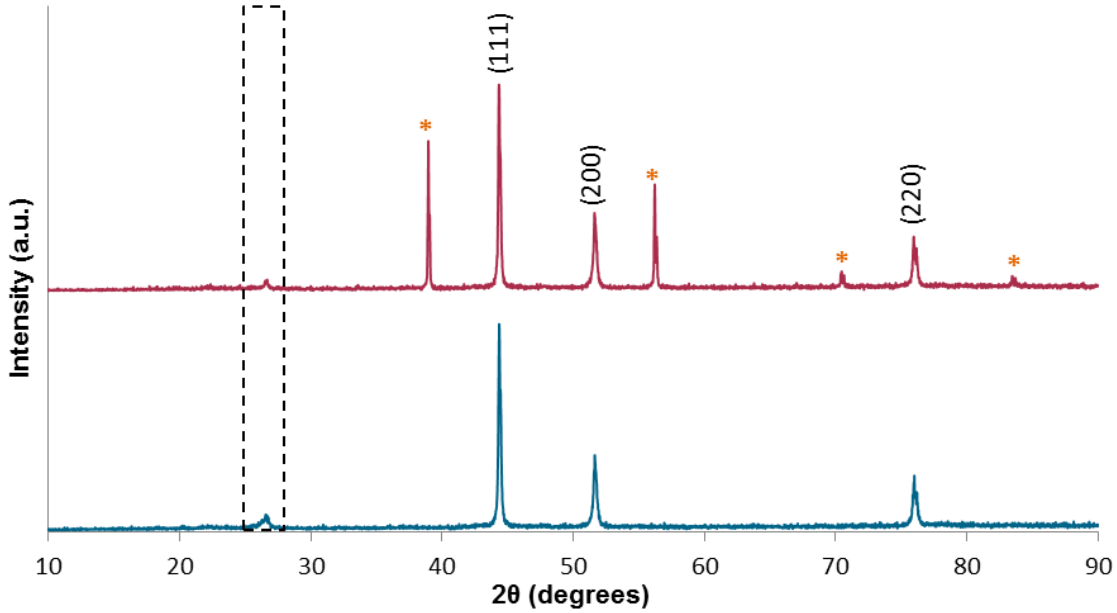

Figure 93: XRPD spectra of undoped (blue) and ~9 wt. % Na doped (red) cobalt carbonate based catalysts after the synthesis reaction, with the cobalt peaks indexed, the carbon peaks highlighted by the black box and the NaF peaks highlighted by orange asterisks. Radiation source: $CuK_{\alpha 1,2}$ = 1.54 Å.

During the course of this study, a paper on in-situ analysis of high temperature graphite synthesis using cobalt nanocomposites was released.[465] In this work metal cobalt (0.3 - 0.5 nm thick) was deposited onto a ~10 nm amorphous carbon film and heated to 600 - 800 °C on a 20 µm tungsten filament in the TEM sample heating holder. Although cobalt metal was deposited, it was found to convert to polycrystalline Co_3O_4 particles at room temperature, and CoO at 600 °C. The authors found that the CoO particles aggregated on the amorphous carbon upon elevating the temperature to 600 - 800 °C and formed a “liquefied state” which corresponded to a solid mass of metallic cobalt that exhibited both fluidity and crystallinity. It was observed that amorphous carbon was absorbed from the underlying carbon layer at the front edge of the moving particle, while randomly rotated polycrystalline graphite sheets were left behind on the

amorphous carbon over which the particle had passed. Electron diffraction data was used to characterise the cobalt species, which converted from β-Co to Co_3C during the course of the experiment, with graphite being synthesised at all the transient stages between those two species. Given the similar temperatures used and the presence of cobalt metal (as seen in the XRPD data) it may be that the graphitised carbon products of the present study formed via a similar mechanism, using ethanol as the source of carbon to form Co_3C.

5.3 Characterisation of carbon material grown over catalysts

The thermal decomposition of ethanol has been found to be a complicated process with over ten possible decomposition reactions. The major routes for dissociation are generally accepted to be as follows, where C_2H_4, CH_3 and CH_2OH represent reaction intermediates:[469-471]

$$C_2H_5OH \rightarrow C_2H_4 + H_2O$$

$$\rightarrow CH_3 + CH_2OH$$

Ethanol has been shown to be a suitable source for producing graphitic carbon at temperatures above 600 °C,[472] however at temperatures above ~1050 °C there is evidence of soot formation,[473] limiting the maximum growth temperature for this feedstock under standard reaction conditions. Alcohols have been reported as favourable liquid hydrocarbon feedstocks for controlling CNT growth as the oxygen from the hydroxyl group can form species that etch away amorphous carbon, resulting in a high quality product.[474-476] It has been shown that these oxygen containing species do not result in measurable doping or oxidation effect in the synthesised carbon materials,[477] which is another important factor to consider when selecting a feedstock. Ethanol also has the advantage of being low cost, easy to handle, and obtainable from renewable sources, making it an ideal feedstock for the bulk scale synthesis of graphene.

5.3.1 Synthesis of the carbon material

Solid carbon was grown on the cobalt carbonate based catalysts via CVD, using ethanol as the carbon source. In these experiments a predetermined amount of catalyst (0.5-0.6 g) in an alumina boat was positioned in the centre of a tube furnace

and heated to 800 °C under a flow of argon, at which temperature ethanol was sprayed into the furnace tube (figure 94). A colour change in the solid material was observed from purple/pink initially to black at the end of the reaction. The carbon material was separated from the catalyst by stirring the as-obtained solid in hydrochloric acid (6 M) overnight, rinsing and drying. The purified product was a black powdery solid, almost identical in appearance to the unpurified material.

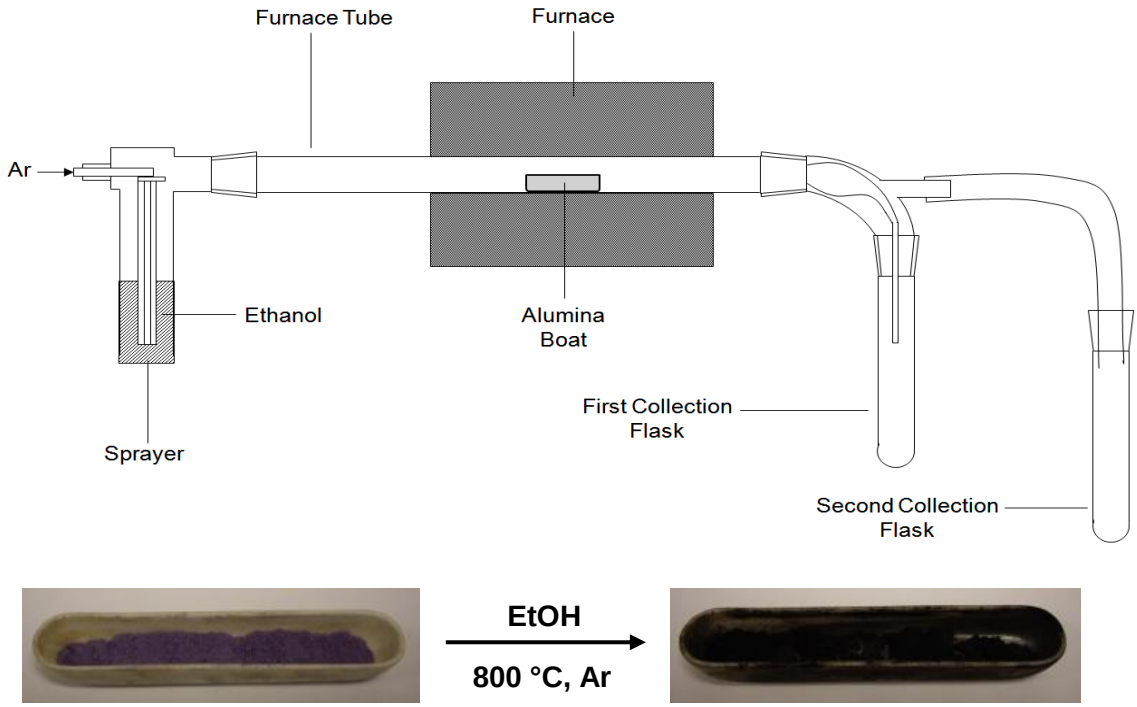

Figure 94: Furnace apparatus (top) and reaction schematic (bottom), showing the cobalt carbonate precursor (left) and carbon product (right.) Collection flasks were positioned at the back end of the furnace apparatus in case any powder was disturbed by the gas flow during carbon synthesis, but no evidence of this was actually observed.

The reaction afforded 0.4 g of purified carbon solid from 0.5 g of the undoped cobalt carbonate based catalyst and ~50 mL ethanol; which can be considered as 0.8 g of carbon per g of catalyst or 8 mg of carbon per mL of solvent. This yield is higher than many of the values previously reported for bulk scale graphene synthesis methods (table 22). It should also be noted that the reaction conditions in the current study have not been optimised, so it could be that greater yields may have been afforded under different conditions, for example greater amounts of ethanol, higher temperatures or a different physical configuration of the catalyst (e.g. more catalyst surface directly exposed to carbon source.)

Table 22: Carbon yields from a number of bulk scale, 'bottom-up' graphene synthesis reactions reported in the literature in order of descending yield per g of catalysts.

Reaction	Yield	Ref
CVD of CH_4 over Fe_2O_3	6 g carbon per 1 g Fe_2O_3	478
Current study	0.8 g carbon from 1 g $CoCO_3$	-
Solvothermal synthesis (Na/ethanol)	0.25 g carbon per 1 g Na	281
Calcination of $CaCO_3$ with Mg	0.2 g carbon per 2.4 g Mg and 10 g $CaCO_3$	283
Burning Mg in dry ice	0.225 g carbon per 1 g Mg	282

Scanning electron microscopy (SEM) of the purified material deposited on Si revealed large, film-like sheets with lateral dimensions in the order of ten microns (figure 95). The rippled appearance of the sheets, most likely caused by crumpling of the material during spin-coating, and the low contrast with the silicon substrate, indicated that the material was thin. There was evidence of small holes in a number of sheets, which may have been formed during growth of the materials or may have been produced due to the mechanical stresses inflicted during purification or SEM sample preparation (mechanical stirring and bath sonication). While there was evidence of some small impurities on the silicon surface, there was no evidence of other forms of nanocarbons such as tubes or fibers, suggesting that sheets were made preferentially by the catalyst. This is promising as various different forms of carbon, including CNTS, fibers and carbon encapsulated metal particles have been reported over relatively narrow temperature ranges for CVD over iron based catalysts[478, 479]; a metal that is thought to grow graphene via the same mechanisms as cobalt.[217]

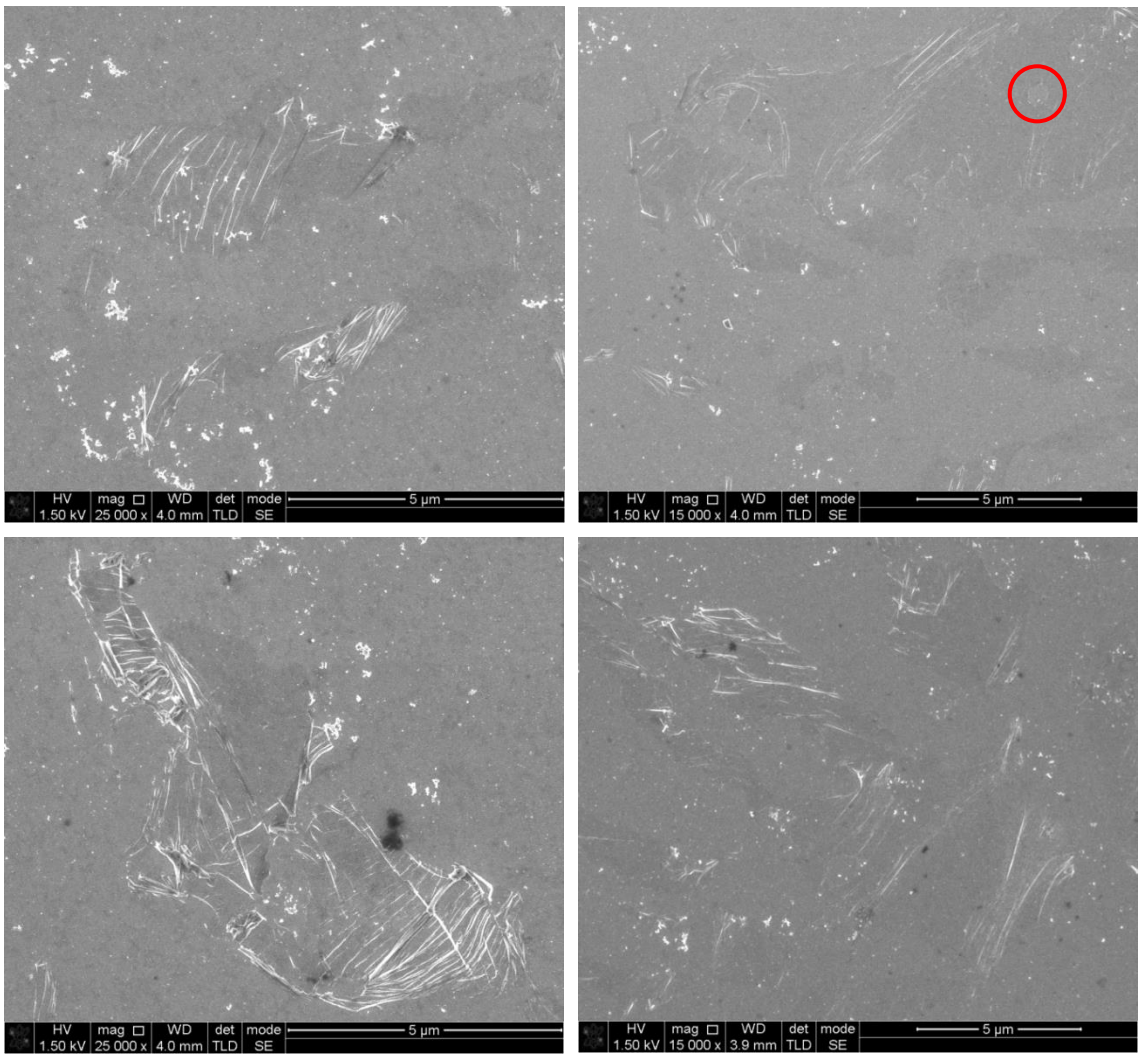

Figure 95: SEM images of the carbon product produced by CVD over undoped cobalt carbonate catalyst spin coated onto a silicon substrate. High contrast lines indicate the rippling of the carbon and the red circle highlights a hole in a carbon sheet.

TEM revealed a number of agglomerated sheets with dimensions of around 1 µm. Note that large film-like sheets were not observed in the TEM, which may be due to the different sample preparation for the TEM than for the SEM (drop casting versus spin coating), or as a consequence of smaller sheets preferentially adhering to the lacey carbon support of the TEM grids. As per the SEM, there was no evidence of other carbon nanomaterials such as CNTs and nano-onions observed via TEM, and in all cases very few traces of residual catalyst were observed. Typical BF TEM showed crumpled and overlapping sheets with a degree of scrolling at the edges, which is indicative of thin material (figure 96). The HRTEM image of one of the upturned edges of the sheet revealed that the sheet consisted of 9 graphitic layers. The interlayer spacing measured using a line profile of the upturned edge was 0.363 ± 0.061 nm (error due to pixel size) which is close to the value expected for graphitic stacking

(0.335 nm).[480] The interlayer spacing is consistent, within error, for all the measured gaps and the stacking itself appears to be regular and ordered over the field of view, suggesting that the material is well-graphitised.

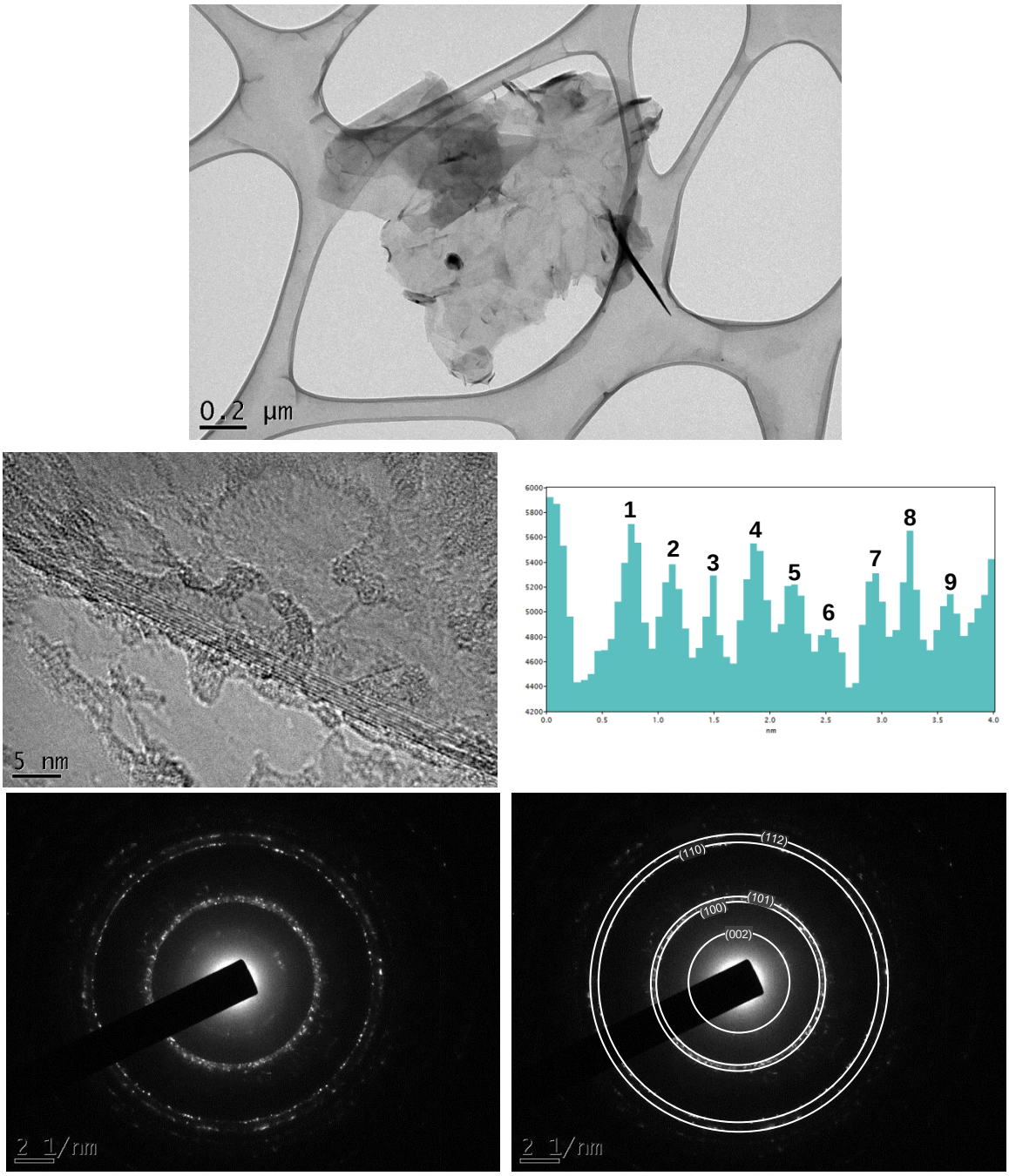

Figure 96: A bright field image (top), HRTEM image (centre left) and electron diffraction pattern (bottom left) of the purified carbon material grown over the undoped cobalt carbonate based catalysts. The line profiles of the HRTEM image (centre right) and indexed electron diffraction pattern (bottom right) show the interlayer spacing of the carbon sheets and the assignment of diffraction rings respectively.

The SAED of the sheet also supported the conclusion that the material was well graphitized, as evidenced by the sharp spots that constitute the diffraction rings, rather than diffuse rings as would be expected for amorphous carbon. The spots have been indexed to the interlayer spacings of graphite including, notably, the (100) and (110) Miller indices of graphite corresponding to the in-plane spacings of ~2.1 Å and ~ 1.2 Å respectively, as present in all graphitic materials.[302, 418] The presence of multiple sets of spots rather than a single set of six discrete spots suggests that the sheets are polycrystalline or that the sheets are turbostratic; with stacked layers that are rotated and translated relative to one another (see section 2.1.2). The ring corresponding to the (002) interlayer spacing was visible due to the upturned edges of the sheets, and confirmed that the interlaying spacing was ~3.4 Å, consistent with the HRTEM result and the expected value for graphite.

The morphology of the carbon product was less complex and more sheet-like than the products of the majority of bottom-up, bulk scale graphene synthesis methods reported in the literature (figure 97), with the exception of the material formed by CVD of acetylene over iron oxide particles at 850 °C, which has been shown to grow as relatively large, flat, crystalline sheets.[479]

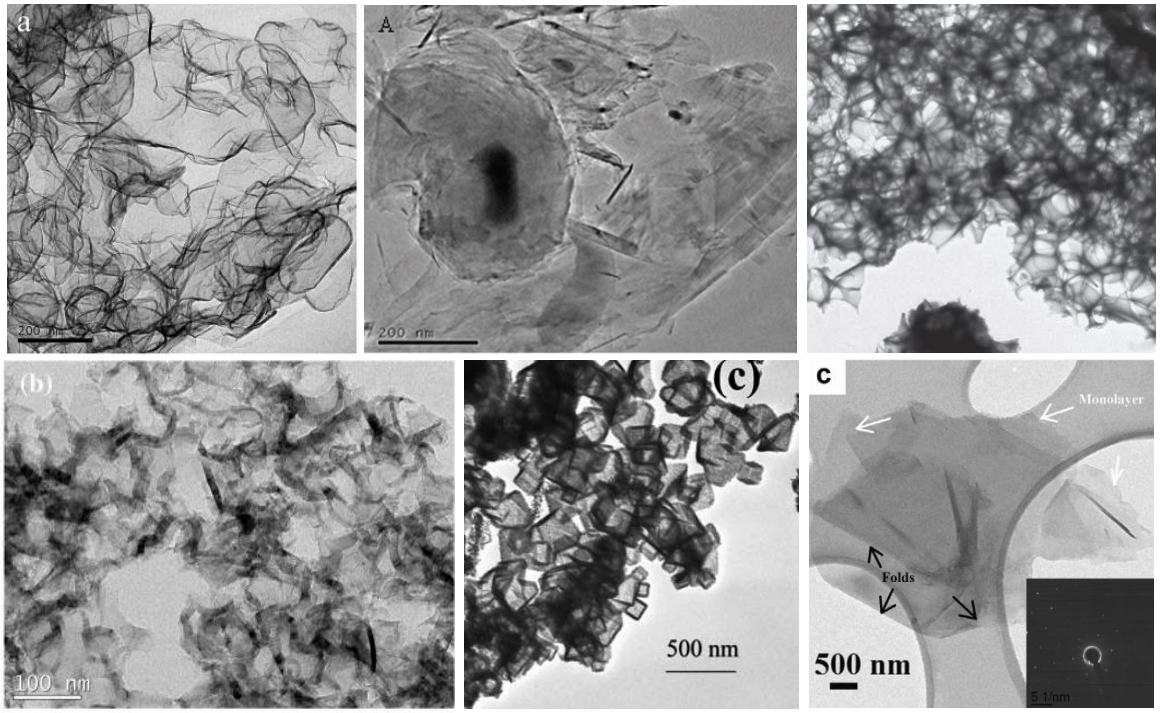

Figure 97: TEM images of the carbon products of bulk scale 'bottom-up' synthesis reaction of graphene reported in the literature for CVD of CH_4 over Co/MgO (top left),[481] CVD of CH_4 over Fe_2O_3 (top middle),[478] solvothermal synthesis using Na/ethanol (top right),[281] calcination of $CaCO_3$ with Mg (bottom left),[283] burning Mg in dry ice (bottom middle),[282] and CVD of C_2H_2 over Fe_2O_3 (bottom right).[479]

In addition to being used as a tool to gauge sample thickness, HRTEM was also used to qualitatively assess the quality of the material in terms of in-plane crystallinity (figure 98). Highly ordered regions were visible via HRTEM but there were also regions which appeared to be amorphous in proximity to these highly ordered regions. The fast Fourier transform (FFT) of the HRTEM image showed two sets of six spots rotated ~25 ° relative to one another, indicating that the probed area contains two different crystalline domains (see section 2.1.1). The calculated spacing between spots corresponds to a spacing of 2.07 ± 0.08 Å, which itself can be indexed to the (100) in-plane spacing of graphite.[418]

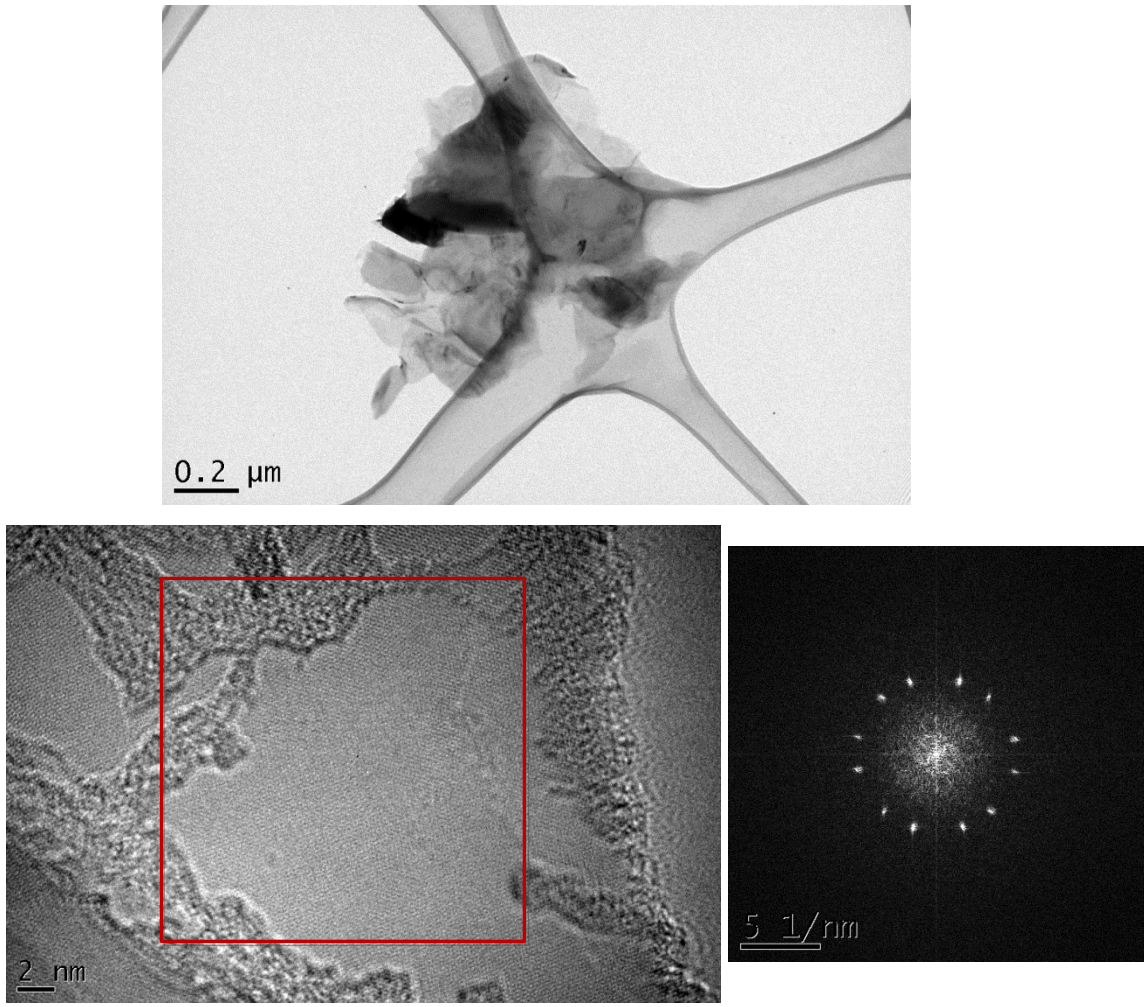

Figure 98: A bright field image (top), and HRTEM image (bottom left) of the purified carbon material grown over the undoped cobalt carbonate based catalysts. The FFT (bottom right) was collected over the portion of the HRTEM image outlined in red.

EFTEM thickness mapping was carried out on a number of sheets to probe the thickness of specific regions of the material. To do this, the values from the t/λ map

(where t is the thickness and λ is the inelastic mean path of the electron) were converted to number of graphitic layers using the correction factor calculated based on natural graphite measurement on the same microscope (see section 2.1.4). Analysis of the data for two regions of different sheets (figure 99) revealed t/λ values of ~ 0.4 ± 2 and 0.2 ± 0.1 λ, which correspond to 40 ± 26 and 20 ± 13 layers of graphene respectively. The errors associated with these measurements are large; where the values at the lower end of the calculated ranges (13 and 7 layers respectively) are similar to those seen via HRTEM and the values at the upper end (66 and 33 layers respectively) are much higher than expected.

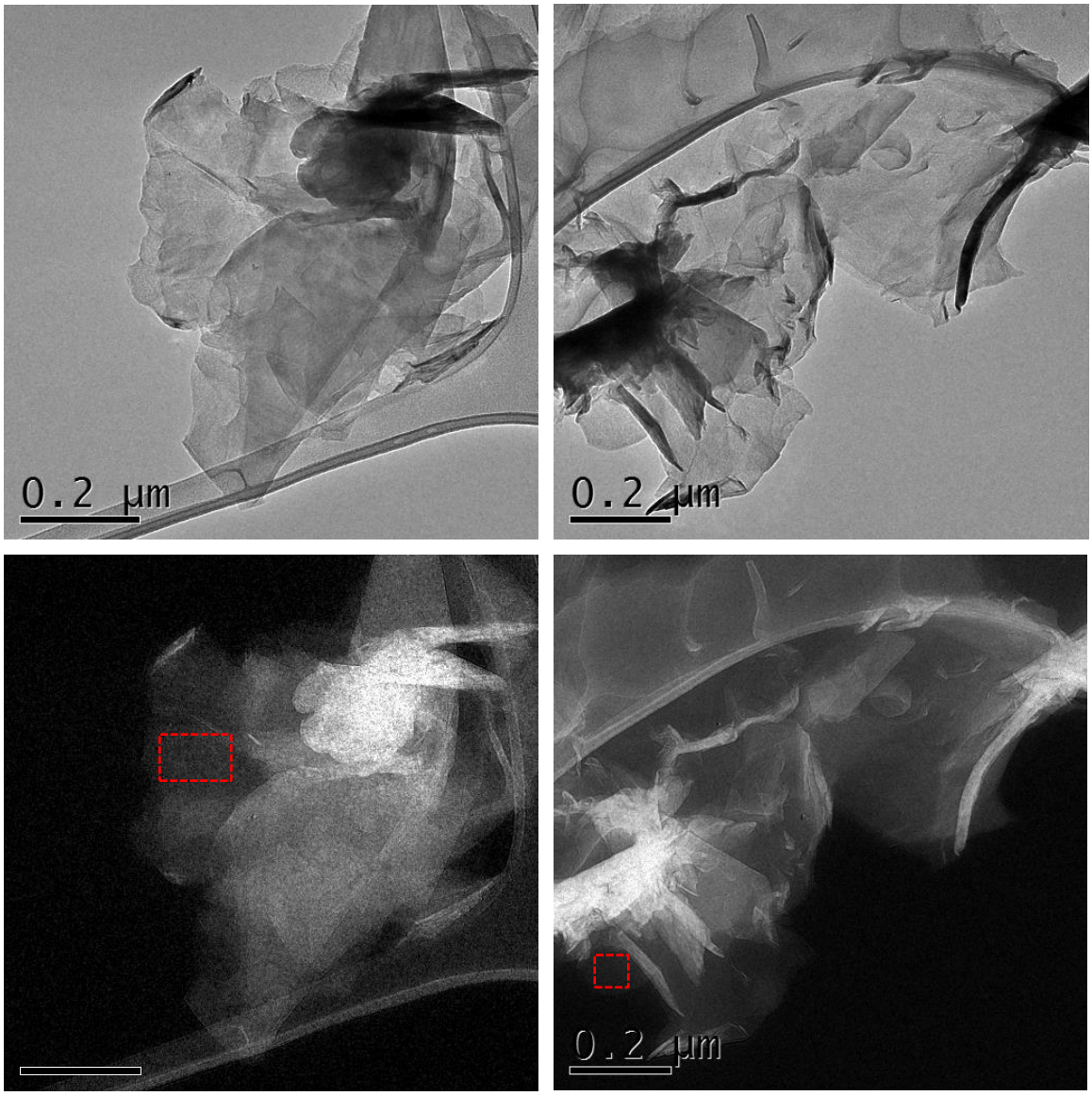

Figure 99: BF images (top) and EFTEM thickness maps (bottom) for stacked and crumpled sheets of purified carbon material grown over the undoped cobalt carbonate based catalysts. The red boxes on the EFTEM maps indicate the regions from which the thickness calculations were performed.

High energy (>50 eV) EELS was used to examine the energy of core shell electrons in the sheets, and hence gain information on the binding environment (figure 100). The presence of a sharp peak at ~286 eV, corresponding to the 1s → π* transition (and therefore to sp^2 carbon) confirmed the graphitised nature of the sample.[310] The peak at ~291 eV corresponding to the 1s → σ* transition was also expected for graphitic material, as discussed in section 2.1.3.

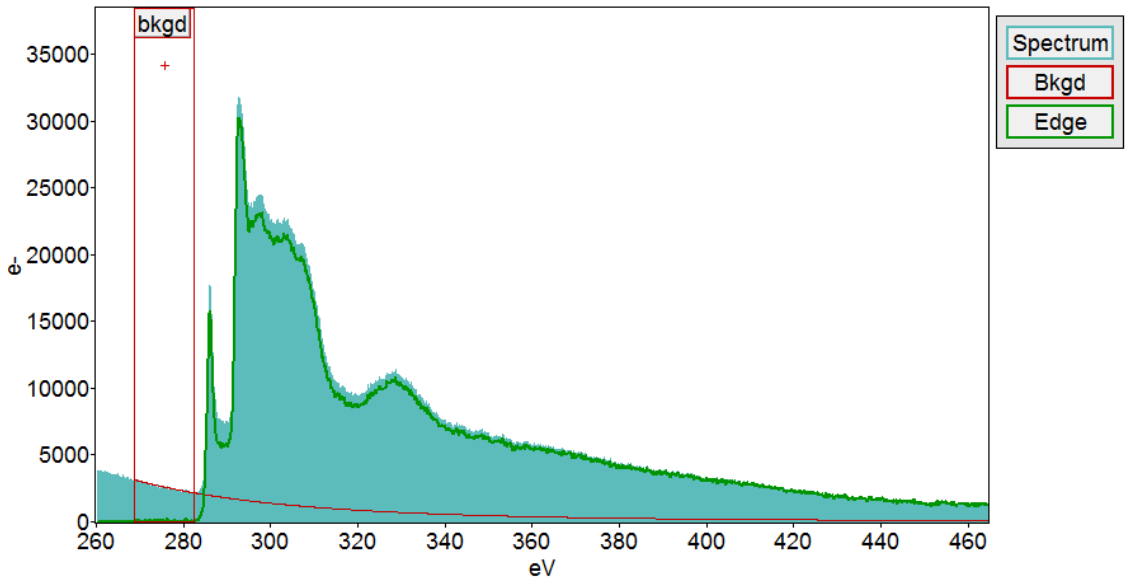

Figure 100: EELS spectrum of purified carbon material grown over the undoped cobalt carbonate based catalysts.

The Raman spectrum (figure 101) of the carbon product revealed bands at ~1350 cm^{-1}, ~1580 cm^{-1} and ~2685 cm^{-1}, which can be assigned to the D, G and 2D bands of graphitic material.[351] The presence of the D band indicated the existence of defects within the graphitic sheets, and the average I_D/I_G ratio across 3 regions of 0.37 ± 0.02 suggested that the average distance between these defects was ~20 nm.[354] The 2D band appeared as a single, symmetrical, but relatively broad peak (2650 - 2800 cm^{-1}), which supported the suggestion that the carbon material produced in these experiments had a turbostratic graphite-like structure.[351] The appearance of the Raman spectrum suggested a more disordered system than would be expected for pristine graphene (see section 2.4), however based on the apparent I_D/I_G the material is comparable to,[478] or less defective than,[282, 283, 481] a number of other graphene products reported in the literature that have been made via bulk-scale, 'bottom-up' synthesis methods, particularly as in a number of these cases the D band is more intense than the G peak.[9,10]

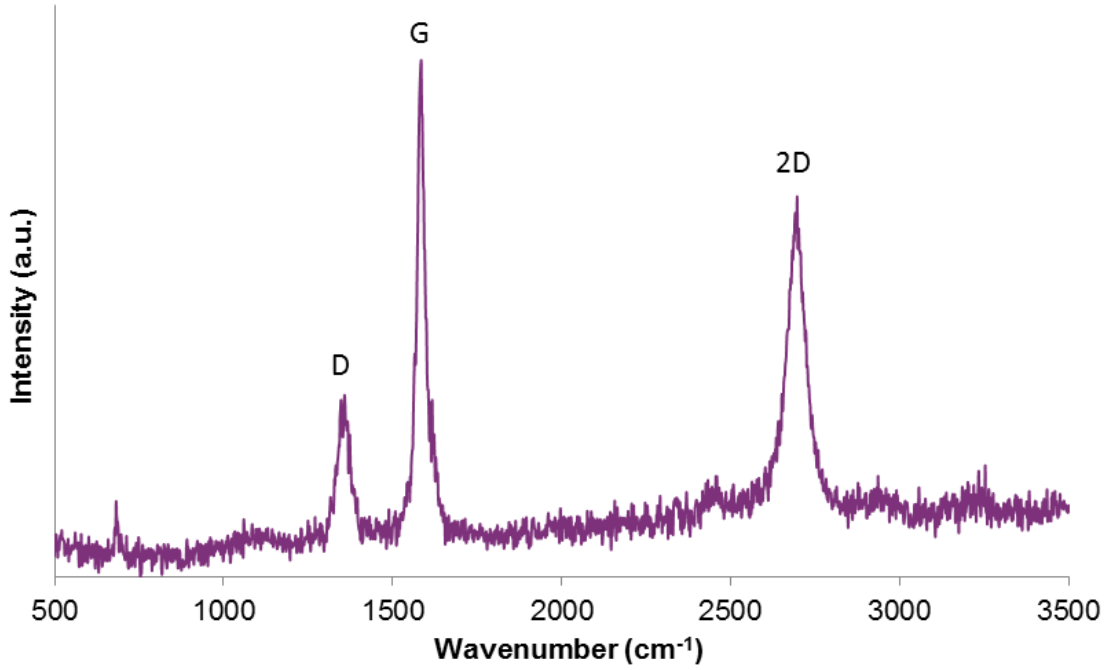

Figure 101: Raman spectrum of purified carbon material grown over the undoped cobalt carbonate based catalysts.

The FTIR spectrum of the purified carbon material (figure 102) revealed a relatively featureless transmittance lineshape, with no evidence of oxygen containing groups such as carboxylic acids (1630 – 1730 cm^{-1}), phenyl hydroxyl groups (~1100 cm^{-1}) and epoxides (~930 cm^{-1}.) The absence of these vibrational bands suggested that no oxygenation of the carbon sheet occurred during synthesis or purification. It also indicated that the defects observed via Raman were not due to oxygen functionalities, and were instead likely to be caused by scattering events such as grain boundaries, sheet-edges and in-plane defects (e.g. bond-angle and bond-length disorder).[351, 353]

The TGA profile of the carbon material showed a weight loss of less than 1 wt. % for temperatures below 500 °C suggesting that the product was free from water (figure 103). The residual at end of profile was below 2 wt. %, suggesting that dissolving the catalyst in HCl at room temperature is a suitable method of purification. The onset of burn for the material was 570 °C, which is higher than previously reported for graphene formed by exfoliation of graphite (500 °C),[115] suggesting that the material was well graphitised. The thermal onset was lower than that expected for graphite which could be as a result of the reduced interlayer interactions for graphene compared with graphite.[115, 386]

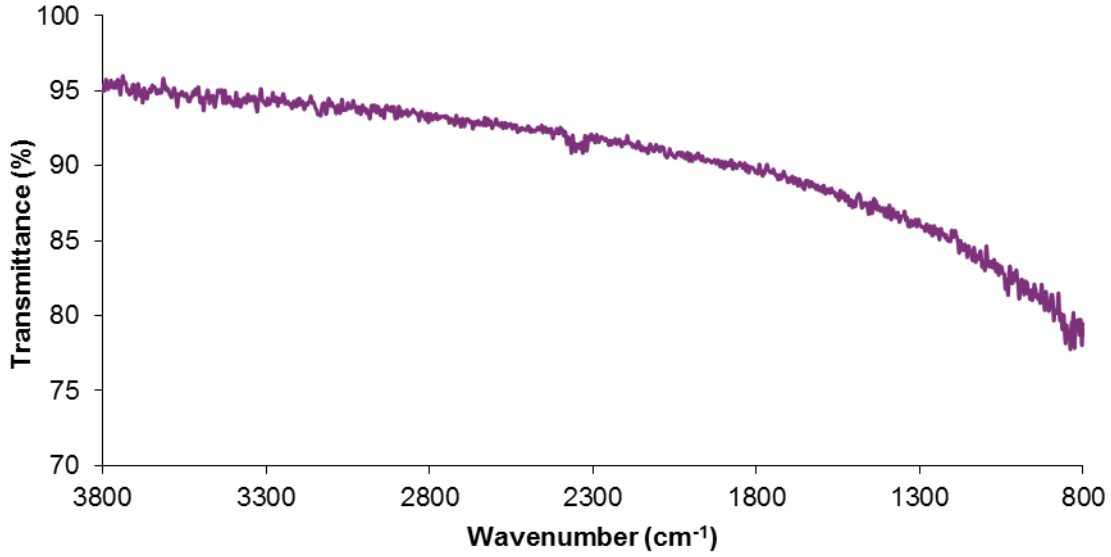

Figure 102: FTIR spectrum of purified carbon material grown over the undoped cobalt carbonate based catalysts.

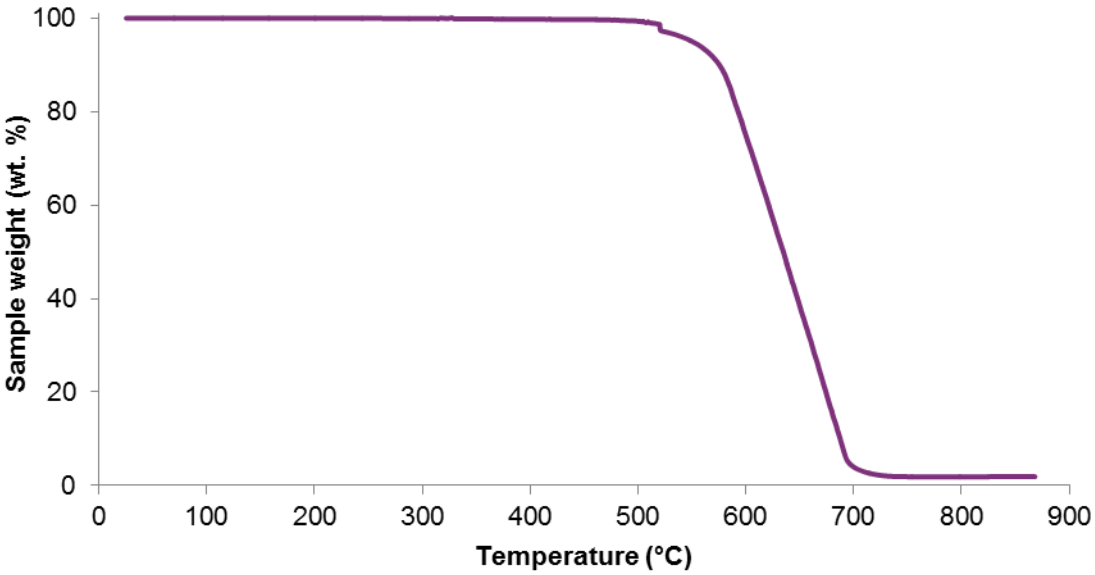

Figure 103: TGA spectrum of purified carbon material grown over the undoped cobalt carbonate based catalysts heated in air at a ramp rate of 10 °C/min.

XRPD of the purified carbon material was carried out on Al (111) plates for the range 2θ = 5 - 45° (figure 104). The Al (111) peak at 2θ = 38.5° was used to correct for shifting across the carbon samples. The (110) lattice spacing was calculated as 2.12 Å from the peak at 2θ = 42.7°, and was consistent with the SAED data. The (110) spacing was not observed as it lies outside the range of measured 2θ values (at 2θ ≈ 77°). The peak at 2θ ≈ 26.5° corresponds to the (002) interlayer distance, and has

a calculated value of 3.36 ± 0.02 Å, which is consistent with the expected value for graphite and with the SAED data presented above.

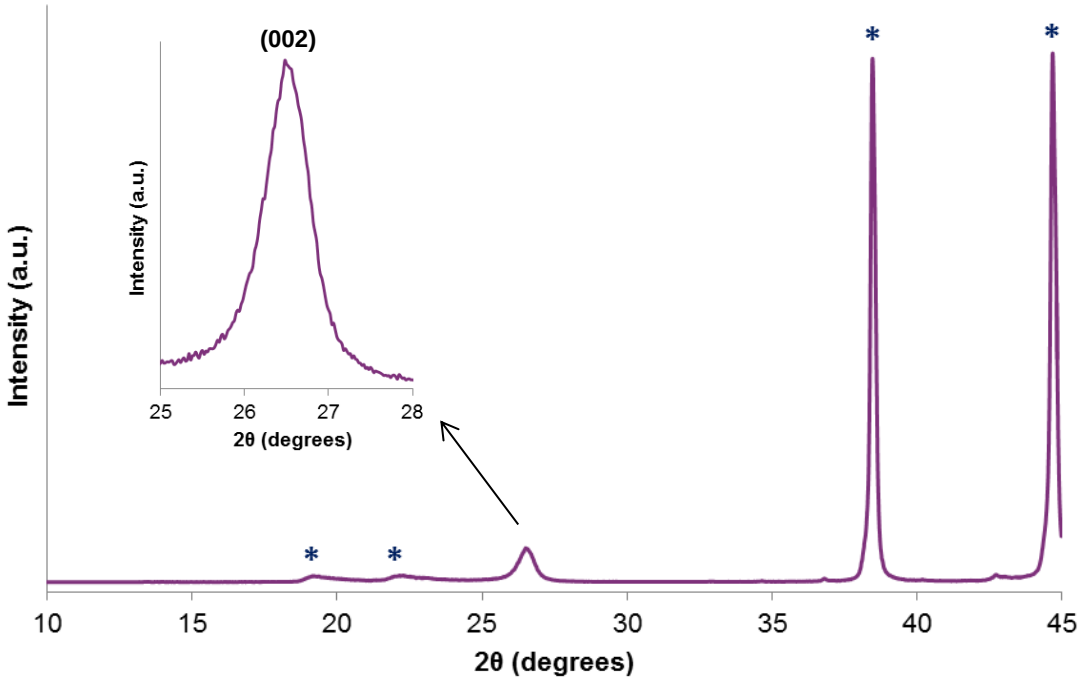

Figure 104: XRD spectrum of purified carbon product on an Al plate, with a magnified view of the graphitic (002) peak (inset). The peaks relating to the underlying Al plate are indicated by dark blue asterisks. Radiation source: Cu $K_{\alpha 1,2}$ = 1.54 Å.

In 2011, during the course of the current research, Jana *et al.* demonstrated that graphene sheets and hydrogen gas could be produced by the decomposition of methane over cobalt based catalysts at 1000 °C and atmospheric pressure.[464] In this study cobalt oxide (Co_3O_4) was produced by 4 h calcination in air of cobalt species produced by three different methods: precipitation with urea in aqueous medium, precipitation with sodium carbonate in ethylene glycol, and thermal decomposition of cobalt nitrate. All catalysts were found to be pure cubic crystalline Co_3O_4 via XRPD but the BET surface area and crystallite size were variable. The carbon products synthesised on the different catalysts varied, indicating that the physical characteristics of the catalysts were important to the resultant carbon morphology. The catalyst with the largest surface area (and smallest particle size) was found to be the optimal catalyst; forming electron transparent thin sheets throughout the sample, while a mixture of thin sheets, graphite deposits and metallic cobalt particles encapsulated with graphitic layers were observed for another of the catalysts. The TEM images reported

for the optimal catalyst closely resemble those synthesised in the current work; showing crumpled/agglomerated sheets with isolated thin regions (figure 105). Consistent with the current work, the material was determined to be crystalline based on the spots in the electron diffraction pattern and the presence of a distinguishable (002) graphitic peak in the XRPD. The Raman spectra for carbon grown on the different catalysts varied in terms of the apparent D/G ratio; with one ratio appearing higher and one lower than the value reported in the current study. The reported number of stacked sheets based on AFM height profile measurements was 6 – 28, which is comparable to the sheet thickness observed in the current study. Based on the available data, a similar quality of material was produced in both studies. This is encouraging as in the current study there was no calcination step of the catalyst before the reaction (compared with 4 h calcination in air), a lower temperature was used (800 °C compared with 1000 °C), and an alternative carbon feedstock was used; which is low cost and easy to handle. In addition the current study demonstrates formation of graphene sheets on a scale over 25 times larger than that reported by Jana *et al.*

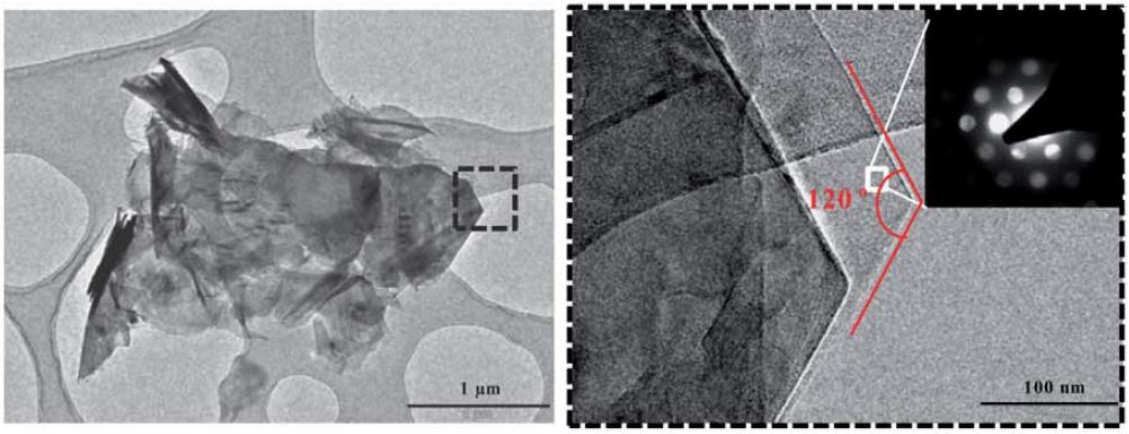

Figure 105: Carbon deposit formed on optimal catalyst after the methane decomposition reaction performed by Jana et al. (left) and HRTEM with inset electron diffraction pattern of highlighted region (right).[464]

5.4 Effect of doping cobalt carbonate

The quantitative inhibiting effect of group I-III cations on the growth of carbon nanotubes was reported in 2008.[467] In this study CNTs were formed from CH_4/H_2 via CVD over iron oxide nanoparticles supported on MgO doped with various quantities of additives. The addition of NaCl was found to have a non-linear impact on the mass of carbon formed, with a general trend of decreasing carbon mass with increasing NaCl. As the trend in I_D/I_G from the Raman spectra of the carbon products was found to be independent of the percentage NaCl added, the authors inferred that the NaCl inhibited

carbon growth in a non-selective manner rather than preferentially inhibiting either amorphous carbon or graphitic CNT growth. Sodium chloride has also been shown to limit the growth of carbon on cobalt nanoparticles.[482] Here, carbon encapsulated cobalt rather than CNTs were formed on cobalt nanoparticles on NaCl substrates under the same conditions as CNTs were formed using alternative substrates. Given the evidence of these studies, the effect of sodium doping was investigated as a potential means of controlling the growth of the carbon in the current system to favour thin sheet formation. For the study of CNTs on cobalt nanoparticles the inhibiting effects of NaCl were found to be greater than those of NaF, which is attributed to the closer proximity of the reaction temperature (600 °C) to the melting point of NaCl (800 °C) than to the melting point of NaF (996 °C).[482] It was postulated that the relatively high diffusion coefficient and thermal conductivity of the NaCl phase might strongly interfere with the build-up of the temperature gradient inside the cobalt particles, a factor which has been shown to be important in the growth of carbon filaments.[483] The reaction temperature for the current study (800 °C) was too high to use with NaCl and hence NaF was chosen as the sodium-based dopant.

The weights of the as-synthesised and purified products from the CVD of ethanol over doped cobalt carbonate catalysts showed that the unpurified yields and the purified yields followed the same trend, where the masses obtained had a non-linear relationship with the weight percentage of sodium (figure 106). The XRPD data of the unpurified products (figure 93 and appendix C) showed that the only crystalline form of cobalt present at the end of the reaction was cobalt metal. In agreement with this finding, the calculated mass of carbon based on subtracting the mass of NaF and the mass of cobalt metal from the unpurified mass, is approximately equal to the actual mass of carbon obtained after purification (table 23). On average the purified mass was 6 % higher than expected based on the calculation, which is likely to be a due to a combination of small inorganic residuals in the purified product and low levels of Co and NaF evaporation during the course of the reaction.

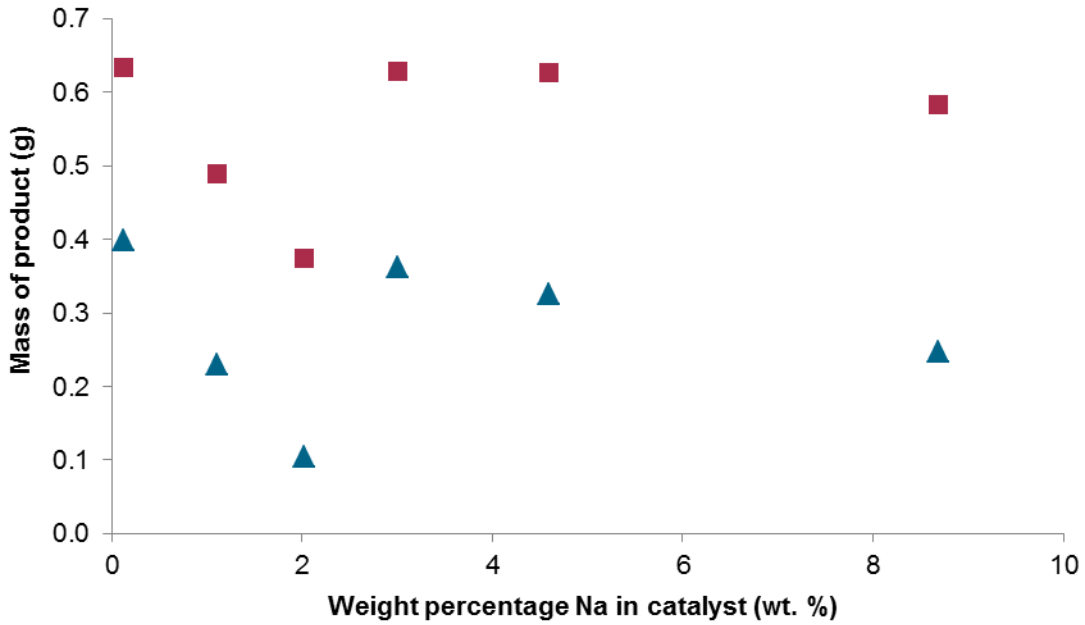

Figure 106: Plot of the relationship between the weight percentage sodium in the catalyst and the unpurified (red squares) and purified (blue triangles) yields of the CVD reaction.

Table 23: Unpurified and purified yields of material from catalysts doped with various amounts of NaF. The yield calculation is based on the mass of unpurified catalyst at the end of the reaction minus the mass of NaF and Co present at the start of the reaction.

Sodium in catalyst (wt. %)	Unpurified yield (g)	Mass of cobalt in boat (g)	Mass of NaF in boat (g)	Calculated yield of carbon (g)	Actual yield of carbon (g)
0.12	0.634	0.268	0.000	0.366	0.398
1.11	0.489	0.266	0.010	0.212	0.230
2.02	0.375	0.258	0.019	0.097	0.104
3.00	0.628	0.265	0.029	0.334	0.362
4.59	0.626	0.256	0.046	0.324	0.325
8.69	0.583	0.256	0.096	0.231	0.247

In the present study the carbon yields and surface areas appeared to follow a similar trend but were not exactly correlated (figure 107). The surface areas of the 1.11 Na wt. % and 2.02 Na wt. % cobalt carbonate were significantly higher than the other weight percentages in this study, while the amounts of carbon produced for these catalysts were significantly lower. Note that this trend is counter to what would normally be expected for a catalytic system, where larger surface areas usually results in

increased activity. This may signify an increase in side-reactions for higher surface area catalysts, or it may be that the increased surface area correlates with a change in the doped cobalt carbonate that itself leads to a lower carbon yield. Alternatively, it could be that the presence of sodium has an impact on the reaction that is dependent on the surface area, hence the correlation between yield and surface area is masking the correlation between yield and sodium content.

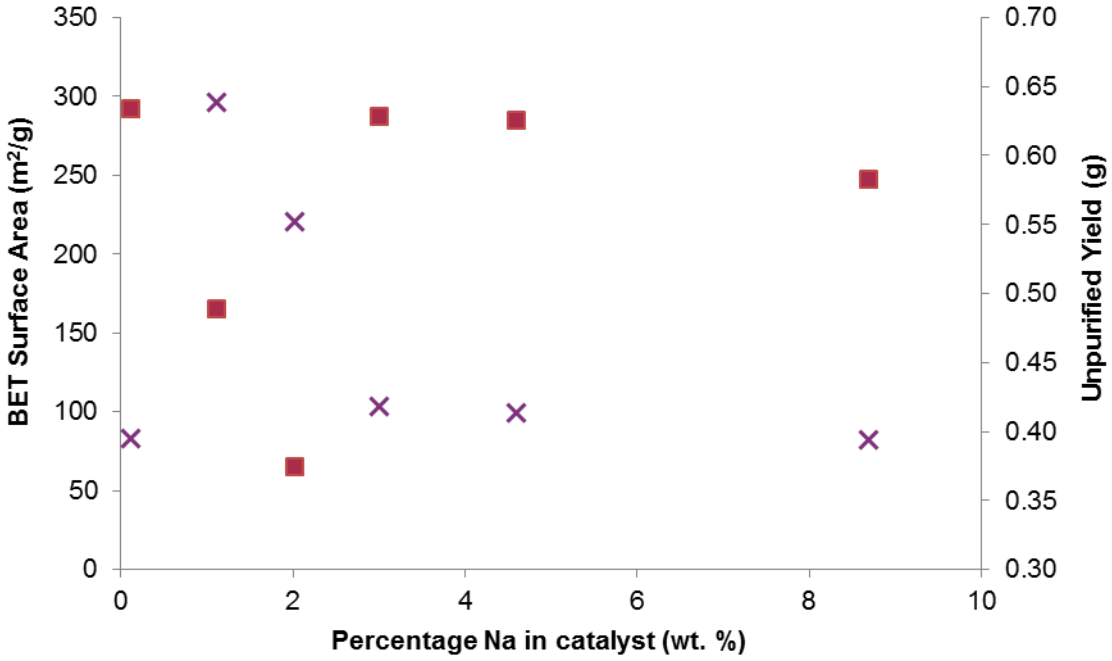

Figure 107: Plot to show the relationship between BET surface area (purple crosses), unpurified yield (red squares) and weight percentage of sodium in catalyst, showing a general inverse relationship between BET surface area and unpurified yield.

The effect of low levels of sodium doping of Co_3O_4 precursors on the catalytic activity of cobalt oxide have been reported for NO and N_2O decomposition reactions.[484-486] In all these cases the Co_3O_4 was formed using a similar method to the one used in this study, involving the precipitation of solid from a solution of cobalt nitrate and sodium carbonate/bicarbonate, but with an additional step of calcination at 400 °C to obtain the Co_3O_4 product. Interestingly, similar patterns were observed for the effect of low sodium dopings on the catalysts as were seen in the present study (figure 108).

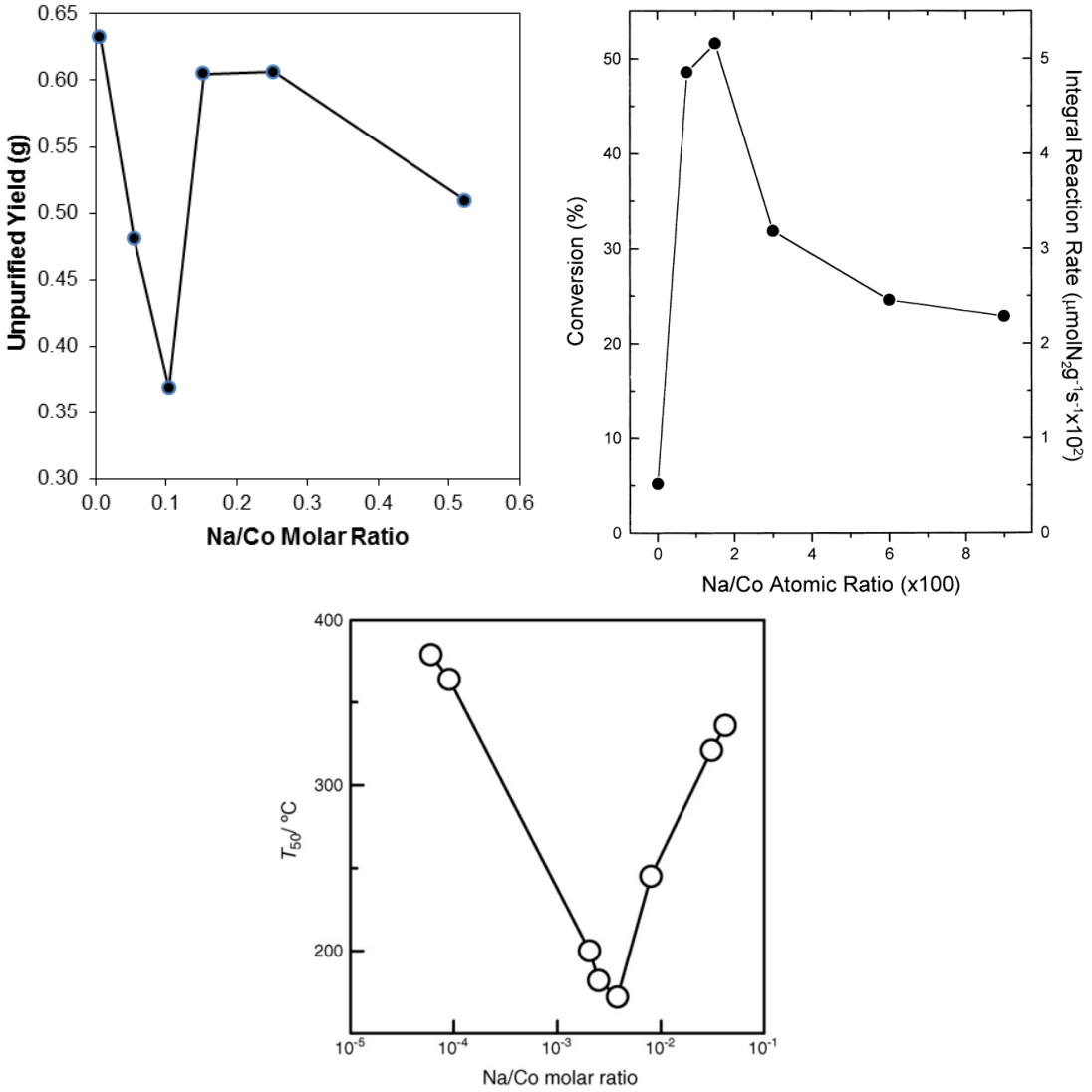

Figure 108: Unpurified carbon yield as a function of Na/Co ratio for the present study (top left), NO decomposition as a function of Na/Co ratio (top right),[485] and temperature of 50% N_2O conversion as a function of Na/Co ratio (bottom).[484]

The trend in the N_2O decomposition as a function of Na/Co ratio is explained in terms of the relative sodium content in the bulk and at the surface of Co_3O_4 particles.[484] The authors suggest that sodium ions in the bulk affect the electronic structure of the Co_3O_4 leading to an enhancement in catalyst activity, but that sodium ions on the surface deactivate the catalyst; thus the rate of catalysis is based on the balance between these two opposing processes (resulting in a non-linear relationship.) At low sodium concentrations diffusion into the bulk is more likely to occur, whereas at higher dopings, when the bulk is saturated, more sodium is likely to remain on, or segregate to, the surface. Blocking of catalytic sites at the surface could account for the reduced carbon yields observed for larger surface area samples in the current data set.

The trend in the NO decomposition as a function of Na/Co ratio is explained in terms of the presence of different amounts of sodium impeding the sintering of the Co_3O_4 catalysts to different extents.[485, 486] While one study found that in addition to affecting the surface area, the presence of sodium also had a direct impact on the catalyst (by facilitating the formation of Co^{2+}),[485] the other reported that the trend in catalyst activity followed the surface area trend more closely,[486] although the authors state that in addition to affecting the surface area, the sodium also affected the specific activity per surface area; possibly as a result of the creation of catalytically active sites on the surface of the Co_3O_4 by interaction with sodium. These results highlight the interesting relationship between sodium doping, surface area, and catalytic ability in other cobalt based systems, and suggest that further work into the effect of sodium doping could yield interesting outcomes.

In order to gain further insight into the work and to test the reproducibility of the system, repeat experiments were performed. The same procedure was followed for the initial synthesis of the cobalt carbonate, but grinding of the carbonate with NaF was performed in a glove box rather than open air for the later batches. Consistent with the initial batch, the later batches showed a similar trend between the carbon yields and surface areas for the doped cobalt carbonate (figure 109). The relationship is seen most clearly at the extremes, where the highest carbon yields were measured for catalysts with the lowest BET surface areas.

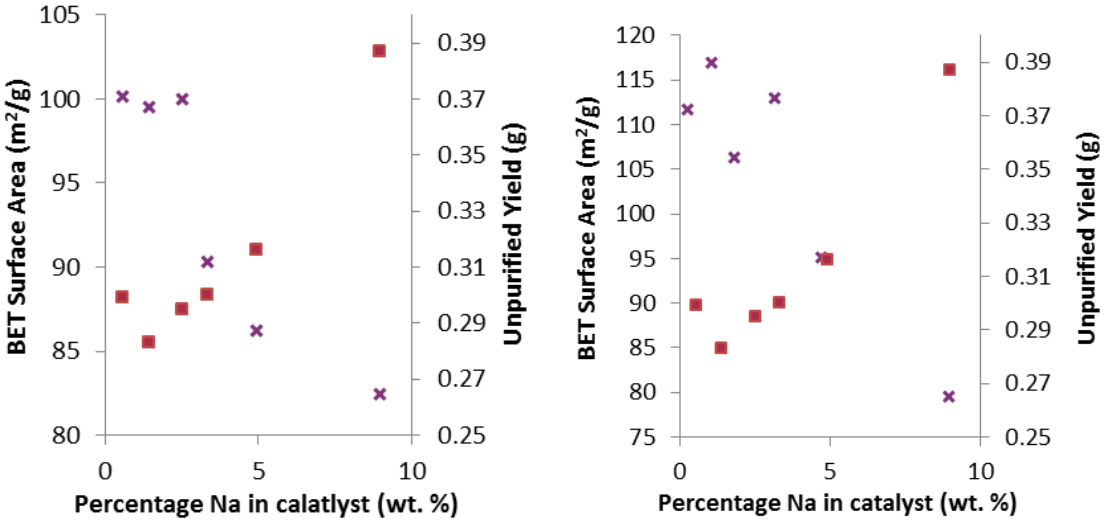

Figure 109: Plots to show the relationship between BET surface area (purple crosses), unpurified yield (red squares) and weight percentage of sodium in catalyst for the second (left) and third (right) batches of doped catalysts.

Comparison of the results from later batches with the initial batch revealed that both the variation in the BET surface areas of the catalysts and the variation in the unpurified yields were lower for the second two batches than for the first (table 29). The unpurified yield obtained per surface area of catalysts is consistent for the second two batches, and consistent within errors for the first batch. This suggests that the activity of the catalyst is relatively independent of the batch of cobalt carbonate used. The combined results of the batches support the assertion that the surface area of the catalyst has a clear impact on the activity of the catalyst and that the presence of NaF does not affect the mass of carbon formed on a given surface area of catalyst.

Table 24: A summary of the yield and surface area results for three different batches of doped cobalt carbonate.

Batch No.	Unpurified yield (g)	BET (m^2/g)	Unpurified yield/BET (g^2/m^2)
1	0.50 ± 0.13	190 ± 100	0.005 ± 0.003
2	0.34 ± 0.05	90 ± 10	0.004 ± 0.001
3	0.41 ± 0.05	100 ± 20	0.004 ± 0.001

The effect of NaF doping on the morphology and crystallinity of the carbon product was investigated using a number of different techniques. Electron microscopy revealed that the morphology of the material produced using doped catalyst was the same as that produced using the undoped catalysts (figure 110), as thin, sheet-like carbon was observed in all cases.

The crystallinity of the carbon products was investigated using XRD and Raman. Theoretical work by Fujimoto showed that the graphitic 002 diffraction peak broadens and shifts to lower angles as the crystallite size decreases.[487] This has also been observed experimentally when analysing ball milled nanocrystalline graphite.[488] The fact that the (002) peaks for the carbon formed on the doped cobalt carbonate were all at approximately the same 2θ values (see appendix C) and of similar width (table 25), with no trend in either values, supports the conclusion that sodium doping does not affect the crystallinity of the carbon products. Similarly there is no trend in the D/G ratios calculated from the Raman spectra (table 25), which acts as further evidence that doping the catalyst with NaF does not affect the crystallinity of the carbon products.

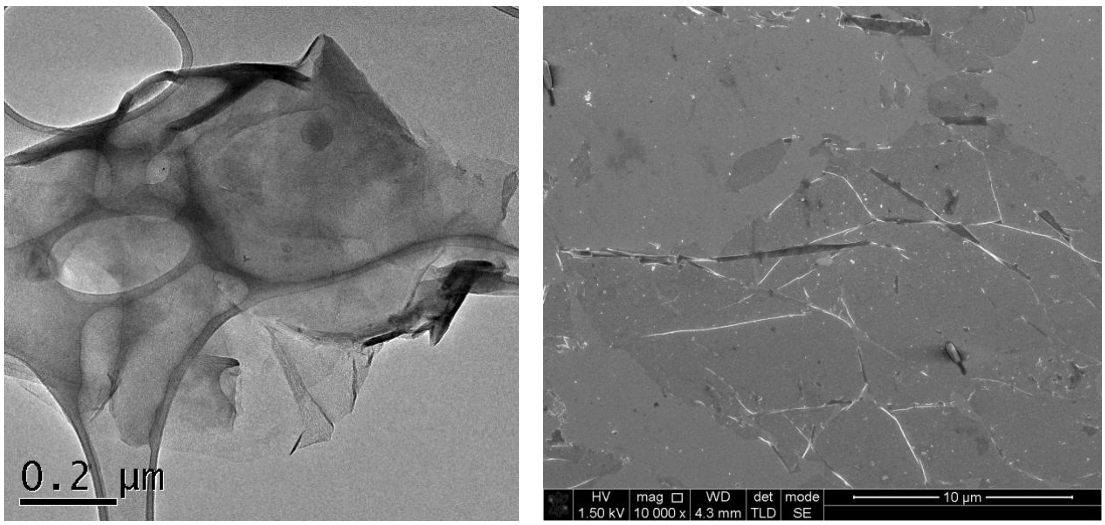

Figure 110: Bright field TEM image of carbon product from catalyst with 5 wt. % Na (left) and SEM image of carbon product from catalyst with 9 wt. % Na (right), showing that the morphology of the carbon product is unaffected by the presence of sodium.

Table 25: Raman and XRD results for the carbon products of various batches of NaF doped cobalt carbonate.

	Raman I_D/I_G			**FWHM of (002) peak in XRD**	
Approximate Na in catalyst (wt. %)	**Batch 1**	**Batch 2**	**Batch 3**	**Batch 1**	**Batch 2**
0	0.4	0.4	0.4	0.66	0.34
1	0.4	0.4	0.4	0.62	0.42
2	0.6	0.5	0.4	0.76	0.44
3	0.6	0.4	0.4	0.62	0.46
5	0.8	0.6	0.4	0.62	0.38
9	0.6	0.6	0.4	0.60	0.42

The thermal stability of the different carbon products grown over doped catalysts was investigated via TGA. The line profiles for the products were similar for all samples (see figure 111 and appendix C), with no observable trend between the onsets of burn (~590 °C) and the amount of NaF present, as evidenced by the fact that the burn profiles of the carbon from the ~1 and ~9 wt. % Na catalysts almost exactly overlap, whereas the profile for ~3 wt. % Na is offset. The appearance of the TGA profile can vary depending on the surface area and weight of the sample, so small variations in lineshapes should not be considered significant.

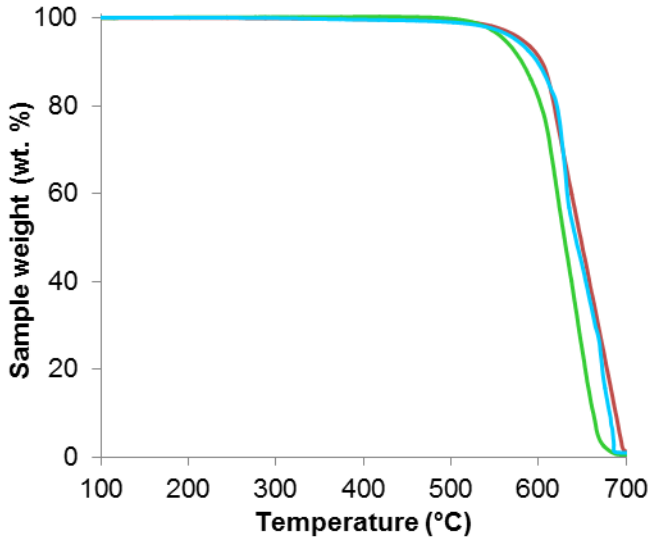

Na in catalyst (wt. %)	TGA Onset (°C)
0.12	570
1.11	600
2.02	610
3.00	590
4.59	570
8.69	610

Figure 111: TGA profile of purified carbon products of 1 wt. % Na (red), 3 wt. % Na (green) and 9 wt.% Na (blue) cobalt carbonate catalysts (left) and table to show the calculated onsets of burn for the entire set of carbon products produced from batch one of the NaF doped catalysts (right). Samples were heated in air at a ramp rate of 10 °C/min.

5.5 Conclusions and future work

Cobalt carbonate and sodium doped cobalt carbonate were successfully used to catalyse the high temperature conversion of ethanol to solid carbon. The morphology of the carbon products was large, thin, graphitic sheets, which appear to be turbostratic in nature; with graphene layers in the sheets rotated and translated relative to one another. The products had good thermal stability (~590 °C) and, based on FTIR data, seemed to be free of oxygen containing groups. The synthesis method used was simple and scalable and used a feedstock that is easy to handle and can be sourced from plants (bio ethanol). There was no firm evidence to show that the presence of sodium had an impact on the yield or the morphology of the carbon product, although the results do not preclude that the sodium had a surface area based effect on catalyst, either by blocking available surface catalytic sites or by impacting the sintering of the particles during heating. Regardless of the potential impact of sodium on the surface area of the catalyst, it could be considered positive that the addition of salt did not appear to affect the crystallinity of the product, since this suggests that the current system is relatively robust.

While there is still work to be done regarding investigating the effects of different reaction parameters on the growth of graphene on cobalt carbonate, this work

demonstrates positive steps toward the goal of achieving bulk-scale ‘bottom-up’ growth of graphene platelets. The morphology of the sheets produced in the current study was better than for the majority of other ‘bottom-up’ syntheses of graphene platelets and the yield per g of catalyst is also one of the highest reported to date. Further to this the catalyst preparation is both fast and simple, with no pre-annealing step required. The presence of the D band in the Raman spectrum of the material suggests that further improvement to the method is possible, but as the defect level appears low in comparison with other products of ‘bottom-up’ synthesis, it is clear that this system merits further study.

An interesting next step would be to scale up the reaction to create sufficient material to test in a number of bulk scale applications such as energy storage systems and composite materials. As discussed in section 1.2.2, the precise qualities of graphene required for a particular application will vary, so it is important to have a range of different graphene materials to select from if the potential of graphene to enhance properties of everyday systems is to be realised.

Chapter 6: Graphene synthesis via chemical vapour deposition over transition metal based templates

6.1 Introduction

The main focus for 'bottom-up' synthesis of graphene has been the growth of high quality graphene films for electronic applications, rather than bulk scale graphene sheets. There is also a growing body of work related to the 'bottom-up' synthesis of shape- and edge- controlled graphene nanoribbons;[288] which can be considered a research area in its own right, of interest because the properties of nanoribbons have been found to vary according to their precise morphology.[489, 490] Graphene nanoribbons have been theorised and shown experimentally to have band gaps which are inversely proportional to their width,[491] where ~1 nm wide nanoribbons synthesised from molecular precursors have been shown to have band gaps of 2.3 ± 1 eV.[492] While there is not, to our knowledge, a specific demand for larger, shape-controlled graphene in terms of property tuning, it is obvious that maximum control over any synthesis method is desirable in terms of obtaining a reliable and reproducible product. Achieving a well-defined product is likely to be of particular importance for bulk scale applications of graphene such as composite materials, where different size sheets have been found to have different composite reinforcing effects.[463, 493] It also follows that knowledge gained at a larger scale may help to understand and inform processes at a smaller scale, and hence studying the templated synthesis of graphene platelets may contribute to the successful growth of shape and size controlled graphene nanoribbons. With this in mind, the following chapter contains work that is aimed towards the bulk scale synthesis of graphene with a controlled shape and size using 'bottom-up' methodologies.

There is limited evidence of shape controlled growth of graphene-based materials in the scientific literature (table 26). Relevant studies include graphene growth on metallic wires; which were either pressed against a substrate to yield graphene strips,[494] or etched away to yield collapsed tubes of graphene,[495] and growth of porous graphene on different oxide based catalysts.[496, 497] Of particular interest is the growth of well-defined graphene ribbons templated on ZnS ribbons 0.5 – 5 μm wide and 10s to 100s of micrometres long (figure 112).[498] The graphene produced using this approach was few-layer and contained a number of defects, as evidenced by presence of the D band in the Raman spectroscopy, although HRTEM did confirm a degree of crystalline

stacking in the ribbons. A more highly graphitised product was achieved for growth of graphene over Ni particles,[499] where graphene was formed as a crumpled layer over the Ni nanoparticles (figure 113). The templating effect was less controlled in this case, as graphene sheets were observed to bridge gaps of hundreds of nanometres between particles rather than being confined to the discrete size and shape of the nickel particles. The ideal template would combine the shape control of ZnS template with the high graphitisation levels of Ni template.

Table 26: A summary of shape controlled graphene-based materials in scientific publications

Template	Carbon Source	Temp (°C)	Size/shape control	Comments	Ref
Cu wires (50 μm diameter)	CH_4	1000	Yes	Well graphitised based on Raman (I_D/I_G<<1)	494
Ni nanowires (70 nm diameter)	C_2H_4	750	Yes	Well graphitised based on Raman (I_D/I_G<<1)	495
ZnO nanowires	C_2H_2	780	Yes	High defect levels based on Raman (I_D/I_G>1)	496
Porous MgO	CH_4	900	Yes	Very high defect levels based on Raman (I_D/I_G>>1)	497
ZnS ribbons	CH_4	750	Yes	Some defects based on Raman (I_D/I_G<1)	498
Ni particles (<30 μm)	CH_4	1000	Partial	Well graphitised based on Raman (I_D/I_G<<1)	499

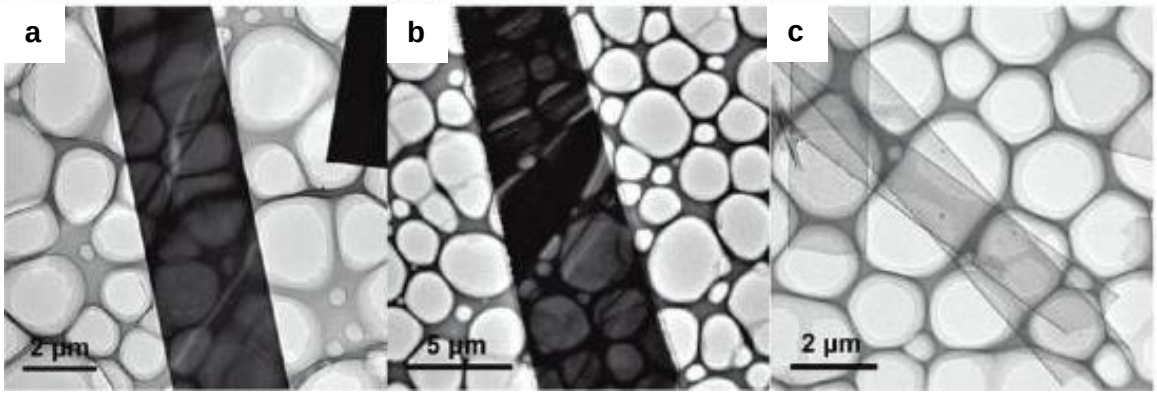

Figure 112: TEM images of a ZnS ribbon before (a) and after (b) carbon growth, and the carbon ribbons produced by etching away of the ZnS templates (c). Adapted from reference 498.

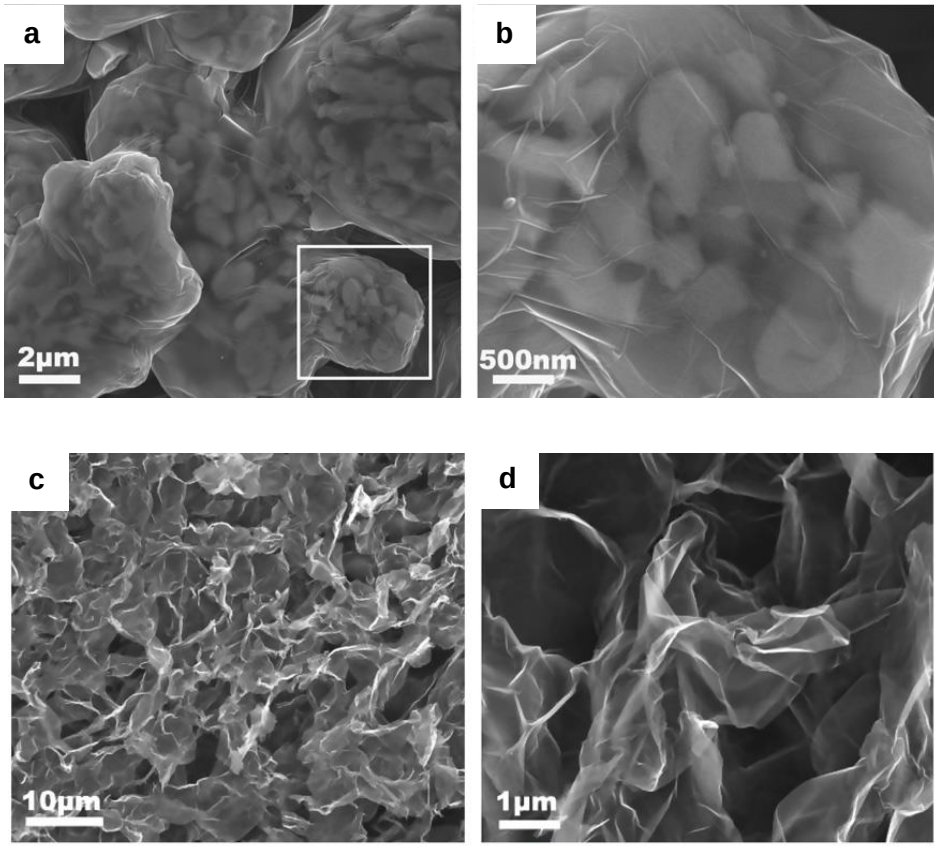

Figure 113: SEM images of Ni particles coated with carbon (a, b) and carbon material remaining after etching of Ni (c, d), showing a crumpled array of graphene sheets. Adapted from reference 499.

The first step in designing a new system for the bottom-up, templated growth of graphene is to select a suitable template. Given the proven ability of transition metal foils to catalyse highly crystalline graphene, it was decided that the initial focus should be on transition metal-based templates. The shape and facet controlled growth of metal nanocrystals is a complex field in its own right, and is an active area of research due to the wide range of potential applications for these highly-tuneable structures.[500, 501] In view of this, a suitable metal template was selected from the literature rather than a novel system being devised. In order to achieve large graphene sheets, metal-based microcrystals rather than nanocrystals are desirable, with a preference towards single crystal systems. Copper is one of most commonly studied metal substrates for growth of CVD graphene films as it is low cost and readily available. Furthermore, growth of graphene over copper has been shown to be self-limiting to mono-layer graphene under certain conditions (due to growth via a surface catalysed mechanism),[240] which is a desirable feature for graphene synthesis as thickness control over other metals (e.g. Ni) has been shown to be affected by a range of different factors, and hence is difficult to achieve.[213] Copper is also of particular interest as graphene has been shown to grow

over grain boundaries in copper films, resulting in higher quality material.[240, 256, 502] If graphene can grow over grain boundaries the importance of using single-crystalline templates becomes reduced, and hence there would be additional scope to utilise templates that could be cheaper, more easily prepared, and larger than their single crystal counterparts. A summary of the desirable features for graphene templates and brief justifications for the importance of these features is given below (table 27).

Table 27: A summary of desirable features for graphene templates

Template feature	Importance of feature
Effective catalyst	Required to promote breakdown of feedstock and form a well graphitised product
Narrow lateral size and thickness distribution	Required to obtain a well-defined product in terms of lateral size and number of graphitic layers
Flat surfaces	Ridges in the template surface may cause defects in the as-grown graphene
High surface area to volume ratio	Required to maximise the yield per gram of catalyst
Thermally stable	Template must maintain its morphology at the growth temperature to yield a controlled product
Cheap/easy to make	Template is etched to release graphene so the template must be cheap to render the process cost effective

The reaction conditions for CVD of carbon feedstocks over metal foils have been found to significantly impact the film thickness and crystallinity of the resulting graphene films, so it follows that selecting the correct growth conditions for bottom-up, templated growth poses a major challenge for this technique. The effect of temperature in particular is likely to have a strong influence on the metal nano/microcrystals due to large surface area-to-volume ratios of small crystals leading to melting point depression/lower thermal stability than for metal foils.[503, 504] The sensitivity of iron oxide nanoparticles to growth temperature has already been mentioned; where different morphologies of carbon were produced under different reaction conditions.[478, 479] In the following chapter both methane and ethanol were considered as carbon feedstocks in order to achieve a wider range of growth temperatures than would be feasible using only methane; the most common carbon feedstock for CVD of graphene. Ethanol has been used to produce graphitic carbon via CVD at temperatures as low as 600 °C,[472] although the quality of graphene produced via CVD of ethanol over copper has been

found to increase with increasing temperature, up to 850 °C.[477] While higher temperatures are known to result in better graphitisation,[505] the negative effect of temperature on the templates could negate this effect, so the selection of reaction conditions needs to be a balance of these factors.

6.2 Copper (I) oxide templates

6.2.1 Characterisation of copper (I) oxide templates

Copper (I) oxide has shown promise for a number of different applications such as catalysts, gas sensors, energy conservation and magnetic storage,[506] and as such its controlled growth has been previously studied. The copper (I) oxide templates used in the current work were prepared using the method of Sun *et al.*[507] The authors described the work as template-free synthesis of well-defined truncated-edge polyhedral Cu_2O architectures, where the basic procedure involved adding sodium hydroxide and D-glucose to an aqueous solution of cupric acetate held at different temperatures (25 – 98 °C). The proposed reactions that govern this synthesis method are provided in scheme 1, and show the use of sodium hydroxide as a coordination agent and the use of D-glucose as a mild reducing agent. CH_3COO^- does not feature in these reactions but is believed to play a key role in the morphology evolution of the polyhedra via promoting preferential growth and/or etching to particular faces.

$$Cu^{2+}(aq) + 2OH^-(aq) \rightarrow Cu(OH)_2(s)$$

$$Cu(OH)_2(s) + 2OH^-(aq) \rightarrow [Cu(OH)_4]^{2-}(aq)$$

$$2[Cu(OH_4)]^{2-}(aq) + C_5H_{11}O_5\text{-}CHO(aq) \rightarrow Cu_2O(s) + C_5H_{11}O_5\text{-}COOH(aq) + 4OH^-(aq) + 2H_2O(l)$$

Scheme 1: Proposed chemical equations involved in the synthesis of Cu_2O truncated polyhedra, with the Cu_2O product highlighted in red.[507]

Eight different truncated polyhedra were described in the paper, synthesised using the same core method but with variation in the concentration of reagents and the reaction time and/or temperature. For the purposes of creating a template for graphene it was decided that the polyhedra with the lowest amount of truncation, i.e. the largest square faces, would be most suitable, and the reaction conditions were selected accordingly.

In order to analyse the polyhedra, and as a way of supporting the templates during the synthesis reaction, dispersions of the polyhedra in ethanol were spin-coated onto silicon substrates. SEM images of the polyhedra (figure 114) showed that the spin-coating resulted in an uneven coverage of the silicon surface, with some blank regions, some isolated polyhedra, and some aggregated polyhedra. The size of the majority of the as-synthesised Cu_2O polyhedra (~4 μm) and the surface finish was consistent with the original article, although there was a wider size and shape distribution than expected. The polyhedra had slightly roughened surfaces which appeared to be adorned with flecks of material. Flecks of material were also observed on the silicon surface, suggesting that these flecks were loose material rather than features of the polyhedra themselves. It should be noted that a number of the polyhedra had tail-like protrusions, which were not previously reported.

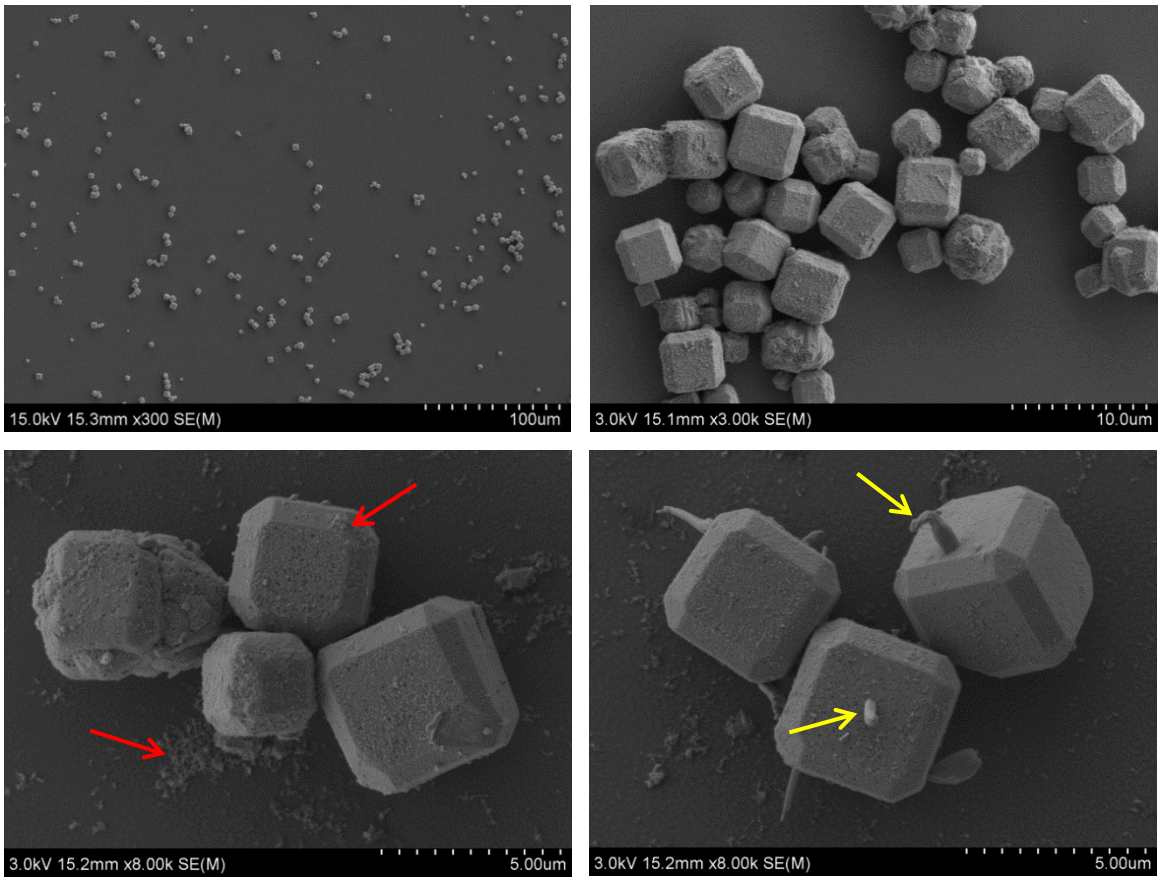

Figure 114: SEM images of the as-synthesised Cu_2O polyhedra, revealing that the majority of the polyhedra are truncated edge cubes with lateral dimensions of around 4 μm. The red arrows point to fleck of material on the Si surface and the polyhedra and the yellow arrows point to 'tail-like' protrusions from the Cu_2O surface.

EDXS analysis collected for the polyhedra in the SEM and the XRPD pattern of the polyhedra (figure 115) confirmed that the polyhedra were made of copper and oxygen, with no detectable impurities. The XRPD pattern confirms that the polyhedra had the standard cubic structure of Cu_2O, with space group $Pn\bar{3}m$ (JCPDS card no. 05-0667), and were free from other crystalline copper impurities such as metallic copper or CuO. The faces of the polyhedra can be indexed to three pairs of (100) facets, four pairs of (111) facets and six pairs of (110) facets (figure 116).[507, 508]

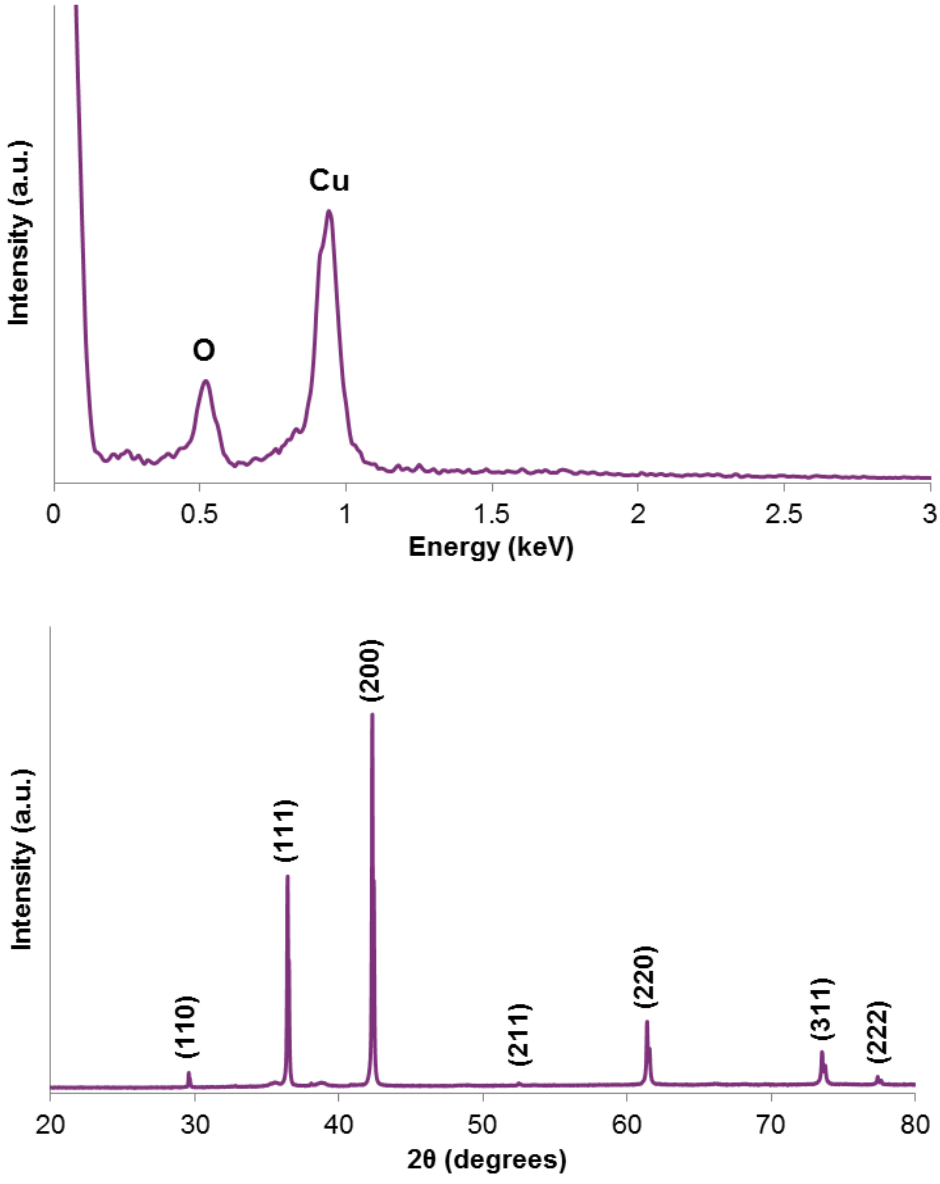

Figure 115: EDXS spectrum (top) and XRPD pattern (bottom) of the Cu_2O polyhedra. For XRPD Cu $K_{\alpha 1,2}$ = 1.54 Å.

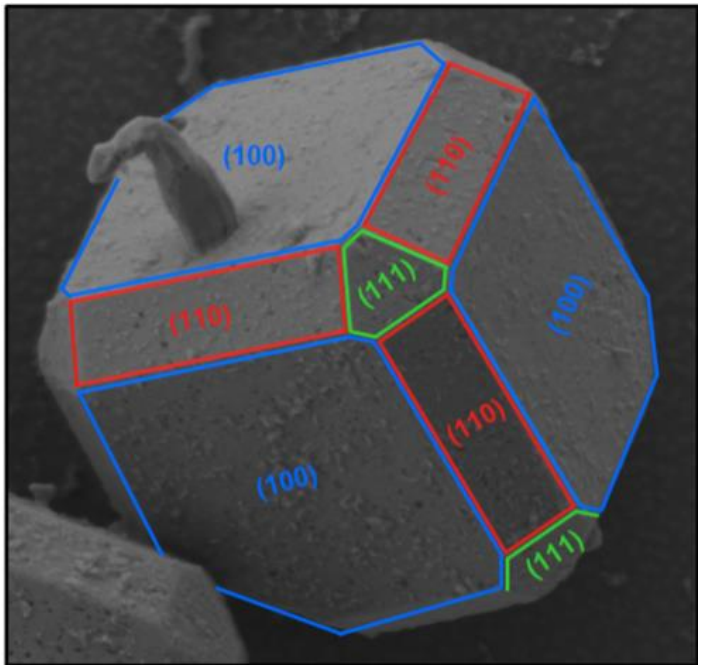

Figure 116: SEM image of a Cu_2O polyhedron with the different crystallographic faces labelled.

To gain an understanding of the how the morphology of the polyhedra changed upon heating in an inert atmosphere, silicon substrates with polyhedra spin coated over the surface were heated to 650°C, 800 °C and 1000 °C, held at temperature for 30 min then allowed to gradually cool to room temperature. SEM images of the polyhedra after heating to 650 °C showed that the polyhedra maintained their overall morphology; appearing as truncated edge polyhedra of the same approximate size, however it can be seen that the polyhedra had a number of square pits and cuboid protrusions that were not evident before heating (figure 117). Furthermore there was no evidence of the tail-like protrusions that were observed before heating. EDXS of the polyhedra confirmed that both the bulk polyhedra and the cuboid protrusions contained copper and oxygen (and a silicon signal due to the underlying substrate), suggesting that the protrusions were not caused by a change in chemical nature of the polyhedra, for example reduction to metallic copper.

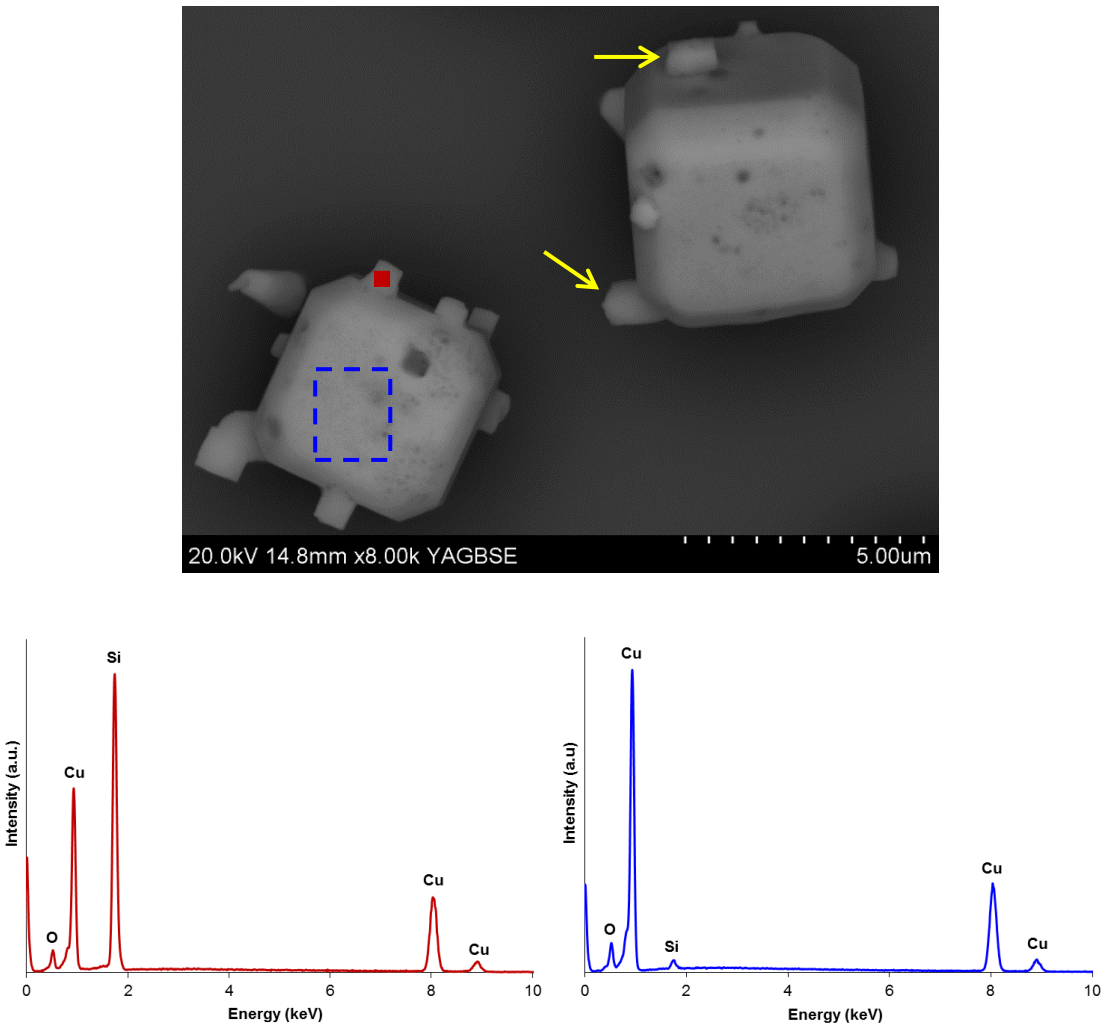

Figure 117: Backscatter electron SEM image of the Cu_2O polyhedra after heating to 650 °C, holding at temperature for 30 min and cooling to room temperature under a constant flow of argon (top) with associated EDXS spectra for the highlighted regions (bottom).The yellow arrows point to cuboid protrusions of the polyhedra.

SEM images of the Cu_2O polyhedra heated to 800 °C showed that the polyhedra still had the same overall size and morphology as the polyhedra before heating (figure 118). The number of rectangular pits in the surface appeared to be higher than observed at 650 °C, as the whole of the (100) and (110) surfaces appeared to be covered with shallow pits, resulting in a greater degree of roughening for these surfaces upon heating. Interestingly the (111) faces, at the corners of the cube-like polyhedra, appeared smooth and unpitted. The different faces of Cu_2O have previously been shown to have different photocatalytic activities; with the (110) face showing a greater activity to photodegrade methyl orange than the (111) face,[509] and the (111) face showing a greater activity to photodegrade methyl orange than the (100).[510, 511] The difference in photocatalytic ability of the different faces has been attributed to the

relative number of dangling bonds (and hence surface charge) of the different faces,[509, 511] where the (100) has the lowest activity due to the complete absence of dangling bonds. The susceptibility of the faces to pitting is clearly governed by different factors as the (100) face was highly prone to pitting in the current study. The cuboid protrusions from the Cu_2O polyhedra appeared smooth, with no pitting of the surface, suggesting that the protrusions contain a thermally stable phase of the material.

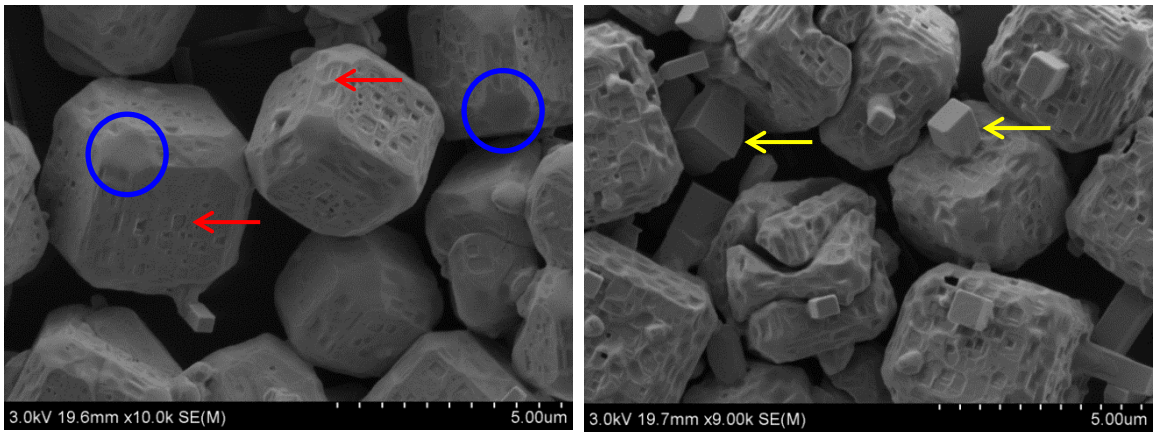

Figure 118: SEM images of the Cu_2O polyhedra after heating to 800 °C, holding at temperature for 30 min and cooling to room temperature under a constant flow of argon. The yellow arrows point to cuboid protrusions, the red arrows point to surface pits on the (100) and (110) faces, and the blue circles highlight (111) faces; which appear smooth and unpitted.

SEM images of the polyhedra after heating to 1000 °C (figure 119) showed that the polyhedra deformed, resulting in structures with a multitude of small angular facets, many of which had deep pits in their centre. In addition the polyhedra seemed to have partially disintegrated, forming a spread of nanometer sized structures around the base of the polyhedra. These results indicated that 1000 °C was too high a growth temperature for the Cu_2O polyhedra under the heat-up conditions used in these experiments, and as such the synthesis of graphene at 800 °C or lower became the focus of the investigation.

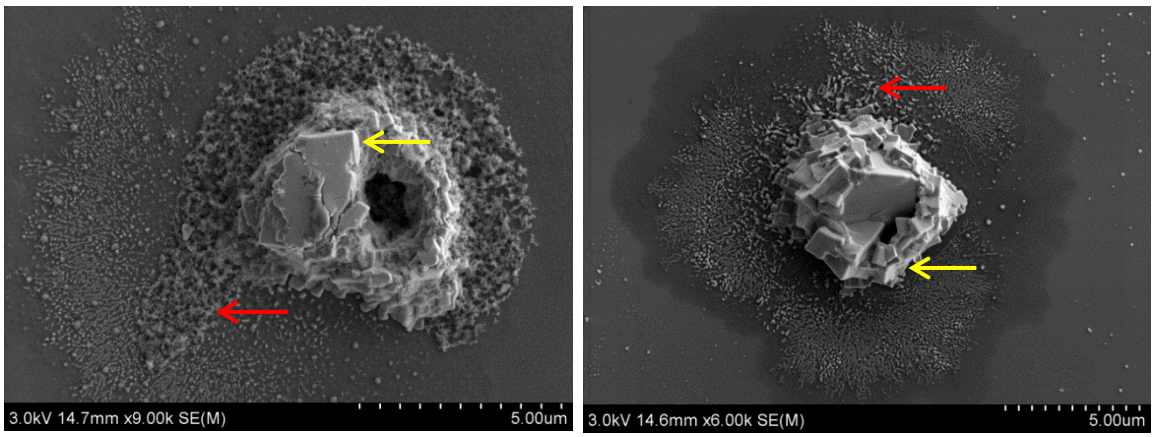

Figure 119: SEM images of Cu_2O polyhedra after heating to 1000 °C, holding at temperature for 30 min and cooling to room temperature under a constant flow of argon. The yellow arrows point to angular facets of the Cu_2O and the red arrows point to evidence of disintegration of the polyhedra.

6.2.2 Characterisation of carbon material grown over templates

The growth of graphene films on the surface of copper has been confirmed for a range of Cu crystal faces, including polycrystalline Cu.[513, 514] For growth over Cu(111) there are discrepancies with regard to the shape and behaviour of the graphene islands, as rotationally misaligned dendritic islands that grow over Cu step edges have been reported by some,[515] while others report the growth of rotationally aligned rectangular islands,[38] or the growth of non-descript shaped islands which primarily terminate at Cu step edges.[516, 517] For Cu(100), graphene growth has been reported to proceed via four-lobed graphene islands in multiple studies, where the islands have been shown to be polycrystalline in nature and able to grow across Cu step edges and other defects such as adatoms and vacancies.[518, 519] The growth of graphene films on polycrystalline Cu films has been reported for a range of different growth conditions and surface pre-treatments, as discussed in detail elsewhere.[211, 239, 257] Importantly while graphene islands have been observed to nucleate in a variety of different shapes, the growth of graphene is always seen on the surface of the copper. A number of studies utilising C^{13} and C^{12} methane have confirmed that the growth of graphene on copper occurs via a surface adsorption method, where the carbon atoms remain on the surface of the metal rather than dissolving into the bulk.[242, 243, 520] It has been calculated that the energy barrier for diffusion of carbon atoms over the surface of copper is low, and that the weak Cu-C interactions lead to favourable formation of dimers and larger graphene islands from C adatoms on Cu surfaces.[521] Based on these observations it was

expected that graphene would form on the surface of the copper-based templates regardless of the form of copper present at the growth temperature.

In the following investigation ethanol was introduced into the CVD apparatus via bubbling argon gas through a reservoir of ethanol during heat up (room temperature to 800 °C at 20 °C/min) and for 30 minutes at reaction temperature (800 °C). A piece of silicon wafer with Cu_2O polyhedra spin-coated on the surface was positioned in the centre of the furnace for the entirety of the reaction (figure 120). The argon flow, and hence ethanol vapour, was stopped during slow cooling of the system to room temperature.

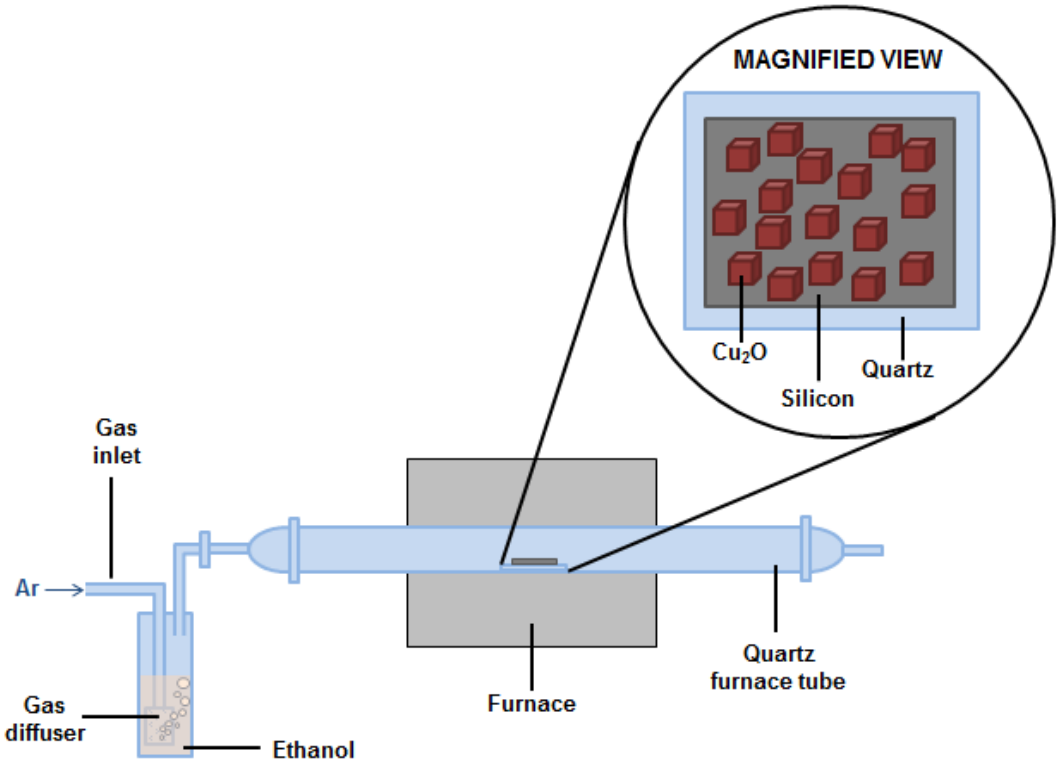

Figure 120: Furnace apparatus for CVD growth of graphene over Cu_2O polyhedra.

The SEM images of the product of the CVD synthesis reaction revealed the formation of an unusual carbon product (figure 121). From inspection of the images and the accompanying EDXS spectra, it seemed that rather than the anticipated product of copper polyhedra with thin carbon coatings, carbon cuboids containing particles of copper metal were formed. These carbon cuboids appeared to be the same approximate size as the copper-based polyhedra, which were evident alongside the carbon structures. There was also evidence of copper-based polyhedra with mottled surfaces, similar examples of which showed a weak carbon signal in the EDXS (see appendix D).

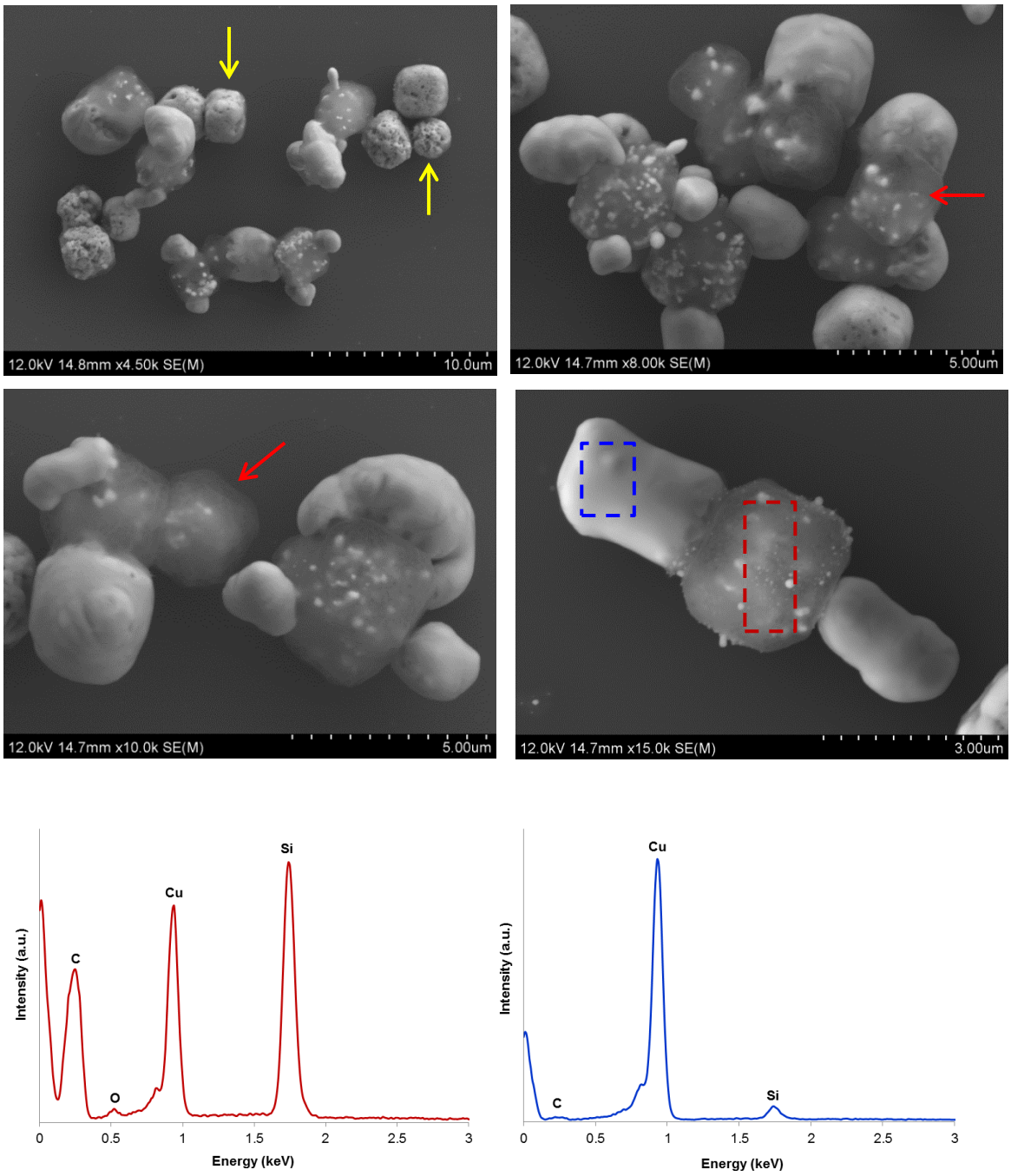

Figure 121: SEM images of the carbon grown via CVD of ethanol over the Cu_2O polyhedra, showing the formation of carbon cubes (top, middle), and associated EDXS spectra for highlighted regions (bottom). The yellow arrows point to copper-based polyhedra with mottled surfaces and the red arrows point to carbon cuboids.

Due to the unusual nature of these results over ten repeat experiments were conducted using the same Cu_2O polyhedra, where each yielded evidence of the carbon cuboids. It should be noted that some carbon nanotubes, in addition to other unusual carbon structures were observed alongside the carbon cuboids for each of the repeats (see appendix D). These structures were not prevalent (<10 % of the polyhedra) and are

thought to arise due to polydispersity and/or contaminants in the starting material. Close inspection of the carbon cuboids synthesised in the repeat experiments revealed that the 3D structures seemed to be constructed of rippled carbon sheets (figures 122 and 123). EDXS of the carbon materials showed the presence of residual copper and also small amounts of oxygen, whereas EDXS of the high contrast areas of the image showed the presence of copper only, suggesting that the Cu_2O at the surface had been completely reduced to metallic Cu. SEM images of the reaction products appeared to show the copper-based polyhedra at various stages in the formation of the carbon cuboids, where the copper seemed to have phase-separated from the carbon, leaving behind a three dimensional carbon structure (figure 124).

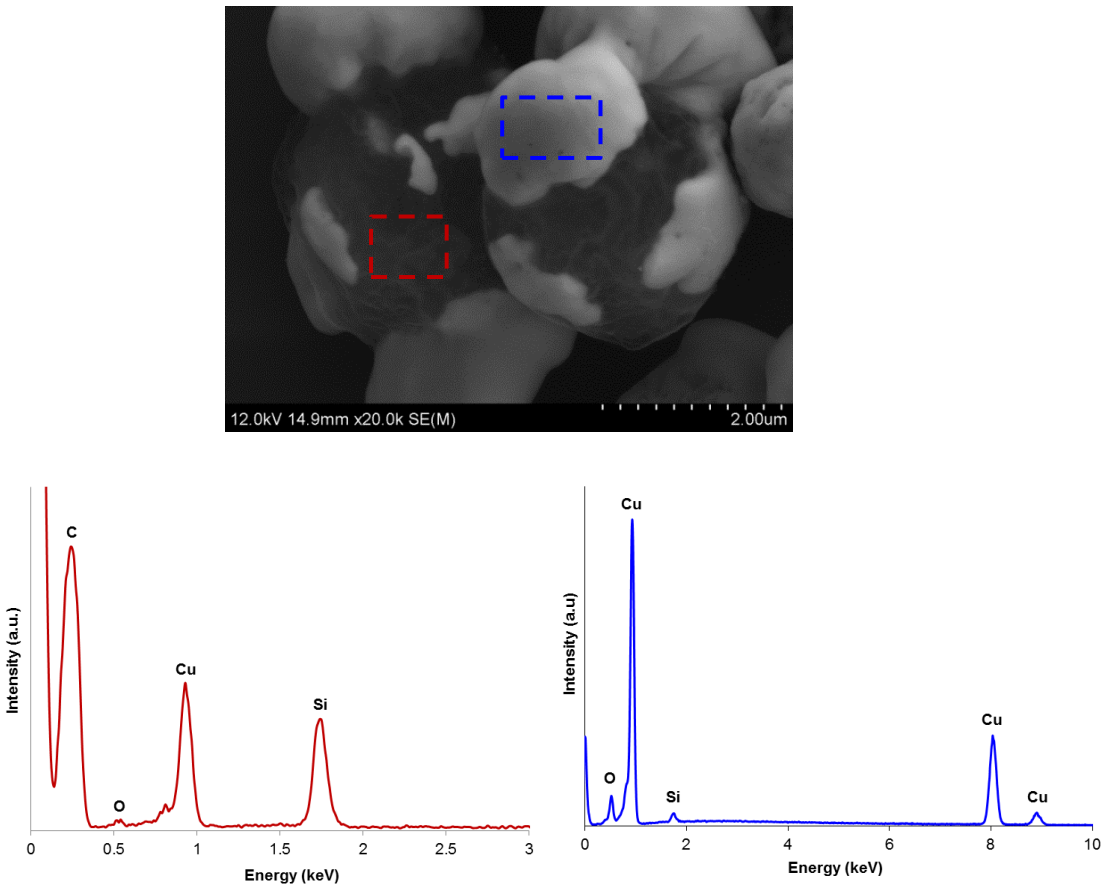

Figure 122: SEM image of the carbon grown via CVD of ethanol over the Cu_2O polyhedra (repeat experiment), showing the formation of carbon cuboids that appear to be made up of rippled sheets (top), and associated EDXS for highlighted regions (bottoms).

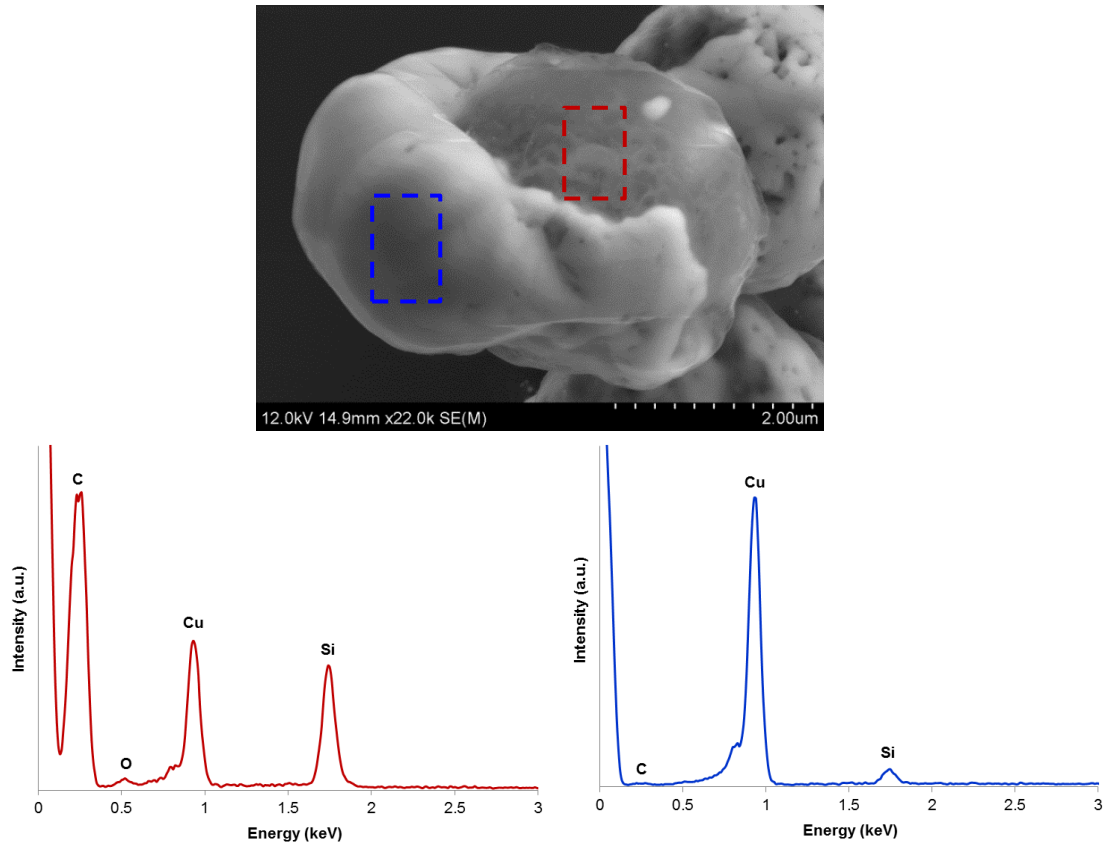

Figure 123: SEM image of the carbon grown via CVD of ethanol over the Cu_2O polyhedra (repeat experiment), showing the formation of carbon cuboids that appear to be made up of rippled sheets (top), and associated EDXS for highlighted regions (bottom).

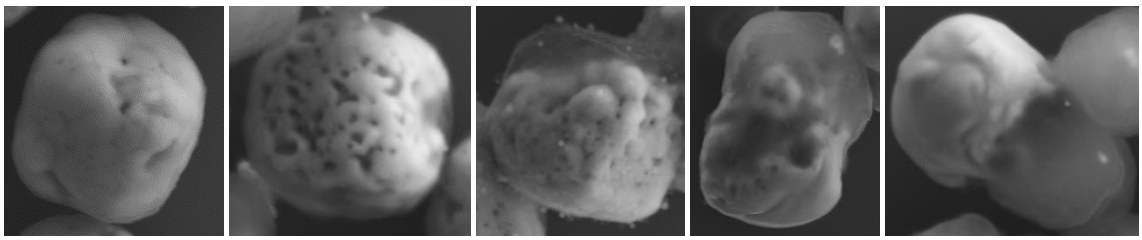

Figure 124: A series of SEM images from the CVD of ethanol over Cu_2O polyhedra arranged in a sequence to show a possible growth process for the cuboids of carbon (left to right).

The growth of carbon on copper structures has been reported for numerous different morphologies of carbon including graphene/carbon coated copper nanoparticles,[512, 522, 523] carbon fibres,[524-526] CNTs[527, 528] and graphene films.[239] The use of copper as a catalyst for carbon has mixed views in the literature, with some studies stating that copper is not a good catalyst for CNTs due to its low carbon solubility (~0.0001 wt. % at 1100 °C compared with ~1 wt. % for Fe, Ni and Co),[529] and resorting to tactics such

as depositing thin layers of nickel onto copper to promote CNT growth on copper surfaces,[530, 531] while other studies show that growth of CNTs directly on copper can be achieved (under the correct reaction conditions.)[527, 528] Although Cu has been shown to catalyse the formation of only thin layers of graphene, the formation of large quantities of carbon fibres from copper catalysts has been reported previously, for example ~75 g of carbon fibres from 1 g Cu,[524] and ~340% mass yield for carbon fibres from acetylene.[526] In all these examples carbon either grows on the surface of the copper (in the case of graphene and carbon coated nanoparticles) or is extruded out of the metal particle leaving the metal particle intact (in the case of CNTs and carbon fibres), rather than the carbon diffusing into the copper and the copper then migrating to leave behind a carbon structure. For this reason it is the morphology of the carbon product, rather than the quantity of carbon present, which is most unexpected in the current study. To the best of our knowledge there is no evidence of similar carbon structures having been catalytically grown. The closest analogue that could be found was carbon cuboids synthesised via the high temperature pyrolysis (1000 °C) of metal-organic frameworks (MOFs) (figure 125). These structures have lateral dimensions of the same order of magnitude as in the current study, and shown promise as cathode materials for high density capacitors.[532]

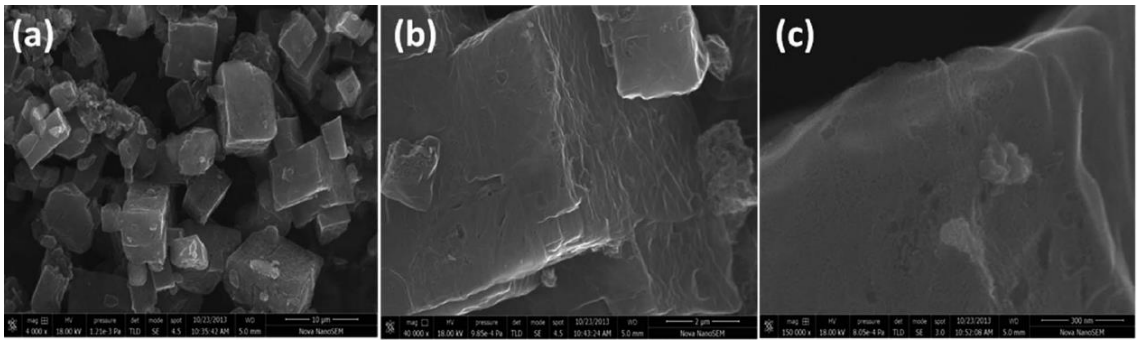

Figure 125: SEM images of MOF derived carbon at different magnifications. Adapted from reference 532.

6.2.3 Effect of reaction conditions on carbon growth

Previously it has been noted that the melting point of metals can be decreased up to a few hundred degrees in the presence of carbon,[533] so as a variation on the CVD reaction described above, an adapted bubbler was used such that the ethanol could be inserted when the reaction reached temperature, rather than being present for the entire reaction (figure 126). It was hoped that this strategy would ensure that the morphology of the polyhedra at 800 °C would be intact to the same extent, or better, as observed in the initial studies involving heating in argon alone (see section 6.2.1).

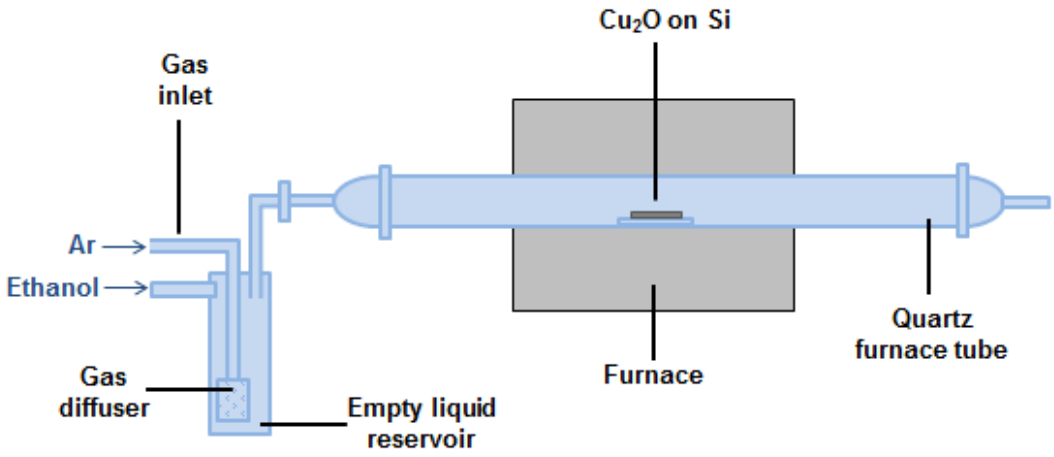

Figure 126: Adapted furnace set-up to allow ethanol to be added to the liquid reservoir during the reaction rather than at the start.

SEM images of the products of this reaction showed that the majority of the polyhedra appeared to have a carbon coating, with the bulk metal still at the centre of the structure (figure 127). EDXS mapping confirmed the presence of carbon coatings on the copper structures, and hence confirmed that this result was markedly different from the case where ethanol was present during the heating stage. This difference could be as a result of the reduction in the total amount of ethanol that entered the system, or could be due to the absence of the low temperature reactions of the polyhedra with ethanol. An alternative theory is that when the ethanol was added at 800 °C it quickly decomposed to form a protective shell around the polyhedra that did not form when ethanol decomposition increased gradually (as would have been the case in the original experiment). It should be noted that there was some evidence of segregated structures seen in the original experiments, but this was observed for <5% of the polyhedra.

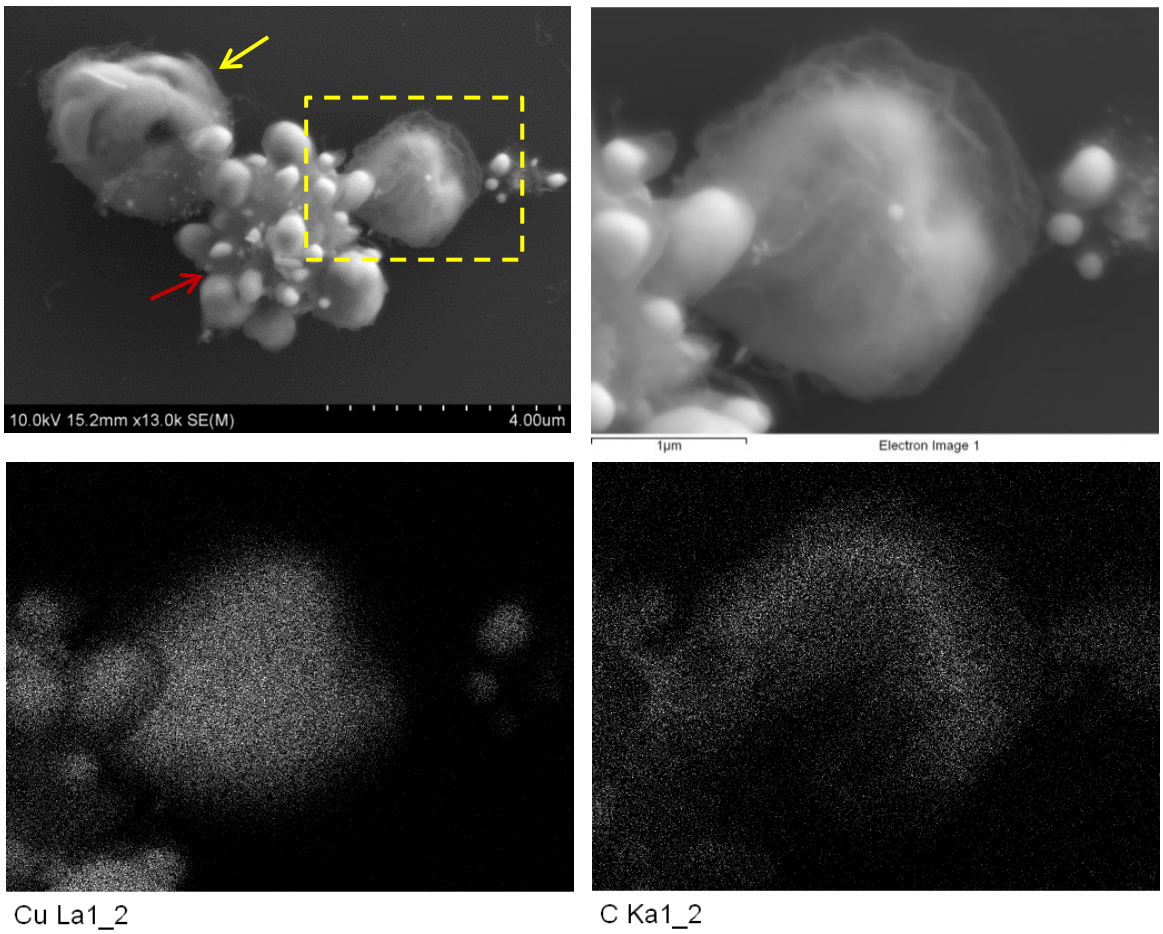

Figure 127: SEM image of the carbon grown via CVD of ethanol over batch one of the Cu_2O polyhedra when exposure to ethanol was minimised (top left), with magnified image of highlighted area (top right) and corresponding copper (bottom left) and carbon (bottom right) EDXS maps. The yellow arrow points to a carbon coating on a copper species and the red arrow points to a polyhedron where the copper appears to be segregating to the surface of the carbon species.

A number of other strategies were employed to try to maximise the probability of the polyhedra remaining intact and to investigate the carbon formation mechanism. These strategies all involved adding the ethanol while at reaction temperature (using the adapted set-up) and included the following:

1. Performing CVD reactions at a lower temperature (650 °C)
2. Heating the polyhedra to 800 °C in a different environment (in the presence of H_2 gas)
3. Minimising the timescale over which the polyhedra were exposed to the reaction temperature

For the reaction at 650 °C the polyhedra did not remain fully intact (figure 127,left) and no carbon was detected by EDXS, suggesting that this temperature was too low to yield the growth of carbon under the current reaction conditions. The appearance of the polyhedra suggested that despite the lack of carbon growth, the presence of ethanol did have an impact on the reaction product; as the structures are more distorted than when heating to 650 °C and dwelling for 30 min in argon only (see section 6.2.1).

Heating copper in the presence of hydrogen has previously been shown to remove surface irregularities,[534] so it was envisaged that heating in hydrogen may result in smooth cubes, potentially without metallic growths protruding from the surface. SEM images of the reaction product show that heating in hydrogen pitted the surface of the polyhedra (figure 127, right), and while there was a weak carbon signal in the EDXS spectra of the polyhedra (see appendix D), there was no evidence of wispy carbon sheets. This could be due to either etching of the carbon by the hydrogen,[535] disruption of the break-down of the carbon containing source due to the presence of hydrogen (as previously reported for growth of graphene on copper surfaces),[536] or due to the chemical effect of hydrogen on the Cu_2O polyhedra, since hydrogen has been shown to reduce Cu_2O to metallic Cu at 330 °C.[537]

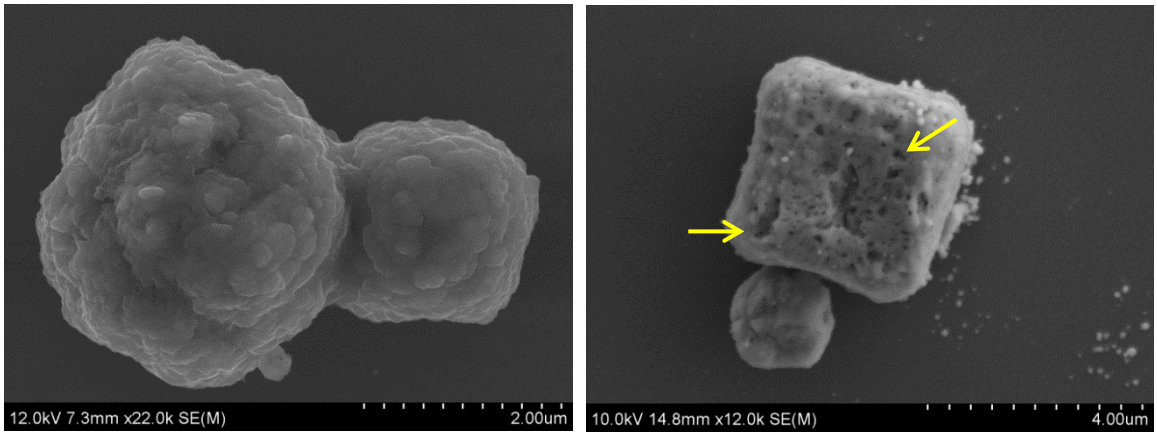

Figure 127: SEM images of products of CVD of ethanol over Cu_2O polyhedra when exposure to ethanol was minimised for a growth temperature of 650 °C (left) and a growth temperature of 800 °C but with the addition of H_2 gas from room temperature to 800 °C (right). The yellow arrows point to pits in the surface of the polyhedra.

In order to minimise the exposure of the polyhedra to heat, the silicon substrate was kept outside of the furnace during heat-up, inserted into the hot zone for the duration of the reaction (30 minutes) then extracted from the hot zone for rapid cooling (figure 128). Flash cooling has previously been used as a strategy to produce thin graphene layer of nickel films,[538] and has also been employed in the growth of graphene over copper,[534] however in this instance the thermal shock appeared to shatter the polyhedra, resulting in an array of carbon nanotubes and nanofibers for the entire sample (figure 129, top). SEM images showed the presence of copper particles at the tips of the CNTs, suggesting that the interaction of the copper nanoparticles with the silicon surface was weak, and that growth of CNTs occurred via a tip growth mechanism.[539] The SEM images also showed a number of carbon fibres with regularly shaped, rhombic copper particles at the nodes of two fibres, similar in appearance to carbon nanofibers grown on copper catalysts from acetylene at 250 °C.[524, 526] TEM images of the tubes (figure 129, bottom) revealed that the structure was bamboo-like, and confirmed the presence of catalyst particles at the tips and the centres of the carbon structures. The growth of bamboo-like CNTs and fibres has been previously reported in the literature for CVD of methane or ethanol over copper catalysts,[540, 541] where the bamboo-like structure is believed to originate from the expansion and contraction of the 'tail' of the copper particle during growth, as observed by HRTEM for growth of bamboo-like tubes on Ni particles.[542, 543]

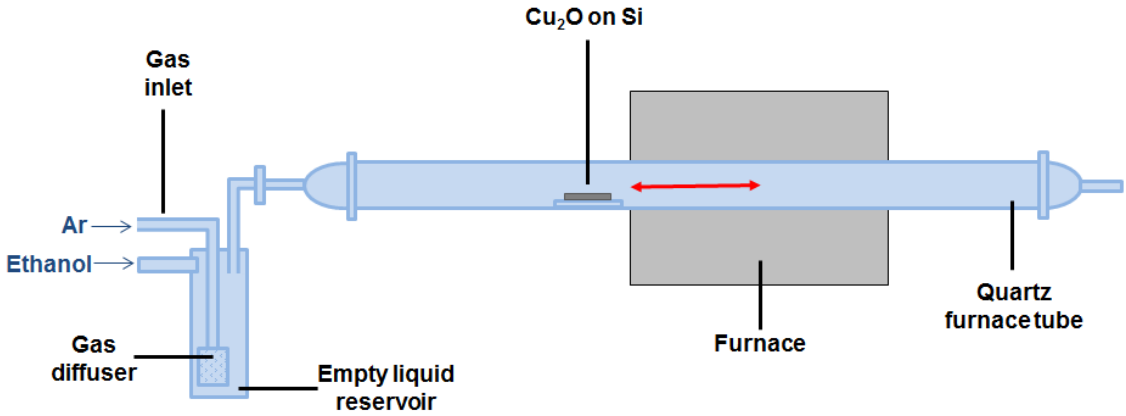

Figure 128: Adapted furnace set-up to allow the substrate to be moved in and out of the furnace (red arrow) during the experimental run.

Interestingly, the appearance of the silicon visibly changed upon extraction from the hotzone at the end of the reaction, where a rapid colour change from grey to black was observed. If the CNTs and fibres were formed during cooling this would act as further evidence that the carbon diffused in the bulk metal whilst at 800 °C, which would

support the findings of the initial study. To clarify this two additional experiments would be required; one where the substrate was moved into the furnace at temperature and cooled in situ and one where the substrate was heated in situ and moved out of the furnace for cooling. These experiments form part of the future work required to understand this system further. The experiments already performed show that the system is sensitive to both the conditions during heat-up and to the growth temperature; as cuboids of carbon were not produced in any of the adapted runs. The product of the reaction where the ethanol was only present at 800 °C rather than during heat-up (i.e. polyhedra coated with carbon) was closest to the original aim of the work, and as such this reaction should be studied further.

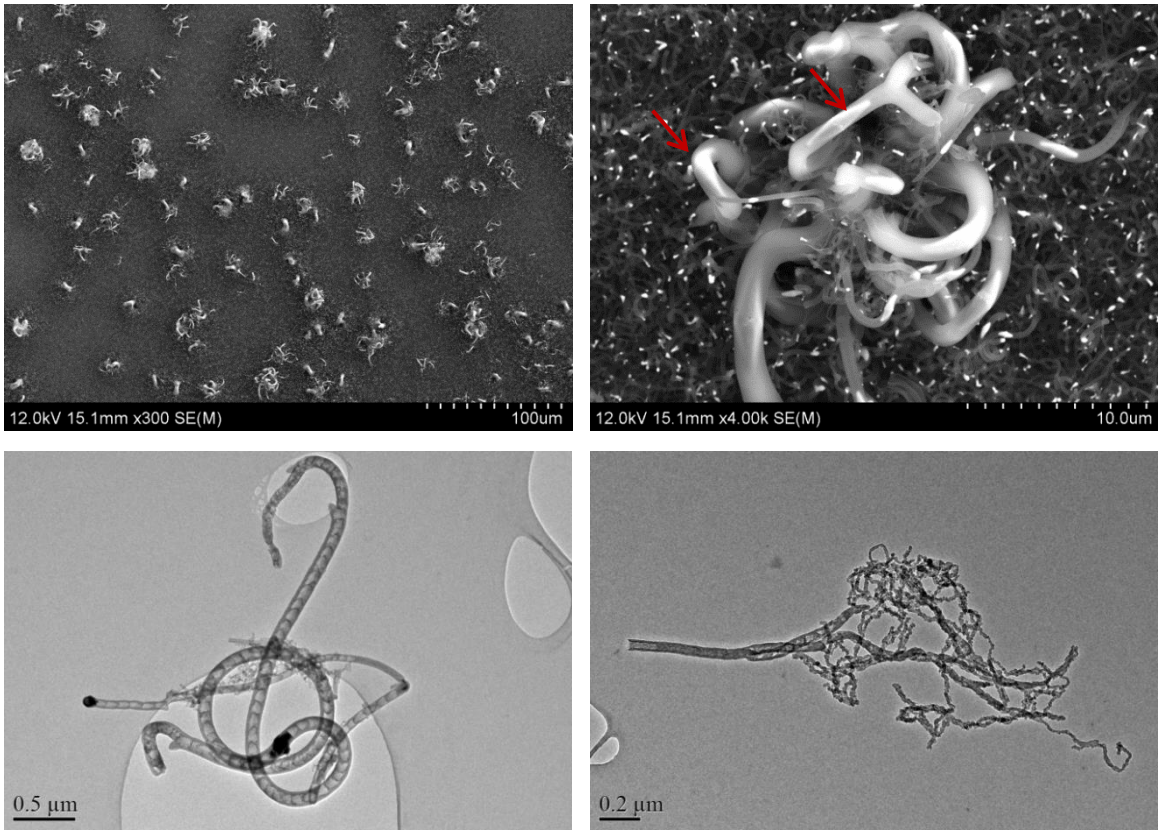

Figure 129: SEM images of products of CVD of ethanol over Cu_2O polyhedra when exposure to ethanol was minimised and the polyhedra were inserted and removed from the hotzone at reaction temperature (800 °C.) The red arrows point to rhombic shaped copper particle inside the electron transparent carbon fibres.

6.2.4 Growth mechanism of carbon cuboids

As the morphology of the carbon product in the current study appears unique it has been difficult to find an appropriate growth mechanism. Taking into account other related studies on carbon and the observations made while studying the growth of

carbon on Cu_2O under different reaction conditions, the following growth mechanism is proposed for the current study:

1. The ethanol decomposed on the surface of the copper-based polyhedra
2. The carbon diffused into the bulk polyhedra, possibly aided by the pits in the surfaces and by vacancies in the structure due to the removal of oxygen and/or the proximity to the melting point of the metallic species (as noted elsewhere in the literature[544])
3. The copper diffused through the carbon to the surface of the carbon polyhedra in order to minimise the C-Cu interactions, leaving behind a shell of carbon that either formed initially via diffusion into the polyhedra or that formed as the copper diffused to the surface (i.e. that was produced via the formation of carbon layers on a continuously changing copper surface)

As previously discussed, the exposure of Cu to carbon sources at high temperature usually results in formation of carbon on the Cu surface, which in its simplest form cannot explain the formation of the 3D carbon obtained in the present investigation. Careful inspection of the literature yielded some examples of diffusion of copper through carbon, although reported cases are limited. One particularly relevant example is the bulk diffusion of copper particles through an amorphous carbon film deposited on the copper surface during the synthesis of CNTs from ethanol at temperatures in the range of 700 – 900 °C.[541] In this study copper particles were observed to diffuse from the catalyst layer to form agglomerated particles both within and on-top of the amorphous carbon film. The diffusion of copper in carbon has also been reported for annealing of copper-doped carbon films and copper-carbon nanocomposite thin films at temperatures of 600 °C and 500-700 °C respectively, again reporting the bulk diffusion and coalescence of copper, forming particles within and on-top of the carbon films.[545, 546] These accounts support the mechanism proposed in the current study.

6.3 Conclusions and future work

Cu_2O polyhedra have been used to template the growth of 3D carbon structures, which represent a unique product for CVD of carbon on copper. While the reaction space has not been fully investigated in terms of the effect of different growth parameters, it appears that the conditions trialled initially offer an interesting system to gain further insight into the mechanism of carbon formation on copper. Electron backscatter diffraction (EBSD) and in-situ SEM have recently been used to monitor the growth of graphene via segregation of bulk-dissolved carbon on polycrystalline Ni surfaces,[547]

where an SEM with a heated stage was use to heat a Ni surface coated with carbon to observe the graphene growth, and EBSD was used to determine the effects of Ni grain orientation on graphene growth; revealing that graphene did not form on Ni (001) grain. This would be an interesting technique to try for the current system as it would provide more conclusive evidence on the mechanism of the carbon cuboid formation and on the behaviour of the Cu_2O polyhedra upon heating in terms of the chemical identity of the polyhedra at growth temperature. The growth of carbon fibres has been shown to proceed at different rates from different copper crystalline faces, [524, 548] so assuming the morphology of the starting material affects the morphology Cu at the growth temperature, it would be interesting to study the effect of different Cu_2O polyhedra (with different proportions of the relative crystalline faces) on the carbon product. Further to this there are a whole range of other factors that could be investigated including the effect of different heat/cooling rates and environments, the length and concentration of exposure to the carbon source, and the effect of using different sources of carbon. Ideally the reaction would be optimised such that all the products were at the same stage (e.g. the bulk diffusion of copper to the surface of the polyhedra had occurred in all cases), so that the reaction product could be fully characterised.

In terms of the templated growth of graphene platelets on the surface of metal microcrystals, the current study shows some promise in terms of producing carbon coated metal on the micron scale under certain growth conditions; however the underlying template did not retain its precise morphology (unlike the case for growth of graphene on ZnS ribbons[498]) suggesting that Cu_2O polyhedra were not suitable templates for controlled graphene synthesis under the reaction conditions studied. As there are a wide range of other copper-based species and different metals from which to choose templates, in addition to a broad range of growth conditions to be trialled, the limited success of this study is not a major set-back, and there is much future scope for work in this novel area of graphene synthesis.

Chapter 7: Experimental Section

7.1 Equipment methodology

7.1.1 X-ray photoelectron spectroscopy (XPS)

XPS analysis was performed at the NEXUS facility at Newcastle University on a Thermo Scientific K-Alpha spectrometer, using a monochromatic Al K alpha and dual-beam charge neutralisation. Samples were submitted to this service as dry powders drop cast onto ~1 cm^2 pieces of clean silicon wafer. Three repeats were collected for each sample. The data analysis was completed off site using CASA XPS software, using the fitting parameters detailed in table 28. The peak maximum of the C 1s spectra was aligned to 284.5 eV before peak fitting to compensate for sample charging. The errors in the reported peak fits are given as 95 % confidence levels based on the results of the three repeats.

Table 28: Fitting parameters for C1s XPS peak.

Peak	C=C	C-C	C-O	C=O	COOH	Pi-Pi
Line shape	RGO*	GL(30)	GL(30)	GL(30)	GL(30)	GL(30)
Position constraint	284.5 ± 0.1	285.5 ± 0.3	286.3 ± 0.3	287.7 ± 0.3	289.0 ± 0.3	290.8 ± 0.3
FWHM constraint	0.8 – 1.2	1 – 1.5	1 – 1.5	1 – 1.5	1 – 1.5	1 - 4

*Line shape obtained from the experimental line shape of GO reduced using hydrazine hydrate.[394]

C/O ratios were calculated from the C1s peak fit by multiplying the relative area of each peak by the C/O ratio of the peak, as outline in table 29. A similar process has been utilised elsewhere to analyse the degree of reduction of GO.[549]

Table 29: Carbon/oxygen ratios of the different components of the C1s peak.

Component	C=C	C-C	C-O	C=O	COOH	π-π*
C:O ratio	1:0	1:0	1:1	1:1	1:2	1:0

7.1.2 Solid state nuclear magnetic resonance (SSNMR)

^{13}C solid state nuclear magnetic resonance (SSNMR) was performed at the EPSRC UK National Solid-state NMR Service at Durham University. Spectra were recorded at 100.56 MHz using a Varian VNMRS spectrometer and a 4 mm (rotor o.d.) magic-angle spinning probe. Single pulse experiments were conducted with no proton decoupling, a 1 s recycle delay, and a 9.6 ms contact time, at ambient probe temperature (~25 °C) and a sample spin-rate of 14 kHz. Between 30000 and 60000 repetitions were accumulated. Spectral referencing was with respect to an external sample of neat tetramethylsilane (carried out by setting the high-frequency signal from adamantane to 38.5 ppm). Data processing, including phase correction, multipoint background correction, truncating the FID and peak fitting (Lorentzian-Gaussian line shape) was performed on MestReNova.

7.1.3 Scanning electron microscopy (SEM)

Microscopy was conducted on a FEI Helios NanolabTM or SU70 Hitachi microscope operated in the range of 3 - 15 keV under high vacuum conditions. Samples for SEM were produced by spin coating (Model WS 400B 6NPP) onto pre-cleaned silicon a suspension of the material in the chosen solvent, prepared by 5 min of bath sonication (Ultrawave, U50, 30-40 kHz). Samples were dried in air before imaging and were not coated prior to imaging. Images were collected using a SE detector unless otherwise stated, where some images were collected using a YAG BSE detector. EDXS was collected using an Oxford Instruments EDXS system (INCA x-act LN2-free analytical Silicon Drift Detector), and the data analysis was performed on the proprietary INCA software**.**

7.1.4 Transmisson electron microscopy (TEM)

Microscopy was conducted on a JOEL-2100 FEG TEM operated at 80 kV under high vacuum conditions. Samples for TEM were prepared by drop depositing onto holey or lacey carbon TEM grids (Cu, 300 mesh, SPI Supplies) a suspension of the material in the chosen solvent, prepared by 5 min bath sonication. Samples were dried in air before imaging and loaded into the TEM using a Gatan model 914 single tilt holder. BF and HRTEM images were collected on a Gatan Orius camera, while EELS and EFTEM was collected using Gatan GIF tridiem with a 4 megapixel Ultrascan^{TM}

1000 CCD camera. Data analysis was conducted using the proprietary Digital Micrograph software.

7.1.5 X-ray powder diffraction (XRPD)

XRPD was conducted on a Siemens D5000 powder diffractometer H1534 or on a Bruker AXS d8 Advance X-ray powder diffractometer; both automated diffractometers operated at 40 kV and 40 mA, with flat-plane geometry, and using a Cu $K_{\alpha 1,2}$ X-ray source (λ = 1.5406 Å). A Lynx-Eye detector was used containing 192 silicon strip detectors to provide high resolution data. Samples were prepared by sieving the material through an 80 mesh sieve onto glass plates covered with a thin layer of Vaseline. For air sensitive samples this preparation was carried out in the glove box (N_2 atmosphere), and the silica plates were secured inside an air-tight device, the top of which allowed X-rays to pass through it, prior to removal from the glove box. Data was collected for 2θ values between 2 and 90°, or 2 and 50° for GO based samples (step size 0.02).

7.1.6 Variable temperature X-ray powder diffraction (XRPD) under H_2/N_2 atmosphere

XRPD was conducted on a Bruker AXS d8 Advance X-ray powder diffractometer, operated at 40 kV and 40 mA, and using a $CuK_{\alpha 1,2}$ X-ray source (λ = 1.5406 Å). A Lynx-Eye detector was used containing 192 silicon strip detectors to provide high resolution data. An Anton Paar HTK1200 furnace was used to heat the sample between room temperature and 800 °C. The furnace control was integrated with Bruker's XRD Commander software, and was programmed in step/scan mode. Samples were prepared by sieving the material through an 80 mesh sieve onto silica plates covered with a thin layer of Vaseline and positioned inside the XRPD furnace. The sample chamber was flushed with a 5% H_2/N_2 gas mixture the 20 min scans were taken every 25 °C for the temperature range 29 - 800 °C. The furnace was maintained at 800 °C for 210 min, to run 10 scans at this temperature. Data was collected for 2θ values between 8 and 90°.

7.1.7 Variable temperature X-ray powder diffraction (XRPD) under Ar atmosphere

XRPD was conducted on a Bruker AXS d8 Advance X-ray Powder Diffractometer using an Anton Paar HTK1200 furnace, as above. Samples were prepared by sieving the material through an 80 mesh sieve onto silica plates covered with a thin layer of Vaseline and position inside the XRPD furnace. The sample chamber was flushed with argon gas then 40 min scans were taken every 40 °C between 80 - 800 °C. The furnace was maintained at 800 °C for 360 min, to collect 9 scans at this temperature. Data was collected for 2θ = 8 - 90°.

7.1.8 Elemental analysis

Elemental analysis was conducted on a Horiba Jobin Yvon Ultima 2, which uses Inductively Coupled Plasma, Optical Emission Spectroscopy (ICP-OES) to determine weight percentages of the constituent elements. Samples of the cobalt containing materials were prepared by acid digestion in concentrated nitric acid.

7.1.9 BET surface area analysis

BET surface area analysis was conducted on a Micromeritics Tristar 3000 gas adsorption porosimeter instrument. Analysis was done using a BET isotherm, produced from ten measurements taken between relative nitrogen pressures of 0.05 and 0.3 mmHg. Samples were dried in a vacuum oven (60 °C) prior to loading into the machine.

7.1.10 Raman spectroscopy

Raman spectra were recorded using a Horiba Jobin Yvon LabRam Evolution HR spectrometer in a back scattered confocal configuration using a Nd:YAG laser (532 nm, 2.33 eV.) The spectrometer was equipped with a CCD detector. Samples of the carbon material were prepared by drop casting onto glass slides solutions of the material dispersed in diethyl ether, produced by ~5 min sonication in an ultrasonic bath (Ultrawave U50, 30-40 kHz.) Samples were dried in air before analysing. All spectra were referenced to the position of the A_{1g} Raman active mode of Silicon at 520 cm^{-1}. Analysis of the data was performed using the proprietary Labspec 6 data, where peak

fits were obtained using classical least square (CLS) fitting with lineshapes that were permitted to have asymmetric, Gaussian and Lortenzian character.

7.1.11 Fourier transform infrared spectroscopy (FTIR)

FTIR spectra were recorded on a Perkin Elmer Spectrum100 equipped with a Pike ATR fitted with a germanium crystal. Spectra were taken from 800 to 4000 cm^{-1} at a resolution of 4 cm^{-1}. Measurements were performed on solid samples of carbon material mounted under compression.

7.1.12 Thermogravimetric analysis (TGA)

TGA was carried out using a Perkin Elmer Pyris I. Carbon samples (1-10 mg) were heated under compressed air in a ceramic pan from room temperature to 900 ^{o}C at a rate of 10 ^{o}C per min. For GO samples a 30 min dwell at 30 °C was included before the ramp to 900 °C to minimise adsorbed gas/moisture.

7.1.13 UV-Vis Spectroscopy

UV-vis spectroscopy was performed on a Perkin Elmer Lambda 900 UV/Vis/NIR spectrometer over a wavelength range of 200 – 1100 nm. Dispersions of graphitic material were prepared for UV-vis by probe sonicating (probe model: Cole Parmer Ultrasonic Processor (750 W), ½" probe tip) 25 mg of solid powder in 25 mL of liquid for 15 min (30 % amplitude, pulse 5 sec on:5 sec off (total time 30 min)), using an external ice baths to cool the mixture. Samples were measured 24 h after sonication (to allow poorly dispersed material to settle) and 7 days after the first measurement. Where necessary the samples were diluted prior to measurement, such that the absorbance of the sample remained below 1, and the absorbance of the original solution was found by multiplying the obtained value by the dilution factor. Measurements were taken using paired quartz cuvettes for the sample and the blank.

7.1.14 Electrical measurements on thin films

Sheet resistance measurements were conducted on thin films of samples (13 mm diameter) prepared by vacuum filtration of aqueous dispersions of the samples over

polycarbonate membranes (0.2 μm pore size). All films were <50 μm thick based on measurements from a number of different techniques. The electrical measurements were recorded using a Keithley 2602 Source Measure Unit (SMU) and a Guardian SRM232-PROBE-625-45-TC-R=10-FH4-point, in-line probe head. The voltage was swept between -2 to 2 V with a 150 points linear sweep, a compliance of 0.1 A and a sweep delay of 100 ms, and correction factors were applied to correct for the sample geometry.[550]

7.1.15 Electrical measurements on powder compacts

Bulk electrical measurements were conducted on 50 mg compacts of sample, held within a bespoke powder press (figure 130). The heights of the compacts/pellets were measured indirectly via the offset of the top/plunger using electronic callipers. The electrical measurements were recorded using a Keithley 2602 Source Measure Unit (SMU), via sweeping the voltage between -1 to 1 V with a 151 points linear sweep, a compliance of 0.1 A and a sweep delay of 100 ms.

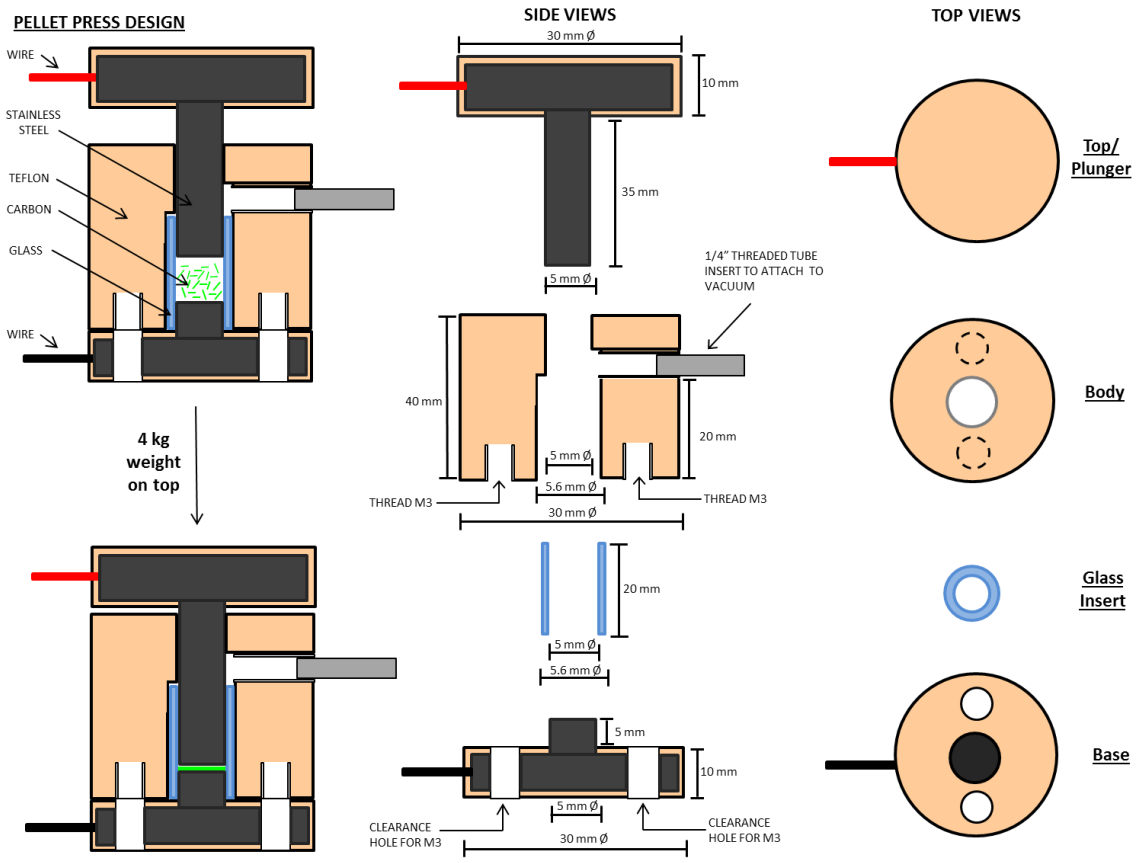

Figure 130: Design of bespoke powder press for bulk conductivity measurements. A similar press has been used elsewhere for the measurement of graphene, graphite, MWNT and carbon black compacts.[551]

7.2 Experimental synthesis

All reagents and solvents were purchased from Sigma Aldridge or Fisher Scientific and used without further purification.

7.2.1 Synthesis of 'post-wash' graphite oxide

Sulfuric acid (18 M, 23 mL) was added to a stirred mixture of graphite flakes (325 mesh, 1 g) and sodium nitrate (0.5 g). The resultant mixture was cooled to 0 °C, potassium permanganate (3 g) was added slowly such that the reaction temperature remained below 20 °C, and the mixture was warmed to 35 °C, and stirred for 30 min. High purity water (46 mL) was slowly added causing an increase in temperature to ~98 °C, which was maintained for 15 min before slow addition of further high purity water (140 mL) and hydrogen peroxide (30 %, 1 mL). The solid product was collected by filtration over Whatman filter paper and rinsed with warm high purity water until a wet paste was obtained that would no longer filter. The final rinse step was performed in a centrifuge (Eppendorf 5804, 6000 rpm) via repeated water washes until the supernatant was pH neutral. The product was stored as a gel-like solid. This method follows the reaction described by Hummers and Offeman.[156]

7.2.2 Synthesis of 'pre-wash' graphite oxide

Sulfuric acid (18 M, 23 mL) was added to a stirred mixture of graphite flakes (325 mesh, 1 g) and sodium nitrate (0.5 g). The resultant mixture was cooled to 0 °C, potassium permanganate (3 g) was added slowly such that the reaction temperature remained below 20 °C, and the mixture was warmed to 35 °C, and stirred for 30 min. High purity water (46 mL) was slowly added causing an increase in temperature to ~98 °C, which was maintained for 15 min before slow addition of further high purity water (140 mL) and hydrogen peroxide (30 %, 1 mL). The solid product was collected by filtration over Whatman filter paper and stored as a damp, yellow/brown solid.

7.2.3 Refluxing 'post-wash' graphite oxide in water

Post-wash GO (20-25 mL of undried material, ~5 wt. % solids) was refluxed in high purity water (100 mL) for 24 h. The solid product was collected by filtration over a

polycarbonate membrane (0.2 μm track etched), rinsed with high purity water until the washings were pH neutral, and dried overnight in a vacuum oven (<10 mbar) at 80 °C.

7.2.4 Refluxing 'pre-wash' graphite oxide in water/production of 'water-refluxed' graphene oxide

'Pre-wash' GO (~0.75g) was refluxed in high purity water (250 mL) for 4, 6, 12, 24 or 120 h. The solid product was collected by filtration over a polycarbonate membrane (0.2 μm track etched), rinsed with high purity water until the washings were pH neutral, and dried overnight in a vacuum oven (<10 mbar) at 80 °C.

7.2.5 Refluxing 'pre-wash' graphite oxide in water then 0.1 M KOH

'Pre-wash' GO was refluxed in high purity water (250 mL) for 4 h. The solid product was collected by filtration over a polycarbonate membrane (0.2 μm track etched) and rinsed with high purity water until the washings were pH neutral. The damp solid was dispersed in 0.1 M KOH (250 mL), refluxed for 4 h, then collected by filtration over a polycarbonate membrane (0.2 μm track etched) and rinsed with high purity water until the washings were pH neutral. The solid product was dried overnight in a vacuum oven (<10 mbar) at 80 °C.

7.2.6 Base-washing 'post-wash' graphite oxide/production of 'base-washed' graphene oxide

'Post-wash' GO (3.20 g of undried material, ~5 wt. % solids) was dispersed in high purity water (1.2 L) and stirred for 24 h. NaOH (4.67 g) was added to the aqueous GO solution, which was subsequently refluxed for 1 h and allowed to cool. The solid material was separated from the basic solution via centrifugation (11000 rpm, 30 min) then redispersed in 1.0 M HCl (1.2 L). The acidic solution was refluxed for 1 h, allowed to cool, and the solid material was collected by centrifugation (11000 rpm, 30 min). The solid product was washed with water (1.2 L) then collected via centrifugation (11000 rpm, 30 min), and dried overnight in a vacuum oven (<10 mbar) at 80 °C. This method follows the reaction described by Rourke *et al.*[433]

7.2.7 Base-washing ‘post-wash’ graphite oxide then refluxing in water

‘Post-wash’ GO (50 mL of undried material, ~5 wt. % solids) was dispersed in high purity water (200 mL) and stirred for 24 h. NaOH (1.0 g) was added to the aqueous GO solution, which was subsequently refluxed for 1 h and allowed to cool. The solid material was separated from the basic solution via centrifugation (11000 rpm, 30 min) then redispersed in 1.0 M HCl (250 mL). The acidic solution was refluxed for 1 h, allowed to cool, and the solid material was collected by centrifugation (11000 rpm, 30 min). The solid product was washed with water (250 mL), collected via centrifugation (11000 rpm, 30 min), and redispersed in high purity water (250 mL). The aqueous solution was refluxed for 120 h and allowed to cool. The solid product was collected by filtration over a polycarbonate membrane (0.2 μm track etched), rinsed with high purity water until the washings were pH neutral, and dried overnight in a vacuum oven (<10 mbar) at 80 °C.

7.2.8 Refluxing ‘pre-wash’ graphite oxide in 0.5 M arginine in water

‘Pre-wash’ graphite oxide (~0.75 g) was refluxed in 0.5 M arginine in water (250 mL) for 1, 4, 8 or 24 h. The solid product was collected by filtration over a polycarbonate membrane (0.2 μm track etched), rinsed with high purity water until the washings were pH neutral, and dried overnight in a vacuum oven (<10 mbar) at 80 °C.

7.2.9 Refluxing ‘pre-wash’ graphite oxide in 0.1 M arginine in water

‘Pre-wash’ GO (~0.75 g) was refluxed in 0.1 M arginine in water (250 mL) for 4 h. The solid product was collected by filtration over a polycarbonate membrane (0.2 μm track etched), rinsed with high purity water until the washings were pH neutral, and dried overnight in a vacuum oven (<10 mbar) at 80 °C.

7.2.10 Refluxing ‘pre-wash’ graphite oxide in 0.1 M potassium hydroxide

‘Pre-wash’ GO (~0.75 g) was refluxed in 0.1 M KOH (250 mL) for 4 h. The solid product was collected by filtration over a polycarbonate membrane (0.2 μm track etched), rinsed with high purity water until the washings were pH neutral, and dried overnight in a vacuum oven (<10 mbar) at 80 °C.

7.2.11 Chemical reduction of 'post-wash' graphite oxide

A solution of 'post wash' GO (100 mg) in high purity water (100 mL) was probe sonicated for 15 min (40% amplitude, pulsed 5 sec on: 5 sec off, total time 30 min). After addition of hydrazine monohydrate (34 μL), this suspension was heated to 80 °C for 12 h with stirring, then allowed to cool to room temperature. The solid product was collected by filtration over a polycarbonate membrane (0.2 μm track etched), rinsed with high purity water until the washings were pH neutral, and dried overnight in a vacuum oven (<10 mbar) at 80 °C. This method follows the reaction described by Park *et al.*[394]

7.2.12 Chemical reduction of 'post-wash' graphite oxide in the presence of 0.5 M arginine

A solution of 'post wash' GO (100 mg) in 0.5 M arginine in water (100 mL) was probe sonicated for 15 min (40% amplitude, pulsed 5 sec on: 5 sec off, total time 30 min). After addition of hydrazine monohydrate (34 μL), this suspension was heated to 80 °C for 12 h with stirring, then allowed to cool to room temperature. The solid product was collected by filtration over a polycarbonate membrane (0.2 μm track etched), rinsed with high purity water until the washings were pH neutral, and dried overnight in a vacuum oven (<10 mbar) at 80 °C.

7.2.13 Chemical reduction of 'base-washed' graphene oxide

A solution of 'base-washed' GO (100 mg) in high purity water (100 mL) was probe sonicated for 15 min (40% amplitude, pulsed 5 sec on: 5 sec off, total time 30 min). After addition of hydrazine monohydrate (34 μL), this suspension was heated to 80 °C for 12 h with stirring, then allowed to cool to room temperature. The solid product was collected by filtration over a polycarbonate membrane (0.2 μm track etched), rinsed with high purity water until the washings were pH neutral, and dried overnight in a vacuum oven (<10 mbar) at 80 °C. This method was based on the reaction described by Park *et al.*[394]

7.2.14 Chemical reduction of 'base-washed' graphene oxide in the presence of 0.5 M arginine

A solution of 'base-washed' GO (100 mg) in 0.5 M arginine in water (100 mL) was probe sonicated for 15 min (40% amplitude, pulsed 5 sec on: 5 sec off, total time 30 min). After addition of hydrazine monohydrate (34 μL), this suspension was heated to 80 °C for 12 h with stirring, then allowed to cool to room temperature. The solid product was collected by filtration over a polycarbonate membrane (0.2 μm track etched), rinsed with high purity water until the washings were pH neutral, and dried overnight in a vacuum oven (<10 mbar) at 80 °C.

7.2.15 Chemical reduction of 'water-refluxed' graphene oxide

'Water-refluxed' GO was prepared by refluxing 'pre-wash' GO in water for 24 h (section 7.2.4). A solution of the 'water-refluxed' GO (100 mg) in high purity water (100 mL) was probe sonicated for 15 min (40% amplitude, pulsed 5 sec on: 5 sec off, total time 30 min). After addition of hydrazine monohydrate (34 μL), this suspension was heated to 80 °C for 12 h with stirring, then allowed to cool to room temperature. The solid product was collected by filtration over a polycarbonate membrane (0.2 μm track etched), rinsed with high purity water until the washings were pH neutral, and dried overnight in a vacuum oven (<10 mbar) at 80 °C. This method was based on the reaction described by Park *et al.*[394]

7.2.16 Chemical reduction of 'water-refluxed' graphite oxide in the presence of 0.5 M arginine

'Water-refluxed' GO was prepared by refluxing 'pre-wash' GO in water for 24 h (section 7.2.4). A solution of 'water-refluxed' GO (100 mg) in 0.5 M arginine in water (100 mL) was probe sonicated for 15 min (40% amplitude, pulsed 5 sec on: 5 sec off, total time 30 min). After addition of hydrazine monohydrate (34 μL), this suspension was heated to 80 °C for 12 h with stirring, then allowed to cool to room temperature. The solid product was collected by filtration over a polycarbonate membrane (0.2 μm track etched), rinsed with high purity water until the washings were pH neutral, and dried overnight in a vacuum oven (<10 mbar) at 80 °C.

7.2.17 Production of graphene oxide foam

'Post-wash' GO (25 mL of undried material, ~5 wt. % solids) was diluted to a total volume of 100 mL using high purity water. The resulting solution was split into five separate aliquots of 20 mL, and each aliquot was probe sonicated for 15 min (40% amplitude, pulsed 5 sec on: 5 sec off, total time 30 min). The aliquots were combined and diluted to a total volume of 250 mL using high purity water. The graphene oxide solution (250 mL) was bath sonicated for 30 min, and then the water was removed using a freeze drier, yielding a pale brown foam.

7.2.18 Heating graphene oxide foams to 100 °C in air

Small pieces of the GO foam (total mass 50 mg) were placed in a quartz boat and position in the centre of a tube furnace lined with a quartz tube. The furnace was heated to 100 °C at a rate of 20 °C/min and held at temperature for 24 or 120 h. The foam was removed from the furnace after the system had cooled to room temperature.

7.2.19 Heating graphene oxide foams to 150 °C in air

Small pieces of the GO foam (total mass 50 mg) were placed in a quartz boat and position in the centre of a tube furnace lined with a quartz tube. The furnace was heated to 150 °C at a rate of 20 °C/min and held at temperature for 24 h. The foam was removed from the furnace after the system had cooled to room temperature.

7.2.20 Dispersion of graphite in water via bath sonication

A solution of graphite (325 mesh, 25 mg) in high purity water (25 mL) was bath sonicated for 15 min, the water in the bath was replaced with cold water, and the solution of graphite in water was sonicated for a further 15 min.

7.2.21 Dispersion of graphite in water via probe sonication

A solution of graphite (325 mesh, 25 mg) in high purity water (25 mL) was probe sonicated for 15 min (30 % amplitude, pulse 5 sec on:5 sec off (total time 30 min)), using an external ice bath to cool the mixture.

7.2.22 Dispersion of 'post-wash' graphite oxide in water via bath sonication

A solution of 'post-wash' GO (25 mg) in high purity water (25 mL) was bath sonicated for 15 min, the water in the bath was replaced with cold water, and the solution of graphite in water was sonicated for a further 15 min.

7.2.23 Dispersion of 'post-wash' graphite oxide in water via probe sonication

A solution of 'post-wash' GO (25 mg) in high purity water (25 mL) was probe sonicated for 15 min (30 % amplitude, pulse 5 sec on:5 sec off (total time 30 min)), using an external ice bath to maintain a constant temperature.

7.2.24 Synthesis of cobalt carbonate

A stirred solution of $Co(NO_3)_2$ in high purity water (0.5 M, 100 mL) was heated to near boiling point and added dropwise to a stirred solution of Na_2CO_3 in high purity water (0.65 M, 100 mL) also heated to near boiling point. The resulting solution was maintained at just below boiling point for 15 min, allowed to cool, and centrifuged. The product was purified in the centrifuge with repeated water washed until the supernatant was pH neutral. The purple precipitate was isolated by vacuum filtration, rinsed with high purity water, and then allowed to dry in air at room temperature overnight. The dried product was transferred to the glove box for storage in a nitrogen atmosphere. This method was based on the reaction described by Schlessinger.[468]

7.2.25 Synthesis of doped sodium cobalt carbonate (batch one)

Varying amounts of $CoCO_3$ (as synthesised) and NaF were weighed in the glove box, ground for 15 min in air (table 30), then immediately transferred to a glove box (<5 ppm H_2O and <5 ppm O_2) for storage in a nitrogen atmosphere.

Table 30: Masses of $CoCO_3$ and NaF that were ground together to achieve different sodium doping levels.

Na wt. %	Mass $CoCO_3$ (g)	Mass NaF (g)
0.12	0.750	-
1.11	0.792	0.015
2.02	0.784	0.029
3.00	0.762	0.043
4.59	0.760	0.073
8.69	0.720	0.146

7.2.26 Synthesis of doped sodium cobalt carbonate (batches two and three)

Method completed as per batch one, except 0.776 g $CoCO_3$ and 0.048 g NaF were used for the 3 wt. % Na sample, and the 15 min of grinding was carried out inside the glove box. Note that although the same $CoCO_3$ and NaF masses were used as for batch one, slightly different sodium weight percentages were produced due to the errors associated with the glove box balance.

7.2.27 Synthesis of carbon products on doped cobalt carbonate via chemical vapour deposition

A predetermined amount of doped $CoCO_3$ (table 31) was weighed into an alumina boat in the glove box then removed and immediately positioned at the centre of the Carbolite tube furnace inside a quartz furnace tube. The furnace system was purged with argon (60 mL/min) for 5 min then heated to 800 °C (20 °C/min) under the flow of argon (60 mL/min.) Approximately 15 min after 800 °C had been reached the argon flow was increased to 200 mL/min to induce spraying of absolute ethanol (~50 mL), then returned to 60 mL/min after the ethanol had sprayed (~45 min) for the duration of the time at 800 °C. The furnace was held at 800 °C for a total of 4 h. The argon flow was maintained at 60 mL/min during cooling of the furnace to room temperature.

Table 31: Amount of NaF doped $CoCO_3$ catalysts used in each furnace run.

Na wt. %	Mass of doped cobalt catalyst in boat (g)
0.12	0.500
1.11	0.510
2.02	0.519
3.00	0.528
4.59	0.548
8.69	0.602

7.2.28 Purification of the products from chemical vapour deposition of ethanol over doped and undoped cobalt carbonate

The raw products of the experiments were purified by stirring overnight in hydrochloric acid (6 M, 100 ml). The solution was diluted with high purity water and vacuum filtered over a polycarbonate membrane (0.2 μm pore size). The carbon product was washed by a process of redispersing the solid from the filter in high purity water (100 ml) by bath sonication (15 min) and re-filtering it. This step was repeated three times. The final rinse was performing in absolute ethanol (100 ml), then the purified carbon product was collected via vacuum filtration, and dried overnight in a vacuum oven (100 °C).

7.2.29 Synthesis of copper (I) oxide polyhedra

$Cu(CH_3COO)_2.H_2O$ (0.724 g) was dissolved in high purity water (40 mL) under constant stirring at 70 °C. NaOH (6 M, 5 mL) was added dropwise and after 5 min of stirring at temperature, D-glucose (2 g) was added, and the mixture was stirred for a further 3 min. The solution was allowed to cool to room temperature and the dark red precipitate was separated by repeated washing and centrifugation using high purity water and ethanol. The solid was dried overnight in a vacuum oven at 60 °C then stored in a glove box under N_2. A yield of 30 % was achieved. This method follows the reaction described by Sun *et al.*[507]

7.2.30 Deposition of copper (I) oxide polyhedra on silicon

A dispersion of Cu_2O polyehdra in ethanol was spin coated onto silicon wafers (~20 x 10 mm) using the following spin regime:

1. 30 s at 500 rpm (Cu_2O dispersion deposited)
2. 90 s at 1000 rpm
3. 180 s at 4000 rpm

7.2.31 Heating of copper (I) oxide polyhedra to various temperatures in argon

A piece of silicon wafer with Cu_2O polyhedra spin coated on the surface was rested on a square of quartz (~2 cm^2) and positioned at the centre of the Carbolite tube furnace inside a quartz furnace tube. The furnace system was purged with argon (160 mL/min) then heated to 650 °C, 800 °C or 1000 °C (20 °C/min) and held at the reaction temperature for 30 min before being allowed to cool to room temperature. Argon (160 mL/min) was flowed into the furnace tube for the duration of the heating, dwelling and cooling steps.

7.2.32 Synthesis of carbon products on copper (I) oxide via chemical vapour deposition

A piece of silicon wafer with Cu_2O polyhedra spin coated on the surface was rested on a square of quartz (~2 cm^2) and positioned at the centre of the Carbolite tube furnace inside a quartz furnace tube. The furnace system was purged with argon (160 mL/min) then heated to 800 °C (10 °C/min, 40 min) under the same flow of argon. The furnace was maintained at 800 °C for 30 min then the argon was stopped and the system was allowed to cool to room temperature. The argon gas was bubbled through a reservoir of absolute ethanol for the duration of the heating and dwelling steps.

7.2.33 Variation on synthesis of carbon products on copper (I) oxide polyhedra via chemical vapour deposition; ethanol at reaction temperature only

A piece of silicon wafer with Cu_2O polyhedra spin coated on the surface was rested on a square of quartz (~2 cm^2) and positioned at the centre of the Carbolite tube furnace

inside a quartz furnace tube. The furnace system was purged with argon (160 mL/min) then heated to 800 °C (10 °C/min, 40 min) under the same flow of argon. The furnace was maintained at 800 °C for 30 min then the argon was stopped and the system was allowed to cool to room temperature. Argon gas was bubbled through a reservoir of absolute ethanol for the dwelling step only.

7.2.34 Variation on synthesis of carbon products on doped cobalt carbonate via chemical vapour deposition; lower reaction temperature

A piece of silicon wafer with Cu_2O polyhedra spin coated on the surface was rested on a square of quartz (~2 cm^2) and positioned at the centre of the Carbolite tube furnace inside a quartz furnace tube. The furnace system was purged with argon (160 mL/min) then heated to 650 °C (10 °C/min, 40 min) under the same flow of argon. The furnace was maintained at 800 °C for 30 min then the argon was stopped and the system was allowed to cool to room temperature. Argon gas was bubbled through a reservoir of absolute ethanol for the dwelling step only.

7.2.35 Variation on synthesis of carbon products on doped cobalt carbonate via chemical vapour deposition; hydrogen during heating

A piece of silicon wafer with Cu_2O polyhedra spin coated on the surface was rested on a square of quartz (~2 cm^2) and positioned at the centre of the Carbolite tube furnace inside a quartz furnace tube. The furnace system was purged with argon (160 mL/min) then heated to 800 °C (10 °C/min) under the same flow of argon. Hydrogen gas (10 mL/min) was added to the argon flow when the temperature reacted 200 °C and stopped when the temperature reached 800 °C. The furnace was maintained at 800 °C for 30 min then the argon was stopped and the system was allowed to cool to room temperature. Argon gas was bubbled through a reservoir of absolute ethanol for the dwelling step only.

7.2.36 Variation on synthesis of carbon products on copper (I) oxide polyhedra via chemical vapour deposition; 'flash' cooling/heating

A piece of silicon wafer with Cu_2O polyhedra spin coated on the surface was rested on a square of quartz (~2 cm^2) and positioned outside of the Carbolite tube furnace inside a quartz furnace tube. The furnace system was purged with argon (60 mL/min) then heated to 800 °C (10 °C/min, 40 min) under the same flow of argon. When the furnace

reached 800 °C the quartz tube was moved such that the silicon wafer was in the centre of the furnace. The furnace was maintained at 800 °C for 30 min then the argon was stopped and the quartz tube was moved such that the silicon wafer was outside the furnace, then the system was allowed to cool to room temperature. Argon gas was bubbled through a reservoir of absolute ethanol for the dwelling step only.

Chapter 8: References

1. K. S. Novoselov, A. K. Geim, S. V. Morozov, D. Jiang, Y. Zhang, S. V. Dubonos, I. V. Grigorieva and A. A. Firsov, *Science*, 2004, 306, 666-669.
2. J. L. Delgado, M. a. A. Herranz and N. Martin, *J. Mater. Chem.*, 2008, 18, 1417-1426.
3. J. Robertson, *Mater. Sci. Eng., R*, 2002, 37, 129-281.
4. N. Savage, *Nature*, 2012, 483, S30-S31.
5. E. P. Randviir, D. A. C. Brownson and C. E. Banks, *Mater. Today*, 2014, 17, 426-432.
6. V. Fal'ko, A. Geim, S. D. Sarma, A. MacDonald and P. Kim, *Solid State Commun.*, 2009, 149, 1039-1040.
7. S. Z. Butler, S. M. Hollen, L. Y. Cao, Y. Cui, J. A. Gupta, H. R. Gutierrez, T. F. Heinz, S. S. Hong, J. X. Huang, A. F. Ismach, E. Johnston-Halperin, M. Kuno, V. V. Plashnitsa, R. D. Robinson, R. S. Ruoff, S. Salahuddin, J. Shan, L. Shi, M. G. Spencer, M. Terrones, W. Windl and J. E. Goldberger, *ACS Nano*, 2013, 7, 2898-2926.
8. F. Bonaccorso, A. Lombardo, T. Hasan, Z. P. Sun, L. Colombo and A. C. Ferrari, *Mater. Today*, 2012, 15, 564-589.
9. M. Inagaki and F. Y. Kang, *J. Mater. Chem., A*, 2014, 2, 13193-13206.
10. M. Pumera and C. H. A. Wong, *Chem. Soc. Rev.*, 2013, 42, 5987-5995.
11. L. Ma, J. L. Wang and F. Ding, *ChemPhysChem*, 2013, 14, 47-54.
12. M. Bacon, S. J. Bradley and T. Nann, *Part. Part. Syst. Char.*, 2014, 31, 415-428.
13. L. L. Jiang and Z. J. Fan, *Nanoscale*, 2014, 6, 1922-1945.
14. P. Vogt, P. De Padova, C. Quaresima, J. Avila, E. Frantzeskakis, M. C. Asensio, A. Resta, B. Ealet and G. Le Lay, *Phys. Rev. Lett.*, 2012, 108, 155501.
15. D. Pacile, J. C. Meyer, C. O. Girit and A. Zettl, *Appl. Phys. Lett.*, 2008, 92, 133107.
16. D. C. Elias, R. R. Nair, T. M. G. Mohiuddin, S. V. Morozov, P. Blake, M. P. Halsall, A. C. Ferrari, D. W. Boukhvalov, M. I. Katsnelson, A. K. Geim and K. S. Novoselov, *Science*, 2009, 323, 610-613.
17. N. Narita, S. Nagai, S. Suzuki and K. Nakao, *Phys. Rev., B*, 1998, 58, 11009-11014.
18. A. K. Geim and K. S. Novoselov, *Nat. Mater.*, 2007, 6, 183-191.
19. B. Partoens and F. M. Peeters, *Phys. Rev., B*, 2006, 74, 075404.
20. A. Fasolino, J. H. Los and M. I. Katsnelson, *Nat. Mater.*, 2007, 6, 858-861.
21. J. C. Meyer, A. K. Geim, M. I. Katsnelson, K. S. Novoselov, T. J. Booth and S. Roth, *Nature*, 2007, 446, 60-63.
22. E. Stolyarova, K. T. Rim, S. Ryu, J. Maultzsch, P. Kim, L. E. Brus, T. F. Heinz, M. S. Hybertsen and G. W. Flynn, *Proc. Natl. Acad. Sci. U. S. A.*, 2007, 104, 9209-9212.
23. K. F. Mak, J. Shan and T. F. Heinz, *Phys. Rev. Lett.*, 2010, 104, 176404.
24. S. Horiuchi, T. Gotou, M. Fuijwara, R. Sotoaka, M. Hirata, K. Kimoto, T. Asaka, T. Yokosawa, Y. Matsui, K. Watanabe and M. Sekita, *Jpn. J. Appl. Phys., Part 2*, 2003, 42, L1073-L1076.
25. L. M. Malard, M. A. Pimenta, G. Dresselhaus and M. S. Dresselhaus, *Phys. Rep.*, 2009, 473, 51-87.
26. X. Jia, J. Campos-Delgado, M. Terrones, V. Meunier and M. S. Dresselhaus, *Nanoscale*, 2011, 3, 86-95.
27. M. Acik and Y. J. Chabal, *Jpn. J. Appl. Phys.*, 2012, 51, 039201.
28. D. Wei and Y. Liu, *Adv. Mater.*, 2010, 22, 3225-3241.
29. S. Dutta and S. K. Pati, *J. Mater. Chem.*, 2010, 20, 8207-8223.
30. K. Wakabayashi and S. Dutta, *Solid State Commun.*, 2012, 152, 1420-1430.

31. J. S. Bunch, S. S. Verbridge, J. S. Alden, A. M. van der Zande, J. M. Parpia, H. G. Craighead and P. L. McEuen, *Nano Lett.*, 2008, 8, 2458-2462.
32. C. Lee, X. Wei, J. W. Kysar and J. Hone, *Science*, 2008, 321, 385-388.
33. A. A. Balandin, S. Ghosh, W. Z. Bao, I. Calizo, D. Teweldebrhan, F. Miao and C. N. Lau, *Nano Lett.*, 2008, 8, 902-907.
34. R. R. Nair, P. Blake, A. N. Grigorenko, K. S. Novoselov, T. J. Booth, T. Stauber, N. M. R. Peres and A. K. Geim, *Science*, 2008, 320, 1308-1308.
35. K. S. Kim, Y. Zhao, H. Jang, S. Y. Lee, J. M. Kim, K. S. Kim, J.-H. Ahn, P. Kim, J.-Y. Choi and B. H. Hong, *Nature*, 2009, 457, 706-710.
36. A. A. Balandin, *Nat. Mater.*, 2011, 10, 569-581.
37. A. H. Castro Neto, F. Guinea, N. M. R. Peres, K. S. Novoselov and A. K. Geim, *Rev. Mod. Phys.*, 2009, 81, 109-162.
38. C. N. Lau, W. Z. Bao and J. Velasco, *Mater. Today*, 2012, 15, 238-245.
39. S. V. Morozov, K. S. Novoselov, M. I. Katsnelson, F. Schedin, D. C. Elias, J. A. Jaszczak and A. K. Geim, *Phys. Rev. Lett.*, 2008, 100, 016602.
40. K. I. Bolotin, K. J. Sikes, Z. Jiang, M. Klima, G. Fudenberg, J. Hone, P. Kim and H. L. Stormer, *Solid State Commun.*, 2008, 146, 351-355.
41. X. Du, I. Skachko, A. Barker and E. Y. Andrei, *Nat. Nanotechnol.*, 2008, 3, 491-495.
42. K. S. Novoselov, Z. Jiang, Y. Zhang, S. V. Morozov, H. L. Stormer, U. Zeitler, J. C. Maan, G. S. Boebinger, P. Kim and A. K. Geim, *Science*, 2007, 315, 1379-1379.
43. A. Shytov, M. Rudner, N. Gu, M. Katsnelson and L. Levitov, *Solid State Commun.*, 2009, 149, 1087-1093.
44. T. Ohta, A. Bostwick, T. Seyller, K. Horn and E. Rotenberg, *Science*, 2006, 313, 951-954.
45. E. McCann and M. Koshino, *Rep. Progr. Phys.*, 2013, 76, 056503.
46. F. Miao, S. Wijeratne, Y. Zhang, U. C. Coskun, W. Bao and C. N. Lau, *Science*, 2007, 317, 1530-1533.
47. S. Das Sarma, S. Adam, E. H. Hwang and E. Rossi, *Rev. Mod. Phys.*, 2011, 83, 407-470.
48. Q. Z. Li, E. H. Hwang and E. Rossi, *Solid State Commun.*, 2012, 152, 1390-1399.
49. S. Roche, N. Leconte, F. Ortmann, A. Lherbier, D. Soriano and J.-C. Charlier, *Solid State Commun.*, 2012, 152, 1404-1410.
50. G. H. Lee, R. C. Cooper, S. J. An, S. Lee, A. van der Zande, N. Petrone, A. G. Hammerherg, C. Lee, B. Crawford, W. Oliver, J. W. Kysar and J. Hone, *Science*, 2013, 340, 1073-1076.
51. H. S. Skulason, P. E. Gaskell and T. Szkopek, *Nanotechnology*, 2010, 21, 295709.
52. M. Klintenberg, S. Lebegue, C. Ortiz, B. Sanyal, J. Fransson and O. Eriksson, *J. Phys. Condens. Matter*, 2009, 21, 335502.
53. A. Z. AlZahrani and G. P. Srivastava, *J. Phys. Condens. Matter*, 2009, 21, 495503.
54. S. Ghosh, W. Z. Bao, D. L. Nika, S. Subrina, E. P. Pokatilov, C. N. Lau and A. A. Balandin, *Nat. Mater.*, 2010, 9, 555-558.
55. Y. Zhang and C. Pan, *Diamond Relat. Mater.*, 2012, 24, 1-5.
56. X. Zhang, B. R. S. Rajaraman, H. H. Liu and S. Ramakrishna, *R. Soc. Chem. Adv.*, 2014, 4, 28987-29011.
57. D. Wei and Y. Liu, *Adv. Mater*, 2010, 22, 3225-3241.
58. W. Choi, I. Lahiri, R. Seelaboyina and Y. S. Kang, *Crit. Rev. Solid State Mater. Sci.*, 2010, 35, 52-71.
59. V. Singh, D. Joung, L. Zhai, S. Das, S. I. Khondaker and S. Seal, *Prog. Mater. Sci.*, 2011, 56, 1178-1271.
60. F. Schwierz, *Nat Nano*, 2010, 5, 487-496.
61. D. Wei and J. Kivioja, *Nanoscale*, 2013, 5, 10108-10126.

62. B. Sukang, K. Sang Jin, S. Dolly, A. Jong-Hyun and H. Byung Hee, *Phys. Scr.*, 2012, 2012, 014024.
63. J. H. Du, S. F. Pei, L. P. Ma and H. M. Cheng, *Adv. Mater*, 2014, 26, 1958-1991.
64. L. Huang, Y. Huang, J. Liang, X. Wan and Y. Chen, *Nano Res.*, 2011, 4, 675-684.
65. X. Huang, X. Y. Qi, F. Boey and H. Zhang, *Chem. Soc. Rev.*, 2012, 41, 666-686.
66. V. Mittal, *Macromol. Mater. Eng.*, 2014, 299, 906-931.
67. Y. Liu, X. Dong and P. Chen, *Chem. Soc. Rev.*, 2012, 41, 2283-2307.
68. F. Yavari and N. Koratkar, *J. Phys. Chem. Lett.*, 2012, 3, 1746-1753.
69. D. Haag and H. H. Kung, *Top. Catal.*, 2014, 57, 762-773.
70. C. Chung, Y. K. Kim, D. Shin, S. R. Ryoo, B. H. Hong and D. H. Min, *Acc. Chem. Res.*, 2013, 46, 2211-2224.
71. M. Segal, *Nat Nano*, 2009, 4, 612-614.
72. N. Savage, *Nature*, 2012, 483, S38-S39.
73. A. Kasry, M. A. Kuroda, G. J. Martyna, G. S. Tulevski and A. A. Bol, *ACS Nano*, 2010, 4, 3839-3844.
74. Y. Wang, X. Chen, Y. Zhong, F. Zhu and K. P. Loh, *Appl. Phys. Lett.*, 2009, 95, 063302.
75. T. Palacios, *Nature*, 2012, 483, S40-S41.
76. M. I. Katsnelson, *Mater. Today*, 2007, 10, 20-27.
77. D. A. Siegel, C.-H. Park, C. Hwang, J. Deslippe, A. V. Fedorov, S. G. Louie and A. Lanzara, *Proc. Natl. Acad. Sci. U. S. A.*, 2011, 108, 11365-11369.
78. X. Wang, Y. Ouyang, L. Jiao, H. Wang, L. Xie, J. Wu, J. Guo and H. Dai, *Nat. Nano*, 2011, 6, 563-567.
79. V. M. Pereira, A. H. Castro Neto and N. M. R. Peres, *Phys. Rev., B*, 2009, 80, 045401.
80. R. Lv and M. Terrones, *Mater. Lett.*, 2012, 78, 209-218.
81. D. Wei, Y. Liu, Y. Wang, H. Zhang, L. Huang and G. Yu, *Nano Lett.*, 2009, 9, 1752-1758.
82. Z. Jin, J. Yao, C. Kittrell and J. M. Tour, *ACS Nano*, 2011, 5, 4112-4117.
83. K. S. Novoselov, V. I. Falko, L. Colombo, P. R. Gellert, M. G. Schwab and K. Kim, *Nature*, 2012, 490, 192-200.
84. Y. Hernandez, M. Lotya, D. Rickard, S. D. Bergin and J. N. Coleman, *Langmuir*, 2010, 26, 3208-3213.
85. N. Saravanan, R. Rajasekar, S. Mahalakshmi, T. P. Sathishkumar, K. S. K. Sasikumar and S. Sahoo, *J. Reinf. Plast. Compos.*, 2014, 33, 1158-1180.
86. V. Georgakilas, M. Otyepka, A. B. Bourlinos, V. Chandra, N. Kim, K. C. Kemp, P. Hobza, R. Zboril and K. S. Kim, *Chem. Rev.*, 2012, 112, 6156-6214.
87. M. D. Stoller, S. J. Park, Y. W. Zhu, J. H. An and R. S. Ruoff, *Nano Lett.*, 2008, 8, 3498-3502.
88. C. Liu, Z. Yu, D. Neff, A. Zhamu and B. Z. Jang, *Nano Lett.*, 2010, 10, 4863-4868.
89. S. Alwarappan, S. Boyapalle, A. Kumar, C.-Z. Li and S. Mohapatra, *J. Phys. Chem. C*, 2012, 116, 6556-6559.
90. J. D. Roy-Mayhew, D. J. Bozym, C. Punckt and I. A. Aksay, *ACS Nano*, 2010, 4, 6203-6211.
91. H.-C. Wu, Y.-Y. Li and A. Sakoda, *Int. J. Hydrogen Energy*, 2010, 35, 4123-4130.
92. H. Hibino, S. Tanabe, S. Mizuno and H. Kageshima, *J. Phys. D: Appl. Phys.*, 2012, 45, 154008.
93. Y.-M. Lin, C. Dimitrakopoulos, K. A. Jenkins, D. B. Farmer, H.-Y. Chiu, A. Grill and P. Avouris, *Science*, 2010, 327, 662.
94. Y.-M. Lin, A. Valdes-Garcia, S.-J. Han, D. B. Farmer, I. Meric, Y. Sun, Y. Wu, C. Dimitrakopoulos, A. Grill, P. Avouris and K. A. Jenkins, *Science*, 2011, 332, 1294-1297.

95. E. Kymakis, E. Stratakis, M. M. Stylianakis, E. Koudoumas and C. Fotakis, *Thin Solid Films*, 2011, 520, 1238-1241.
96. X. Lv, Y. Huang, Z. Liu, J. Tian, Y. Wang, Y. Ma, J. Liang, S. Fu, X. Wan and Y. Chen, *Small*, 2009, 5, 1682-1687.
97. H. C. Pham, T. V. Cuong, S. H. Hur, E. W. Shin, J. S. Kim, J. S. Chung and E. J. Kim, *Carbon*, 2010, 48, 1945-1951.
98. Z.-S. Wu, S. Pei, W. Ren, D. Tang, L. Gao, B. Liu, F. Li, C. Liu and H.-M. Cheng, *Adv. Mater*, 2009, 21, 1756-1760.
99. L. J. Cote, F. Kim and J. Huang, *J. Am. Chem. Soc.*, 2008, 131, 1043-1049.
100. P. Avouris and C. Dimitrakopoulos, *Mater. Today*, 2012, 15, 86-97.
101. R. O. Brennan, *J. Chem. Phys.*, 1952, 20, 40-48.
102. http://ec.europa.eu/enterprise/policies/raw-materials/critical/index_en.htm., Accessed 25/01/2015.
103. M. Inagaki, *New Carbons - Control of Structure and Functions*, Elsevier Science, Oxford, 2000.
104. G. Wang, B. Wang, J. Park, Y. Wang, B. Sun and J. Yao, *Carbon*, 2009, 47, 3242-3246.
105. D. A. C. Brownson, J. P. Metters, D. K. Kampouris and C. E. Banks, *Electroanalysis*, 2011, 23, 894-899.
106. C.-Y. Su, A.-Y. Lu, Y. Xu, F.-R. Chen, A. N. Khlobystov and L.-J. Li, *ACS Nano*, 2011, 5, 2332-2339.
107. K. Parvez, R. Li, S. R. Puniredd, Y. Hernandez, F. Hinkel, S. Wang, X. Feng and K. Muellen, *ACS Nano*, 2013, 7, 3598-3606.
108. K. Parvez, Z. S. Wu, R. J. Li, X. J. Liu, R. Graf, X. L. Feng and K. Mullen, *J. Am. Chem. Soc.*, 2014, 136, 6083-6091.
109. J. Wang, K. K. Manga, Q. Bao and K. P. Loh, *J. Am. Chem. Soc.*, 2011, 133, 8888-8891.
110. H. Huang, Y. Xia, X. Tao, J. Du, J. Fang, Y. Gan and W. Zhang, *J. Mater. Chem.*, 2012, 22, 10452-10456.
111. D. Van Thanh, L. J. Li, C. W. Chu, P. J. Yen and K. H. Wei, *R. Soc. Chem. Adv.*, 2014, 4, 6946-6949.
112. C. T. J. Low, F. C. Walsh, M. H. Chakrabarti, M. A. Hashim and M. A. Hussain, *Carbon*, 2013, 54, 1-21.
113. C. Vallés, C. Drummond, H. Saadaoui, C. A. Furtado, M. He, O. Roubeau, L. Ortolani, M. Monthioux and A. Pénicaud, *J. Am. Chem. Soc.*, 2008, 130, 15802-15804.
114. X. Li, G. Zhang, X. Bai, X. Sun, X. Wang, E. Wang and H. Dai, *Nat Nano*, 2008, 3, 538-542.
115. L. M. Viculis, J. J. Mack, O. M. Mayer, H. T. Hahn and R. B. Kaner, *J. Mater. Chem.*, 2005, 15, 974-978.
116. US. Pat., 1191383, 1916.
117. D. D. L. Chung, *J. Mater. Sci.*, 1987, 22, 4190-4198.
118. T. Wei, Z. Fan, G. Luo, C. Zheng and D. Xie, *Carbon*, 2009, 47, 337-339.
119. S. Malik, A. Vijayaraghavan, R. Erni, K. Ariga, I. Khalakhan and J. P. Hill, *Nanoscale*, 2010, 2, 2139-2143.
120. W. Gu, W. Zhang, X. Li, H. Zhu, J. Wei, Z. Li, Q. Shu, C. Wang, K. Wang, W. Shen, F. Kang and D. Wu, *J. Mater. Chem.*, 2009, 19, 3367-3369.
121. S. R. Dhakate, N. Chauhan, S. Sharma, J. Tawale, S. Singh, P. D. Sahare and R. B. Mathur, *Carbon*, 2011, 49, 1946-1954.
122. W. Fu, J. Kiggans, S. H. Overbury, V. Schwartz and C. Liang, *Chem. Commun.*, 2011, 47, 5265-5267.
123. A. Safavi, M. Tohidi, F. A. Mahyari and H. Shahbaazi, *J. Mater. Chem.*, 2012, 22, 3825-3831.
124. N.-W. Pu, C.-A. Wang, Y. Sung, Y.-M. Liu and M.-D. Ger, *Mater. Lett.*, 2009, 63, 1987-1989.
125. K. S. Suslick and G. J. Price, *Annu. Rev. Mater. Sci.*, 1999, 29, 295-326.

126. P. Blake, P. D. Brimicombe, R. R. Nair, T. J. Booth, D. Jiang, F. Schedin, L. A. Ponomarenko, S. V. Morozov, H. F. Gleeson, E. W. Hill, A. K. Geim and K. S. Novoselov, *Nano Lett.*, 2008, 8, 1704-1708.
127. Y. Hernandez, V. Nicolosi, M. Lotya, F. M. Blighe, Z. Sun, S. De, I. T. McGovern, B. Holland, M. Byrne, Y. K. Gun'ko, J. J. Boland, P. Niraj, G. Duesberg, S. Krishnamurthy, R. Goodhue, J. Hutchison, V. Scardaci, A. C. Ferrari and J. N. Coleman, *Nat. Nanotechnol.*, 2008, 3, 563-568.
128. U. Khan, A. O'Neill, M. Lotya, S. De and J. N. Coleman, *Small*, 2010, 6, 864-871.
129. U. Khan, H. Porwal, A. O'Neill, K. Nawaz, P. May and J. N. Coleman, *Langmuir*, 2011, 27, 9077-9082.
130. S. Barwich, U. Khan and J. N. Coleman, *J. Phys. Chem. C*, 2013, 117, 19212-19218.
131. X. Zhang, A. C. Coleman, N. Katsonis, W. R. Browne, B. J. van Wees and B. L. Feringa, *Chem. Commun.*, 2010, 46, 7539-7541.
132. A. O'Neill, U. Khan, P. N. Nirmalraj, J. Boland and J. N. Coleman, *J. Phys. Chem. C*, 2011, 115, 5422-5428.
133. M. Lotya, Y. Hernandez, P. J. King, R. J. Smith, V. Nicolosi, L. S. Karlsson, F. M. Blighe, S. De, Z. Wang, I. T. McGovern, G. S. Duesberg and J. N. Coleman, *J. Am. Chem. Soc.*, 2009, 131, 3611-3620.
134. M. Lotya, P. J. King, U. Khan, S. De and J. N. Coleman, *ACS Nano*, 2010, 4, 3155-3162.
135. R. J. Smith, M. Lotya and J. N. Coleman, *New J. Phys.*, 2010, 12, 125008.
136. P. May, U. Khan, J. M. Hughes and J. N. Coleman, *J. Phys. Chem., C*, 2012, 116, 11393-11400.
137. A. Ciesielski and P. Samori, *Chem. Soc. Rev.*, 2014, 43, 381-398.
138. J. N. Coleman, *Adv. Funct. Mater.*, 2009, 19, 3680-3695.
139. J. N. Coleman, *Acc. Chem. Res.*, 2013, 46, 14-22.
140. K. R. Paton, E. Varrla, C. Backes, R. J. Smith, U. Khan, A. O'Neill, C. Boland, M. Lotya, O. M. Istrate, P. King, T. Higgins, S. Barwich, P. May, P. Puczkarski, I. Ahmed, M. Moebius, H. Pettersson, E. Long, J. Coelho, S. E. O'Brien, E. K. McGuire, B. M. Sanchez, G. S. Duesberg, N. McEvoy, T. J. Pennycook, C. Downing, A. Crossley, V. Nicolosi and J. N. Coleman, *Nat. Mater.*, 2014, 13, 624-630.
141. E. Varrla, K. R. Paton, C. Backes, A. Harvey, R. J. Smith, J. McCauley and J. N. Coleman, *Nanoscale*, 2014, 6, 11810-11819.
142. A. Dimiev, D. V. Kosynkin, L. B. Alemany, P. Chaguine and J. M. Tour, *J. Am. Chem. Soc.*, 2012, 134, 2815-2822.
143. P. Solis-Fernandez, J. I. Paredes, S. Villar-Rodil, L. Guardia, M. J. Fernandez-Merino, G. Dobrik, L. P. Biro, A. Martinez-Alonso and J. M. D. Tascon, *J. Phys. Chem. C*, 2011, 115, 7956-7966.
144. T. Kuila, A. K. Mishra, P. Khanra, N. H. Kim and J. H. Lee, *Nanoscale*, 2013, 5, 52-71.
145. C. K. Chua and M. Pumera, *Chem. Soc. Rev.*, 2014, 43, 291-312.
146. S. Pei and H.-M. Cheng, *Carbon*, 2012, 50, 3210-3228.
147. D. R. Dreyer, S. Park, C. W. Bielawski and R. S. Ruoff, *Chem. Soc. Rev.*, 2010, 39, 228-240.
148. S. Mao, H. H. Pu and J. H. Chen, *R. Soc. Chem. Adv.*, 2012, 2, 2643-2662.
149. S. Eigler and A. Hirsch, *Angew. Chem. Int. Ed*, 2014, 53, 7720-7738.
150. S. Stankovich, R. D. Piner, X. Q. Chen, N. Q. Wu, S. T. Nguyen and R. S. Ruoff, *J. Mater. Chem.*, 2006, 16, 155-158.
151. F. Perrozzi, S. Prezioso and L. Ottaviano, *J. Phys. Condens. Matter*, 2015, 27, 013002.
152. D. R. Dreyer, A. D. Todd and C. W. Bielawski, *Chem. Soc. Rev.*, 2014, 43, 5288-5301.
153. A. Lerf, H. He, M. Forster and J. Klinowski, *J. Phys. Chem., B*, 1998, 102, 4477-4482.

154. H. He, J. Klinowski, M. Forster and A. Lerf, *Chem. Phys. Lett.*, 1998, 287, 53-56.
155. A. Buchsteiner, A. Lerf and J. Pieper, *J. Phys. Chem., B*, 2006, 110, 22328-22338.
156. W. S. Hummers and R. E. Offeman, *J. Am. Chem. Soc.*, 1958, 80, 1339-1339.
157. D. C. Marcano, D. V. Kosynkin, J. M. Berlin, A. Sinitskii, Z. Sun, A. Slesarev, L. B. Alemany, W. Lu and J. M. Tour, *ACS Nano*, 2010, 4, 4806-4814.
158. N. I. Kovtyukhova, P. J. Ollivier, B. R. Martin, T. E. Mallouk, S. A. Chizhik, E. V. Buzaneva and A. D. Gorchinskiy, *Chem. Mater.*, 1999, 11, 771-778.
159. G. Shao, Y. Lu, F. Wu, C. Yang, F. Zeng and Q. Wu, *J. Mater. Sci.*, 2012, 47, 4400-4409.
160. S. Lee, J. Oh, R. S. Ruoff and S. Park, *Carbon*, 2012, 50, 1442-1444.
161. H.-M. Ju, S. H. Huh, S.-H. Choi and H.-L. Lee, *Mater. Lett.*, 2010, 64, 357-360.
162. K. S. Subrahmanyam, S. R. C. Vivekchand, A. Govindaraj and C. N. R. Rao, *J. Mater. Chem.*, 2008, 18, 1517-1523.
163. A. Ganguly, S. Sharma, P. Papakonstantinou and J. Hamilton, *J. Phys. Chem. C*, 2011, 115, 17009-17019.
164. M. Agharkar, S. Kochrekar, S. Hidouri and M. A. Azeez, *Mater. Res. Bull.*, 2014, 59, 323-328.
165. S. Y. Toh, K. S. Loh, S. K. Kamarudin and W. R. W. Daud, *Chem. Eng. J.*, 2014, 251, 422-434.
166. Y. Zhu, S. Murali, M. D. Stoller, A. Velamakanni, R. D. Piner and R. S. Ruoff, *Carbon*, 2010, 48, 2118-2122.
167. L. Huang, Y. Liu, L.-C. Ji, Y.-Q. Xie, T. Wang and W.-Z. Shi, *Carbon*, 2011, 49, 2431-2436.
168. H. Guo, M. Peng, Z. Zhu and L. Sun, *Nanoscale*, 2013, 5, 9040-9048.
169. V. Eswaraiah, S. S. Jyothirmayee Aravind and S. Ramaprabhu, *J. Mater. Chem.*, 2011, 21, 6800-6803.
170. S. Stankovich, D. A. Dikin, R. D. Piner, K. A. Kohlhaas, A. Kleinhammes, Y. Jia, Y. Wu, S. T. Nguyen and R. S. Ruoff, *Carbon*, 2007, 45, 1558-1565.
171. Y. H. Ding, P. Zhang, Q. Zhuo, H. M. Ren, Z. M. Yang and Y. Jiang, *Nanotechnology*, 2011, 22, 215601.
172. T. Kuila, S. Bose, A. K. Mishra, P. Khanra, N. H. Kim and J. H. Lee, *Prog. Mater. Sci.*, 2012, 57, 1061-1105.
173. S. Farhat and C. D. Scott, *J. Nanosci. Nanotechnol.*, 2006, 6, 1189-1210.
174. K. S. Subrahmanyam, L. S. Panchakarla, A. Govindaraj and C. N. R. Rao, *J. Phys. Chem., C*, 2009, 113, 4257-4259.
175. Y. Chen, H. Zhao, L. Sheng, L. Yu, K. An, J. Xu, Y. Ando and X. Zhao, *Chem. Phys. Lett.*, 2012, 538, 72-76.
176. B. Shen, J. Ding, X. Yan, W. Feng, J. Li and Q. Xue, *Appl. Surf. Sci.*, 2012, 258, 4523-4531.
177. L. P. Huang, B. Wu, J. Y. Chen, Y. Z. Xue, D. C. Geng, Y. L. Guo, G. Yu and Y. Q. Liu, *Small*, 2013, 9, 1330-1335.
178. S. Dey, A. Govindaraj, K. Biswas and C. N. R. Rao, *Chem. Phys. Lett.*, 2014, 595, 203-208.
179. D. V. Kosynkin, A. L. Higginbotham, A. Sinitskii, J. R. Lomeda, A. Dimiev, B. K. Price and J. M. Tour, *Nature*, 2009, 458, 872-876.
180. P. Kumar, L. S. Panchakarla and C. N. R. Rao, *Nanoscale*, 2011, 3, 2127-2129.
181. L. Jiao, L. Zhang, X. Wang, G. Diankov and H. Dai, *Nature*, 2009, 458, 877-880.
182. L. Valentini, *Diamond Relat. Mater.*, 2011, 20, 445-448.
183. K. Nakada, M. Fujita, G. Dresselhaus and M. S. Dresselhaus, *Phys. Rev., B*, 1996, 54, 17954-17961.
184. L. Xie, H. Wang, C. Jin, X. Wang, L. Jiao, K. Suenaga and H. Dai, *J. Am. Chem. Soc.*, 2011, 133, 10394-10397.
185. S. Cho, K. Kikuchi and A. Kawasaki, *Carbon*, 2011, 49, 3865-3872.
186. Y.-R. Kang, Y.-L. Li and M.-Y. Deng, *J. Mater. Chem.*, 2012, 22, 16283-16287.

187. P. Sutter, *Nat. Mater.*, 2009, 8, 171-172.
188. K. V. Emtsev, A. Bostwick, K. Horn, J. Jobst, G. L. Kellogg, L. Ley, J. L. McChesney, T. Ohta, S. A. Reshanov, J. Rohrl, E. Rotenberg, A. K. Schmid, D. Waldmann, H. B. Weber and T. Seyller, *Nat. Mater.*, 2009, 8, 203-207.
189. C. Virojanadara, M. Syvaejarvi, R. Yakimova, L. I. Johansson, A. A. Zakharov and T. Balasubramanian, *Phys. Rev., B*, 2008, 78, 245403.
190. Luxmi, N. Srivastava, R. M. Feenstra and P. J. Fisher, *J. Vac. Sci. Technol., B*, 2010, 28, C5C1-C5C7.
191. R. M. Tromp and J. B. Hannon, *Phys. Rev. Lett.*, 2009, 102, 106104.
192. Q. Huang, X. Chen, J. Liu, W. Wang, G. Wang, W. Wang, R. Yang, Y. Liu and L. Guo, *Chem. Commun.*, 2010, 46, 4917-4919.
193. V. Y. Aristov, G. Urbanik, K. Kummer, D. V. Vyalikh, O. V. Molodtsova, A. B. Preobrajenski, A. A. Zakharov, C. Hess, T. Haenke, B. Buechner, I. Vobornik, J. Fujii, G. Panaccione, Y. A. Ossipyan and M. Knupfer, *Nano Lett.*, 2010, 10, 992-995.
194. A. Ouerghi, A. Balan, C. Castelli, M. Picher, R. Belkhou, M. Eddrief, M. G. Silly, M. Marangolo, A. Shukla and F. Sirotti, *Appl. Phys. Lett.*, 2012, 101, 021603-021605.
195. A. Ouerghi, M. Marangolo, R. Belkhou, S. El Moussaoui, M. G. Silly, M. Eddrief, L. Largeau, M. Portail, B. Fain and F. Sirotti, *Phys. Rev., B*, 2010, 82, 125445.
196. J. Hass, W. A. de Heer and E. H. Conrad, *J. Phys. Condens. Matter*, 2008, 20, 323202.
197. N. Srivastava, G. He, Luxmi, P. C. Mende, R. M. Feenstra and Y. Sun, *J. Phys. D: Appl. Phys.*, 2012, 45, 154001.
198. C. Riedl, C. Coletti and U. Starke, *J. Phys. D: Appl. Phys.*, 2010, 43, 374009.
199. J. B. Hannon and R. M. Tromp, *Phys. Rev., B*, 2008, 77, 241404.
200. J. Hicks, K. Shepperd, F. Wang and E. H. Conrad, *J. Phys. D: Appl. Phys.*, 2012, 45, 154002.
201. E. J. Mele, *J. Phys. D: Appl. Phys.*, 2012, 45, 154004.
202. Luxmi, N. Srivastava, G. He, R. M. Feenstra and P. J. Fisher, *Phys. Rev., B*, 2010, 82, 235406.
203. Z.-Y. Juang, C.-Y. Wu, C.-W. Lo, W.-Y. Chen, C.-F. Huang, J.-C. Hwang, F.-R. Chen, K.-C. Leou and C.-H. Tsai, *Carbon*, 2009, 47, 2026-2031.
204. A. A. Woodworth and C. D. Stinespring, *Carbon*, 2010, 48, 1999-2003.
205. T. Yoneda, M. Shibuya, K. Mitsuhara, A. Visikovskiy, Y. Hoshino and Y. Kido, *Surf. Sci.*, 2010, 604, 1509-1515.
206. C. Y. Kang, L. L. Fan, S. Chen, Z. L. Liu, P. S. Xu and C. W. Zou, *Appl. Phys. Lett.*, 2012, 100, 251604-251605.
207. J. D. Caldwell, T. J. Anderson, J. C. Culbertson, G. G. Jernigan, K. D. Hobart, F. J. Kub, M. J. Tadjer, J. L. Tedesco, J. K. Hite, M. A. Mastro, R. L. Myers-Ward, C. R. Eddy, P. M. Campbell and D. K. Gaskill, *ACS Nano*, 2010, 4, 1108-1114.
208. S. Unarunotai, Y. Murata, C. E. Chialvo, H.-s. Kim, S. MacLaren, N. Mason, I. Petrov and J. A. Rogers, *Appl. Phys. Lett.*, 2009, 95, 202101-202103.
209. F. Varchon, R. Feng, J. Hass, X. Li, B. N. Nguyen, C. Naud, P. Mallet, J. Y. Veuillen, C. Berger, E. H. Conrad and L. Magaud, *Phys. Rev. Lett.*, 2007, 99, 126805.
210. W. Norimatsu and M. Kusunoki, *Phys. Chem. Chem. Phys.*, 2014, 16, 3501-3511.
211. C. M. Seah, S. P. Chai and A. R. Mohamed, *Carbon*, 2014, 70, 1-21.
212. P. Wu, W. H. Zhang, Z. Y. Li and J. L. Yang, *Small*, 2014, 10, 2136-2150.
213. A. Dahal and M. Batzill, *Nanoscale*, 2014, 6, 2548-2562.
214. M. Batzill, *Surf. Sci. Rep.*, 2012, 67, 83-115.
215. R. Munoz and C. Gomez-Aleixandre, *Chem. Vap. Deposition*, 2013, 19, 297-322.
216. H. An, W.-J. Lee and J. Jung, *Curr. Appl. Phys.*, 2011, 11, S81-S85.

217. D. Kondo, K. Yagi, M. Sato, M. Nihei, Y. Awano, S. Sato and N. Yokoyama, *Chem. Phys. Lett.*, 2011, 514, 294-300.
218. E. Sutter, P. Albrecht and P. Sutter, *Appl. Phys. Lett.*, 2009, 95, 133109.
219. P. W. Sutter, P. M. Albrecht and E. A. Sutter, *Appl. Phys. Lett.*, 2010, 97, 213101.
220. E. Sutter, P. Albrecht, F. E. Camino and P. Sutter, *Carbon*, 2010, 48, 4414-4420.
221. S. M. Wang, Y. H. Pei, X. Wang, H. Wang, Q. N. Meng, H. W. Tian, X. L. Zheng, W. T. Zheng and Y. C. Liu, *J. Phys. D: Appl. Phys.*, 2010, 43, 455402.
222. M. E. Ramon, A. Gupta, C. Corbet, D. A. Ferrer, H. C. P. Movva, G. Carpenter, L. Colombo, G. Bourianoff, M. Doczy, D. Akinwande, E. Tutuc and S. K. Banerjee, *ACS Nano*, 2011, 5, 7198-7204.
223. N. Zhan, G. Wang and J. Liu, *Appl. Phys., A*, 2011, 105, 341-345.
224. H. Ago, Y. Ito, N. Mizuta, K. Yoshida, B. Hu, C. M. Orofeo, M. Tsuji, K.-i. Ikeda and S. Mizuno, *ACS Nano*, 2010, 4, 7407-7414.
225. E. V. Rut'kov, A. V. Kuz'michev and N. R. Gall, *Physics of the Solid State*, 2011, 53, 1092-1098.
226. S. Roth, J. Osterwalder and T. Greber, *Surf. Sci.*, 2011, 605, L17-L19.
227. F. Mueller, S. Grandthyll, C. Zeitz, K. Jacobs, S. Huefner, S. Gsell and M. Schreck, *Phys. Rev., B*, 2011, 84, 075472.
228. C. Vo-Van, A. Kimouche, A. Reserbat-Plantey, O. Fruchart, P. Bayle-Guillemaud, N. Bendiab and J. Coraux, *Appl. Phys. Lett.*, 2011, 98, 181903.
229. A. Reina, X. Jia, J. Ho, D. Nezich, H. Son, V. Bulovic, M. S. Dresselhaus and J. Kong, *Nano Lett.*, 2009, 9, 30-35.
230. A. Reina, S. Thiele, X. Jia, S. Bhaviripudi, M. S. Dresselhaus, J. A. Schaefer and J. Kong, *Nano Res.*, 2009, 2, 509-516.
231. L. G. De Arco, Y. Zhang, C. W. Schlenker, K. Ryu, M. E. Thompson and C. Zhou, *ACS Nano*, 2010, 4, 2865-2873.
232. Y. Zhang, L. Gomez, F. N. Ishikawa, A. Madaria, K. Ryu, C. Wang, A. Badmaev and C. Zhou, *J. Phys. Chem. Lett.*, 2010, 1, 3101-3107.
233. S. J. Chae, F. Guenes, K. K. Kim, E. S. Kim, G. H. Han, S. M. Kim, H.-J. Shin, S.-M. Yoon, J.-Y. Choi, M. H. Park, C. W. Yang, D. Pribat and Y. H. Lee, *Adv. Mater*, 2009, 21, 2328-2333.
234. W. Liu, B. L. Jackson, J. Zhu, C.-Q. Miao, C.-H. Chung, Y.-J. Park, K. Sun, J. Woo and Y.-H. Xie, *ACS Nano*, 2010, 4, 3927-3932.
235. S.-Y. Kwon, C. V. Ciobanu, V. Petrova, V. B. Shenoy, J. Bareno, V. Gambin, I. Petrov and S. Kodambaka, *Nano Lett.*, 2009, 9, 3985-3990.
236. Y. Murata, S. Nie, A. Ebnonnasir, E. Starodub, B. B. Kappes, K. F. McCarty, C. V. Ciobanu and S. Kodambaka, *Phys. Rev., B*, 2012, 85, 205443.
237. T. Gao, S. Xie, Y. Gao, M. Liu, Y. Chen, Y. Zhang and Z. Liu, *ACS Nano*, 2011, 5, 9194-9201.
238. B. J. Kang, J. H. Mun, C. Y. Hwang and B. J. Cho, *J. Appl. Phys.*, 2009, 106, 104309.
239. C. Mattevi, H. Kim and M. Chhowalla, *J. Mater. Chem.*, 2011, 21, 3324-3334.
240. X. Li, W. Cai, J. An, S. Kim, J. Nah, D. Yang, R. Piner, A. Velamakanni, I. Jung, E. Tutuc, S. K. Banerjee, L. Colombo and R. S. Ruoff, *Science*, 2009, 324, 1312-1314.
241. W. Liu, H. Li, C. Xu, Y. Khatami and K. Banerjee, *Carbon*, 2011, 49, 4122-4130.
242. X. Li, C. W. Magnuson, A. Venugopal, J. An, J. W. Suk, B. Han, M. Borysiak, W. Cai, A. Velamakanni, Y. Zhu, L. Fu, E. M. Vogel, E. Voelkl, L. Colombo and R. S. Ruoff, *Nano Lett.*, 2010, 10, 4328-4334.
243. X. Li, C. W. Magnuson, A. Venugopal, R. M. Tromp, J. B. Hannon, E. M. Vogel, L. Colombo and R. S. Ruoff, *J. Am. Chem. Soc.*, 2011, 133, 2816-2819.
244. Y. Lee, S. Bae, H. Jang, S. Jang, S.-E. Zhu, S. H. Sim, Y. I. Song, B. H. Hong and J.-H. Ahn, *Nano Lett.*, 2010, 10, 490-493.
245. Z. Luo, Y. Lu, D. W. Singer, M. E. Berck, L. A. Somers, B. R. Goldsmith and A. T. C. Johnson, *Chem. Mater.*, 2011, 23, 1441-1447.

246. T. Oznuluer, E. Pince, E. O. Polat, O. Balci, O. Salihoglu and C. Kocabas, *Appl. Phys. Lett.*, 2011, 98, 183101.
247. N. Liu, L. Fu, B. Dai, K. Yan, X. Liu, R. Zhao, Y. Zhang and Z. Liu, *Nano Lett.*, 2011, 11, 297-303.
248. X. Liu, L. Fu, N. Liu, T. Gao, Y. Zhang, L. Liao and Z. Liu, *J. Phys. Chem. C*, 2011, 115, 11976-11982.
249. S. Chen, L. Brown, M. Levendorf, W. Cai, S.-Y. Ju, J. Edgeworth, X. Li, C. W. Magnuson, A. Velamakanni, R. D. Piner, J. Kang, J. Park and R. S. Ruoff, *ACS Nano*, 2011, 5, 1321-1327.
250. S. Chen, W. Cai, R. D. Piner, J. W. Suk, Y. Wu, Y. Ren, J. Kang and R. S. Ruoff, *Nano Lett.*, 2011, 11, 3519-3525.
251. R. S. Weatherup, B. C. Bayer, R. Blume, C. Ducati, C. Baehtz, R. Schlögl and S. Hofmann, *Nano Lett.*, 2011, 11, 4154-4160.
252. B. Dai, L. Fu, Z. Zou, M. Wang, H. Xu, S. Wang and Z. Liu, *Nat. Commun.*, 2011, 2, 522.
253. R. John, A. Ashokreddy, C. Vijayan and T. Pradeep, *Nanotechnology*, 2011, 22, 165701.
254. H. Gullapalli, A. L. M. Reddy, S. Kilpatrick, M. Dubey and P. M. Ajayan, *Small*, 2011, 7, 1697-1700.
255. S. Bae, H. Kim, Y. Lee, X. Xu, J.-S. Park, Y. Zheng, J. Balakrishnan, T. Lei, H. R. Kim, Y. I. Song, Y.-J. Kim, K. S. Kim, B. Ozyilmaz, J.-H. Ahn, B. H. Hong and S. Iijima, *Nat. Nanotechnol.*, 2010, 5, 574-578.
256. Q. Yu, L. A. Jauregui, W. Wu, R. Colby, J. Tian, Z. Su, H. Cao, Z. Liu, D. Pandey, D. Wei, T. F. Chung, P. Peng, N. P. Guisinger, E. A. Stach, J. Bao, S.-S. Pei and Y. P. Chen, *Nat. Mater.*, 2011, 10, 443-449.
257. R. S. Edwards and K. S. Coleman, *Acc. Chem. Res.*, 2012, 46, 23-30.
258. S. Thiele, A. Reina, P. Healey, J. Kedzierski, P. Wyatt, P.-L. Hsu, C. Keast, J. Schaefer and J. Kong, *Nanotechnology*, 2010, 21, 015601.
259. S. Bhaviripudi, X. Jia, M. S. Dresselhaus and J. Kong, *Nano Lett.*, 2010, 10, 4128-4133.
260. S. Kumar, N. McEvoy, T. Lutz, G. P. Keeley, V. Nicolosi, C. P. Murray, W. J. Blau and G. S. Duesberg, *Chem. Commun.*, 2010, 46, 1422-1424.
261. B. Zhang, W. H. Lee, R. Piner, I. Kholmanov, Y. Wu, H. Li, H. Ji and R. S. Ruoff, *ACS Nano*, 2012, 6, 2471-2476.
262. T. Yamada, J. Kim, M. Ishihara and M. Hasegawa, *J. Phys. D: Appl. Phys.*, 2013, 46, 063001.
263. T. Terasawa and K. Saiki, *Carbon*, 2012, 50, 869-874.
264. G. D. Yuan, W. J. Zhang, Y. Yang, Y. B. Tang, Y. Q. Li, J. X. Wang, X. M. Meng, Z. B. He, C. M. L. Wu, I. Bello, C. S. Lee and S. T. Lee, *Chem. Phys. Lett.*, 2009, 467, 361-364.
265. S. Kataria, S. Wagner, J. Ruhkopf, A. Gahoi, H. Pandey, R. Bornemann, S. Vaziri, A. D. Smith, M. Ostling and M. C. Lemme, *Phys. Status Solidi A*, 2014, 211, 2439-2449.
266. X. Liang, B. A. Sperling, I. Calizo, G. Cheng, C. A. Hacker, Q. Zhang, Y. Obeng, K. Yan, H. Peng, Q. Li, X. Zhu, H. Yuan, A. R. H. Walker, Z. Liu, L.-m. Peng and C. A. Richter, *ACS Nano*, 2011, 5, 9144-9153.
267. N. Liu, Z. Pan, L. Fu, C. Zhang, B. Dai and Z. Liu, *Nano Res.*, 2011, 4, 996-1004.
268. V. P. Verma, S. Das, I. Lahiri and W. Choi, *Appl. Phys. Lett.*, 2010, 96, 203108.
269. Z.-Y. Juang, C.-Y. Wu, A.-Y. Lu, C.-Y. Su, K.-C. Leou, F.-R. Chen and C.-H. Tsai, *Carbon*, 2010, 48, 3169-3174.
270. Y. Wang, Y. Zheng, X. Xu, E. Dubuisson, Q. Bao, J. Lu and K. P. Loh, *ACS Nano*, 2011, 5, 9927-9933.
271. M. Zheng, K. Takei, B. Hsia, H. Fang, X. Zhang, N. Ferralis, H. Ko, Y.-L. Chueh, Y. Zhang, R. Maboudian and A. Javey, *Appl. Phys. Lett.*, 2010, 96, 063110.
272. H. Ji, Y. Hao, Y. Ren, M. Charlton, W. H. Lee, Q. Wu, H. Li, Y. Zhu, Y. Wu, R. Piner and R. S. Ruoff, *ACS Nano*, 2011, 5, 7656-7661.

273. J. M. Garcia, R. He, M. P. Jiang, P. Kim, L. N. Pfeiffer and A. Pinczuk, *Carbon*, 2011, 49, 1006-1012.
274. Z. Yan, Z. Peng, Z. Sun, J. Yao, Y. Zhu, Z. Liu, P. M. Ajayan and J. M. Tour, *ACS Nano*, 2011, 5, 8187-8192.
275. Z. Sun, Z. Yan, J. Yao, E. Beitler, Y. Zhu and J. M. Tour, *Nature*, 2010, 468, 549-552.
276. H.-J. Shin, W. M. Choi, S.-M. Yoon, G. H. Han, Y. S. Woo, E. S. Kim, S. J. Chae, X.-S. Li, A. Benayad, L. Duong Dinh, F. Gunes, Y. H. Lee and J.-Y. Choi, *Adv. Mater*, 2011, 23, 4392-4397.
277. G. Ruan, Z. Sun, Z. Peng and J. M. Tour, *ACS Nano*, 2011, 5, 7601-7607.
278. A. Dato, V. Radmilovic, Z. Lee, J. Phillips and M. Frenklach, *Nano Lett.*, 2008, 8, 2012-2016.
279. A. Dato and M. Frenklach, *New J. Phys.*, 2010, 12, 125013.
280. C. R. Herron, K. S. Coleman, R. S. Edwards and B. G. Mendis, *J. Mater. Chem.*, 2011, 21, 3378-3383.
281. M. Choucair, P. Thordarson and J. A. Stride, *Nat. Nanotechnol.*, 2009, 4, 30-33.
282. A. Chakrabarti, J. Lu, J. C. Skrabutenas, T. Xu, Z. Xiao, J. A. Maguire and N. S. Hosmane, *J. Mater. Chem.*, 2011, 21, 9491-9493.
283. J. Zhao, Y. Guo, Z. Li, Q. Guo, J. Shi, L. Wang and J. Fan, *Carbon*, 2012, 50, 4939-4944.
284. Z. Xu, H. Li, W. Li, G. Cao, Q. Zhang, K. Li, Q. Fu and J. Wang, *Chem. Commun.*, 2011, 47, 1166-1168.
285. X. Wang, L. Zhi, N. Tsao, Ž. Tomović, J. Li and K. Müllen, *Angew. Chem. Int. Ed*, 2008, 47, 2990-2992.
286. C. D. Simpson, J. D. Brand, A. J. Berresheim, L. Przybilla, H. J. Räder and K. Müllen, *Chem. Eur. J.*, 2002, 8, 1424-1429.
287. L. Chen, Y. Hernandez, X. L. Feng and K. Mullen, *Angew. Chem. Int. Ed.*, 2012, 51, 7640-7654.
288. J. M. Tour, *Chem. Mater.*, 2014, 26, 163-171.
289. http://graphene-flagship.eu/, Accessed 25/01/2015.
290. M. Segal, *Nature*, 2012, 483, S43-S44.
291. W. Sigle, *Annu. Rev. Mater. Res.*, 2005, vol. 35, pp. 239-314.
292. J. C. Meyer, F. Eder, S. Kurasch, V. Skakalova, J. Kotakoski, H. J. Park, S. Roth, A. Chuvilin, S. Eyhusen, G. Benner, A. V. Krasheninnikov and U. Kaiser, *Phys. Rev. Lett.*, 2012, 108, 196102.
293. P. Y. Huang, C. S. Ruiz-Vargas, A. M. van der Zande, W. S. Whitney, M. P. Levendorf, J. W. Kevek, S. Garg, J. S. Alden, C. J. Hustedt, Y. Zhu, J. Park, P. L. McEuen and D. A. Muller, *Nature*, 2011, 469, 389-393.
294. B. Butz, C. Dolle, F. Niekiel, K. Weber, D. Waldmann, H. B. Weber, B. Meyer and E. Spiecker, *Nature*, 2014, 505, 533-537.
295. J. Huang, L. Qi and J. Li, *Nano Res.*, 2010, 3, 43-50.
296. Z. Liu, K. Suenaga, P. J. F. Harris and S. Iijima, *Phys. Rev. Lett.*, 2009, 102, 015501.
297. J. H. Warner, M. H. Rümmeli, T. Gemming, B. Büchner and G. A. D. Briggs, *Nano Lett.*, 2008, 9, 102-106.
298. M. H. Gass, U. Bangert, A. L. Bleloch, P. Wang, R. R. Nair and A. K. Geim, *Nat. Nanotechnol.*, 2008, 3, 676-681.
299. A. Hashimoto, K. Suenaga, A. Gloter, K. Urita and S. Iijima, *Nature*, 2004, 430, 870-873.
300. S. Park, H. C. Floresca, Y. Suh and M. J. Kim, *Carbon*, 2010, 48, 797-804.
301. N. R. Wilson, P. A. Pandey, R. Beanland, R. J. Young, I. A. Kinloch, L. Gong, Z. Liu, K. Suenaga, J. P. Rourke, S. J. York and J. Sloan, *ACS Nano*, 2009, 3, 2547-2556.
302. Z. Czigány and L. Hultman, *Ultramicroscopy*, 2010, 110, 815-819.
303. J. C. Meyer, A. K. Geim, M. I. Katsnelson, K. S. Novoselov, D. Obergfell, S. Roth, C. Girit and A. Zettl, *Solid State Commun.*, 2007, 143, 101-109.

304. S. Amelinckx, A. Lucas and P. Lambin, *Rep. Progr. Phys.*, 1999, 62, 1471-1524.
305. J. C. Meyer, M. Paillet, G. S. Duesberg and S. Roth, *Ultramicroscopy*, 2006, 106, 176-190.
306. C. S. Allen, C. Zhang, G. Burnell, A. P. Brown, J. Robertson and B. J. Hickey, *Carbon*, 2011, 49, 4961-4971.
307. R. F. Egerton and M. Malac, *J. Electron Spectrosc. Relat. Phenom.*, 2005, 143, 43-50.
308. S. R. P. Silva and V. Stolojan, *Thin Solid Films*, 2005, 488, 283-290.
309. P. Kovarik, E. B. D. Bourdon and R. H. Prince, *Phys. Rev., B*, 1993, 48, 12123-12129.
310. B. M. Kincaid, A. E. Meixner and P. M. Platzman, *Phys. Rev. Lett.*, 1978, 40, 1296-1299.
311. J. Robertson, *Semicond. Sci. Technol.*, 2003, 18, S12-S19.
312. N. Bernier, F. Bocquet, A. Allouche, W. Saikaly, C. Brosset, J. Thibault and A. Charai, *J. Electron Spectrosc. Relat. Phenom.*, 2008, 164, 34-43.
313. M. D. Rossell, C. Kuebel, G. Ilari, F. Rechberger, F. J. Heiligtag, M. Niederberger, D. Koziej and R. Erni, *Carbon*, 2013, 61, 404-411.
314. J. M. Plitzko and J. Mayer, *Ultramicroscopy*, 1999, 78, 207-219.
315. R. D. Leapman, C. E. Fiori and C. R. Swyt, *J. Microsc.*, 1984, 133, 239-253.
316. M. A. Aronova, Y. C. Kim, G. Zhang and R. D. Leapman, *Ultramicroscopy*, 2007, 107, 232-244.
317. Z. Q. Niu, J. Chen, H. H. Hng, J. Ma and X. D. Chen, *Adv. Mater*, 2012, 24, 4144-4150.
318. X. C. Dong, J. Chen, Y. W. Ma, J. Wang, M. B. Chan-Park, X. M. Liu, L. H. Wang, W. Huang and P. Chen, *Chem. Commun.*, 2012, 48, 10660-10662.
319. L. Zhang, Z. Li, Y. Tan, G. Lolli, N. Sakulchaicharoen, F. G. Requejo, B. S. Mun and D. E. Resasco, *Chem. Mater.*, 2006, 18, 5624-5629.
320. X. Zhang, A. Cao, B. Wei, Y. Li, J. Wei, C. Xu and D. Wu, *Chem. Phys. Lett.*, 2002, 362, 285-290.
321. J. Ji, G. Zhang, H. Chen, S. Wang, G. Zhang, F. Zhang and X. Fan, *Chem. Sci.*, 2011, 2, 484-487.
322. D. Briggs and J. T. Grant, *Surface Analysis by Auger and X-ray Photoelectron Spectroscopy*, IM Publications and SurfaceSpectra Limited, England, 2003.
323. C. K. Chua, A. Ambrosi and M. Pumera, *Analyst*, 2013, 138, 7012-7015.
324. R. Rozada, J. Paredes, S. Villar-Rodil, A. Martínez-Alonso and J. D. Tascón, *Nano Res.*, 2013, 6, 216-233.
325. R. Meier, *Vib. Spectrosc.*, 2005, 39, 266-269.
326. E. B. Brauns and R. J. Meier, *Vib. Spectrosc.*, 2009, 49, 303-304.
327. S. Doniach and M. Sunjic, *J. Phys., C: Solid State Phys.*, 1970, 3, 285.
328. F. Sette, G. K. Wertheim, Y. Ma, G. Meigs, S. Modesti and C. T. Chen, *Phys. Rev., B*, 1990, 41, 9766-9770.
329. P. M. T. M. van Attekum and G. K. Wertheim, *Phys. Rev. Lett.*, 1979, 43, 1896-1898.
330. H. Estrade-Szwarckopf, *Carbon*, 2004, 42, 1713-1721.
331. D.-Q. Yang and E. Sacher, *Langmuir*, 2005, 22, 860-862.
332. J. Filik, P. W. May, S. R. J. Pearce, R. K. Wild and K. R. Hallam, *Diamond Relat. Mater.*, 2003, 12, 974-978.
333. T. Y. Leung, W. F. Man, P. K. Lim, W. C. Chan, F. Gaspari and S. Zukotynski, *J. Non-Cryst. Solids*, 1999, 254, 156-160.
334. S. T. Jackson and R. G. Nuzzo, *Appl. Surf. Sci.*, 1995, 90, 195-203.
335. S. Kaciulis, *Surf. Interface Anal.*, 2012, 44, 1155-1161.
336. S. Tougaard and C. Jansson, *Surf. Interface Anal.*, 1992, 19, 171-174.
337. C. Jansson, H. S. Hansen, C. Jung, W. Braun and S. Tougaard, *Surf. Interface Anal.*, 1992, 19, 217-221.
338. J. A. Leiro, M. H. Heinonen, T. Laiho and I. G. Batirev, *J. Electron Spectrosc. Relat. Phenom.*, 2003, 128, 205-213.

339. D. Yang, A. Velamakanni, G. Bozoklu, S. Park, M. Stoller, R. D. Piner, S. Stankovich, I. Jung, D. A. Field, C. A. Ventrice Jr and R. S. Ruoff, *Carbon*, 2009, 47, 145-152.
340. S. V. Tkachev, E. Y. Buslaeva, A. V. Naumkin, S. L. Kotova, I. V. Laure and S. P. Gubin, *Inorg. Mater.*, 2012, 48, 796-802.
341. L. Calliari, *Diamond Relat. Mater.*, 2005, 14, 1232-1240.
342. A. P. Dementjev and K. I. Maslakov, *Appl. Surf. Sci.*, 2006, 253, 1095-1100.
343. G. C. Smith and P. J. Shuff, *Appl. Surf. Sci.*, 1996, 103, 199-203.
344. J. C. Lascovich, R. Giorgi and S. Scaglione, *Appl. Surf. Sci.*, 1991, 47, 17-21.
345. B. Lesiak, J. Zemek, J. Houdkova, A. Kromka, Oacute and A. Zwik, *Anal. Sci.*, 2010, 26, 217-222.
346. M. S. Dresselhaus, G. Dresselhaus, R. Saito and A. Jorio, *Phys. Rep.*, 2005, 409, 47-99.
347. A. Jorio, R. Saito, G. Dresselhaus and M. S. Dresselhaus, *Philos. Trans. R. Soc. London, Ser. A*, 2004, 362, 2311-2336.
348. H. Kuzmany, R. Pfeiffer, M. Hulman and C. Kramberger, *Philos. Trans. R. Soc. London, Ser. A*, 2004, 362, 2375-2406.
349. S. Prawer and R. J. Nemanich, *Philos. Trans. R. Soc. London, Ser. A*, 2004, 362, 2537-2565.
350. A. C. Ferrari and J. Robertson, *Philos. Trans. R. Soc. London, Ser. A*, 2004, 362, 2477-2512.
351. M. S. Dresselhaus, A. Jorio, M. Hofmann, G. Dresselhaus and R. Saito, *Nano Lett.*, 2010, 10, 751-758.
352. F. Tuinstra and J. L. Koenig, *J. Chem. Phys.*, 1970, 53, 1126-1130.
353. A. C. Ferrari and J. Robertson, *Phys. Rev., B*, 2000, 61, 14095-14107.
354. A. Jorio, E. H. M. Ferreira, M. V. O. Moutinho, F. Stavale, C. A. Achete and R. B. Capaz, *Phys. Status Solidi B*, 2010, 247, 2980-2982.
355. A. C. Ferrari, *Solid State Commun.*, 2007, 143, 47-57.
356. C. Casiraghi, A. Hartschuh, H. Qian, S. Piscanec, C. Georgi, A. Fasoli, K. S. Novoselov, D. M. Basko and A. C. Ferrari, *Nano Lett.*, 2009, 9, 1433-1441.
357. A. K. Gupta, Y. Tang, V. H. Crespi and P. C. Eklund, *Phys. Rev., B*, 2010, 82, 241406.
358. J. M. Caridad, F. Rossella, V. Bellani, M. S. Grandi and E. Diez, *J. Raman Spectrosc.*, 2011, 42, 286-293.
359. A. C. Ferrari, J. C. Meyer, V. Scardaci, C. Casiraghi, M. Lazzeri, F. Mauri, S. Piscanec, D. Jiang, K. S. Novoselov, S. Roth and A. K. Geim, *Phys. Rev. Lett.*, 2006, 97.
360. L. G. Cançado, K. Takai, T. Enoki, M. Endo, Y. A. Kim, H. Mizusaki, N. L. Speziali, A. Jorio and M. A. Pimenta, *Carbon*, 2008, 46, 272-275.
361. A. Kaniyoor and S. Ramaprabhu, *AIP Advances*, 2012, 2, 032183.
362. X. Diez-Betriu, S. Alvarez-Garcia, C. Botas, P. Alvarez, J. Sanchez-Marcos, C. Prieto, R. Menendez and A. de Andres, *J. Mater. Chem., C*, 2013, 1, 6905-6912.
363. M. A. Pimenta, G. Dresselhaus, M. S. Dresselhaus, L. G. Cancado, A. Jorio and R. Saito, *Phys. Chem. Chem. Phys.*, 2007, 9, 1276-1290.
364. K. N. Kudin, B. Ozbas, H. C. Schniepp, R. K. Prud'homme, I. A. Aksay and R. Car, *Nano Lett.*, 2007, 8, 36-41.
365. T. V. Cuong, V. H. Pham, Q. T. Tran, S. H. Hahn, J. S. Chung, E. W. Shin and E. J. Kim, *Mater. Lett.*, 2010, 64, 399-401.
366. K. Krishnamoorthy, M. Veerapandian, R. Mohan and S. J. Kim, *Appl. Phys., A*, 2012, 106, 501-506.
367. C. Mattevi, G. Eda, S. Agnoli, S. Miller, K. A. Mkhoyan, O. Celik, D. Mastrogiovanni, G. Granozzi, E. Garfunkel and M. Chhowalla, *Adv. Funct. Mater.*, 2009, 19, 2577-2583.
368. S. D. Bergin, Z. Sun, D. Rickard, P. V. Streich, J. P. Hamilton and J. N. Coleman, *ACS Nano*, 2009, 3, 2340-2350.

369. B. Zhou, Y. Lin, H. P. Li, W. J. Huang, J. W. Connell, L. F. Allard and Y. P. Sun, *J. Phys. Chem. B*, 2003, 107, 13588-13592.
370. D. Li, M. B. Mueller, S. Gilje, R. B. Kaner and G. G. Wallace, *Nat. Nanotechnol.*, 2008, 3, 101-105.
371. D. Luo, G. Zhang, J. Liu and X. Sun, *J. Phys. Chem. C*, 2011, 115, 11327-11335.
372. Z. Luo, Y. Lu, L. A. Somers and A. T. C. Johnson, *J. Am. Chem. Soc.*, 2009, 131, 898-899.
373. E. Abou-Hamad, M. R. Babaa, M. Bouhrara, Y. Kim, Y. Saih, S. Dennler, F. Mauri, J. M. Basset, C. Goze-Bac and T. Wågberg, *Phys. Rev., B*, 2011, 84, 165417.
374. C. Engtrakul, M. F. Davis, K. Mistry, B. A. Larsen, A. C. Dillon, M. J. Heben and J. L. Blackburn, *J. Am. Chem. Soc.*, 2010, 132, 9956-9957.
375. C. Engtrakul, V. M. Irurzun, E. L. Gjersing, J. M. Holt, B. A. Larsen, D. E. Resasco and J. L. Blackburn, *J. Am. Chem. Soc.*, 2012, 134, 4850-4856.
376. A. Lerf, H. He, T. Riedl, M. Forster and J. Klinowski, *Solid State Ionics*, 1997, 101–103, Part 2, 857-862.
377. W. Gao, L. B. Alemany, L. Ci and P. M. Ajayan, *Nat. Chem.*, 2009, 1, 403-408.
378. H. He, T. Riedl, A. Lerf and J. Klinowski, *J. Phys. Chem.*, 1996, 100, 19954-19958.
379. W. W. Cai, R. D. Piner, F. J. Stadermann, S. Park, M. A. Shaibat, Y. Ishii, D. X. Yang, A. Velamakanni, S. J. An, M. Stoller, J. H. An, D. M. Chen and R. S. Ruoff, *Science*, 2008, 321, 1815-1817.
380. L. B. Casablanca, M. A. Shaibat, W. W. W. Cai, S. Park, R. Piner, R. S. Ruoff and Y. Ishii, *J. Am. Chem. Soc.*, 2010, 132, 5672-5676.
381. H. B. Li, W. J. Hua, Z. J. Lin and Y. Luo, *J. Phys. Chem. B*, 2012, 116, 12641-12650.
382. H. R. Thomas, S. P. Day, W. E. Woodruff, C. Valles, R. J. Young, I. A. Kinloch, G. W. Morley, J. V. Hanna, N. R. Wilson and J. P. Rourke, *Chem. Mater.*, 2013, 25, 3580-3588.
383. N. Lu, Y. Huang, H. B. Li, Z. Y. Li and J. L. Yang, *J. Chem. Phys.*, 2010, 133, 034502.
384. G. S. B. McKee and K. S. Vecchio, *J. Phys. Chem., B*, 2005, 110, 1179-1186.
385. D. Bom, R. Andrews, D. Jacques, J. Anthony, B. Chen, M. S. Meier and J. P. Selegue, *Nano Lett.*, 2002, 2, 615-619.
386. H. Y. Nan, Z. H. Ni, J. Wang, Z. Zafar, Z. X. Shi and Y. Y. Wang, *J. Raman Spectrosc.*, 2013, 44, 1018-1021.
387. E. Titus, N. Ali, G. Cabral, J. Gracio, P. Ramesh Babu and M. J. Jackson, *J. Mater. Eng. Perform.*, 2006, 15, 182-186.
388. M. Zhang, M. Yudasaka, A. Koshio and S. Iijima, *Chem. Phys. Lett.*, 2002, 364, 420-426.
389. H. K. Jeong, M. H. Jin, K. P. So, S. C. Lim and Y. H. Lee, *J. Phys. D: Appl. Phys.*, 2009, 42.
390. X. Mei and J. Ouyang, *Carbon*, 2011, 49, 5389-5397.
391. F. Barroso-Bujans, A. n. Alegría and J. Colmenero, *J. Phys. Chem., C*, 2010, 114, 21645-21651.
392. M. J. McAllister, J.-L. Li, D. H. Adamson, H. C. Schniepp, A. A. Abdala, J. Liu, M. Herrera-Alonso, D. L. Milius, R. Car, R. K. Prud'homme and I. A. Aksay, *Chem. Mater.*, 2007, 19, 4396-4404.
393. C. Dezhi, L. Lidong and G. Lin, *Nanotechnology*, 2011, 22, 325601.
394. S. Park, J. An, J. R. Potts, A. Velamakanni, S. Murali and R. S. Ruoff, *Carbon*, 2011, 49, 3019-3023.
395. C. Zhao, L. Ji, H. Liu, G. Hu, S. Zhang, M. Yang and Z. Yang, *J. Solid State Chem.*, 2004, 177, 4394-4398.
396. J. D. Saxby, S. P. Chatfield, A. J. Palmisano, A. M. Vassallo, M. A. Wilson and L. S. K. Pang, *J. Phys. Chem.*, 1992, 96, 17-18.

397. L. S. K. Pang, J. D. Saxby and S. P. Chatfield, *J. Phys. Chem.*, 1993, 97, 6941-6942.
398. C. Botas, A. M. Pérez-Mas, P. Álvarez, R. Santamaría, M. Granda, C. Blanco and R. Menéndez, *Carbon*, 2013, 63, 576-578.
399. C. Botas, P. Álvarez, C. Blanco, R. Santamaría, M. Granda, P. Ares, F. Rodríguez-Reinoso and R. Menéndez, *Carbon*, 2012, 50, 275-282.
400. J. Chen, B. Yao, C. Li and G. Shi, *Carbon*, 2013, 64, 225-229.
401. K. Krishnamoorthy, M. Veerapandian, K. Yun and S. J. Kim, *Carbon*, 2013, 53, 38-49.
402. X. Tong, H. Wang, G. Wang, L. Wan, Z. Ren, J. Bai and J. Bai, *J. Solid State Chem.*, 2011, 184, 982-989.
403. J. Zhao, S. Pei, W. Ren, L. Gao and H.-M. Cheng, *ACS Nano*, 2010, 4, 5245-5252.
404. S. Eigler, M. Enzelberger-Heim, S. Grimm, P. Hofmann, W. Kroener, A. Geworski, C. Dotzer, M. Roeckert, J. Xiao, C. Papp, O. Lytken, H.-P. Steinrueck, P. Mueller and A. Hirsch, *Adv. Mater*, 2013, 25, 3583-3587.
405. L. Zhang, J. Liang, Y. Huang, Y. Ma, Y. Wang and Y. Chen, *Carbon*, 2009, 47, 3365-3368.
406. S. Pan and I. A. Aksay, *ACS Nano*, 2011, 5, 4073-4083.
407. J. Cao, G. Q. Qi, K. Ke, Y. Luo, W. Yang, B. H. Xie and M. B. Yang, *J. Mater. Sci.*, 2012, 47, 5097-5105.
408. H. R. Thomas, C. Valles, R. J. Young, I. A. Kinloch, N. R. Wilson and J. P. Rourke, *J. Mater. Chem., C*, 2013, 1, 338-342.
409. K. P. Loh, Q. Bao, G. Eda and M. Chhowalla, *Nat. Chem.*, 2010, 2, 1015-1024.
410. P. Sun, M. Zhu, K. Wang, M. Zhong, J. Wei, D. Wu, Z. Xu and H. Zhu, *ACS Nano*, 2012, 7, 428-437.
411. H. W. Ha, A. Choudhury, T. Kamal, D.-H. Kim and S.-Y. Park, *ACS Appl. Mater. Interf*, 2012, 4, 4623-4630.
412. W. Ai, J.-Q. Liu, Z.-Z. Du, X.-X. Liu, J.-Z. Shang, M.-D. Yi, L.-H. Xie, J.-J. Zhang, H.-F. Lin, T. Yu and W. Huang, *R. Soc. Chem. Adv.*, 2013, 3, 45-49.
413. G. Wang, B. Wang, J. Park, J. Yang, X. Shen and J. Yao, *Carbon*, 2009, 47, 68-72.
414. S. Stankovich, D. A. Dikin, G. H. B. Dommett, K. M. Kohlhaas, E. J. Zimney, E. A. Stach, R. D. Piner, S. T. Nguyen and R. S. Ruoff, *Nature*, 2006, 442, 282-286.
415. W. Li, X.-Z. Tang, H.-B. Zhang, Z.-G. Jiang, Z.-Z. Yu, X.-S. Du and Y.-W. Mai, *Carbon*, 2011, 49, 4724-4730.
416. F. Kim, J. Luo, R. Cruz-Silva, L. J. Cote, K. Sohn and J. Huang, *Adv. Funct. Mater.*, 2010, 20, 2867-2873.
417. K.-H. Liao, A. Mittal, S. Bose, C. Leighton, K. A. Mkhoyan and C. W. Macosko, *ACS Nano*, 2011, 5, 1253-1258.
418. Y. Wang, J. E. Panzik, B. Kiefer and K. K. M. Lee, *Sci. Rep.*, 2012, 2.
419. C. Fantini, M. A. Pimenta and M. S. Strano, *J. Phys. Chem., C*, 2008, 112, 13150-13155.
420. J. Li, H. Lin, Z. Yang and J. Li, *Carbon*, 2011, 49, 3024-3030.
421. Y. Zhou, Q. L. Bao, L. A. L. Tang, Y. L. Zhong and K. P. Loh, *Chem. Mater.*, 2009, 21, 2950-2956.
422. Y. Shen, S. Yang, P. Zhou, Q. Sun, P. Wang, L. Wan, J. Li, L. Chen, X. Wang, S. Ding and D. W. Zhang, *Carbon*, 2013, 62, 157-164.
423. O. C. Compton, B. Jain, D. A. Dikin, A. Abouimrane, K. Amine and S. T. Nguyen, *ACS Nano*, 2011, 5, 4380-4391.
424. W. Chen and L. Yan, *Nanoscale*, 2010, 2, 559-563.
425. Z.-L. Chen, F.-Y. Kam, V. Keerthi, J. Song, C. Hu, L.-Y. Wong, G.-K. Lim and L.-L. Chua, *J. Mater. Chem., C*, 2013, 1, 7246-7254.
426. C. Zhang, W. Lv, X. Xie, D. Tang, C. Liu and Q.-H. Yang, *Carbon*, 2013, 62, 11-24.
427. B. Shen, D. Lu, W. Zhai and W. Zheng, *J. Mater. Chem., C*, 2013, 1, 50-53.

428. W. Lv, D.-M. Tang, Y.-B. He, C.-H. You, Z.-Q. Shi, X.-C. Chen, C.-M. Chen, P.-X. Hou, C. Liu and Q.-H. Yang, *ACS Nano*, 2009, 3, 3730-3736.
429. C. Botas, P. Álvarez, C. Blanco, R. Santamaría, M. Granda, M. D. Gutiérrez, F. Rodríguez-Reinoso and R. Menéndez, *Carbon*, 2013, 52, 476-485.
430. I. Jung, D. A. Field, N. J. Clark, Y. Zhu, D. Yang, R. D. Piner, S. Stankovich, D. A. Dikin, H. Geisler, C. A. Ventrice and R. S. Ruoff, *J. Phys. Chem., C*, 2009, 113, 18480-18486.
431. P. V. Kumar, N. M. Bardhan, S. Tongay, J. Wu, A. M. Belcher and J. C. Grossman, *Nat. Chem.*, 2014, 6, 151-158.
432. Y. Chen, X. O. Zhang, D. C. Zhang, P. Yu and Y. W. Ma, *Carbon*, 2011, 49, 573-580.
433. J. P. Rourke, P. A. Pandey, J. J. Moore, M. Bates, I. A. Kinloch, R. J. Young and N. R. Wilson, *Angew. Chem. Int. Ed*, 2011, 50, 3173-3177.
434. S. Fogden, R. Verdejo, B. Cottam and M. Shaffer, *Chem. Phys. Lett.*, 2008, 460, 162-167.
435. K. A. Worsley, R. W. Kondrat, S. K. Pal, I. Kalinina and R. C. Haddon, *Carbon*, 2011, 49, 4982-4986.
436. L. S. Shao, J. J. Li, Y. L. Zhang, S. M. Gong, H. Zhang and Y. H. Wang, *J. Mater. Chem., A*, 2014, 2, 14173-14180.
437. Y. Feng, N. Feng and G. Du, *R. Soc. Chem. Adv.*, 2013, 3, 21466-21474.
438. C. Zhu, S. Guo, Y. Fang and S. Dong, *ACS Nano*, 2010, 4, 2429-2437.
439. Y. Wang, Z. Shi and J. Yin, *ACS Appl. Mater. Interf*, 2011, 3, 1127-1133.
440. O. Akhavan, E. Ghaderi, E. Abouei, S. Hatamie and E. Ghasemi, *Carbon*, 2014, 66, 395-406.
441. T. A. Pham, J. S. Kim, J. S. Kim and Y. T. Jeong, *Colloids Surf., A*, 2011, 384, 543-548.
442. C. Chen, J. Li, R. Li, G. Xiao and D. Yan, *New J. Chem.*, 2013, 37, 2778-2783.
443. J. K. Ma, X. R. Wang, Y. Liu, T. Wu, Y. Liu, Y. Q. Guo, R. Q. Li, X. Y. Sun, F. Wu, C. B. Li and J. P. Gao, *J. Mater. Chem., A*, 2013, 1, 2192-2201.
444. S. Bose, T. Kuila, A. K. Mishra, N. H. Kim and J. H. Lee, *J. Mater. Chem.*, 2012, 22, 9696-9703.
445. B. Konkena and S. Vasudevan, *J. Phys. Chem. Lett.*, 2012, 3, 867-872.
446. C.-J. Shih, S. Lin, R. Sharma, M. S. Strano and D. Blankschtein, *Langmuir*, 2011, 28, 235-241.
447. H. Wang and Y. H. Hu, *J. Colloid Interface Sci.*, 2013, 391, 21-27.
448. E. Courvoisier, P. A. Williams, G. K. Lim, C. E. Hughes and K. D. M. Harris, *Chemical Communications*, 2012, 48, 2761-2763.
449. U. Das, G. Hariprasad, A. S. Ethayathulla, P. Manral, T. K. Das, S. Pasha, A. Mann, M. Ganguli, A. K. Verma, R. Bhat, S. K. Chandrayan, S. Ahmed, S. Sharma, P. Kaur, T. P. Singh and A. Srinivasan, *PLoS One*, 2007, 2.
450. T. Arakawa, D. Ejima, K. Tsumoto, N. Obeyama, Y. Tanaka, Y. Kita and S. N. Timasheff, *Biophys. Chem.*, 2007, 127, 1-8.
451. B. M. Baynes, D. I. C. Wang and B. L. Trout, *Biochemistry*, 2005, 44, 4919-4925.
452. D. Shukla, L. Zamolo, C. Cavallotti and B. L. Trout, *J. Phys. Chem., B*, 2011, 115, 2645-2654.
453. J. S. Stevens, A. C. de Luca, M. Pelendritis, G. Terenghi, S. Downes and S. L. M. Schroeder, *Surf. Interface Anal.*, 2013, 45, 1238-1246.
454. Y.-n. Guo, X. Lu, J. Weng and Y. Leng, *J. Phys. Chem., C*, 2013, 117, 5708-5717.
455. Y. Zhang, L. Wang, D. Lu, X. Shi, C. Wang and X. Duan, *Electrochim. Acta*, 2012, 80, 77-83.
456. M. Zhang, B.-C. Yin, X.-F. Wang and B.-C. Ye, *Chem. Commun.*, 2011, 47, 2399-2401.
457. L. Ou, Y. Luo and G. Wei, *J. Phys. Chem., B*, 2011, 115, 9813-9822.
458. A. Hirano, T. Tanaka, H. Kataura and T. Kameda, *Chem. Eur. J.*, 2014, 20, 4922-4930.

459. A. N. Camden, S. A. Barr and R. J. Berry, *J. Phys. Chem., B*, 2013, 117, 10691-10697.
460. J. Gao, F. Liu, Y. Liu, N. Ma, Z. Wang and X. Zhang, *Chem. Mater.*, 2010, 22, 2213-2218.
461. J. Guo, L. Ren, R. Wang, C. Zhang, Y. Yang and T. Liu, *Composites Part B*, 2011, 42, 2130-2135.
462. S. Park, Y. Hu, J. O. Hwang, E.-S. Lee, L. B. Casabianca, W. Cai, J. R. Potts, H.-W. Ha, S. Chen, J. Oh, S. O. Kim, Y.-H. Kim, Y. Ishii and R. S. Ruoff, *Nat Commun*, 2012, 3, 638.
463. C. Valles, A. M. Abdelkader, R. J. Young and I. A. Kinloch, *Faraday Discuss.*, 2014, 173, 379-390.
464. P. Jana, V. A. de la Pena O'Shea, J. M. Coronado and D. P. Serrano, *Energ. Environ. Sci.*, 2011, 4, 778-783.
465. Y. Takanori and T. Yoshizo, *Jpn. J. Appl. Phys.*, 2011, 50, 015103.
466. M. Zhou, F. L. Pasquale, P. A. Dowben, A. Boosalis, M. Schubert, V. Darakchieva, R. Yakimova, L. M. Kong and J. A. Kelber, *J. Phys. Condens. Matter*, 2012, 24, 072201.
467. G. A. Forrest and A. J. Alexander, *Carbon*, 2008, 46, 818-821.
468. G. Schlessinger, *Inorganic Laboratory Preparations*, Chemical Publishing Co.,, New York, 1962.
469. J. Park, R. S. Zhu and M. C. Lin, *J. Chem. Phys.*, 2002, 117, 3224-3231.
470. R. Sivaramakrishnan, M. C. Su, J. V. Michael, S. J. Klippenstein, L. B. Harding and B. Ruscic, *J. Phys. Chem. A*, 2010, 114, 9425-9439.
471. J. Li, A. Kazakov and F. L. Dryer, *J. Phys. Chem. A*, 2004, 108, 7671-7680.
472. J. Y. Sun, C. Wu, F. Silly, A. A. Koos, F. Dillon, N. Grobert and M. R. Castell, *Chem. Commun.*, 2013, 49, 3748-3750.
473. C. Esarte, M. a. Peg, M. a. P. Ruiz, A. n. Millera, R. Bilbao and M. a. U. Alzueta, *Ind. Eng. Chem. Res.*, 2011, 50, 4412-4419.
474. H. Qi, C. Qian and J. Liu, *Chem. Mater.*, 2006, 18, 5691-5695.
475. L. Ya-Li, Z. Liang-Hong, Z. Xiao-Hua and H. W. Alan, *Nanotechnology*, 2007, 18, 225604.
476. O. Guellati, I. Janowska, D. Bégin, M. Guerioune, Z. Mekhalif, J. Delhalle, S. Moldovan, O. Ersen and C. Pham-Huu, *Appl. Catal., A*, 2012, 423–424, 7-14.
477. A. Guermoune, T. Chari, F. Popescu, S. S. Sabri, J. Guillemette, H. S. Skulason, T. Szkopek and M. Siaj, *Carbon*, 2011, 49, 4204-4210.
478. Y. Shen and A. C. Lua, *Sci. Rep.*, 2013, 3, 3037.
479. S. Chen, P. Bao, L. Xiao and G. Wang, *Carbon*, 2013, 64, 158-169.
480. H. Badenhorst, *Carbon*, 2014, 66, 674-690.
481. X. Wang, H. You, F. Liu, M. Li, L. Wan, S. Li, Q. Li, Y. Xu, R. Tian, Z. Yu, D. Xiang and J. Cheng, *Chem. Vap. Deposition*, 2009, 15, 53-56.
482. B. H. Liu, J. Ding, Z. Y. Zhong, Z. L. Dong, T. White and J. Y. Lin, *Chem. Phys. Lett.*, 2002, 358, 96-102.
483. R. T. K. Baker, M. A. Barber, P. S. Harris, F. S. Feates and R. J. Waite, *J. Catal.*, 1972, 26, 51-62.
484. C. Ohnishi, K. Asano, S. Iwamoto, K. Chikama and M. Inoue, *Catal. Today*, 2007, 120, 145-150.
485. P. W. Park, J. K. Kil, H. H. Kung and M. C. Kung, *Catal. Today*, 1998, 42, 51-60.
486. M. Haneda, Y. Kintaichi, N. Bion and H. Hamada, *Appl. Catal., B*, 2003, 46, 473-482.
487. H. Fujimoto, *Carbon*, 2003, 41, 1585-1592.
488. A. Milev, M. Wilson, G. S. K. Kannangara and N. Tran, *Mater. Chem. Phys.*, 2008, 111, 346-350.
489. S. E. Bryan, Y. X. Yang and R. Murali, *J. Phys. Chem. C*, 2011, 115, 10230-10235.
490. D. L. Nika, A. S. Askerov and A. A. Balandin, *Nano Lett.*, 2012, 12, 3238-3244.
491. O. V. Yazyev, *Acc. Chem. Res.*, 2013, 46, 2319-2328.

492. P. Ruffieux, J. Cai, N. C. Plumb, L. Patthey, D. Prezzi, A. Ferretti, E. Molinari, X. Feng, K. Müllen, C. A. Pignedoli and R. Fasel, *ACS Nano*, 2012, 6, 6930-6935.
493. L. Gong, I. A. Kinloch, R. J. Young, I. Riaz, R. Jalil and K. S. Novoselov, *Adv. Mater*, 2010, 22, 2694-2697.
494. C. Y. Su, D. L. Fu, A. Y. Lu, K. K. Liu, Y. P. Xu, Z. Y. Juang and L. J. Li, *Nanotechnology*, 2011, 22.
495. R. Wang, Y. Hao, Z. Wang, H. Gong and J. T. L. Thong, *Nano Lett.*, 2010, 10, 4844-4850.
496. T. Xiao, B. J. Heng, X. Y. Hu and Y. W. Tang, *J. Phys. Chem. C*, 2011, 115, 25155-25159.
497. G. Ning, Z. Fan, G. Wang, J. Gao, W. Qian and F. Wei, *Chem. Commun.*, 2011, 47, 5976-5978.
498. D. Wei, Y. Liu, H. Zhang, L. Huang, B. Wu, J. Chen and G. Yu, *J. Am. Chem. Soc.*, 2009, 131, 11147-11154.
499. Z. Chen, W. Ren, B. Liu, L. Gao, S. Pei, Z.-S. Wu, J. Zhao and H.-M. Cheng, *Carbon*, 2010, 48, 3543-3550.
500. K. Lee, M. Kim and H. Kim, *J. Mater. Chem.*, 2010, 20, 3791-3798.
501. Y. Xia, Y. Xiong, B. Lim and S. E. Skrabalak, *Angew. Chem. Int. Ed*, 2009, 48, 60-103.
502. H. I. Rasool, E. B. Song, M. J. Allen, J. K. Wassei, R. B. Kaner, K. L. Wang, B. H. Weiller and J. K. Gimzewski, *Nano Lett.*, 2010, 11, 251-256.
503. W. H. Qi and M. P. Wang, *Mater. Chem. Phys.*, 2004, 88, 280-284.
504. H. M. Lu, P. Y. Li, Z. H. Cao and X. K. Meng, *J. Phys. Chem. C*, 2009, 113, 7598-7602.
505. P. J. F. Harris, *Int. Mater. Rev.*, 1997, 42, 206-218.
506. K.-J. Lo, H.-Y. Liao, H.-W. Cheng, W.-C. Lin, B.-Y. Yu, J.-J. Shyue and C.-C. Chang, *J. Nanopart. Res.*, 2011, 13, 669-682.
507. S. Sun, F. Zhou, L. Wang, X. Song and Z. Yang, *Cryst. Growth Des.*, 2009, 10, 541-547.
508. H. Y. Zhao, Y. F. Wang and J. H. Zeng, *Cryst. Growth Des.*, 2008, 8, 3731-3734.
509. Y. Zhang, B. Deng, T. R. Zhang, D. M. Gao and A. W. Xu, *J. Phys. Chem. C*, 2010, 114, 5073-5079.
510. H. Xu, W. Wang and W. Zhu, *J. Phys. Chem., B*, 2006, 110, 13829-13834.
511. J.-Y. Ho and M. H. Huang, *J. Phys. Chem., C*, 2009, 113, 14159-14164.
512. N. A. Luechinger, E. K. Athanassiou and W. J. Stark, *Nanotechnology*, 2008, 19.
513. O. Frank, J. Vejpravova, V. Holy, L. Kavan and M. Kalbac, *Carbon*, 2014, 68, 440-451.
514. J. D. Wood, S. W. Schmucker, A. S. Lyons, E. Pop and J. W. Lyding, *Nano Lett.*, 2011, 11, 4547-4554.
515. S. Nie, J. M. Wofford, N. C. Bartelt, O. D. Dubon and K. F. McCarty, *Phys. Rev., B*, 2011, 84, 155425.
516. Y. A. Wu, A. W. Robertson, F. Schaeffel, S. C. Speller and J. H. Warner, *Chem. Mater.*, 2011, 23, 4543-4547.
517. L. Gao, J. R. Guest and N. P. Guisinger, *Nano Lett.*, 2010, 10, 3512-3516.
518. H. I. Rasool, E. B. Song, M. Mecklenburg, B. C. Regan, K. L. Wang, B. H. Weiller and J. K. Gimzewski, *J. Am. Chem. Soc.*, 2011, 133, 12536-12543.
519. J. M. Wofford, S. Nie, K. F. McCarty, N. C. Bartelt and O. D. Dubon, *Nano Lett.*, 2010, 10, 4890-4896.
520. X. Li, W. Cai, L. Colombo and R. S. Ruoff, *Nano Lett.*, 2009, 9, 4268-4272.
521. H. Chen, W. Zhu and Z. Zhang, *Phys. Rev. Lett.*, 2010, 104, 186101.
522. S. K. Sengar, B. R. Mehta, R. Kumar and V. Singh, *Sci. Rep.*, 2013, 3, 2814.
523. E. K. Athanassiou, R. N. Grass and W. J. Stark, *Nanotechnology*, 2006, 17, 1668-1673.
524. Y. Qin, Q. Zhang and Z. Cui, *J. Catal.*, 2004, 223, 389-394.
525. L. Yu, L. Sui, Y. Qin and Z. Cui, *Chem. Eng. J.*, 2008, 144, 514-517.

526. A. Shaikjee and N. J. Coville, *Mater. Chem. Phys.*, 2011, 125, 899-907.
527. W. W. Zhou, Z. Y. Han, J. Y. Wang, Y. Zhang, Z. Jin, X. Sun, Y. W. Zhang, C. H. Yan and Y. Li, *Nano Lett.*, 2006, 6, 2987-2990.
528. K. Bartosz, P. T. Artur, W. Marek, A. G. Piotr and S. Mirosław, *Mater. Res. Express*, 2014, 1, 035040.
529. C. P. Deck and K. Vecchio, *Carbon*, 2006, 44, 267-275.
530. G. Atthipalli, R. Epur, P. N. Kumta, M. J. Yang, J. K. Lee and J. L. Gray, *J. Phys. Chem. C*, 2011, 115, 3534-3538.
531. S. Neupane, M. Lastres, M. Chiarella, W. Li, Q. Su and G. Du, *Carbon*, 2012, 50, 2641-2650.
532. A. Banerjee, K. K. Upadhyay, D. Puthusseri, V. Aravindan, S. Madhavi and S. Ogale, *Nanoscale*, 2014, 6, 4387-4394.
533. V. Jourdain and C. Bichara, *Carbon*, 2013, 58, 2-39.
534. L. Gan and Z. Luo, *ACS Nano*, 2013, 7, 9480-9488.
535. I. Vlassiouk, M. Regmi, P. F. Fulvio, S. Dai, P. Datskos, G. Eres and S. Smirnov, *ACS Nano*, 2011, 5, 6069-6076.
536. M. Losurdo, M. M. Giangregorio, P. Capezzuto and G. Bruno, *Phys. Chem. Chem. Phys.*, 2011, 13, 20836-20843.
537. J. Y. Kim, Y. K. Lee, H. S. Park, J. W. Park, D. K. Park, J. H. Joo, W. H. Lee, Y. K. Ko, P. J. Reucroft and B. R. Cho, *Thin Solid Films*, 1998, 330, 190-195.
538. Y. Miyata, K. Kamon, K. Ohashi, R. Kitaura, M. Yoshimura and H. Shinohara, *Appl. Phys. Lett.*, 2010, 96, 263105.
539. A.-C. Dupuis, *Prog. Mater. Sci.*, 2005, 50, 929-961.
540. B. L. Farmer, D. M. Holmes, L. J. Vandeperre, R. J. Steam and W. J. Clegg, in *Nanomaterials for Structural Applications*, eds. C. C. Berndt, T. E. Fischer, I. Ovidko, G. Skandan and T. Tsakalakos, 2003, vol. 740, pp. 81-86.
541. J. Zhu, J. Jia, F.-l. Kwong and D. H. L. Ng, *Carbon*, 2012, 50, 2504-2512.
542. S. Helveg, C. Lopez-Cartes, J. Sehested, P. L. Hansen, B. S. Clausen, J. R. Rostrup-Nielsen, F. Abild-Pedersen and J. K. Norskov, *Nature*, 2004, 427, 426-429.
543. S. Hofmann, R. Sharma, C. Ducati, G. Du, C. Mattevi, C. Cepek, M. Cantoro, S. Pisana, A. Parvez, F. Cervantes-Sodi, A. C. Ferrari, R. Dunin-Borkowski, S. Lizzit, L. Petaccia, A. Goldoni and J. Robertson, *Nano Lett.*, 2007, 7, 602-608.
544. Y. Homma, H. Liu, D. Takagi and Y. Kobayashi, *Nano Res.*, 2009, 2, 793-799.
545. A. A. Onoprienko and N. I. Danilenko, *Powder Metall. Mat. Ceram.*, 2009, 48, 93-99.
546. M. Berndt, PhD Thesis, Dresden University of Technology, 2009.
547. K. Takahashi, K. Yamada, H. Kato, H. Hibino and Y. Homma, *Surf. Sci.*, 2012, 606, 728-732.
548. A. Shaikjee, P. J. Franklyn and N. J. Coville, *Carbon*, 2011, 49, 2950-2959.
549. F. Perrozzi, S. Prezioso, M. Donarelli, F. Bisti, P. De Marco, S. Santucci, M. Nardone, E. Treossi, V. Palermo and L. Ottaviano, *J. Phys. Chem., C*, 2012, 117, 620-625.
550. http://four-point-probes.com/haldor-topsoe-geometric-factors-in-four-point-resistivity-measurement/#hal, Accessed 25/01/2015.
551. B. Marinho, M. Ghislandi, E. Tkalya, C. E. Koning and G. de With, *Powder Technol.*, 2012, 221, 351-358.

Appendix A Supporting information for Chapter 3

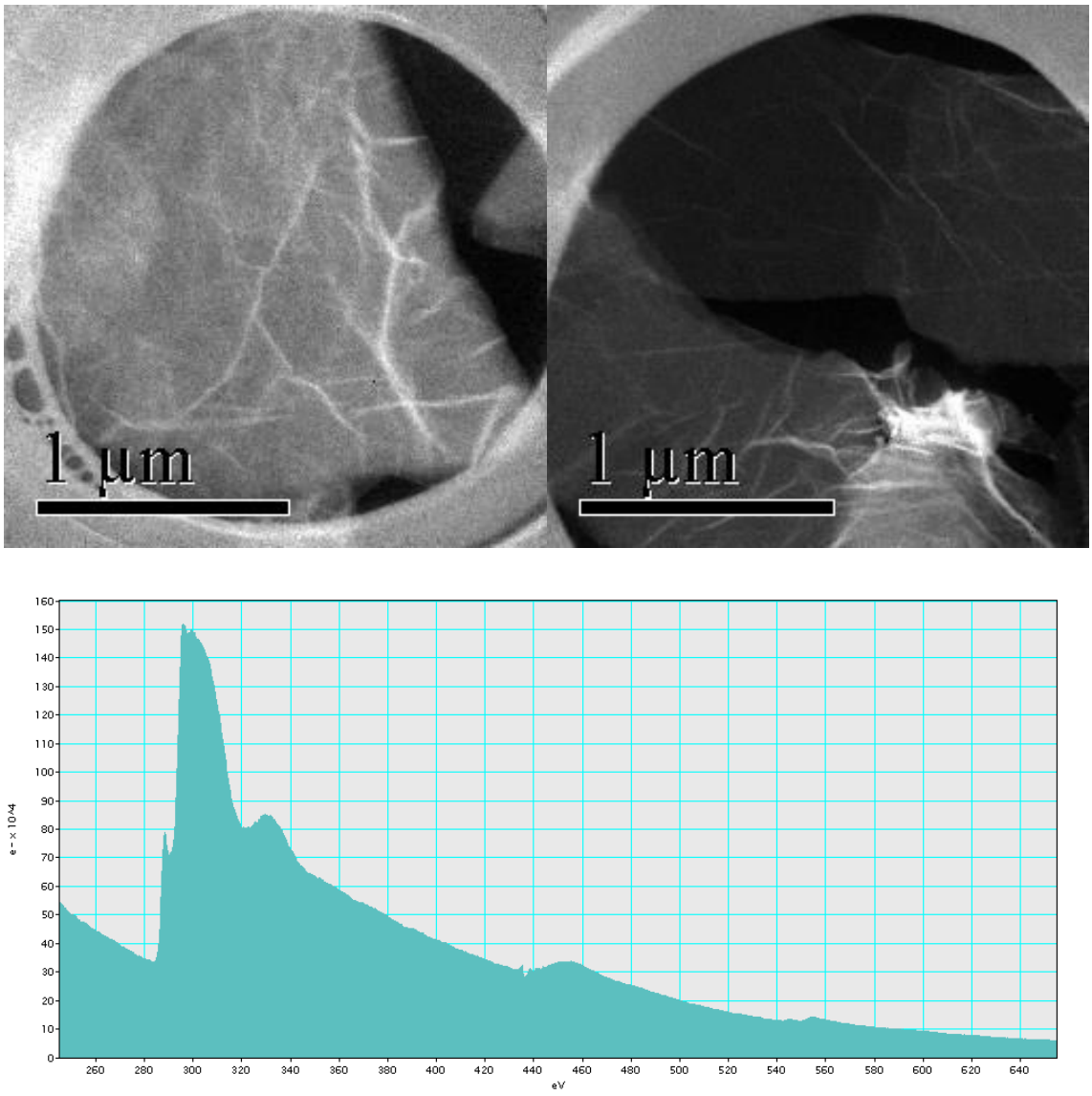

Figure A1: EFTEM carbon maps (top) and C K-edge EELS spectrum (bottom) for 'post-wash' GO refluxed in water for 24 h.

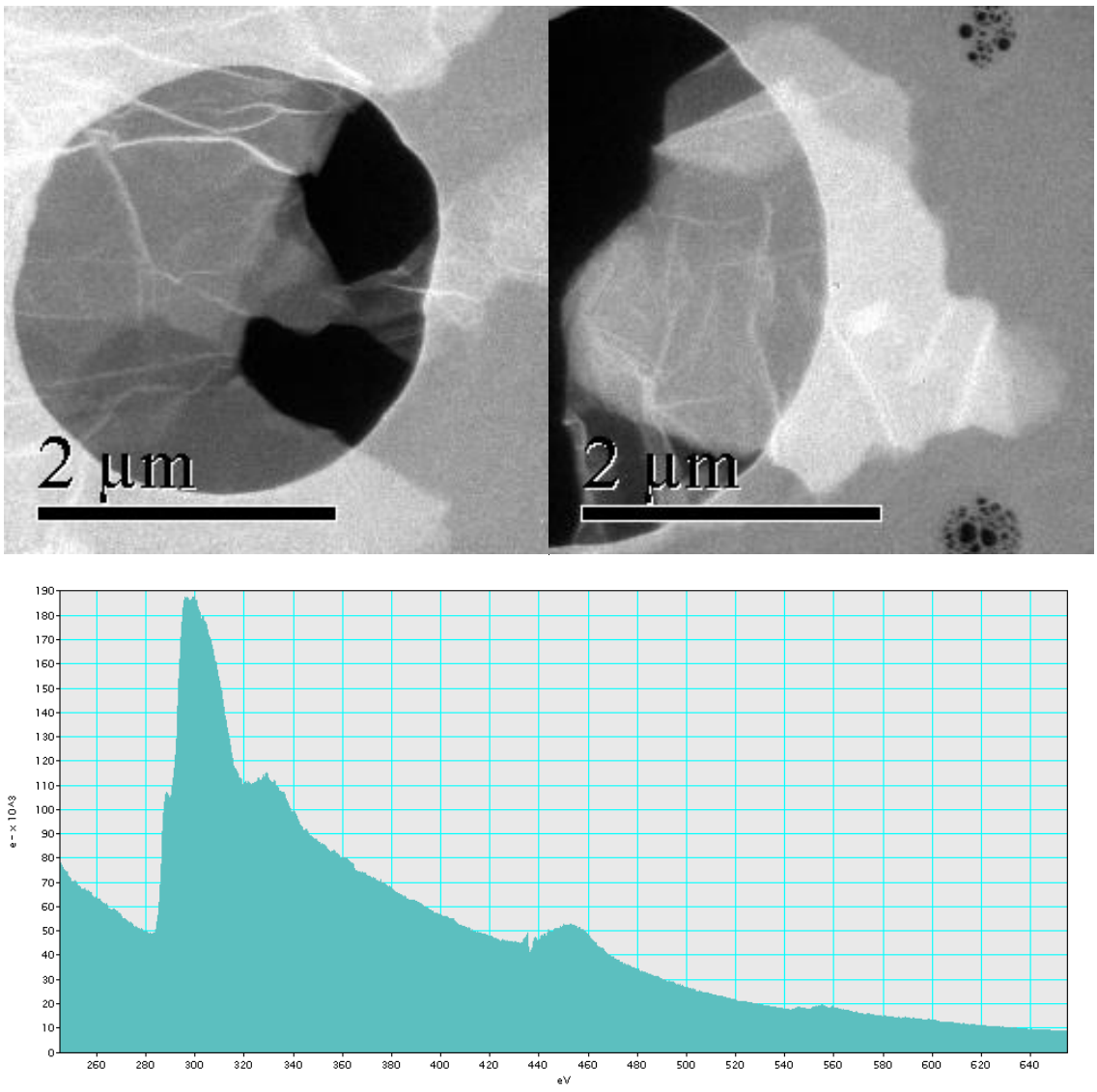

Figure A2: EFTEM carbon maps (top) and C K-edge EELS spectrum (bottom) for ‘pre-wash’ GO refluxed in water for 24 h.

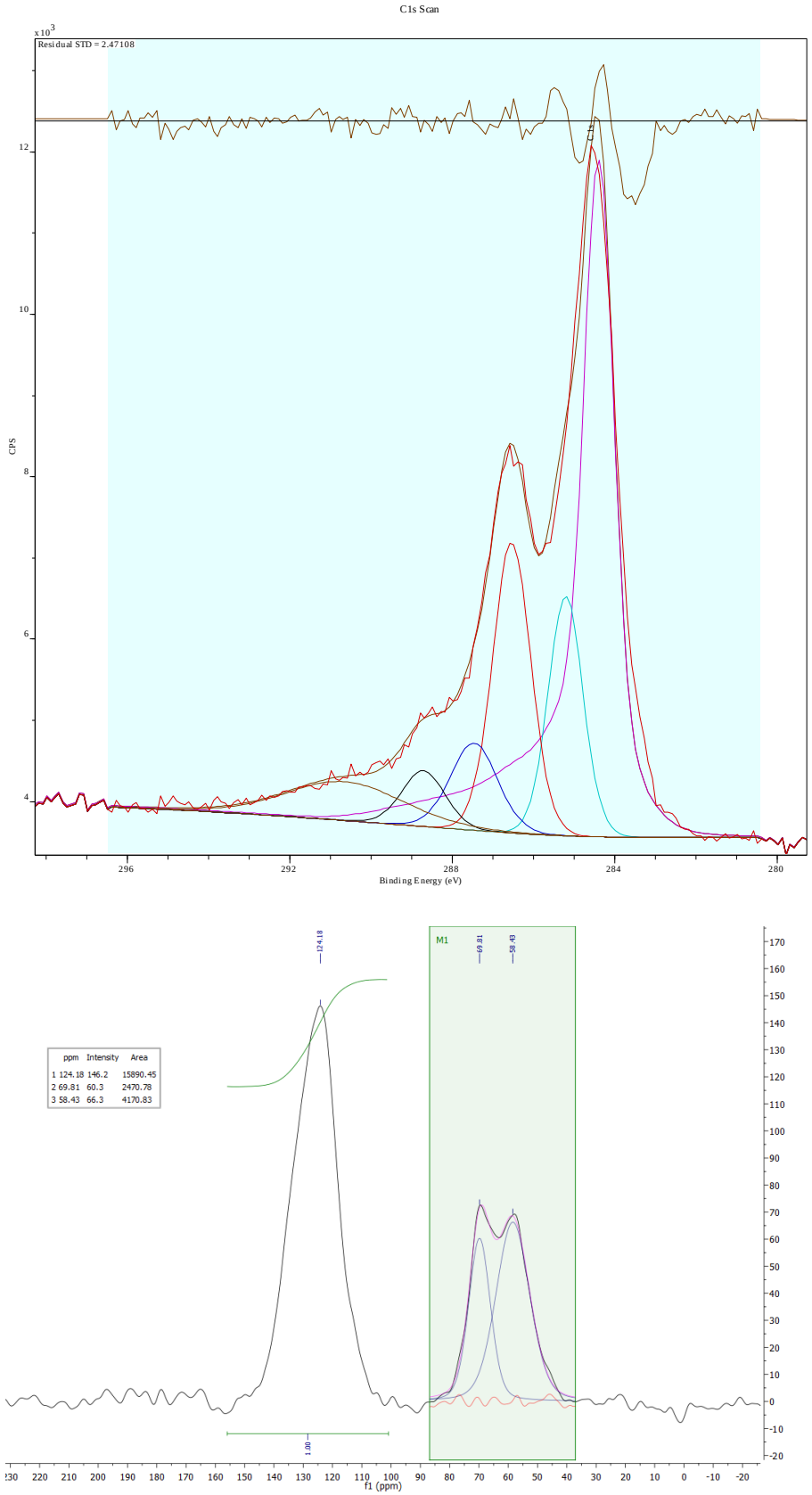

Figure A3: C 1s XPS experimental lineshape (red) for 'post-wash' GO fit into C=C (pink), C-C (green), C-O (red), C=O (blue), COOH (black) and Pi-Pi (brown) components with a Tougaard background using a measured rGO lineshape to fit the C=C (top), and SSNMR spectra for sample (bottom).

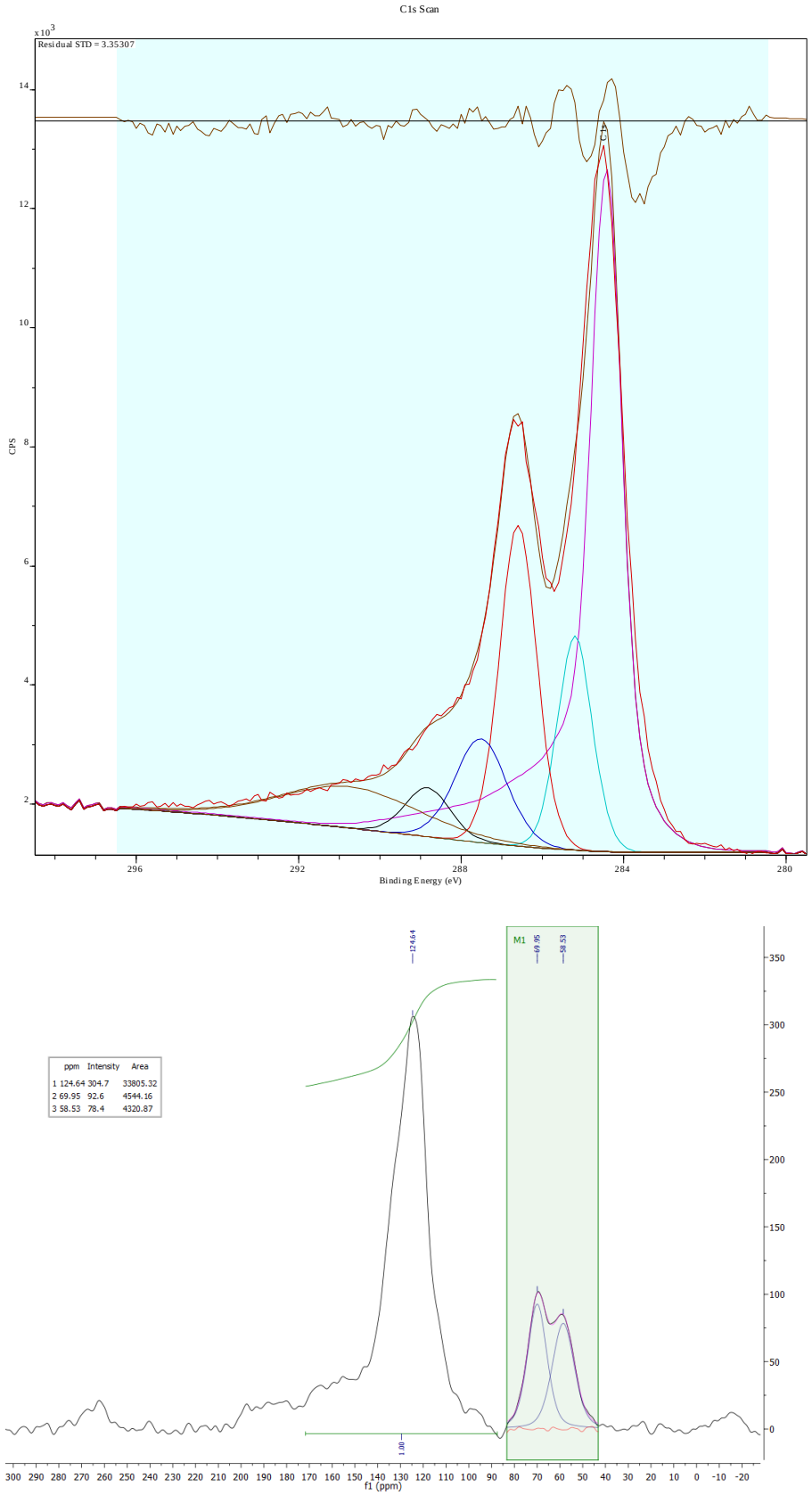

Figure A4: C 1s XPS experimental lineshape (red) for 'pre-wash' GO fit into C=C (pink), C-C (green), C-O (red), C=O (blue), COOH (black) and Pi-Pi (brown) components with a Tougaard background using a measured rGO lineshape to fit the C=C (top), and SSNMR spectra for sample (bottom).

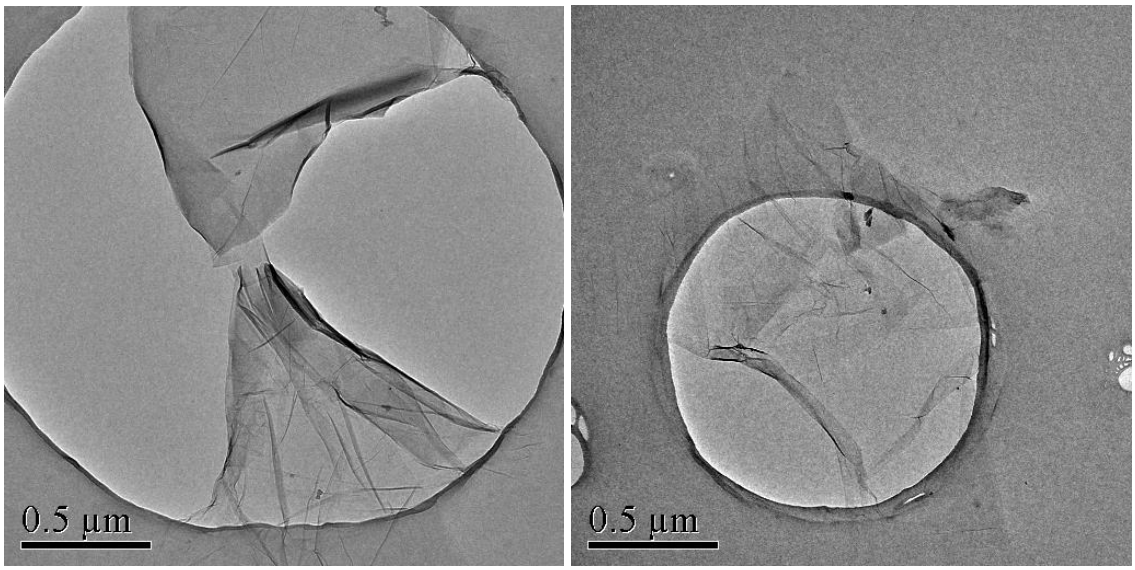

Figure A5: TEM images of ‘pre-wash’ GO refluxed in water for 4 h.

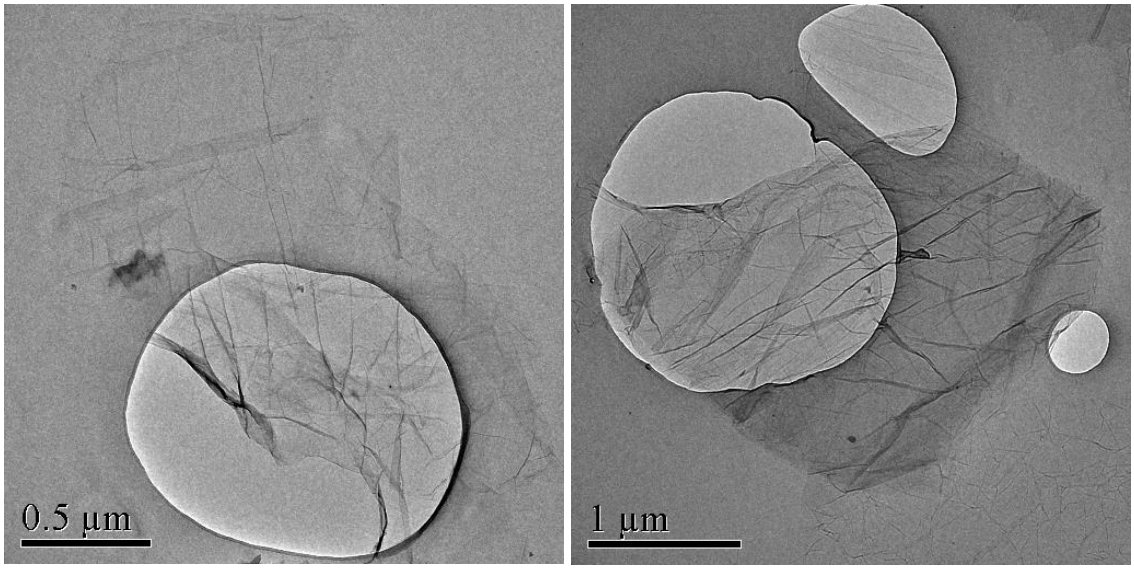

Figure A6: TEM images of ‘pre-wash’ GO refluxed in water for 8 h.

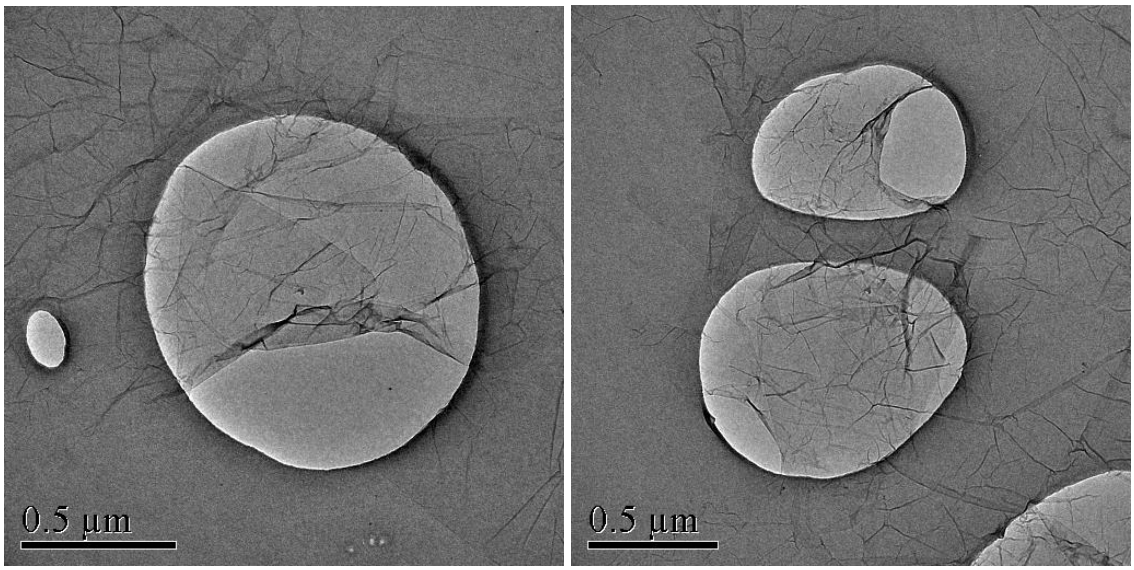

Figure A7: TEM images of ‘pre-wash’ GO refluxed in water for 12 h.

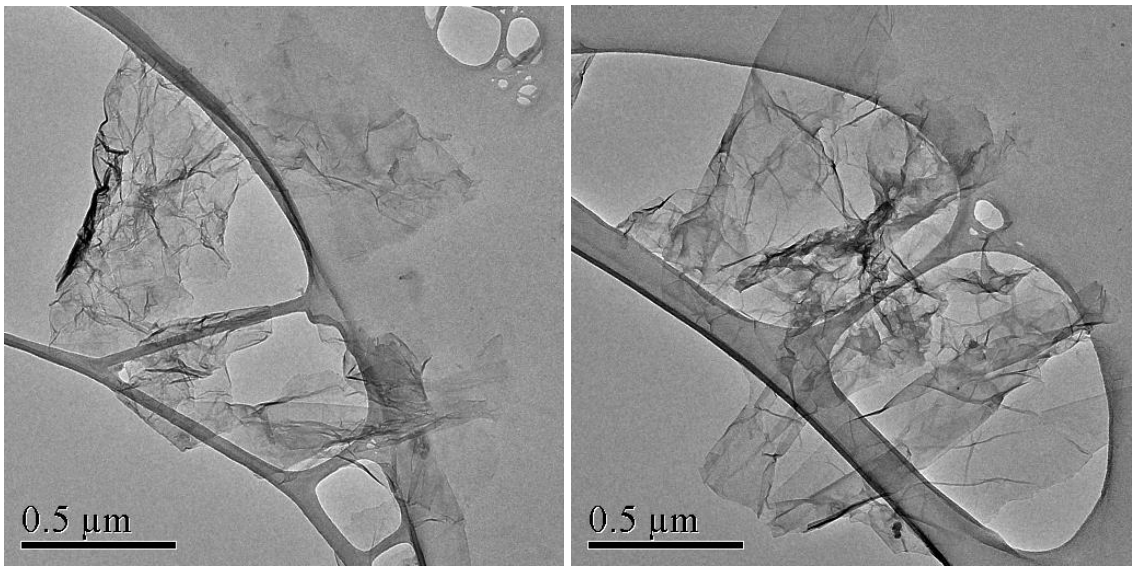

Figure A8: TEM images of ‘pre-wash’ GO refluxed in water for 120 h.

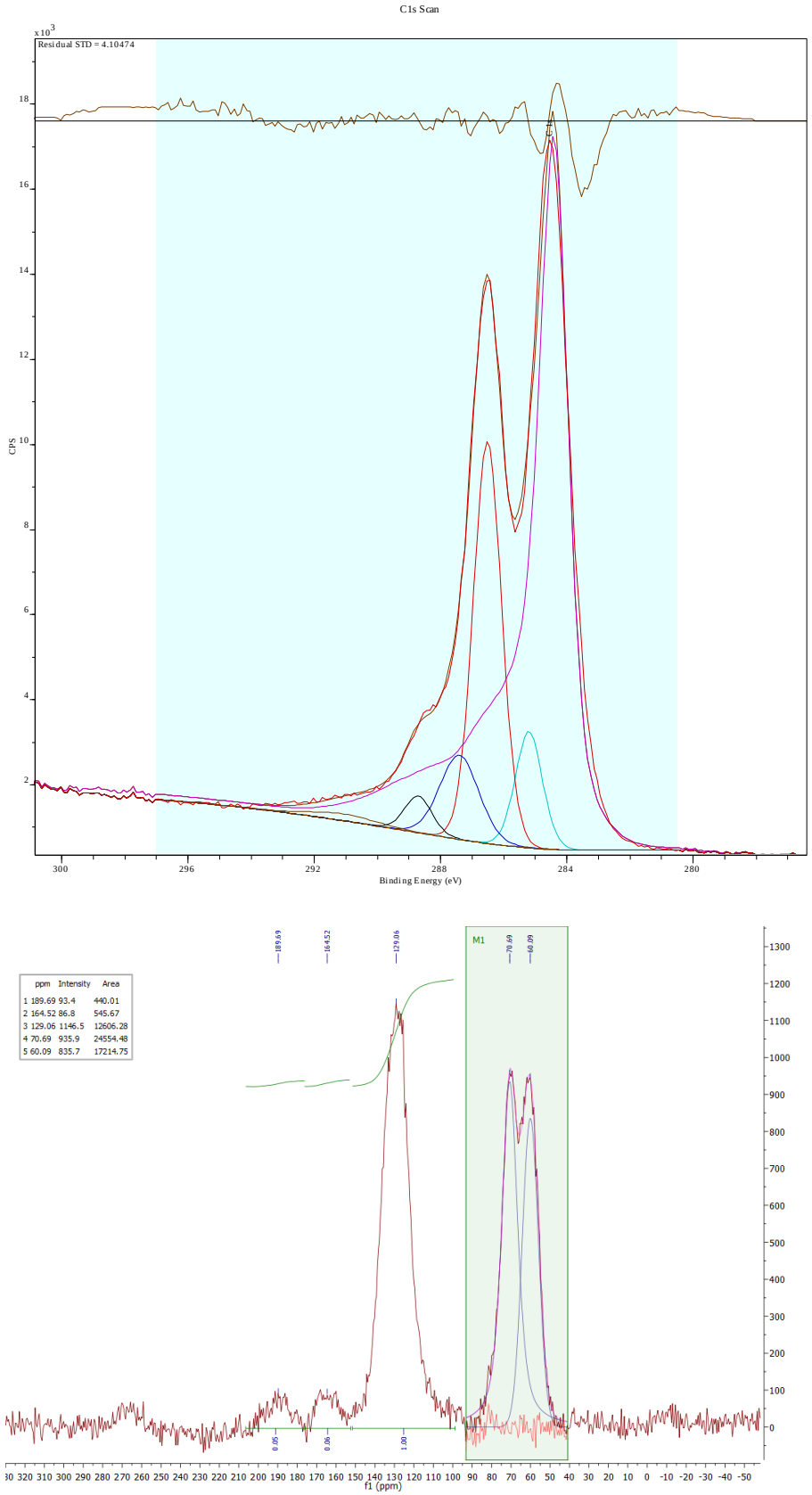

Figure A9: C 1s XPS experimental lineshape (red) for 'pre-wash' GO refluxed in water for 4 h fit into C=C (pink), C-C (green), C-O (red), C=O (blue), COOH (black) and Pi-Pi (brown) components with a Tougaard background using a measured rGO lineshape to fit the C=C (top), and SSNMR spectra for sample (bottom).

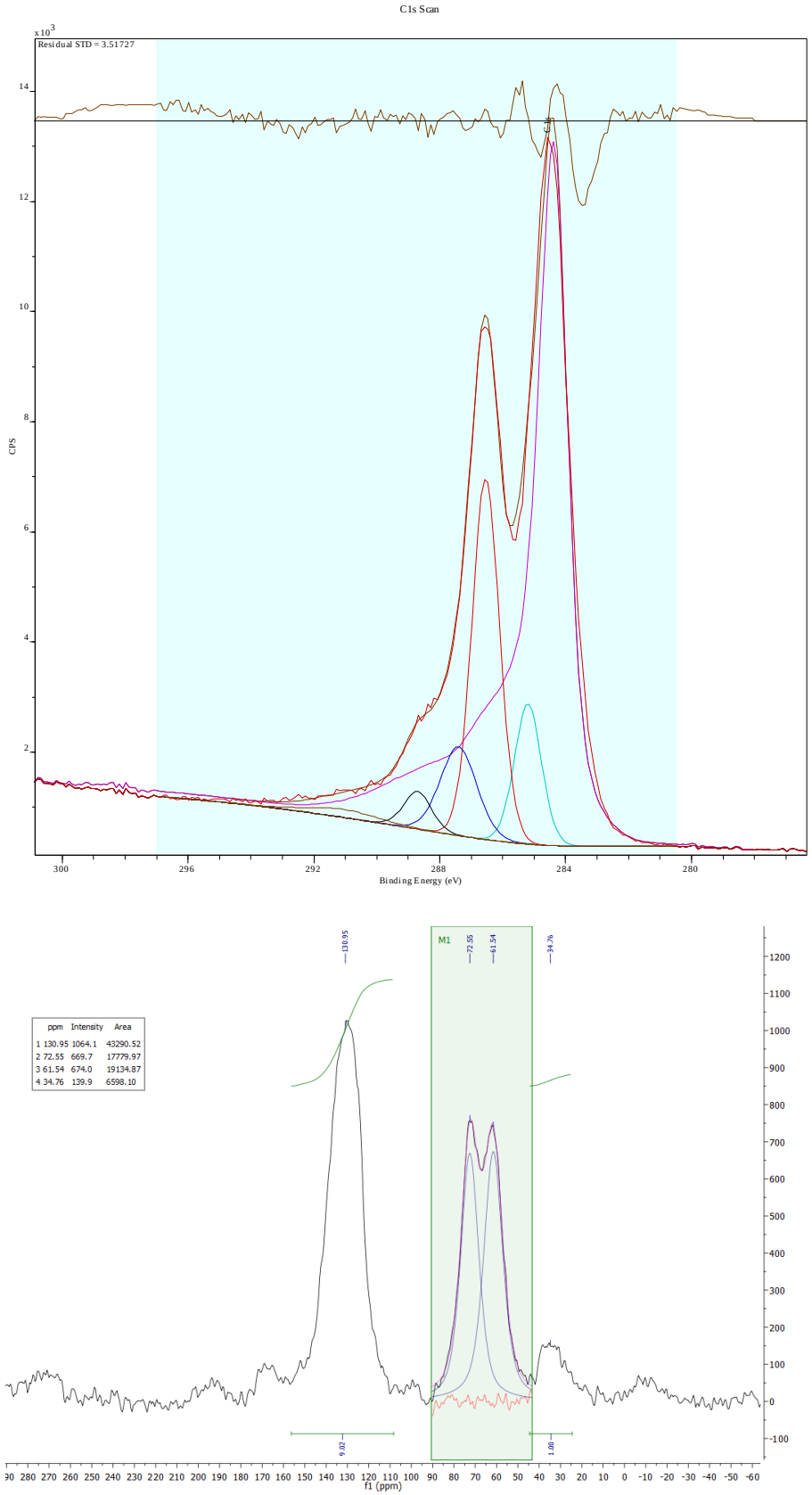

Figure A10: C 1s XPS experimental lineshape (red) for 'pre-wash' GO refluxed in water for 8 h fit into C=C (pink), C-C (green), C-O (red), C=O (blue), COOH (black) and Pi-Pi (brown) components with a Tougaard background using a measured rGO lineshape to fit the C=C (top), and SSNMR spectra for sample (bottom).

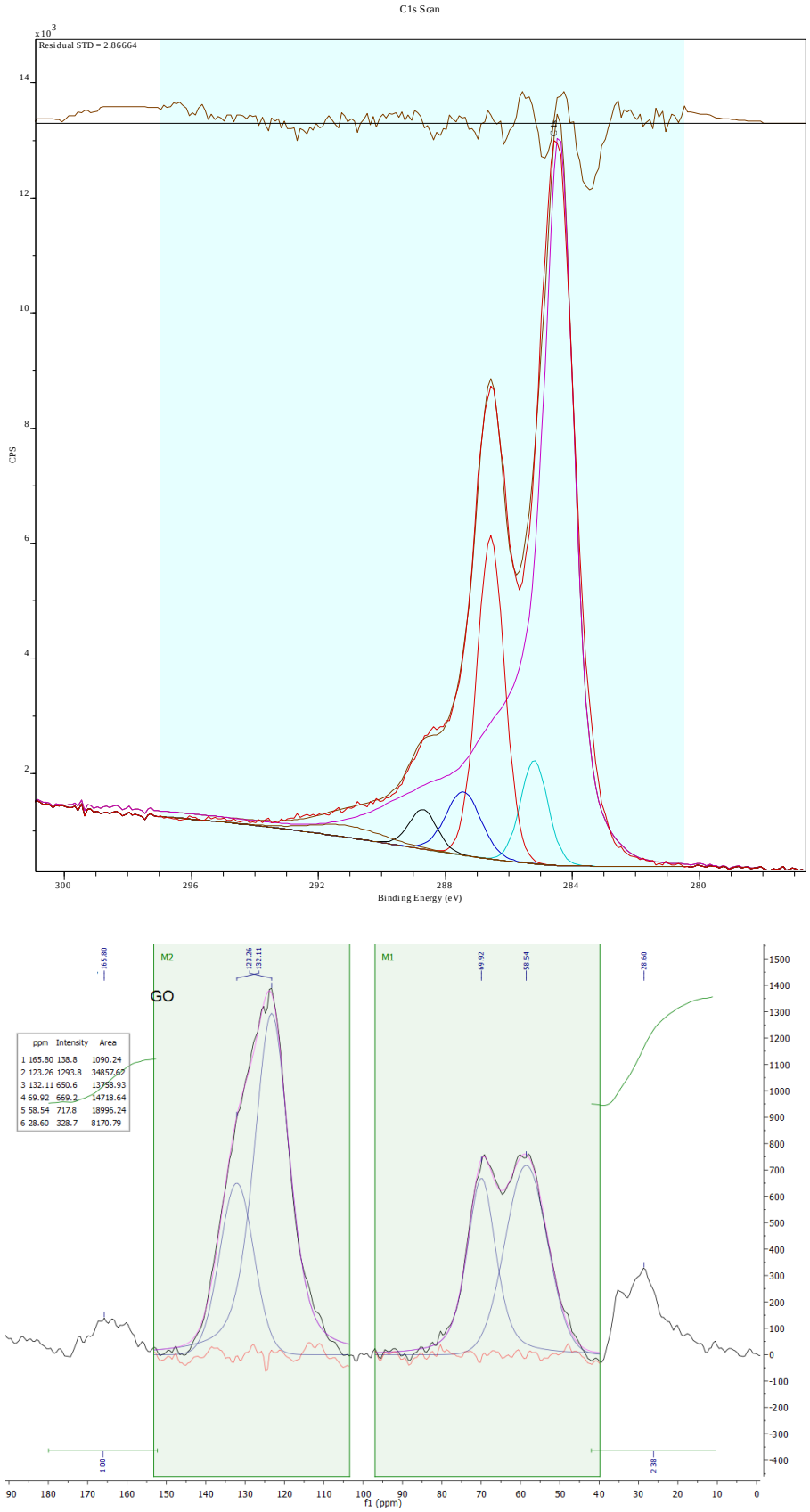

Figure A11: C 1s XPS experimental lineshape (red) for 'pre-wash' GO refluxed in water for 12 h fit into C=C (pink), C-C (green), C-O (red), C=O (blue), COOH (black) and Pi-Pi (brown) components with a Tougaard background using a measured rGO lineshape to fit the C=C (top), and SSNMR spectra for sample (bottom).

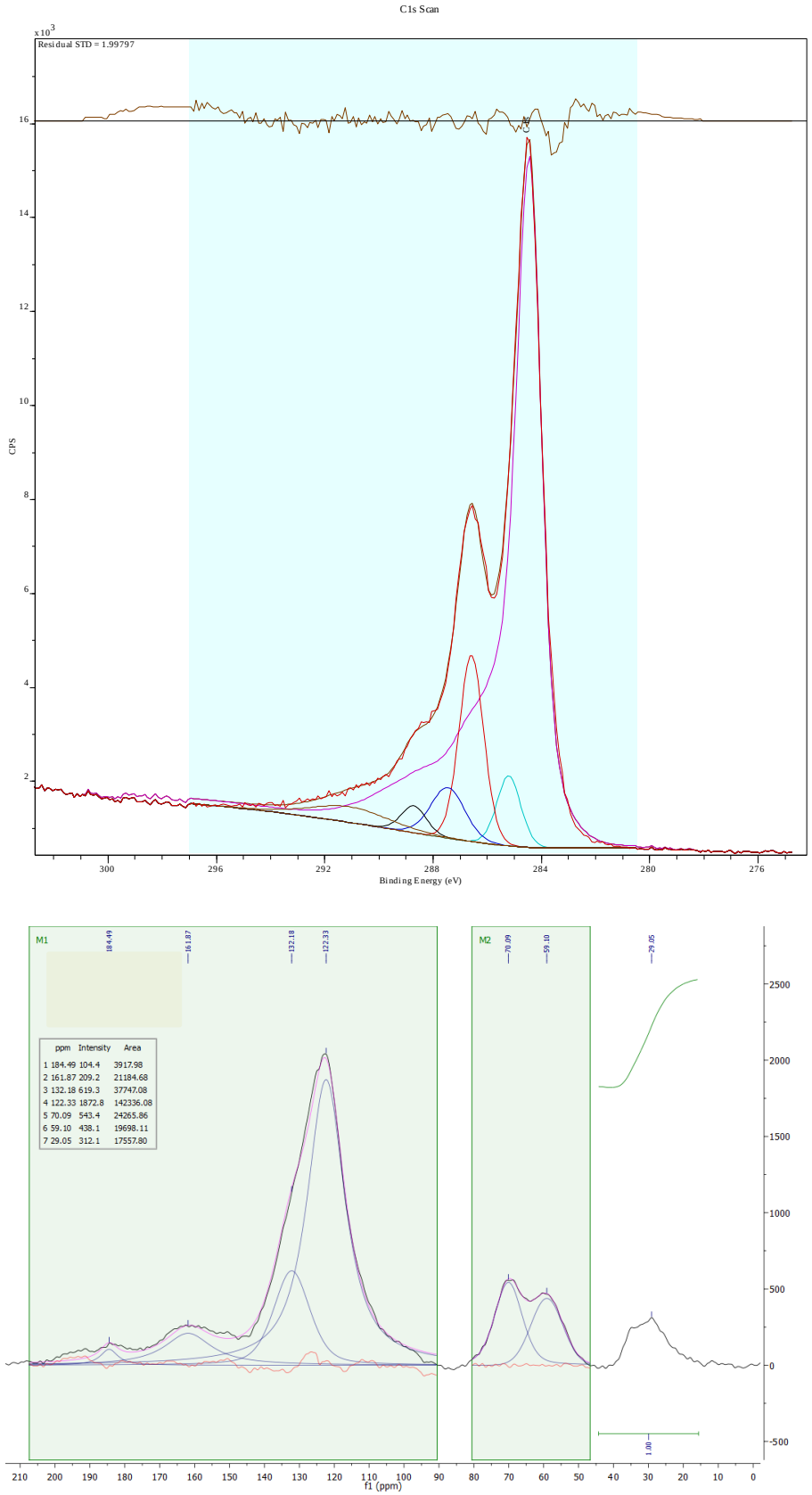

Figure A12: C 1s XPS experimental lineshape (red) for 'pre-wash' GO refluxed in water for 24 h fit into C=C (pink), C-C (green), C-O (red), C=O (blue), COOH (black) and Pi-Pi (brown) components with a Tougaard background using a measured rGO lineshape to fit the C=C (top), and SSNMR spectra for sample (bottom).

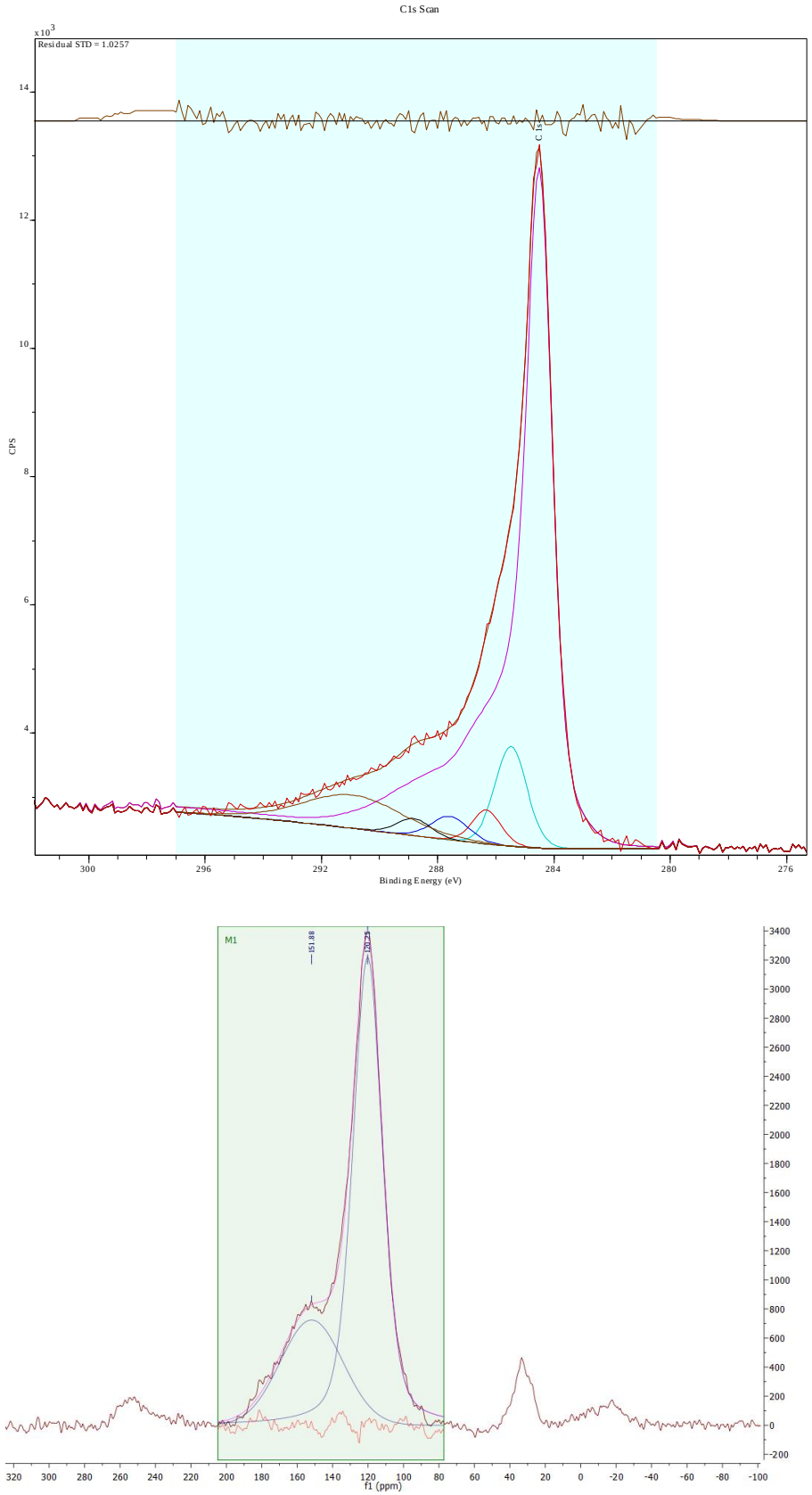

Figure A13: C 1s XPS experimental lineshape (red) for ‘pre-wash’ GO refluxed in water for 120 h fit into C=C (pink), C-C (green), C-O (red), C=O (blue), COOH (black) and Pi-Pi (brown) components with a Tougaard background using a measured rGO lineshape to fit the C=C (top), and SSNMR spectra for sample (bottom).

UV-vis λ_{max} (nm)	Sheet resistance (Ω/□)
266	(2.60 ± 0.02) x 10^3

Figure A14: Photograph (top) and UV-vis and electrical conductivity data (bottom) for GO foam heated in air at 150 °C for 24 h.

Appendix B Supporting information for Chapter 4

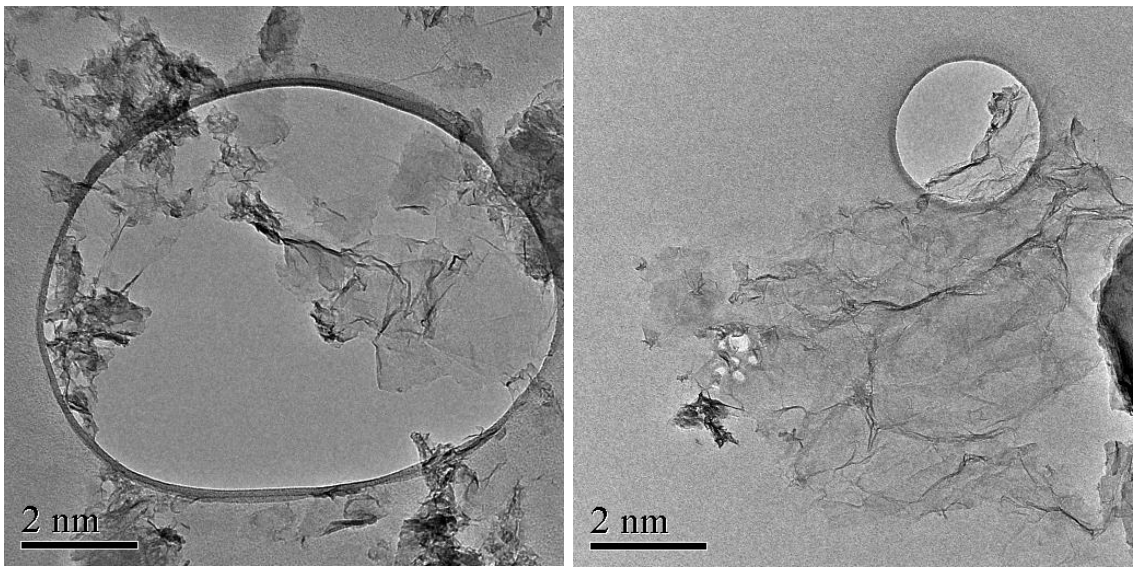

Figure B1: TEM images of ‘pre-wash’ GO refluxed in 0.5 M arginine for 1 h

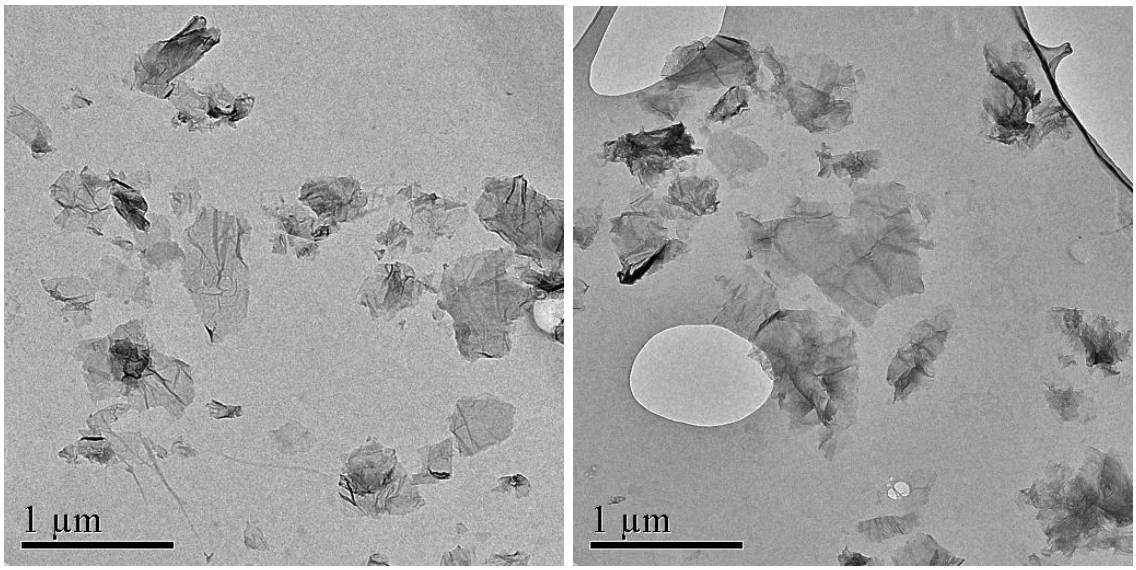

Figure B2: TEM images of ‘pre-wash’ GO refluxed in 0.5 M arginine for 4 h

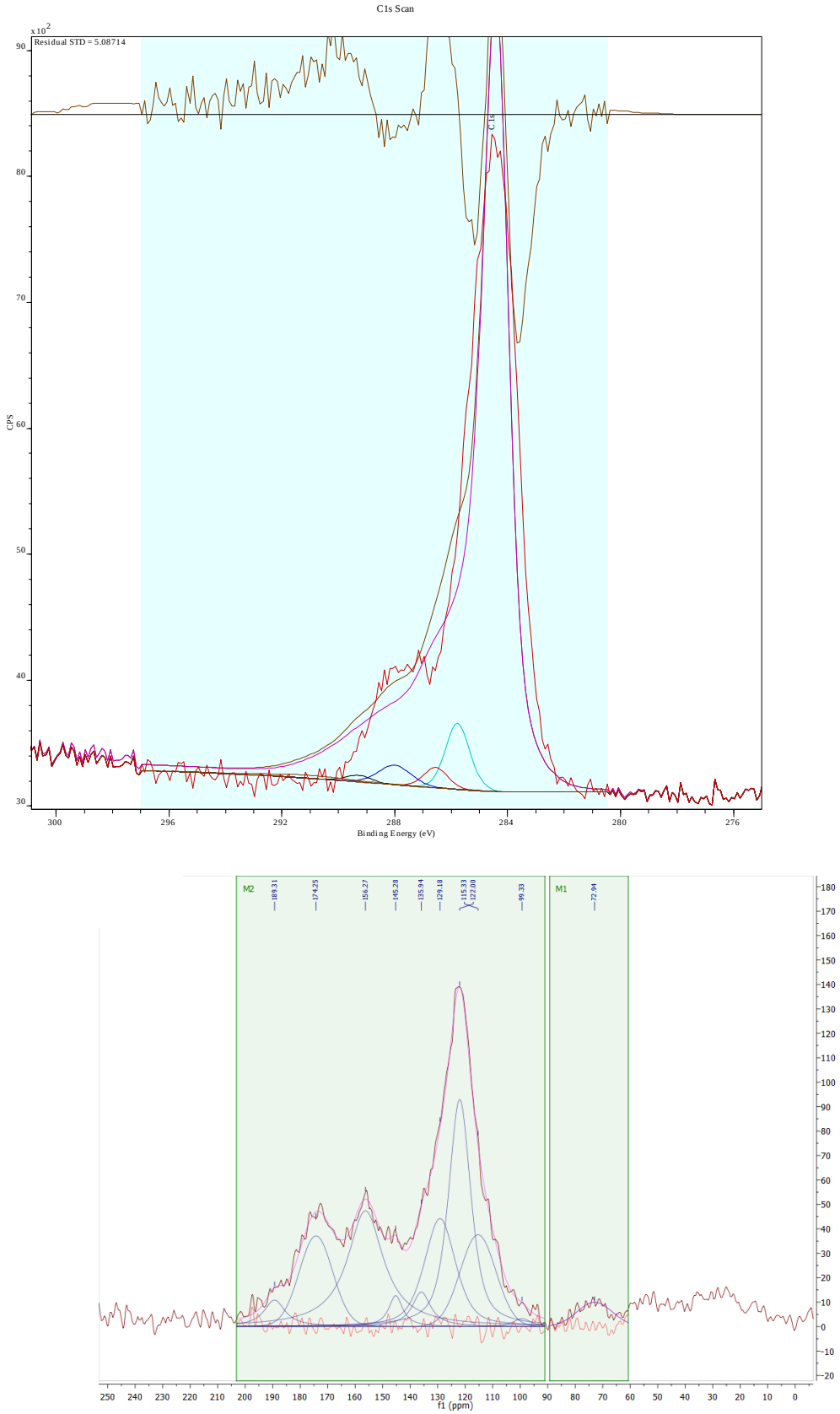

Figure B3: C 1s XPS experimental lineshape (red) for 'pre-wash' GO refluxed in 0.5 M arginine for 1 h fit into C=C (pink), C-C (green), C-O (red), C=O (blue), COOH (black) and Pi-Pi (brown) components with a Tougaard background using a measured rGO lineshape to fit the C=C (top), and SSNMR spectra for sample (bottom).

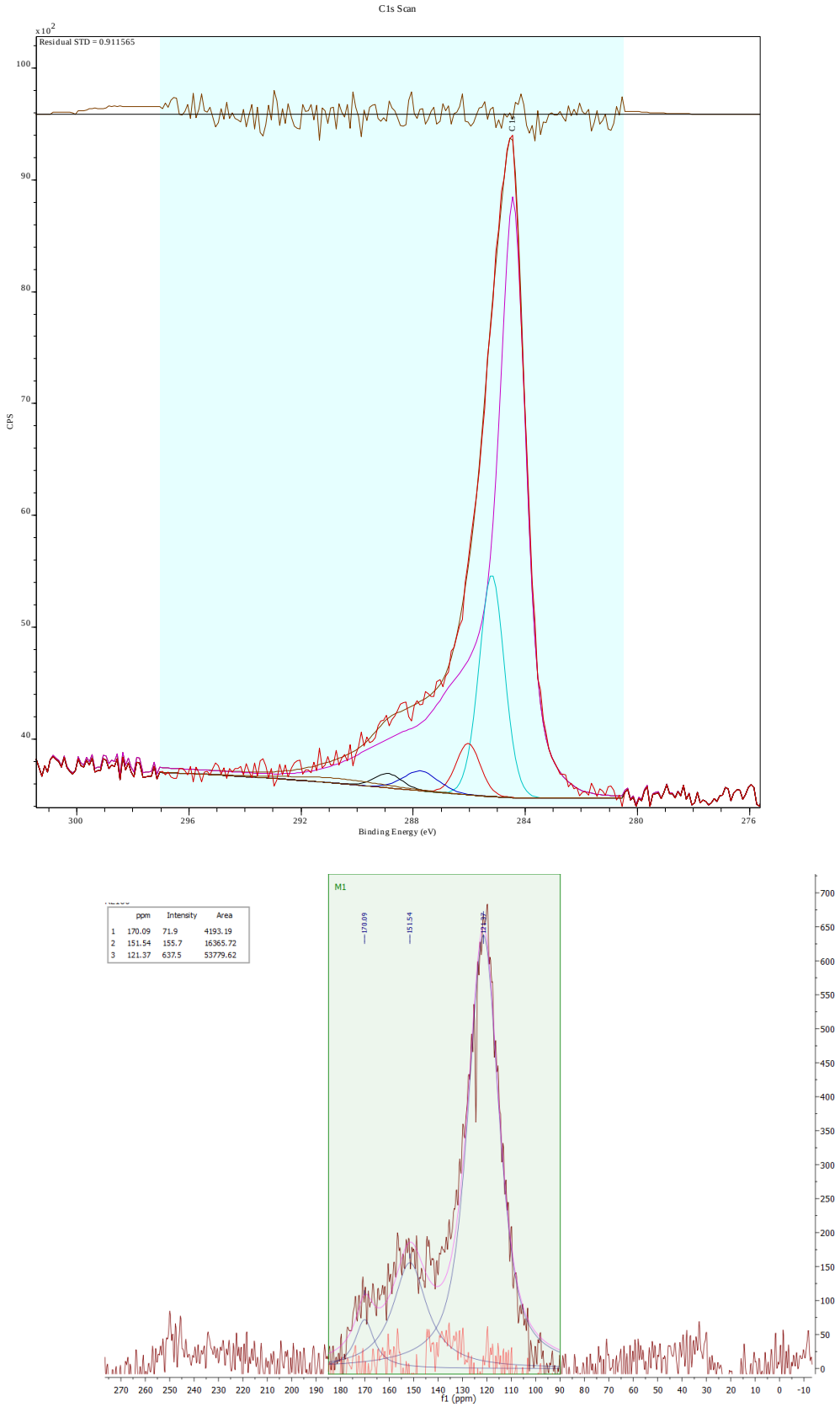

Figure B4: C 1s XPS experimental lineshape (red) for 'pre-wash' GO refluxed in 0.5 M arginine for 4 h fit into C=C (pink), C-C (green), C-O (red), C=O (blue), COOH (black) and Pi-Pi (brown) components with a Tougaard background using a measured rGO lineshape to fit the C=C (top), and SSNMR spectra for sample (bottom).

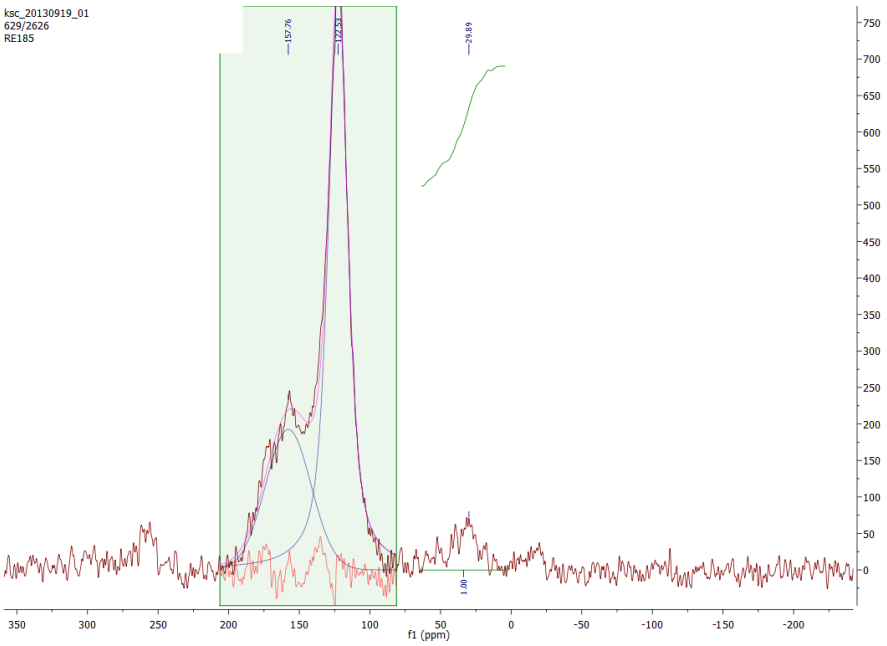

Figure B5: SSNMR spectra for 'pre-wash' GO refluxed in 0.5 M arginine for 8 h. XPS not measured on this sample.

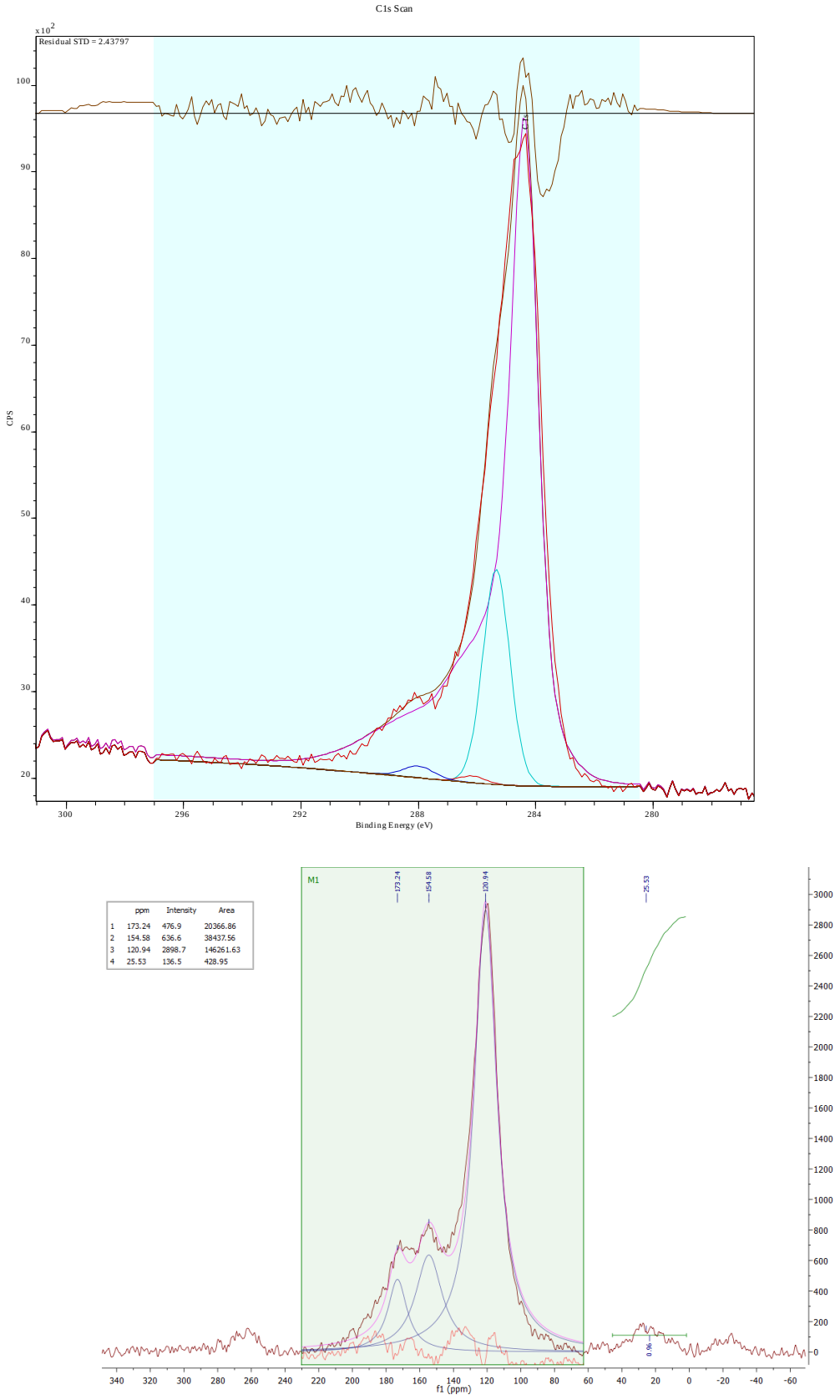

Figure B6: C 1s XPS experimental lineshape (red) for 'pre-wash' GO refluxed in 0.5 M arginine for 24 h fit into C=C (pink), C-C (green), C-O (red), C=O (blue), COOH (black) and Pi-Pi (brown) components with a Tougaard background using a measured rGO lineshape to fit the C=C (top), and SSNMR spectra for sample (bottom).

Appendix C Supporting information for Chapter 5

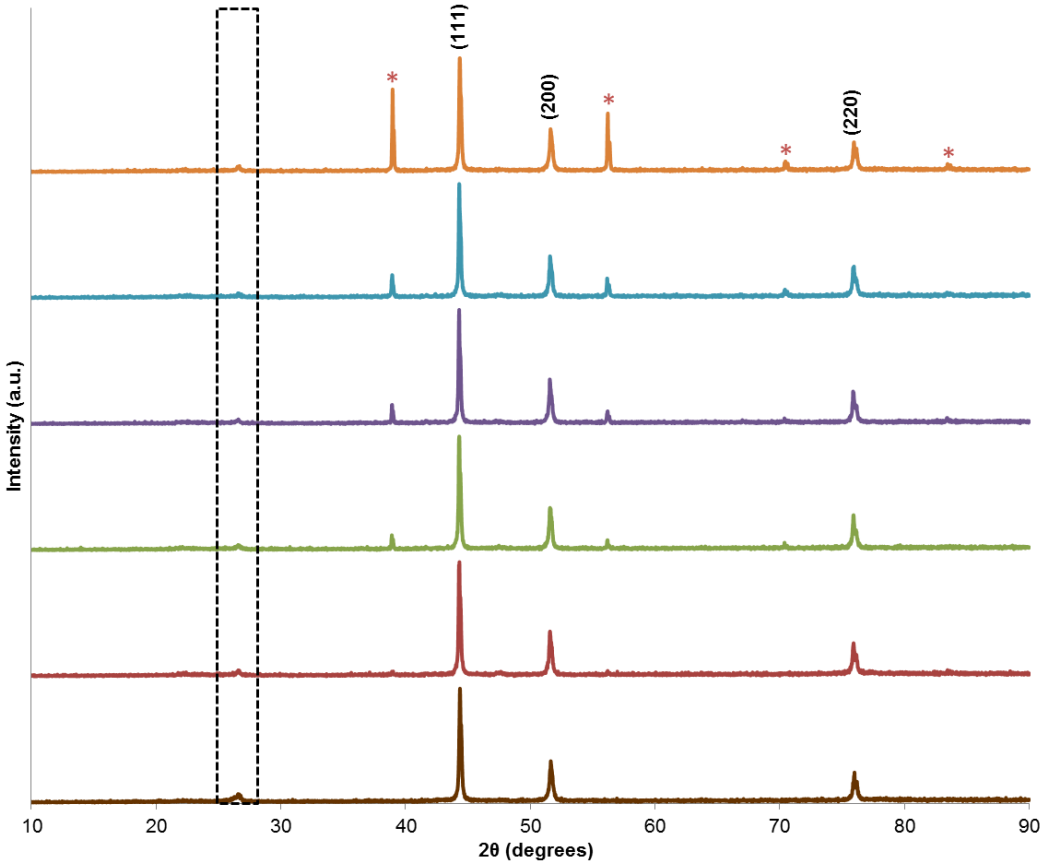

Figure C1: XRPD spectra of the doped cobalt carbonate catalysts after the CVD reaction with ethanol, showing that the only crystalline form of cobalt that is present it $Co^{(0)}$ (indexed on spectra). The relative proportion of the NaF peaks increases with doping level (as anticipated) for ~0 (brown), ~1 (red), ~2 (green), ~3 (purple), ~5 (blue) and ~9 (orange) wt. % Na doped samples. The carbon peak is highlighted by the dashed box.

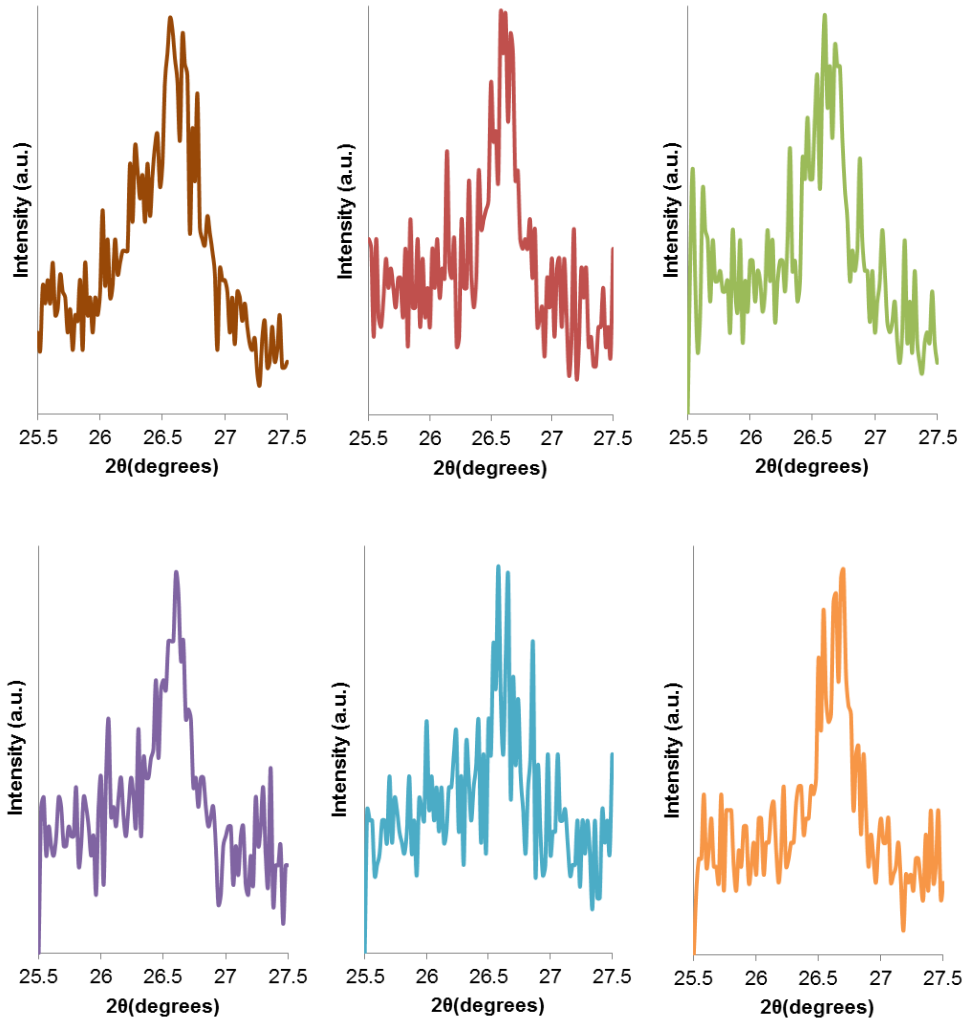

Figure C2: Graphite (002) peaks from the XRPD spectra of the doped cobalt carbonate catalysts after the CVD reaction with ethanol for the ~0 (brown), ~1 (red), ~2 (green), ~3 (purple), ~5 (blue) and ~9 (orange) wt. % Na doped samples.

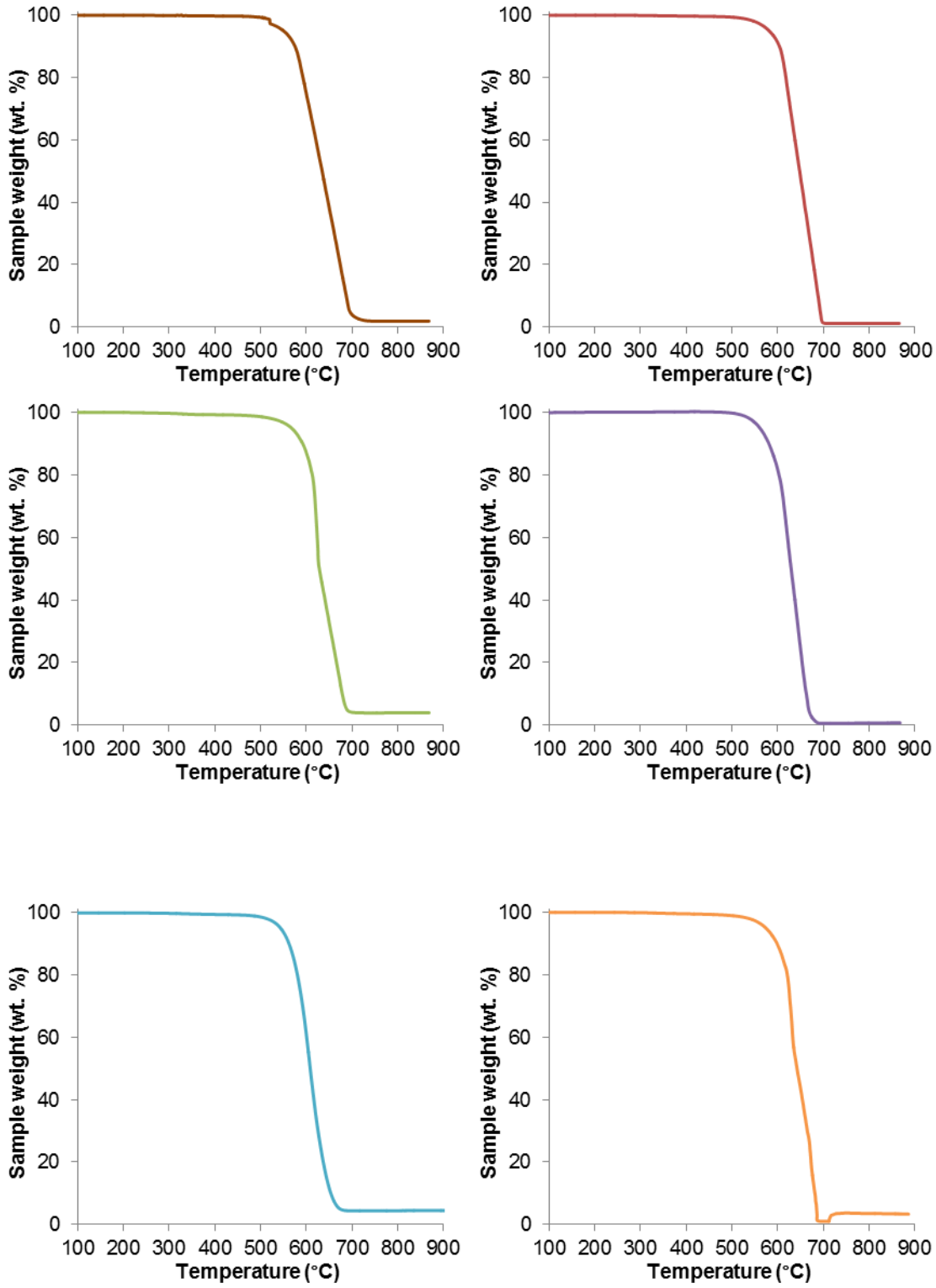

Figure C3: TGA spectra of the purified carbon products from the CVD of ethanol over the doped cobalt carbonate catalysts with ~0 (brown), ~1 (red), ~2 (green), ~3 (purple), ~5 (blue) and ~9 (orange) wt. % Na. Spectra recorded in air at a ramp rate of 10 °C/min.

Appendix D Supporting information for Chapter 6

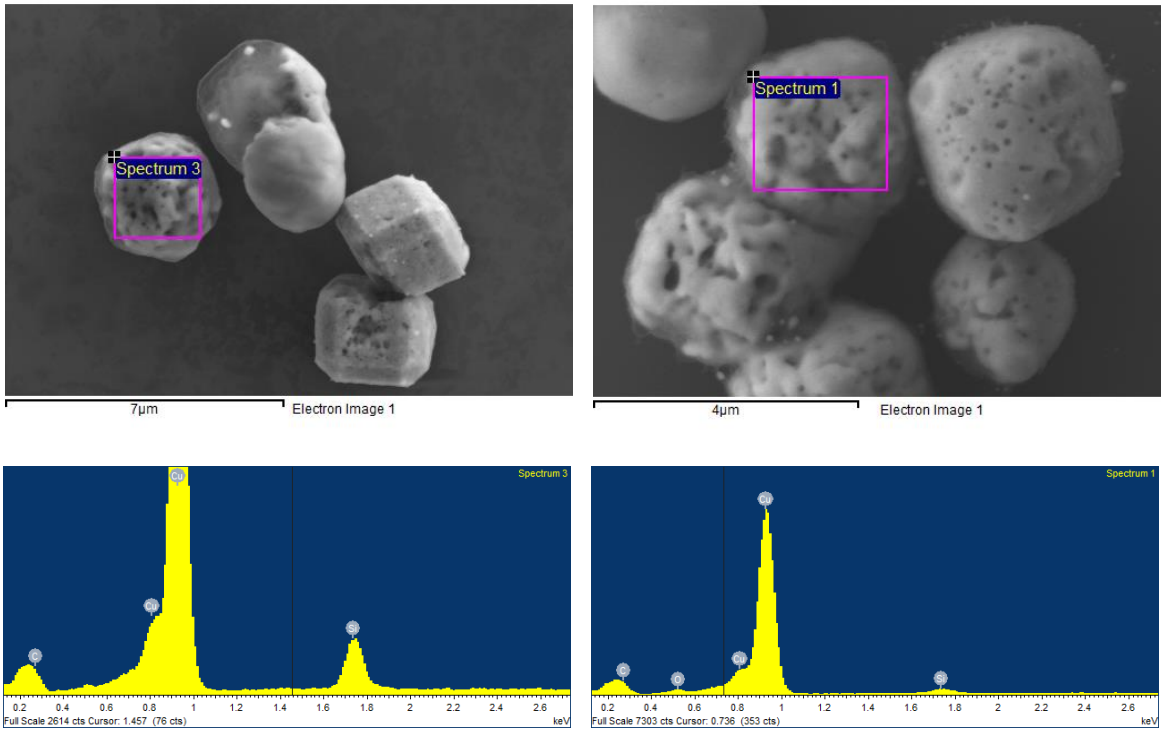

Figure D1: SEM images (top) and associated EDXS spectra (bottom) for Cu_2O polyhedra after the CVD reaction with ethanol (standard run, 800 °C), showing the presence of a carbon signal for the 'mottled' polyhedra.

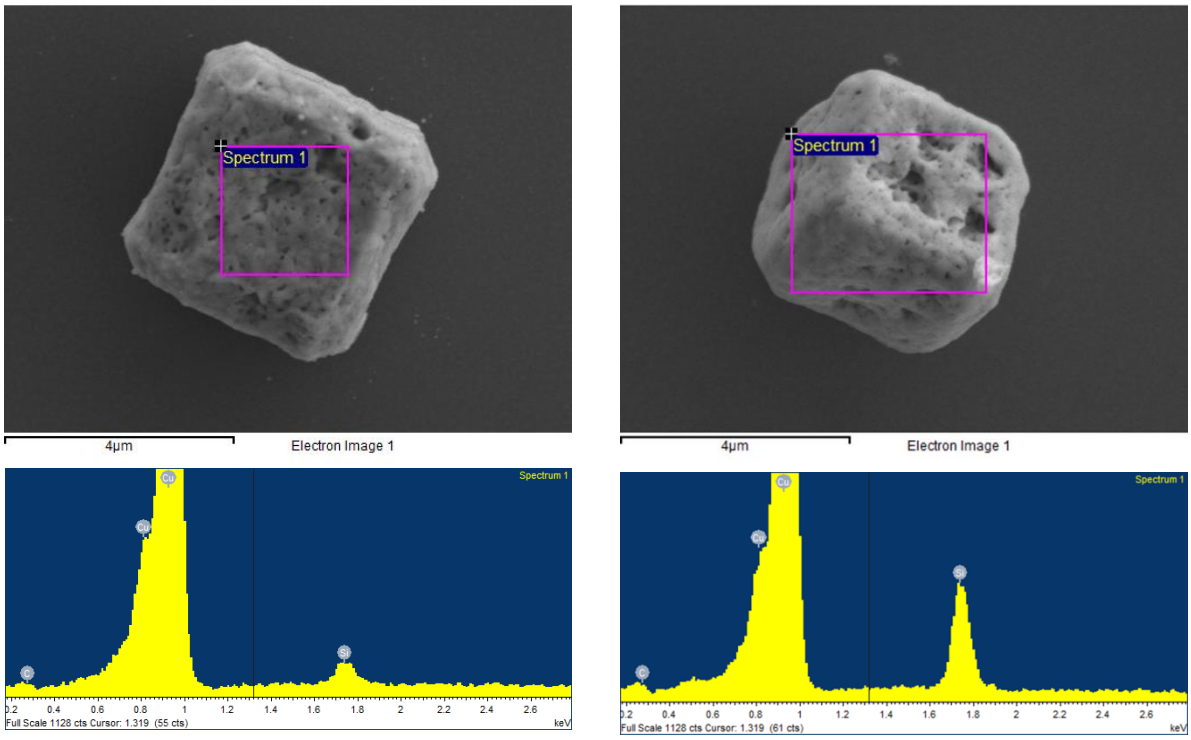

Figure D2: SEM images (top) and associated EDXS (bottom) for Cu_2O polyhedra after heating to 800 °C in Ar/H_2, then exposing to ethanol vapours and Ar during growth, showing a very weak carbon signal in EDXS spectra.

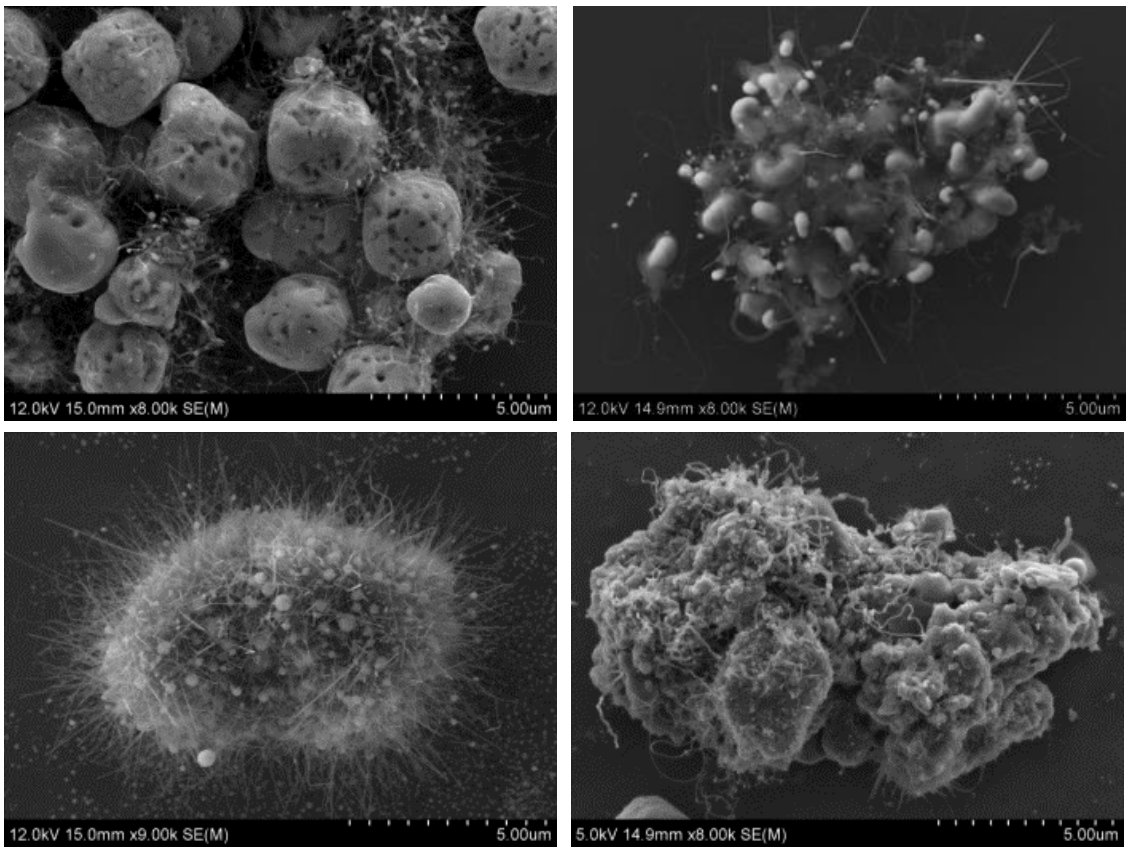

Figure D3: SEM images of the carbon grown via CVD of ethanol over the Cu_2O polyhedra, showing examples of different carbon structures that were grown alongside the carbon cubes..